THE UNIVERSITY OF
TECHNOLOGY, SYDNEY

Faculty of Engineering

# Experimental and Numerical Investigation into Impact Bending Collapse of Rectangular Hollow Sections

A thesis submitted for the degree of

**Doctor of Philosophy**

**Graham Roy Johnson**

February, 2001

## CERTIFICATE OF AUTHORSHIP / ORIGINALITY

I certify that this thesis has not previously been submitted for a degree nor has it been submitted as part of requirements for a degree except as fully acknowledged within the text.

I also certify that the thesis has been written by me. Any help that I have received in my research work and the preparation of the thesis itself has been acknowledged. In addition, I certify that all information sources and literature used are indicated in the thesis.

Signature of Candidate

Production Note:
Signature removed prior to publication.

# ACKNOWLEDGEMENTS

The technical competence of the workshop staff at UTS was outstanding. My thanks go to all of the workshop and technical staff for their help at one stage or another. Their contributions were invaluable and most sincerely appreciated. My specific thanks go to Laurence Stonard, Harold Myers, Bill Firth, Stephen Griffith, Scott Graham, John Grove, Lionel Slade, Charles Evans, Graham Bayley, Stewart Gordan and Ian Gibson.

I would also like to especially thank Chris Chapman for his willing and competent assistance with so many aspects of the laboratory procedures and for the friendship that has developed over the years. The assistance of Dr. Jianchun Li in the operation of the Faculty's shake table facility is also acknowledged.

Special thanks to Bruce Johnson of Electroneering Pty. Ltd. for designing and manufacturing the unique instrumentation used in this thesis. His expert assistance was invaluable. Thanks to Lorenz Eberl for the initial inspiration that sparked this research, for our subsequent discussions and his insightful suggestions.

Funding provided by the school of mechanical engineering for the experimental programme, finite element software licenses and my attendance at the Third International Symposium on Structural Crashworthiness held in England, was much appreciated.

My gratitude also extends to the information technology systems department in the Faculty of Engineering for providing excellent computing facilities and maintaining software licenses. My thanks also go to Compumod Pty. Ltd. for support that extended well beyond the bounds of software maintenance.

My special thanks go to my supervisor Dr. Nong Zhang, for many useful discussions, for guidance, and for his encouragement and comradeship.

I extend my sincere thanks to the many staff within the mechanical engineering school/group who have given me support and encouragement throughout my candidature. In particular I would like to thank Associate Professor Stephen Johnston, Dr. Guang Hong, Dr. Austin Mack, Dr. Fred Sticher, Associate Professor Helen McGregor, Professor John Reizes, Professor Rod Belcher, Professor Frank Swinkels

and Lance Reece. Special thanks also to Associate Professor Stephen Johnston for his excellent editorial comment.

My very special thanks go to Terry Brown, Richard Wiltshire and Dr. Bruce Pearson for their collegiality, their support and encouragement during the tough times and for sharing many great curries. I hope the special friendships that we have developed will be lasting. Thanks also to Richard and Terry for their technical proofing of this thesis. Additionally I wish to thank Richard for the very tangible support he gave this research, whilst he was at UTS.

Lastly, sincere thanks to my family for their patience and steadfast support.

# TABLE OF CONTENTS

Certificate ..... i
Acknowledgements ..... ii
List of Tables ..... xiv
List of Figures ..... xv
List of Plates ..... xxi
Glossary and Notation ..... xxiii
Abstract ..... xxvi

**CHAPTER 1 Introduction** **1**

1.1 BUS ROLLOVER ..... 1
1.2 ADR 59/00 ..... 1
1.3 PLASTIC HINGE RESPONSE IN RHS ..... 4
1.3.1 Performance Parameters ..... 7
1.3.2 Response Phases ..... 7
1.3.3 Effective Hinge Centre ..... 8
1.4 PLASTIC HINGE RESPONSE UNDER IMPACT LOADING ..... 8
1.5 ASSESSING STRUCTURAL RESPONSE TO IMPACT LOADING ..... 9
1.6 ASSESSING PLASTIC HINGE IMPACT RESPONSE ..... 11
1.7 THESIS AIMS & METHODOLOGY ..... 13
1.8 ORIGINAL CONTRIBUTIONS OF THIS THESIS ..... 15
1.9 THESIS OUTLINE ..... 15

**CHAPTER 2 Literature Review** **17**

2.1 HYBRID MODELLING APPROACH FOR STRUCTURAL ANALYSIS ..... 17
2.2 EXPERIMENTAL COLLAPSE OF THIN WALLED MEMBERS ..... 18
2.2.1 Axially Loaded Columns ..... 18
2.2.2 Combined Loading ..... 19
2.2.3 Quasi-Static Bending of RHS ..... 19
2.2.3.1 Initial Elasto-Plastic Post-Buckle Response ..... 19
2.2.3.2 Deep Collapse ..... 20
2.2.3.3 Restricted Collapse ..... 21
2.2.4 Impact Bending Experiments ..... 22
2.2.5 Areas Identified for Investigation ..... 23

2.3 DYNAMIC EFFECTS ..... 24
2.3.1 Influence of Inertia ..... 24
2.3.1.1 Influence of Inertia on Bending Collapse of RHS ..... 26
2.3.1.2 Influence of Inertia - Summary ..... 26
2.3.2 Material Strain Rate Sensitivity ..... 27
2.3.2.1 Strain Rate Sensitivity of Mechanical Properties: yield stress, ultimate tensile strength and ductility ..... 27
2.3.2.2 Strain Rate History ..... 30
2.3.2.3 Material Strain Rate Sensitivity - Summary ..... 30
2.3.2.4 Constitutive Models of Strain Rate Sensitivity ..... 31
2.3.3 Areas Identified for Investigation ..... 33
2.4 NUMERICAL MODELLING ..... 33
2.4.1 Bending Collapse of RHS ..... 34
2.4.2 Mesh Density ..... 35
2.4.3 Material Definition ..... 36
2.4.4 Other Applications of FE Modelling ..... 37
2.4.5 Analytical Models ..... 37
2.4.5.1 Axial Crush ..... 37
2.4.5.2 Bending Models ..... 38
2.4.5.3 Empirical Models ..... 40
2.4.6 Specialised Design Tools ..... 40
2.4.7 Areas Identified for Investigation ..... 41
2.5 QUASI-STATIC DESIGN SCHEMES ..... 41
2.5.1 Theoretical Scaling of Flow Stress ..... 42
2.5.1.1 Choice of Material Strain Rate Sensitivity Model ..... 42
2.5.1.2 Choice of Strain Rate ..... 42
2.5.2 Experimental Scaling of Gross Response ..... 44
2.5.3 Areas Identified for Investigation ..... 46
2.6 RELATED AREAS OF LITERATURE REVIEW ..... 47
2.6.1 Special Considerations for Elevated Strain Rate Material Tests ..... 47
2.6.1.1 Low Strain Rates ..... 47
2.6.1.2 Medium Strain Rates ..... 48
2.6.1.3 High Strain Rates ..... 48
2.6.2 Quasi-Static Mechanical Properties of RHS Material ..... 49
2.6.2.1 RHS Manufacture ..... 49

2.6.2.2 Property Variation around the Section ..... 49
2.6.2.3 Summary of Quasi-Static Properties ..... 53

**CHAPTER 3 Pendulum Bend Test Rig Design** **54**

3.1 INTRODUCTION ..... 54
3.2 SPECIMEN DETAILS ..... 54
3.3 RIG DESIGN ..... 57
3.4 IMPACT PENDULUM DETAILS ..... 59
3.4.1 General Specifications ..... 60
3.4.2 Measurement of Plastic Hinge Response ..... 60
3.4.2.1 Derivation of Hinge Moment from Pendulum Moment ..... 61
3.4.2.2 Calculating Hinge Moment from a Reaction Force ..... 66
3.4.3 Pendulum Acceleration ..... 68
3.4.4 Safety Systems ..... 69
3.4.5 Quasi-Static Test Arrangement ..... 71
3.5 INSTRUMENTATION OVERVIEW ..... 71
3.5.1 Pendulum Travel/Rotation ..... 72
3.5.2 Pendulum Impact Velocity ..... 73
3.5.3 Reaction Force ..... 73
3.5.3.1 Frequency Response of the Strain Amplifier ..... 76
3.5.4 Air Spring Pressure ..... 76
3.5.5 Specimen - Pendulum Contact ..... 76
3.5.6 Hinge Zone Rotation ..... 77
3.5.7 Surface Strains ..... 78
3.5.7.1 Strip Gauge Imbalance, Desensitisation and Cross-talk ..... 79
3.5.7.2 Minimising Cross-Talk, Desensitisation and Imbalance ..... 81
3.5.8 Data Acquisition ..... 81
3.6 CONCLUSIONS ..... 82

**CHAPTER 4 Processing Raw Test Data** **83**

4.1 INTRODUCTION ..... 83
4.2 CHOICE OF ROTATION AND MOMENT MEASURES ..... 84
4.2.1 Hinge Zone Rotation ..... 84
4.2.1.1 A Comment on Cimpoeru's Finite Mechanism Length ..... 86
4.2.2 Hinge Moment ..... 87

4.2.2.1 Cimpoeru's Choice of Hinge Moment ..... 88
4.2.2.2 Calculating Energy Consistent Hinge Moment ..... 88
4.3 Calculating Hinge Moment and Hinge Zone Rotation from Quasi-Static Test Data ..... 91
4.3.1 Buckle Forming on the Pendulum Axis ..... 91
4.3.1.1 Post-Buckle Hinge Moment ..... 91
4.3.1.2 Pendulum Rotation ..... 92
4.3.1.3 Hinge Zone Rotation ..... 92
4.3.2 Buckle Formation "off" the Pendulum Axis ..... 93
4.3.2.1 Post-Buckle Moment Correction ..... 94
4.3.2.2 Pendulum Rotation Correction ..... 96
4.3.2.3 Post-Buckle Hinge Zone Rotation ..... 98
4.3.2.4 Pre-Buckle Hinge Moment ..... 98
4.3.2.5 Impact Test "offset" Buckle Corrections ..... 98
4.4 Specimen Elastic Stiffness ..... 98
4.5 Calculating Hinge Moment and Hinge Zone Rotation from Impact Test Data ..... 101
4.5.1 Identification of Buckle Initiation ..... 101
4.5.2 Impact Test Hinge Zone Rotation ..... 104
4.5.2.1 A Device to Measure Hinge Zone Rotation Directly ..... 104
4.5.3 Impact Test Reaction Force Signal ..... 105
4.5.4 Inverse Analysis ..... 106
4.5.4.1 Measurement of the Specimen Mount FRF ..... 108
4.5.4.2 The Measured Specimen Mount FRF ..... 110
4.5.4.3 FRF Corrected Hinge Moment ..... 111
4.5.5 Low-Pass Filtering ..... 112
4.5.5.1 The Influence of Hinge Vibration on Hinge Moment ..... 113
4.5.5.2 Possible Specimen Natural Frequencies ..... 115
4.5.5.3 Assessment of Hinge Unloading due to Specimen Vibration ..... 117
4.5.5.4 Low-Pass Filter Cut-off Frequency ($f_c$) Selection ..... 119
4.5.6 Inverse Analysis or Low-Pass Filter ..... 121
4.6 Summary of Data Processing Procedures ..... 123
4.6.1 Quasi-Static Procedures ..... 123
4.6.2 Impact Procedures ..... 125
4.7 Conclusions ..... 125

4.8 RECOMMENDATIONS FOR FUTURE WORK ..... 126

**CHAPTER 5 Bend Test Results** **127**

5.1 INTRODUCTION ..... 127
5.2 TEST PROCEDURE DETAILS ..... 128
5.2.1 RHS Specimens ..... 128
5.2.2 Loading Rate ..... 128
5.2.2.1 Quasi-Static Loading Rate ..... 128
5.2.2.2 Pendulum Impact Velocity and Energy ..... 128
5.2.3 Data Acquisition ..... 130
5.3 GENERAL RESULTS ..... 130
5.3.1 Material Failure, Pre-Buckle Plasticity and Collapse ..... 130
5.3.2 Effective Hinge Centre ..... 132
5.3.3 Longitudinal Surface Strain Signals ..... 132
5.4 QUASI-STATIC TEST RESULTS ..... 133
5.4.1 Moment Vs Rotation Response Curves ..... 133
5.4.1.1 Elastic Hinge Stiffness ..... 134
5.4.1.2 Maximum Moment Compared to Fully Plastic Moment ..... 135
5.4.1.3 Curvature at the Onset of Buckling ..... 135
5.4.1.4 Strain at the Onset of Buckling ..... 135
5.4.2 Buckle Mechanism *Moment-Rotation* Response ..... 136
5.4.2.1 Buckle Mechanism Rotation a Relative or Absolute Quantity ..... 137
5.4.3 Modelling the Collapse Phase ..... 140
5.4.4 Average combined Hinge Zone $M$-$\theta$ Response ..... 140
5.4.4.1 Comparison with $M$-$\theta$ Response of Cimpoeru ..... 142
5.4.4.2 Comparison with an Analytical Model of Buckle $M$-$\theta$ Response ..... 143
5.4.5 Gross Specimen Response ..... 144
5.5 IMPACT TEST RESULTS ..... 146
5.5.1 Combined Raw Hinge $M$-$\theta$ ..... 146
5.5.2 Filtered Hinge Zone $M$-$\theta$ Response ..... 148
5.5.3 Buckle Mechanism $M$-$\theta$ Curves ..... 150
5.5.4 Buckle Mechanism Collapse Curve Fits ..... 150
5.5.5 Average Combined $M$-$\theta$ ..... 151
5.5.6 Gross Specimen Response ..... 151

5.6 COMPARISONS AND DISCUSSION ..... 153
5.6.1 Post-Buckle Hinge Response ..... 153
5.6.1.1 Comparison of Hinge Moment ..... 154
5.6.2 Pre-Buckle Hinge Response ..... 155
5.6.2.1 Strain and Curvature at Peak Moment ..... 156
5.6.3 Combined Hinge Zone Response ..... 156
5.6.4 Gross Specimen Response ..... 158
5.7 CONCLUSIONS ..... 161

**CHAPTER 6 Strain Rate Sensitivity of RHS Material 163**

6.1 INTRODUCTION ..... 163
6.2 EXPERIMENTAL APPARATUS AND PROCEDURES ..... 164
6.2.1 Test Coupon Details ..... 164
6.2.2 Choice of Strain Rates and Testing Machines ..... 165
6.2.3 High Strain Rate Tests – Shake Table ..... 166
6.2.3.1 Grips ..... 166
6.2.3.2 Load Take-up System ..... 168
6.2.3.3 Shake Table Drive Profile ..... 168
6.2.4 Low Strain Rate Tests – Shimadzu Universal Testing Machine ..... 170
6.2.5 Instrumentation ..... 171
6.2.5.1 Strain ..... 171
6.2.5.2 Displacement ..... 171
6.2.5.3 Load ..... 172
6.2.5.4 Data Acquisition ..... 173
6.2.6 High-Elongation Strain Gauging ..... 174
6.3 DATA PROCESSING PROCEDURES ..... 175
6.3.1 Engineering Stress and Strain ..... 175
6.3.2 Young's Modulus ..... 177
6.3.3 Uniform Strain and Total Extension ..... 177
6.3.4 Lower Yield Stress ..... 177
6.3.5 True Stress and Log Strain ..... 177
6.3.6 Plastic Log Strain ..... 178
6.3.7 Plastic Strain Energy Density to UTS ..... 178
6.3.8 Strain Rate and Crosshead Velocity ..... 178
6.4 RESULTS ..... 178

6.5 DISCUSSION ..... 181
6.5.1 Coupon Curvature and Residual Stress ..... 181
6.5.2 Variation of Mechanical Properties around the Section ..... 182
6.5.3 Variation of Strain Rate with Strain ..... 182
6.5.4 Strain Rate Sensitivity ..... 184
6.5.4.1 Lower Yield Stress ..... 185
6.5.4.2 UTS ..... 185
6.5.4.3 Comparison Between C350LO and DuraGal ..... 185
6.5.4.4 Strain Energy Density ..... 185
6.5.4.5 Young's Modulus ..... 186
6.5.4.6 Uniform Strain and Total Extension ..... 186
6.5.4.7 Flow Stress ..... 186
6.5.4.8 Order of Magnitude Nature of Strain Rate Sensitivity ..... 187
6.5.5 Strain Rate Sensitivity Models ..... 188
6.5.6 FE Modelling of the Uni-Axial Tensile Test ..... 190
6.5.6.1 Strain Distribution along the Coupon Centreline ..... 191
6.5.7 Influence of Stress Waves and Imposed Loading Oscillations ..... 193
6.6 CONCLUSIONS ..... 195
6.7 RECOMMENDATIONS FOR FUTURE WORK ..... 196

**CHAPTER 7 Finite Element Modelling 198**

7.1 INTRODUCTION ..... 198
7.2 BEAM ELEMENT MODEL ..... 199
7.2.1 Analyses ..... 199
7.2.2 Model Details ..... 199
7.2.2.1 Buckle Topology ..... 199
7.2.2.2 Restraint ..... 200
7.2.2.3 Cantilever Loading and Pendulum Contact ..... 200
7.2.2.4 Material and Section Properties ..... 200
7.2.3 Results ..... 202
7.2.3.1 Static Analysis ..... 202
7.2.3.2 Dynamic Analysis ..... 202
7.2.3.3 Some Interesting Results ..... 207
7.3 SHELL ELEMENT MODEL ..... 210
7.3.1 Aim ..... 210

7.3.2 Model Details ..... 210
7.3.2.1 Model Topology ..... 210
7.3.2.2 Restraint ..... 214
7.3.2.3 Loading ..... 214
7.3.2.4 Pseudo-Dynamic Analysis ..... 215
7.3.2.5 Material Properties ..... 218
7.3.2.6 "Calibration" of Static Material Properties ..... 221
7.3.2.7 Dynamic Properties - Strain Rate Sensitivity ..... 224
7.3.3 Results ..... 225
7.3.3.1 Buckle Mode Shape ..... 225
7.3.3.2 Moment – Rotation Comparisons ..... 228
7.3.3.3 Longitudinal Compression Flange Strain ..... 235
7.3.3.4 Comparison Impact Vs Static ..... 236
7.3.3.5 Full Field Results ..... 237
7.4 CONCLUSIONS ..... 243

**CHAPTER 8 Estimation and use of Dynamic Scaling Factors 245**

8.1 INTRODUCTION ..... 245
8.2 SCALING QUASI-STATIC RESPONSES ..... 246
8.2.1 Theoretical Scaling of Flow Stress ..... 246
8.2.1.1 Material Model ..... 247
8.2.1.2 Strain Rate ..... 248
8.2.1.3 Scaling Flow Stress – FE Models ..... 250
8.2.2 Experimental Scaling of Gross Response ..... 250
8.3 SCALING THE PLASTIC HINGE RESPONSE OF RHS ..... 253
8.3.1 Kecman's Theoretical Scaling Scheme ..... 253
8.3.2 Abramowicz and Jones' Theoretical $F_{dyn}$ Scaling Factor ..... 258
8.3.3 Kecman's Experimental $F_{dyn}$ ..... 259
8.3.3.1 Implications of Non-Scaleable Quasi-Static and Impact Responses .. 260
8.3.4 Examples of Predicted RHS Plastic Hinge Impact Response ..... 260
8.3.5 Possible Developments to Predictive Schemes ..... 263
8.3.6 Scaling Global Structural Response ..... 263
8.4 A GENERAL COMMENT ..... 264
8.5 USING PLASTIC HINGE PROPERTIES IN A "HYBRID" ANALYSIS ..... 264
8.6 CONCLUSIONS ..... 267

8.7 Recommendations for Future Work ..... 270

**CHAPTER 9 Discussion and Conclusions** **271**

9.1 Specific Aims of the Thesis ..... 271
9.2 Predicting Impact Response ..... 273
9.2.1 Detailed Finite Element Modelling ..... 273
9.2.2 Impact Testing ..... 274
9.2.2.1 Uninstrumented Impact Testing ..... 274
9.2.2.2 Instrumented Impact Testing ..... 275
9.2.3 Scaling a Quasi-Static Response ..... 275
9.2.4 General Comment on Component Impact Responses ..... 277
9.3 Additional Key Results and Conclusions ..... 277
9.3.1 Chapter 3 - Test Rig Design ..... 277
9.3.2 Chapter 4 – Processing Raw Test Data ..... 278
9.3.3 Chapter 5 – Bend Test Results ..... 279
9.3.4 Chapter 6 – RHS Material Strain Rate Sensitivity ..... 279
9.3.5 Chapter 7 – Finite Element Modelling ..... 280

**REFERENCES** **281**

**APPENDIX A – Kecman's Analytical Model** **291**

A.1 Integration of Rolling Energy ..... 292
A.1.1 Work done by "Rolling" ..... 292
A.1.2 Rolling Action in the RHS Buckle ..... 294
A.1.2.1 Yield Line GA ..... 296
A.1.2.2 Yield Line KA ..... 297
A.2 Flattening of the Corner Material ..... 297
A.3 The "Combined" Expression for *W* ..... 298
A.4 Significance of these Corrections ..... 299

**APPENDIX B - High-Elongation Strain Measurements** **301**

B.1 Strain Gauge Installation ..... 301
B.1.1 Surface Preparation ..... 301
B.1.2 Adhesive ..... 301
B.1.3 Wiring ..... 302

B.2 LARGE STRAIN SIGNAL CORRECTIONS ..... 303
B.2.1 Background Theory ..... 303
B.2.1.1 Bridge Non-linearity (TN- 507) ..... 303
B.2.1.2 Gauge Factor Non-linearity (TT-605) ..... 303
B.2.1.3 Transverse Sensitivity (TN-509) ..... 304
B.2.2 Final Working Corrections for Large Strain Measurements ..... 305
B.2.2.1 Transverse Sensitivity Correction ..... 305
B.2.2.2 Gauge Factor and Wheatstone Bridge Corrections ..... 306

# LIST OF TABLES


3.1 Data acquisition channels ..... 81

4.1 Dominant frequencies in impact tests and FE analysis ..... 116

5.1 Summary of key result quantities from quasi-static hinge zone $M$-$\theta$ responses ..... 134

5.2 Compression flange strains at depression inception and buckle initiation – quasi-static tests ..... 136

5.3 Summary of key result quantities from impact hinge zone $M$-$\theta$ responses ..... 151

5.4 Compression flange strains at depression inception and buckle initiation – all tests ..... 156

6.1 Shake table drive profile parameters ..... 170

6.2 Sampling rate and filter settings used for material tests ..... 173

6.3a Mechanical properties for grade C350LO RHS wall material ..... 179

6.3b Mechanical properties for DuraGal RHS wall material ..... 179

6.4a Grade C350LO coupon curvature and residual stress ..... 181

6.4b DuraGal coupon curvature and residual stress ..... 182

6.5a Dynamic mechanical properties of grade C350LO RHS wall material ..... 184

6.5b Dynamic mechanical properties of DuraGal RHS wall material ..... 184

6.6a Variation of flow stress with strain rate and plastic strain - C350LO RHS ..... 186

6.6b Variation of flow stress with strain rate and plastic strain - DuraGal RHS ..... 187

6.7 Order of magnitude sensitivity of C350LO – Face A strain energy density at UTS ..... 187

6.8a Cowper-Symonds strain rate sensitivity predictions for C350LO RHS ..... 190

6.8b Cowper-Symonds strain rate sensitivity predictions for DuraGal RHS ..... 190

7.1 Impact : Static plastic strain energy comparisons at peak rotation ..... 237

# LIST OF FIGURES


1.1 Three general classes of $M$-$\theta$ response. Kecman (1979 p. 64) ..... 5

1.2 Typical $M$-$\theta$ Response of a plastic hinge that has formed in a thin-walled RHS member subjected to a uni-axial bending load ..... 6

1.3 Definition of plastic hinge performance parameters ..... 7

1.4 Influence of material strain rate sensitivity on the response of a plastic hinge that has formed in a RHS member under flexural loading ..... 9

2.1 Pure bending test rig of Cimpoeru (1992) ..... 21

2.2 a) Type I and Type II quasi-static load curves, Calladine and English (1984) b) Type I and Type II specimens tested by Tam (1990) ..... 24

2.3 Tensile mechanical properties of EN 2A mild steel, Campbell and Cooper (1966) ..... 28

2.4 Stress-strain curves for 35XF sheet steel, Kassar and Yu (1992) ..... 29

2.5 Three stages of deformation of a square column subject to pure bending. ABAQUS calculation, Wierzbicki et al. (1994) ..... 35

2.6 Typical deformation of a square column under oblique load. PAMCRASH analysis, Han and Park (1999) ..... 36

2.7 Collapse mechanisms, thin-walled box beam a) Seki and Sunami (1978), b) Kecman (1979) ..... 39

2.8 Variation of tensile properties around a RHS. x = Yield Stress, o = UTS Key et al. (1988) ..... 51

2.9 Analytical model for panel removal residual stress, Key and Hancock (1993b) ..... 53

2.10 Analytical model of layering residual stress, Key and Hancock (1993b) ..... 53

3.1 Pendulum – Specimen energy transfer during the initial stages of an impact test ..... 62

3.2a Hinge moment from FE analysis – true and derived from contact force ..... 63

3.2b Hinge moment from FE analysis – true and derived from filtered contact force ..... 63

3.3 Moment-rotation traces from quasi-static and pendulum impact tests – Kecman (1993a) ..... 64

3.4 Unscaled pendulum acceleration and reaction force – physical impact test ..... 64

3.5 Hinge moment from FE analysis – true and derived from reaction force ..... 66

3.6 Schematic of pivoting specimen mount ..... 67

3.7 Residual reaction force - Original, after modification #2 and final ..... 75

3.8 Frequency Response of Charge Amplifier on 2000με range ..... 76

3.9 Strip gauge used to measure compression flange longitudinal strain ..... 78

3.10 Cross-talk sensitivity with a single excitation supply line ..... 80

3.11 Cross-talk sensitivity with two excitation supply lines ..... 80

4.1 Plastic hinge characteristic $M$-$\theta$ response (Fig. 1.3) ..... 84

4.2 Buckle mechanism as modelled by Kecman (1979) ..... 85

4.3 Bend test reaction forces and rotations - Plastic hinge formed on specimen mount pivot axis ..... 91

4.4 Bend test geometry detailing specimen and pendulum contact - plastic hinge formed on specimen mount pivot axis ..... 92

4.5 Bend test reaction forces and rotation - plastic hinge formed "offset" from the specimen mount pivot axis ..... 94

4.6 Hinge moment corrected for offset buckle location. Hinge offset (a) = +17 mm ..... 96

4.7 Pendulum rotation and specimen geometry - Plastic hinge formed "offset" from the specimen mount pivot axis ..... 97

4.8 Specimen elastic stiffness ($\Delta M_h/\Delta\beta'_{elas}$) Vs Hinge zone rotation ..... 99

4.9 Compression flange longitudinal strain Vs Hinge zone rotation. ..... 101

4.10 Strip gauge and hinge moment traces from quasi-static test A5 ..... 103

4.11 Strip gauge and hinge moment traces from impact test A2 ..... 103

4.12 Single input - single output system ..... 106

4.13 Hinge moment correction factor =1/(Normalised FRF of the reaction measurement system) ..... 110

4.14 FRF corrected hinge moment from impact A2 ..... 112

4.15 Effect of hinge elastic unloading on hinge moment signal a) Hinge $M$-$\theta$ curve with unloading b) Corresponding moment signal ..... 114

4.16 $M$-$\theta$ signal showing distortion due to; a) Filtered moment signal or filtered rotation signal and b) both moment and rotation signals filtered ..... 114

4.17 Hinge $M$-$\theta$ response from impact FE analysis ..... 117

4.18 Hinge moment signal interpolated from impact A2 hinge zone rotation a) raw signal and b) low-pass filtered at 200 Hz ..... 118

4.19 Comparison of hinge zone rotation and longitudinal strain from impact test A2 and the dynamic FE analysis of Section 7.2.2 ..... 119

4.20 Hinge moment Vs hinge zone rotation response a) Impact A2 low-pass filtered at $f_c$ = 350 Hz and b) Impact A2 low-pass filtered at $f_c$ = 200 Hz ..... 120

4.21 Comparison of FRF correction and low-pass filtering of impact $M$-$\theta$ response ..... 122

5.1 ADR 59/00 National Code of Practice – Part B, Profile B a) Allowable roll cage cross section and b) Standard hoop deflection collapse mechanism (National Code of Practice 1992) ..... 129

5.2 Compression flange buckle profile – Quasi-static test A3 ..... 132

5.3 Hinge zone $M$-$\theta$ response - Quasi-static tests A1, A3, A5, C1 and C3 ..... 133

5.4 Buckle mechanism $M$-$\theta$ response - Quasi-static tests A1, A3, A5, C1 and C3 ..... 137

5.5 FE predicted responses for different loading conditions and initial imperfections Mechanism rotation – a) absolute definition and b) relative definition ..... 139

5.6 Power law fitted buckle mechanism $M$-$\theta$ response curves – Quasi-static tests A1, A3, A5, C1 and C3 ..... 140

5.7 Hinge zone $M$-$\theta$ curve from quasi-static test A1 ..... 141

5.8 Comparison with experimental $M$-$\theta$ obtained by Cimpoeru and analytical model developed by Kecman ..... 142

5.9 Yield line model of the buckle mechanism, Kecman (1979) ..... 143

5.10 Gross specimen response – pendulum moment Vs pendulum rotation Quasi-static tests A1, A3, A5, C1 and C3 ..... 145

5.11 Hinge zone $M$-$\theta$ response - Impact tests A2, A4, A6 and B2 ..... 146

5.12 Hinge zone $M$-$\theta$ response – Hinge zone rotation derived from rotary potentiometer device and from longitudinal compression flange strains ..... 147

5.13 Filtered hinge zone $M$-$\theta$ response, Impact test A4 – hinge zone rotation derived from the rotary potentiometer device and longitudinal compression flange strains ..... 148

5.14 Filtered hinge zone $M$-$\theta$ response - Impact tests A2, A4, A6 and B2 ..... 149

5.15 Filtered buckle mechanism $M$-$\theta$ responses - Impact tests A2, A4, A6 and B2 ..... 150

5.16 Pendulum work and specimen strain energy – Impact test A2 ..... 152

5.17 Pendulum moment Vs pendulum rotation – Impact tests A2, A4, A6 and B2 ..... 152

5.18 Quasi-static and impact comparison of buckle mechanism plastic $M$-$\theta$ response ..... 154

5.19 Quasi-static and impact comparison of buckle mechanism energy Vs plastic rotation ..... 155

5.20 Quasi-static and impact comparison of a) hinge moment Vs pre-buckle plastic $\theta$ and b) cumulative hinge zone plastic energy Vs pre-buckle plastic $\theta$ ..... 155

5.21 Quasi-static and impact comparison of hinge moment Vs hinge zone plastic rotation ..... 157

5.22 Quasi-static and impact comparison of hinge zone cumulative plastic energy Vs hinge zone plastic rotation ..... 157

5.23 Quasi-static and impact comparison of pendulum moment Vs normalised pendulum plastic rotation ..... 159

5.24 Quasi-static and impact comparison of cumulative specimen plastic strain energy Vs normalised pendulum plastic rotation ..... 159

6.1 Uni-axial tensile coupons a) geometry and b) coupon locations around the tube section ..... 165

6.2 Shake table specifications ..... 169

6.3 Displacement-time drive profile, Velocity and Acceleration time histories for highest rate shake table tests ..... 170

6.4 Effect of coupon curvature on measured engineering stress Vs engineering strain curve ..... 176

6.5 True stress Vs plastic log strain for RHS wall material a) Grade C350LO RHS, b) DuraGal RHS ..... 180

6.6 Engineering strain rate and equivalent crosshead strain rate Vs engineering strain, C350LO RHS Face A1, Nominal $\dot{\varepsilon}=10^{-4}$ $s^{-1}$ ..... 183

6.7 Plastic log strain rate Vs plastic log strain, logarithmic scale – C350LO RHS ..... 183

6.8 Strain rate sensitivity of RHS wall material a) grade C350LO and b) DuraGal ..... 188

6.9 FE model of the tensile test coupon including initial coupon curvature and grips ..... 191

6.10 Tensile surface stresses after clamping the curved coupon ..... 191

6.11 Profile of longitudinal surface strain along the longitudinal centreline of the coupon at various levels of central strain. a) quasi-static loading and b) nominal strain rate = 10 $s^{-1}$ ..... 192

6.12 Variation of central strain rate Vs central strain. FE predictions and experimental results. Equivalent test strain rates of a) $10^{-4}$ $s^{-1}$ and b) 10 $s^{-1}$ ..... 193

6.13 Load oscillations in a tensile test at a nominal strain rate = 10 $s^{-1}$ ..... 194

7.1 Modelling the variation in buckle elastic stiffness. ..... 201

7.2 Static Pendulum moment Vs Pendulum rotation a) pre-buckle and b) post-buckle ..... 203

7.3 Static Hinge moment Vs Hinge rotation a) pre-buckle and b) post-buckle ..... 204

7.4 Dynamic Pendulum moment Vs Pendulum rotation a) pre-buckle and b) post-buckle ..... 205

7.5 Dynamic Hinge moment Vs Hinge zone rotation a) pre-buckle and b) post-buckle ..... 206

7.6 a) Propagation of a "negative" bending wave in the initial stages of impact b) Corresponding hinge moment Vs time ..... 207

7.7 Hinge "negative" response corresponding to pendulum-specimen re-contact ..... 208

7.8 Non-smooth hinge $M$-$\theta$ responses ..... 209

7.9 Detailed model of the RHS specimen using a combination of shell and beam elements ..... 210

7.10 Collapse response for ¼ buckle model and ½ buckle models ..... 212

7.11 Mesh density in the region of the local buckle ..... 213

7.12 Specimen mounting plate restraint ..... 214

7.13 User routine flow chart ..... 216

7.14 Reverse yielding in the buckle. (PEEQ – PEMAG) ..... 221

7.15 FE moment-rotation responses before and after modification of material stress-strain curves ..... 222

7.16a FE buckle mode shape, $\theta = 37°$ ..... 225

7.16b FE buckle mode shape, $\theta = 37°$ ..... 226

7.16c Experimental buckle mode shape, $\theta \approx 35°$ (Plate 5.1) ..... 226

7.17 Progressive development of local buckle. Reading L $\rightarrow$ R then Top $\rightarrow$ Bottom; $\theta = 4.18°$, 7.79°, 11.9°, 18.7°, 28.4° and 35.3° ..... 227

7.18 Buckle asymmetry a) Longitudinal cross-section of buckle at $\theta = 36°$ - FE result and b) Physical buckle ..... 228

7.19 Comparison of FE and experimental gross specimen response a) pre-buckle and b) complete ..... 229

7.20 Comparison of FE and experimental moment – rotation response a) hinge zone and b) buckle mechanism ..... 230

7.21 Normalised pendulum moment Vs Normalised pendulum rotation - Comparison FE and experimental ..... 232

7.22 Hinge zone $M$-$\theta$ impact response – Comparison FE and experimental ..... 232

7.23 Buckle mechanism $M$-$\theta$ impact response – Comparison FE and experimental ..... 233

7.24 Pendulum work and specimen strain energy – Comparison true and derived ..... 234

7.25 Hinge zone $M$-$\theta$ response using Cowper-Symonds material strain rate definition ..... 235

7.26a Pre-buckle longitudinal compression flange strain (40 mm from base plate edge) - Comparison FE and experimental ..... 236

7.26b Buckle profile – Comparison FE and experimental ..... 236

7.27 Equivalent plastic strain, inner surface at $\theta \approx 36°$ ..... 237

7.28 Element plastic strain energy, $\theta \approx 36°$ ..... 238

7.29 Equivalent plastic strain rate, outer surface, a) $\theta \approx 7.8°$ and b) $\theta \approx 36°$ ..... 240

7.30 Energy-weighted equivalent plastic strain rate, outer surface ..... 241

7.31 Relationship between average buckle strain rate, buckle geometry and hinge rotation rate ..... 242

8.1 Comparison of hinge zone $M$-$\theta$ response from quasi-static and impact tests (Figure 5.21) ..... 251

8.2 Performance of various scaling factors compared to the test results from Chapter 5 ..... 261

8.3a Comparison of true and estimated $F_{dyn}$ for pendulum moment Vs pendulum rotation ..... 262

8.3b Comparison of true and estimated $F_{dyn}$ for specimen strain energy Vs pendulum rotation ..... 262

A.1 Yield line model of the buckle mechanism, Kecman (1979) ..... 291

A.2 Rolling deformation - general case ..... 292

A.3 General rolling deformation – movement of material over the roller for an infinitesimal displacement of the roller from O to O′ ..... 292

A.4 Rolling deformation - simplified case ..... 293

A.5 Increment in buckle collapse ..... 294

A.6 Increment in buckle collapse corresponding to an increment in buckle rotation "mapped" onto the undeformed web ..... 295

A.7 Comparison of buckle moment responses Quasi-static test average, Kecman and Kecman – alternative formulation ..... 299

A.8 Comparison of buckle plastic energy responses Quasi-static test average, Kecman and Kecman – alternative formulation ..... 300

B.1 Corrections to indicated strain for Wheatstone bridge and gauge factor non-linearity ..... 308

# LIST OF PLATES


1.1 Sturt Highway, East of Hay N.S.W., 1980 ..... 2

1.2 Mount Tamborine, Gold Coast Qld., 25/9/90 ..... 2

1.3 Mount Tamborine accident under investigation ..... 3

1.4 Paris, 24/4/98 ..... 3

1.5 Code of practice bus frame subjected to a simulated rollover according to ADR 59/00 ..... 4

1.6 Typical local buckle or " plastic hinge" in an isolated RHS member subjected to a uni-axial bending load ..... 6

3.1 Bus ring frame after quasi-static rollover simulation. (Direction and location of quasi-static load shown together with four plastic hinge locations) ..... 55

3.2 A "Plastic Hinge" at the floor bearer to side pillar joint ..... 55

3.3a RHS cantilever bend test specimen – Before and after testing ..... 56

3.3b Close-up of local buckle in RHS cantilever bend test specimen ..... 56

3.4 Accelerated impact pendulum at the Cranfield Impact Centre, Cranfield, England ..... 58

3.5 Accelerated impact pendulum at UTS ..... 59

3.6 Physical specimen mount ..... 68

3.7 Air spring arrangement a) air spring compressed by the pendulum and b) air spring expanded and restrained by straps ..... 70

3.8 Geared electric winch and pulley arrangement for quasi-static testing ..... 71

3.9 Details of the optical head, encoder arc and trigger gate ..... 72

3.10 Final load cell and pre-load arrangement with "zero shear" coupling ..... 75

3.11a Hinge zone rotation device attached to a specimen before testing ..... 77

3.11b Hinge zone rotation device attached to a specimen after testing ..... 78

4.1 Unbent specimen with electromagnetic exciter attached. Note pre-load has not yet been applied ..... 109

5.1 Typical buckle forming in quasi-static and impact specimens ..... 130

5.2a Asymmetrical buckle – effective hinge centre offset from geometric centre ..... 131

5.2b Asymmetrical buckle – Top View ..... 131

6.1a Tensile test fixtures in place on the shake table Close-up before testing ..... 166

6.1b Tensile test fixtures in place on the shake table Overview before testing..... 167
6.1c Overview of tensile test fixtures in place on the shake table after testing..... 167
6.2 Initial curvature in a typical tensile coupon..... 171
6.3 Large strain relief loops on tensile coupons ..... 174

B.1 Tensile coupon - bond curing jig ..... 302
B.2 Large strain relief loops on tensile coupons ..... 302

# GLOSSARY AND NOTATION

**RHS** - Rectangular hollow section. Used in this thesis to cover steel cold-formed thin-walled rectangular and square hollow sections.

**Plastic hinge** - The localised region of plastic deformation and buckling that developed in the cantilever specimen. See § 1.3.

**Effective Hinge Centre** - The point about which the length of specimen beyond the hinge zone appeared to rotate following formation of the hinge buckle. The effective hinge centre was typically located within ±5 mm from the geometric centre of the buckle. See § 1.3.3.

**Hinge Zone** - The 85 mm length of specimen, from the root of the specimen, over which the potentiometer device described in Section 3.5.6 measured relative rotation. See § 3.5.6 and § 4.2.1.

**Energy consistent hinge moment** - Hinge moment defined such that the integral *hinge moment Vs hinge zone rotation* was equal to hinge zone energy. See § 4.2.2, Eqn. 4.1.

**Normalised pendulum rotation** - Approximately the pendulum rotation that would have been measured if the pendulum pivot were at the effective hinge centre. See § 4.3.2.2.

**Normalised pendulum moment** - The work conjugate to normalised pendulum rotation. See § 4.3.2.2.

**Dynamic Factor** - For a given quantity or response the dynamic factor is the ratio of the impact value to the corresponding quasi-static value. See § 4.2.1.

**FRF** - Frequency Response Function. See § 4.5.4.

**MPC** - Multi-point constraint. See § 7.3.2.1.

**UTS** - Ultimate tensile strength.

## Symbols

| | |
|---|---|
| $\theta$ | Hinge zone rotation. |
| $M\text{-}\theta$ | *Hinge moment Vs Hinge zone rotation* response curve. |
| $\beta$ | Pendulum rotation. |
| $\beta'$ | Normalised pendulum rotation. |
| $\phi$ | Pendulum rotation due to elastic + plastic curvature of the length of specimen beyond the hinge zone. |
| $\phi'$ | Normalised pendulum rotation due to elastic + plastic curvature of the length of specimen beyond the hinge zone. |
| $\gamma$ | Specimen tip rotation due to elastic + plastic curvature of the length of specimen beyond the hinge zone. |
| $a$ | Offset of the effective centre from pendulum axis |
| $M_{fp}$ | Fully plastic moment of the RHS section |
| $f_c$ | Low-pass filter cut-off frequency [Hz]. |
| $D$ | Cowper-Symonds coefficient defined in Equation 2.1 [$s^{-1}$] |
| $q$ | Cowper-Symonds coefficient defined in Equation 2.1 |
| $f$ | Flow stress strain rate sensitivity scaling factor. See § 8.2. |
| $F_{dyn}$ | "dynamic factor" used to scale a quasi-static gross hinge or quasi-static specimen response quantity. See § 8.2. |
| $\delta$ | General measure of component displacement. See § 8.2.2 Eqn. 8.3. |

## Superscripts and Subscripts

| | |
|---|---|
| **EC** | Energy consistent. |
| **Pre** | Pre-buckle phase. |
| **Post** | Post-buckle phase. |
| **Trans** | Transitional phase between pre-buckle continuous beam response and post-buckle mechanism response. |
| **pb** | Response post-buckle formation. |
| **h** | Quantity associated with plastic hinge response |
| **elas** | Elastic component of the response. |
| **plas** | Plastic component of the response. |
| **pend** | Quantity associated with pendulum response. |
| **spec** | Quantity associated with specimen response. |
| **hinge zone** | Quantity associated with hinge zone response. |

# ABSTRACT

This thesis describes a program of research into the plastic *moment – rotation* ($M$-$\theta$) response of rectangular hollow section (RHS) steel tubes subjected to impact bending loads. The context for this research was the use of RHS in buses and vehicle rollover protection structures (ROPS) where the "plastic hinges" that form in the RHS members act as energy absorbing "crumple zones".

In the design of such structures for crashworthiness, there is a need to understand the response of the plastic hinges to impact loading and this research has assessed the following methods used to determine the *moment – rotation* characteristics of plastic hinges under impact bending loads:

- physical impact tests;
- finite element modelling; and
- the use of "dynamic magnifiers" to scale the results of quasi-static tests and analyses.

In dynamic tests, the specimen's inertia complicates the measurement of plastic hinge properties. These complications were addressed by the design and development of a novel pendulum bend rig and instrumentation and the meticulous processing of test data. The test rig and procedures were successfully used to measure the bending collapse of 50x50x2 grade C350LO RHS specimens to a hinge rotation of 35°. Comparisons between the measured impact and quasi-static responses enabled the influence of the loading rate on plastic hinge response to be quantified.

It is shown that the difference between the impact and static responses is essentially due to the RHS material's strain rate sensitivity. This influence of strain rate on the mechanical properties of the RHS material was characterised by a programme of uni-axial tensile tests at strain rates ranging from $10^{-4}$ to 10 $s^{-1}$.

Detailed finite element analyses of the local buckling response were conducted using HKS ABAQUS–Standard. Excellent agreement between the predicted and measured impact $M$-$\theta$ responses of the local buckle was obtained using a "pseudo-dynamic" analysis procedure. This procedure correctly accounted for the effect of material strain rate sensitivity within a static analysis by controlling the loading rate.

A critical assessment was made of the quasi-static scaling approach to predicting component impact response. The limitations of predicting impact moment and energy responses using a single scaling factor were demonstrated. It is shown that the most reliable results are obtained using a scaling factor derived experimentally. A theoretical approach proposed in the literature to predict RHS plastic hinge impact response is shown to overestimate the impact response of the RHS tested in this study. An alternative theoretical scaling factor is proposed that gave an improved prediction of RHS impact response.

# CHAPTER 1 INTRODUCTION

## 1.1 BUS ROLLOVER

Bus rollover accidents are particularly dangerous accidents as large numbers of people are exposed to the risk of injury due to the severe deformation of the bus framework. The possibility of occupants being thrown from the bus is also high in rollover accidents. Unfortunately rollover accidents are not rare (Matolcsy 1997; National Road Transport Commission 1997; National Transportation Safety Board 1999). Rollover accidents typically occur when the wheels of a skidding vehicle strike a kerb or soft ground causing the vehicle to roll onto its roof. Other accidents, often more serious, have occurred where the vehicle has rolled down an embankment, Plate 1.2. Plates 1.1 – 1.3 show structural damage from Australian bus rollover accidents. Damage from the 1980 accident is quite severe compared to the 1990 accident. Full details of the 1980 rollover are not known, however it is possible that modern materials and manufacturing techniques have significantly contributed to the apparent increased strength.

To protect occupants in a rollover accident, the bus superstructure should deform and in so doing absorb a significant amount of the vehicle's impact energy. An excessively stiff structure that does not deform in an accident may produce injurious decelerations and is more likely to roll than a bus with a superstructure designed to collapse in a controlled manner. Whilst it is desirable for the structure to deform, it is essential that a survival space be maintained and that the deformed structure be able to support the weight of the overturned vehicle. These safety requirements have been formalised in the European Code ECE Regulation 66 and the Australian Design Rule 59/00.

## 1.2 ADR 59/00

Because of the serious nature of bus rollover accidents, an Australian design rule, ADR 59/00 "Omnibus Rollover Strength", has been in affect since July 1992. This rule requires that new bus structures be capable of absorbing the energy of a standard rollover test without intruding into a defined passenger survival space.

**Plate 1.1:** Sturt Highway, East of Hay N.S.W., 1980

**Plate 1.2:** Mount Tamborine, Gold Coast Qld., 25/9/90


**Plate 1.3:** Mount Tamborine accident under investigation

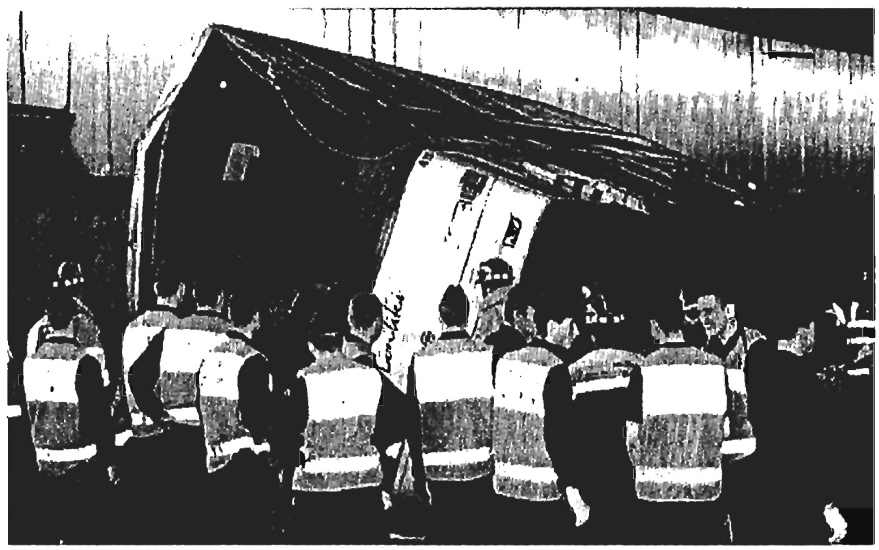

**Plate 1.4:** Paris, 24/4/98

To assist smaller bus manufacturers a National Code of Practice (1992) was developed. Plate 1.5 shows the code of practice bus frame under test according to ADR 59/00. Manufactures who can demonstrate they have followed the code of practice in the construction of a bus superstructure can have that superstructure accepted as complying with the requirements of ADR 59/00, without the need for further testing or analysis.

The ability of a bus superstructure to meet the safety requirements of ADR 59/00 is dependent upon the stiffness, strength, energy capacity and residual strength of the deforming structural members, commonly thin-walled rectangular hollow sections (RHS).

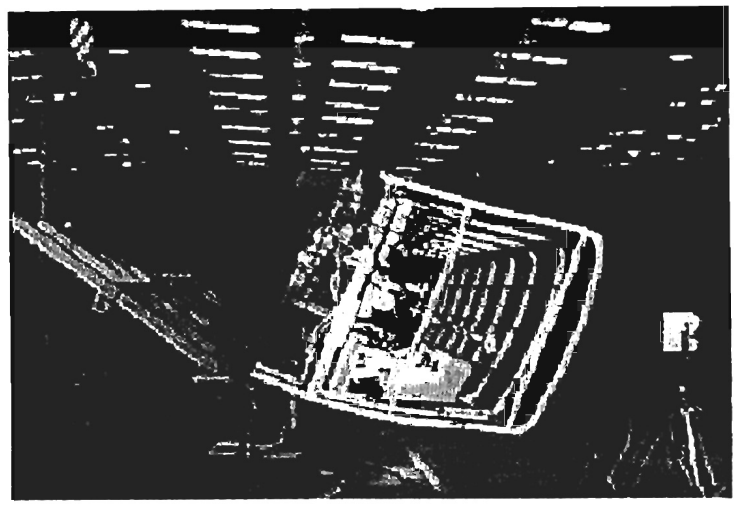

**Plate 1.5:** Code of practice bus frame subjected to a simulated rollover according to ADR 59/00

## 1.3 PLASTIC HINGE RESPONSE IN RHS

In a rollover accident, and in the simulated rollover of ADR 59/00, the structural members of the rollover protection structure (ROPS) are loaded principally in unidirectional bending. When overloading occurs during an accident, localised regions of plastic deformation, buckling, tearing, fracture or other sources of non-linearity occur throughout the structure, commonly at joints. These local regions are referred to as "plastic hinges" because large amounts of plastic energy are absorbed as the undeformed portion of the structural member "rotates" about the local deformation zone. Collapse of the ROPS begins when sufficient plastic hinges have formed to convert the structure into a kinematic system. During collapse the stiffness, energy capacity and residual strength of the structure are governed by the properties of the local plastic hinges. The local plastic hinge is therefore a key energy absorbing element or "crumple zone" in the structure.

Rectangular hollow sections (RHS) are commonly used in the construction of "rollover safe" bus superstructures and other rollover protection structures. The plastic hinges that form in RHS members under flexural loading are often the critical energy absorbing elements in these structures.

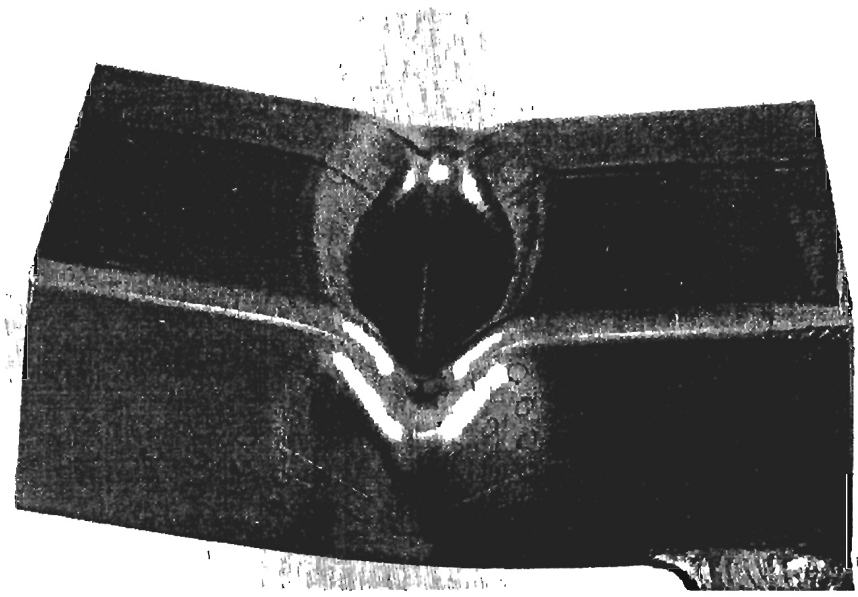

**Plate 1.6:** Typical local buckle or " plastic hinge" in an isolated RHS member subjected to a uni-axial bending load

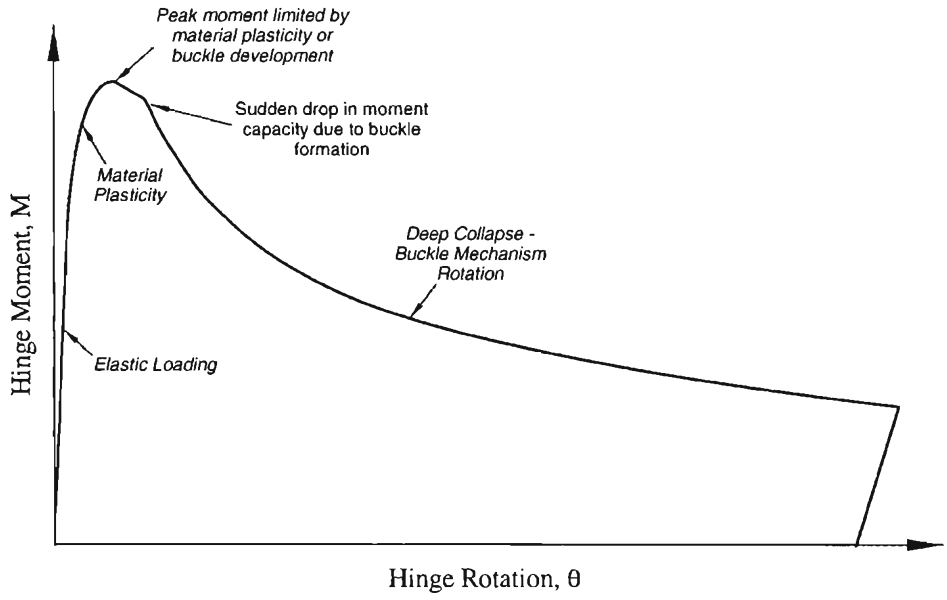


**Figure 1.2:** Typical $M$-$\theta$ Response of a plastic hinge that has formed in a thin-walled RHS member subjected to a uni-axial bending load

From a structural perspective the most notable feature of this response is the significant and sudden drop in moment capacity after buckle initiation. It is understandable then that as an essential part of the design process the location and $M$-$\theta$ response of all plastic hinges contributing to the collapse of a bus structure must be established either by calculation, testing or a combination of both.

## 1.3.1 Performance Parameters

The important hinge performance characteristics for a design from a crashworthiness perspective are stiffness, ultimate strength, suddenness of collapse, energy capacity and residual strength. These parameters are illustrated in Figure 1.3.

## 1.3.2 Response Phases

The typical $M$-$\theta$ response, Figure 1.3, can be divided into the following five phases.

1. Linear elastic loading.
2. Elastic-plastic response from first yield to peak moment. Hinge moment is limited by either full section plasticity or compression flange buckling.
3. Initial buckle development.
4. Deep collapse of the section characterised by a significant drop off in moment capacity associated with further development of the buckle mechanism.
5. Elastic unloading. Due to the geometry of the buckle the elastic unloading stiffness is significantly less than the elastic loading stiffness.

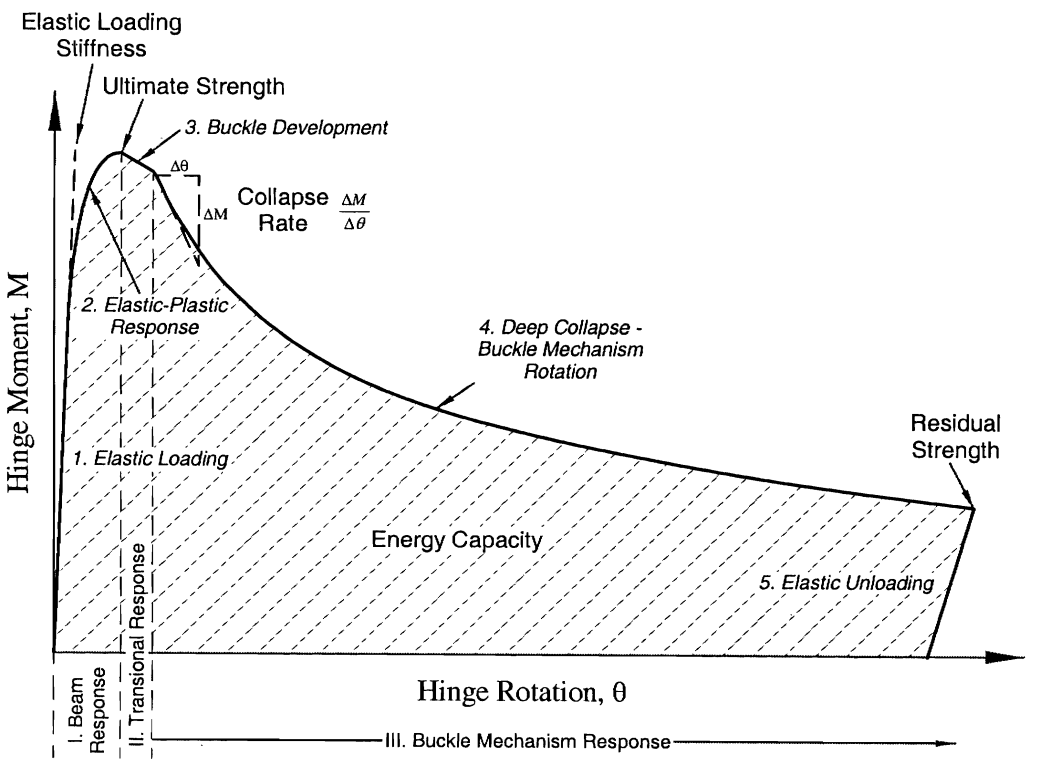


**Figure 1.3:** Definition of plastic hinge performance parameters.

The $M$-$\theta$ response can be also be divided into three rotation phases each associated with different geometry.

**Phase I: Beam Response**

Initially the thin-walled RHS beam deforms with continuous curvature. The measured hinge rotation is the sum of elastic and plastic curvature. The amount of rotation before peak moment is therefore dependent on the length over which hinge rotation is measured.

**Phase II: Transitional Response**

This phase begins at buckle initiation. In this region the geometry of the plastic hinge is in a transitional state, changing from the continuous curvature of Phase I to the local buckling of Phase III. The response is neither that of an elastic-plastic beam nor that of the buckle mechanism.

**Phase III: Buckle Mechanism Response**

In this phase the geometry of the local buckle is established and the $M$-$\theta$ response is governed by the response of the buckle mechanism. Measured hinge rotation is dominated by the relative rotation across the buckle and is independent of the length over which hinge rotation is measured.

### 1.3.3 Effective Hinge Centre

During Phase III the length of RHS beyond the hinge appears to rotate about a point within the buckle. This point can be considered as the "effective hinge centre". During the initial stages of collapse the location of the effective hinge centre moves by an amount dependent on the degree of symmetry of the buckle, however in the latter stages of collapse the effective hinge centre remains relatively fixed. For a symmetrical buckle the effective hinge centre corresponds to the geometric centre of the buckle.

## 1.4 Plastic Hinge Response under Impact Loading

Under crash or impact loading conditions, the strength and energy absorption capacity of a plastic hinge may increase, primarily due to the effects of material strain rate sensitivity, as shown in Figure 1.4. This strain rate enhancement of plastic hinge response may be exploited to achieve an optimum design balance between weight,

strength and safety. In some materials impact loading can have an adverse effect by increasing the possibility of fracture.

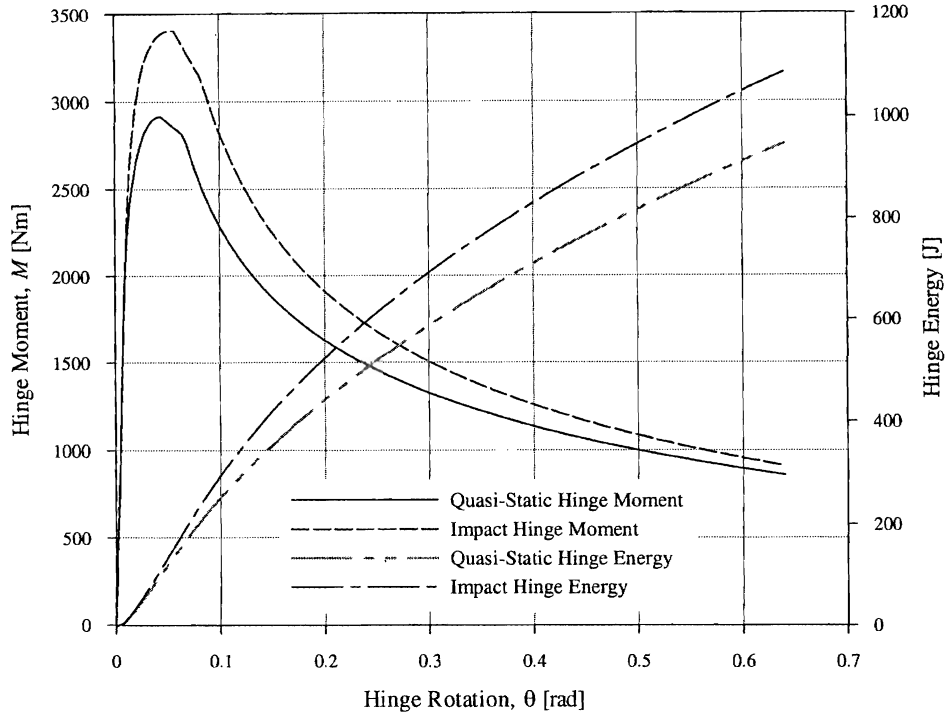


**Figure 1.4:** Influence of material strain rate sensitivity on the response of a plastic hinge that has formed in a RHS member under flexural loading

During an impact event, issues such as inertia, material strain rate sensitivity and material integrity, can influence the global collapse mode of the structure. The design of a crashworthy structure must therefore involve an assessment of structural response under impact loading.

## 1.5 Assessing Structural Response to Impact Loading

Possible approaches for assessing the response of a structure to impact loading are: full scale physical testing; advanced numerical modelling; or a combination of the two.

### Full Scale Impact Testing

The merits of full-scale impact testing are (Kecman 1994):

- The structure is loaded in the most realistic manner;
- The influences of material inertia and strain rate sensitivity on the structure are properly accounted for.

Separate treatment of the component response from the global structure has several advantages (Kecman 1997):

- once the collapse properties of components are known it is possible to greatly, but reliably, simplify the model of the whole structure;
- simplified models enable quick parametric studies in a design optimisation cycle;
- design errors may be rectified before production of the full-scale structure;
- insight is gained as to the contribution of the individual components to the overall performance. This insight simplifies redesign of a failed design and assessment of subsequent designs with structural variations.

Implementation of the "hybrid" design approach usually involves conducting a non-linear, large deflection, beam finite element analysis of the global structure. This analysis can be quasi-static, e.g. using SIMSTAT (Kecman et al. 1993; Kecman 1994) or dynamic, e.g. using ABAQUS (Roca et al. 1997) or DYNA3D (Kecman & Randell 1996). Both approaches have their merits as outlined by Kecman & Randell (1996).

The hybrid modelling approach is preferred over full scale testing as a means of assessing the crashworthiness of a bus superstructure because hybrid modelling provides the designer with the most insight into a structure's performance, is flexible and cost effective, and the approach can be successfully used at both the concept and detail stages of a design. The hybrid design approach has been used and verified extensively by the Cranfield Impact Centre (CIC) and is the basis of the CIC program SIMSTAT. SIMSTAT has been formally accepted for type approval in the UK.

## 1.6 Assessing Plastic Hinge Impact Response

It will be assumed in the balance of this thesis that the hybrid modelling approach has been adopted to assess the crashworthiness of a bus superstructure constructed from RHS. Irrespective of whether the global analysis is static or dynamic, the impact response of the local plastic hinges must be determined. Three methods to determine the plastic hinge response of RHS under impact loading are by:

- physical impact testing;
- numerical modelling;
- "scaling" a quasi-static response.

As outlined below, several issues related to the use of these methods to measurement or prediction of RHS plastic hinge response under impact loading, remain unresolved in the literature.

**Physical Impact Testing**

Experimental studies that characterise the plastic hinge $M$-$\theta$ response of RHS under quasi-static flexural loading have been published. However, to the author's best knowledge, there are no published studies showing the plastic hinge $M$-$\theta$ response of RHS under impact flexural loading. One possible reason why $M$-$\theta$ responses from instrumented impact studies have not been published is that the influence of specimen inertia can significantly complicate the processing of impact test results, as acknowledged by Kecman (1993a, 1993b).

**Numerical Modelling**

The application of advanced finite element codes to the analysis of plastic hinge behaviour involving complex local buckling can provide valuable insights and be very cost effective. Dynamic analyses will account for the influences of material inertia and strain rate sensitivity. However, it is sometimes difficult to extract hinge $M$-$\theta$ response from a dynamic analysis (Vignjevic et al. 1990). When the influence of inertia on local plastic hinge response is negligible, a procedure whereby the influence of material strain rate sensitivity is properly accounted for in a static solution would simplify the extraction of $M$-$\theta$ responses.

The accuracy of a FE analysis is directly affected by the accuracy of the material mechanical property definitions. Although there is a large body of research data on the impact response of tubular sections, the author is unaware of any published test data for the strain rate sensitivity of the material in cold-rolled tube walls. There is thus a question regarding the appropriate definition of strain rate sensitivity for the material in cold-rolled rectangular hollow sections. An associated but more general question is with what accuracy can FE models predict the plastic hinge response of RHS under impact loading?

**Scaling a Quasi-Static Response**

Because of the difficulties involved with conducting and interpreting impact tests, and because numerical modelling requires specialised software and expertise, plastic hinge

impact responses are commonly predicted by scaling known quasi-static performance to account for the influence of material strain rate sensitivity. The prediction of impact response by scaling a static response tacitly assumes that the influence of inertia is negligible. The appropriateness of this assumption for the RHS plastic hinge under investigation has not been quantitatively assessed.

While the procedure for scaling a quasi-static response is simple, the accuracy of the predicted impact response is dependent on the derivation and application of scaling factors. Kecman (1979, 1993a) has proposed theoretical and experimental scaling procedures for predicting the impact $M$-$\theta$ response of RHS. How well do these procedures perform and how can they be improved? To what extent are experimentally derived scaling factors dependent on the conditions of the test? The accuracy of theoretical scaling schemes relies heavily on the appropriate choice of a material model and a representative strain rate. The question of an appropriate material model has already been raised. The question of an appropriate strain rate is, given the complex spatial and temporal variation of strain and strain rate within the buckle, what is a representative strain rate for the buckle?

## 1.7 THESIS AIMS & METHODOLOGY

In summary, it was concluded that the measurement or prediction of RHS plastic hinge response under impact loading using physical impact tests, numerical modelling or quasi-static scaling methods, required investigation of the following issues:

1. Development of testing procedures that address the measurement difficulties in impact testing caused by specimen inertia.
2. Measurement of the plastic hinge $M$-$\theta$ response of RHS under impact flexural loading.
3. The influence of inertia on local plastic hinge response.
4. Modelling the dynamics of an impact in a static FE solution.
5. Appropriate definition of strain rate sensitivity for the material in cold-rolled rectangular hollow sections.
6. Determination of typical strains and strain rates in the buckle.
7. Assessment of how well quasi-static scaling schemes proposed in the literature perform and consideration of how can they be improved.

The research methodology adopted involved four main aspects:

**1. Quasi-Static and Impact Bend Tests**

Instrumented quasi-static and impact tests were conducted to accurately measure the plastic hinge response of RHS under flexural loading. The particular rectangular hollow section tested was 50x50x2 grade 350LO. The test rig and instrumentation were specially designed to measure both the $M$-$\theta$ response of the local buckle and the gross response of the specimen. Accurate measurement of hinge $M$-$\theta$ response enabled direct assessment of the influence of material strain rate sensitivity on hinge strength and energy capacity. Test results were used to validate and calibrate FE models and to assess the performance of scaling schemes.

**2. Material Mechanical Properties**

To determine the nature of RHS wall material strain rate sensitivity, uni-axial tensile tests were conducted at four strain rates, ranging from $10^{-4}$ to 10 $s^{-1}$. The results of this testing provided detailed material property data for finite element analyses and enabled the accuracy of material models used in quasi-static scaling schemes to be assessed.

**3. Finite Element Modelling**

To investigate the influence of inertia on plastic hinge $M$-$\theta$ response and to determine the magnitude and distribution of strain and strain rate within the local buckle, detailed finite element analyses of the RHS specimen under quasi-static and impact loading were conducted using the commercial implicit code HKS – ABAQUS. The insight into buckle behaviour gained from these analyses was used to assess the validity and performance of design schemes that predict impact response by scaling a known quasi-static response. The analyses also clearly demonstrated the predictive design capability of advanced FE codes. FE simulations were also used extensively and successfully to:

- design the test rig and instrumentation;
- derive and validate data processing procedures; and to
- investigate the gross inertial and vibratory response of the specimen.

**4. Assessment of Quasi-Static Design Schemes**

Quasi-static scaling techniques used in the literature to predict plastic hinge impact response during the design phase were assessed by drawing on the results from the

The derivation of plastic hinge $M$-$\theta$ response from raw experimental measurements is described in Chapter 4. Appropriate measures of hinge rotation and hinge moment are defined first and then the relatively simple procedures used to process quasi-static test data are derived. The processing of impact test data is complicated by the need to address the influences of measurement system frequency response and specimen vibration. It is demonstrated that the preferred means of addressing these dynamic effects is to low-pass filter the moment and rotation signals.

The $M$-$\theta$ responses from five quasi-static and four impact tests on 50x50x2 C350LO RHS are presented in Chapter 5. The effect of material strain rate sensitivity on the plastic hinge and specimen as a whole is quantified by comparing quasi-static and impact responses. Quasi-static results are compared with results published by Cimpoeru (1992) for pure bending tests on the same hollow section, and with the analytical model derived by Kecman (1979).

Chapter 6 describes the strain rate sensitivity of RHS wall material, established by uni-axial tensile tests conducted on grade C350LO and DuraGal coupons at four strain rates, ranging from $10^{-4}$ to 10 $s^{-1}$. The measured strain rate sensitivity of RHS wall material is compared with that commonly assumed in the literature.

Chapters 3, 4 and 6 contain quite a high degree of detail. This detail was considered to be necessary to demonstrate the effort taken to ensure that test results could be relied upon.

Chapter 7 presents the modelling details and results for the principal shell element analyses of the local buckle. A novel pseudo-dynamic loading scheme is described. This scheme was devised to properly account for material strain rate sensitivity within a static solution. Details are also given of a beam element model used for a number of supporting proofs and investigations.

The results of Chapters 5, 6 and 7 are brought together in Chapter 8 to discuss and critically assess quasi-static scaling methods used to predict the plastic hinge impact response of structural components during the design phase. An improved theoretical quasi-static scaling factor is derived and recommendations for the proper use of local plastic hinge data in a global hybrid analysis are made.

The main conclusions and contributions of the thesis are summarised in Chapter 9.

Implementation of the "hybrid" design approach to framework analysis usually involves conducting a non-linear, large deflection, beam finite element analysis of the global structure. Kecman (1983), Mahmood et al. (1988) and Kecman et al. (1993) implemented the hybrid design approach for the quasi-static analysis of framework structures. Implementations for the dynamic analysis of frameworks are discussed by Kecman and Randell (1996) using DYNA3D and Roca et al. (1997) using ABAQUS.

Irrespective of whether the global analysis is static or dynamic, the impact response of the local plastic hinges must be determined. Three methods to determine the plastic hinge response of RHS under impact loading are: physical impact testing, numerical modelling and scaling a known quasi-static response. These approaches will now be reviewed.

## 2.2 EXPERIMENTAL COLLAPSE OF THIN WALLED MEMBERS

Many experimental studies into the deep collapse response of various thin-walled members are available in the literature.

### 2.2.1 Axially Loaded Columns

Key and Hancock (1993b) describe a detailed experimental investigation of the quasi-static column behaviour of cold-formed square hollow sections. A large deflection elasto-plastic finite strip analysis, including detailed measurements of yield stress and residual stress, was used to investigate non-linear local buckling behaviour. The analysis accounted for plate imperfections, the variation of yield stress around the section, the wall material *stress-strain* characteristics and the complex pattern of residual stress produced by the cold-forming process.

Published experimental studies into the axial crush of thin-walled tubes under both quasi-static and impact loading include Ohkubo et al. (1974), Thornton (1975), VanKuren and Scott (1977), Gál and Molnár (1978), Abramowicz and Jones (1986) and Langseth and Hopperstad (1996). These references cover tests on square, circular and closed hat sections, with typical principal dimensions of 50 to 100 mm and impact velocities typically less than 10 $ms^{-1}$. Further impact tests are reported by Wierzbicki et al. (1978) and Abramowicz and Jones (1984a; 1984b). Jones and Birch (1990) axially crushed square tubes with various arrangements of axial stiffening. Quasi-static crush tests on steel, aluminium and PVC tubes are reported by Meng et al. (1983). Tani and

Funahashi (1978) report quasi-static and impact axial crush tests on automobile body structural members (closed top hats and variations).

## 2.2.2 Combined Loading

Ohkami et al. (1990) tested curved beams made from closed top hat sections, representative of vehicle chassis members, under quasi-static and impact axial compression. In their arrangement the section was subject to combined bending and axial loads.

Quasi-static combined loading tests on RHS have been conducted by McIvor et al. (1977a, 1977b), Brown and Tidbury (1983) and Todorovska-Azievska and Kecman (1988). Kim and Wierzbicki (2000) conducted a parametric FE study of thin-walled hollow beams, replicating the testing of Brown and Tidbury. McIvor et al. proposed and tested a model of the multi-axial collapse of thin-walled beams, in which it was assumed that the orthogonal stress-resultants were uncoupled and behaved in the same way under multi-axial loading as under uni-axial loading. This approach gave good agreement with two large deformation, combined loading, experiments on 3-D structures. Interaction diagrams plotted by White et al. (1993), also confirmed the approach. The Cranfield Impact Centre program SIMSTAT (previously CRASHD) adopts this approach, of modelling multi-axial collapse on the basis of uni-axial collapse.

## 2.2.3 Quasi-Static Bending of RHS

### 2.2.3.1 Initial Elasto-Plastic Post-buckle Response

Graves-Smith (1972) analysed the post-buckled elasto-plastic behaviour of a thin walled box beam in pure bending. Graves-Smith used the Rayleigh-Ritz energy method and treated the box beam as a system of plates subject to equilibrium and compatibility conditions at their junctions. The analysis produced elasto-plastic loading curves for the section but was not adequate to predict the collapse of the beam associated with the appearance of a secondary buckle mode.

Kim et al. (1997) tested rectangular hollow sections in pure bending through to deep collapse using the test rig design of Cimpoeru (1992). By combining an empirical

prediction of the angle at buckle initiation and a plastic analysis of the section, they obtained a good prediction of peak moment.

#### 2.2.3.2 DEEP COLLAPSE

The most comprehensive studies on the quasi-static deep bending collapse of rectangular hollow sections are Kecman (1979) and Cimpoeru (1992).

Kecman (1979) conducted the first detailed experimental investigation into the bending collapse of rectangular section tubes. This investigation was part of a broader study of bus structure rollover crashworthiness. Kecman conducted quasi-static bend tests on 27 different sections, with aspect ratios ranging from 0.33 to 3.0 and width to wall thickness ratios from 9.14 to 128. This extensive test programme provided fundamental insight, empirical data and validation for the development of an analytical model of rectangular section deep bending collapse. For simplicity the specimens were tested as cantilevers rather than in pure bending. The effect of shear on the collapse was considered negligible because the cantilevers were 1.0 to 1.2 m long. Hinge moment – plastic rotation responses were derived from measurements of load and specimen tip displacement. Hinge moment was calculated at the centre of the buckle, this point being identified after the test. The onset of collapse was assumed to be at the point of maximum moment, so that all pre-buckle plastic curvature was neglected. Plastic rotation was calculated by subtracting elastic rotation from the total rotation, assuming the specimen stiffness was constant and equal to the initial elastic loading stiffness.

Cimpoeru (1992) also conducted an experimental study into the bending collapse of thin-walled tubes. Cimpoeru concentrated on 50x50x2 grade 350 RHS, a section typical of that used in the Australian bus industry. The same section was tested in this study. Thus, Cimpoeru's results provide a comparison for the cantilever tests in this study.

The main focus of Cimpoeru's work was the measurement of RHS *moment-rotation* properties up to and beyond collapse, using a unique test rig, shown in Figure 2.1, that applied a pure bending moment through to large deflections, without the development of significant shear or tensile forces.

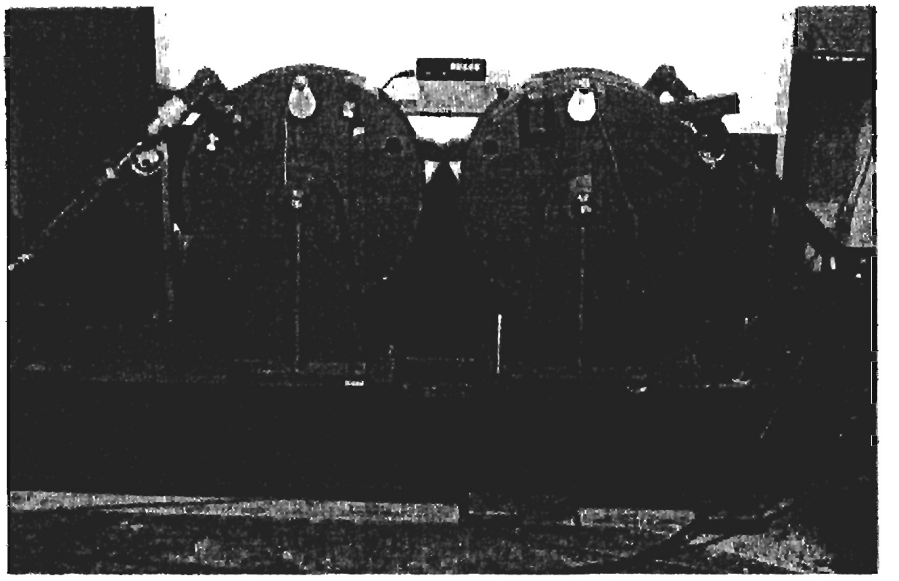

**Figure 2.1:** Pure bending test rig of Cimpoeru (1992)

Cimpoeru preferred pure bending to cantilever loading, because shear and axial loads can develop in certain cantilever test arrangements and because the definition of collapse moment in cantilever loading is uncertain. (Different definitions can exist before and after local buckling). Cimpoeru reasoned that pure bending was the best arrangement to allow the full and proper development of a collapse mechanism so that its formation could be properly studied.

An important conclusion drawn by Cimpoeru was the concept of a "finite mechanism length", defined by Cimpoeru as the finite length of tube that directly contributes to the *moment-rotation* properties of the collapse mechanism. Cimpoeru proposed that it was important that the deformable length of test specimens be limited to the finite mechanism length so that "*an accurate moment-rotation curve can be obtained*" for the local plastic collapse mechanism. A second associated conclusion drawn by Cimpoeru was that the rotation parameter in the analytical model of Kecman should be absolute rotation i.e. hinge rotation measured from the point of initial loading rather than hinge rotation measured relative to any other hinge condition.

#### 2.2.3.3 RESTRICTED COLLAPSE

The local buckling of a thin-walled hollow tube subjected to large bending deformations causes a significant drop in the moment and energy-absorption capacity of the section. In an attempt to minimise localised buckling and thereby improve the energy-absorbing capacity of thin-walled structures subjected to gross plastic deformation, various authors

have investigated the quasi-static collapse of hollow sections filled with various light weight materials. Grzebieta and White (1994) investigated the deep bending collapse of closed hat sections filled with a non-expansive two part epoxy. They found that for moderately thin profiles (b/t > 50) the maximum bending capacity and residual strength of filled beams was up to an order of magnitude higher than for unfilled beams. However at b/t ratios >100 material rupture limited the effectiveness of void filling. Hanssen et al. (2000) conducted quasi-static three point bending tests on aluminium extrusions filled with three different densities of aluminium foam. They found that the denser foam fillers were more effective at resisting section buckling. It was also observed that when the foam core was sufficiently strong the extrusion was able to obtain a fully plastic moment capacity. However, for most cases the development of full plasticity was followed by ductile failure in the tensile flange. The effect of aluminium foam and honeycomb fillers on the torsional crushing behaviour of thin-walled members has been studied numerically by Santosa and Wierzbicki (1997). This work followed previous work, by the same authors, into the axial crushing of filled sections.

### 2.2.4 Impact Bending Experiments

The same literature searches that returned the many papers on impact crushing of thin-walled members failed to return a single paper specifically reporting the results of impact bending tests on RHS. Vignjevic et al. (1993) conducted pendulum impact tests on simple frameworks, where the RHS members collapsed under biaxial bending and torsion. Their paper presented plots of *pendulum displacement Vs time*. Comparative quasi-static results were not presented because the intent of the paper was to validate a numerical dynamic analysis. Kecman (1979) presented the results of quasi-static and pendulum impact tests ($V_0$ = 4.6 $ms^{-1}$) on a bus ring frame. Plots of impact force and frame displacement were compared. The force trace exhibited a high initial peak, caused by inertial forces, followed by a drop in load due to the ring frame bouncing away from the pendulum. Kecman (1993a) presented a representative plot of *pendulum moment Vs pendulum rotation* for quasi-static and impact tests on an unknown component (possibly a RHS beam or joint).

Drazetic et al. (1994) conducted impact bend tests on thin-walled rectangular section beams. The arrangement of the test was such that a plastic hinge developed at the site of a local indentation. Because the intent of the testing was to validate a non-direct

## 2.3 DYNAMIC EFFECTS

The collapse response of a structure subjected to impact loading can differ from the corresponding collapse response under quasi-static loading, due to the influence of the two "dynamic effects": inertia; and material strain rate sensitivity. The fundamental influence of these effects is now considered.

### 2.3.1 Influence of Inertia

Depending upon the nature of a structure, inertia can influence impact response in different ways. Calladine and English (1984) identified two classes of structure, Type I and Type II. Type I structures are characterised by quasi-static *load-deflection* curves that are "flat-topped" or rise and fall gently, whereas *load-deflection* curves for Type II structures have a high initial "peak" followed by a sharp decline, Figure 2.2a. Experiments on the Type I and Type II specimens shown in Figure 2.2b, indicated that the response of the Type II structures was much more velocity sensitive than the Type I structures. The root cause of this behaviour was that the kinematics of the collapse mode in the vicinity of peak load required rapid rotation of the "hinges" in relation to the loading rate. This gives rise to high strain rates in the hinges and high lateral accelerations and hence significant inertial loading.

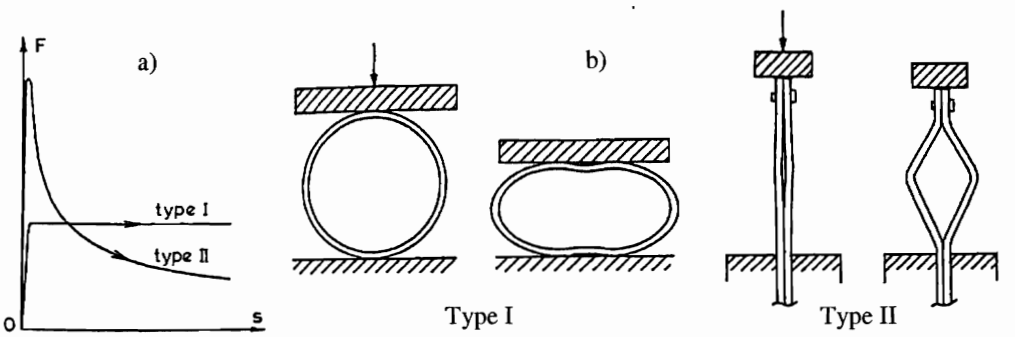


**Figure 2.2:** a) Type I and Type II quasi-static load curves, Calladine and English (1984)
b) Type I and Type II specimens tested by Tam (1990)

Tam (1990) continued the work of Calladine and English and developed a theory for the behaviour of the Type II specimens tested by Calladine and English. Tam identified an initial phase of collapse initiated by the effect of lateral inertia forces on the plates. During this phase a considerable portion of the kinetic energy of the striker was absorbed in axial compression of the plates. Consequently, the deformation produced

under impact was significantly less than that corresponding to an equal amount of energy absorbed under quasi-static loading. This effect was revealed in impact/static energy ratios greater than unity, even after accounting for the effect of strain rate. Tam and Calladine (1991) demonstrated that the amount of energy absorbed in the initial inertial phase was a function of impact velocity, in addition to the initial crookedness and the mass ratio between the striker and the specimen, as previously proposed. Grzebieta and Murray (1986) impacted Type II specimens consisting of initially kinked pin ended struts. As the initial kink angle was reduced, they noticed an increase in the impact/static energy ratio and a significant rise in initial peak load above that predicted after taking the effect of strain rate on yield stress into account. These results were consistent with the increase in inertial effects for Type II structures (small kink angles lead to "peaky" Type II responses).

Vehicle structural members often contain deliberate kinks to limit the initial inertial response and associated large load spikes and to induce a stable crush mode (Gupta 1998; Kitagawa et al. 1992; Langseth & Hopperstad 1996).

Reid (1983, 1984) discussed experiments on laterally compressed one-dimensional tube systems. Reid described an effect where deformation of the system was influenced by a "plastic structural shock wave" which passed from ring to ring. It was clearly demonstrated that ring inertia played a major role in establishing the pattern of deformation in the system as well as the level of the transmitted load pulse. Reid et al. (1993) extended the discussion to two dimensional cellular structures and cellular materials. Reid concluded that there were two prime inertial effects in cellular structures: crushing wave propagation and the inertia of individual cell walls (termed micro-inertia). Micro-inertia, although a difficult effect to quantify, could modify the collapse mechanism of a cell, leading to higher initial crush loads. This effect is synonymous with the effect discussed above in Type II structures.

A case where inertia acted to reduce impact loads was the internal inversion of metal tubes considered by Harrigan et al. (1999). In this case inertial effects reduce the steady state inversion force, compared to quasi-static loading.

Jones (1989a) discussed in detail two different collapse modes of axially impacted hollow sections. Tubes were observed to collapse progressively from one end under quasi-static loading, and also under impact loading when lateral and axial inertia effects

designer when a full dynamic analysis is necessary. The answer to the question also depends on the accuracy that a design requires. Unfortunately, the error associated with the application of a quasi-static design approach is often unknown.

## 2.3.2 Material Strain Rate Sensitivity

Research has shown that the mechanical properties of many materials, in particular mild steels, are dependent on the rate of loading. This phenomenon is known as material strain rate sensitivity. Unlike inertia, the influence of material strain rate sensitivity should be accounted for even at low impact velocities. The following review focuses on the strain rate sensitivity of steels tested at room temperature, at strain rates up to approximately $10^2$ $s^{-1}$ and plastic strains up to ultimate strength. These conditions are typical of those experienced by crashworthy structural members (Davies & Magee 1975).

### 2.3.2.1 Strain Rate Sensitivity of Mechanical Properties: yield stress, ultimate tensile strength and ductility

The frequently cited work of Manjoine (1944) was one of the earliest studies into material strain rate sensitivity. Manjoine conducted tensile tests on annealed commercial low-carbon open-hearth steel at strain rates ranging from $10^{-6}$ $s^{-1}$ to $10^3$ $s^{-1}$. Both the lower yield and ultimate tensile stresses were found to increase with increasing strain rate. The strain rate sensitivity of flow stress decreased progressively with increasing strain. As a consequence, the amount of strain hardening decreased with increasing strain rate, and the *stress-strain* curve "flattened". The length of the lower yield plateau increased with increasing strain rate, whereas uniform strain (engineering strain at UTS) and total elongation (engineering strain at fracture) appeared to be insensitive to strain rate.

Campbell and Cooper (1966) tested annealed En 2A mild steel at mean plastic strain rates in the range $10^{-3}$ $s^{-1}$ to $10^2$ $s^{-1}$, Figure 2.3. The strain rate sensitivity of upper yield stress, lower yield stress and ultimate tensile stress showed the same trends as reported by Manjoine (1944). "Flattening" of the *stress-strain* curve at higher strain rates was again evident and at a strain rate of about 100 $s^{-1}$, the nominal rate of work hardening was zero. The results also indicated that fracture strain decreased i.e. the material became less ductile, as strain rate increased.

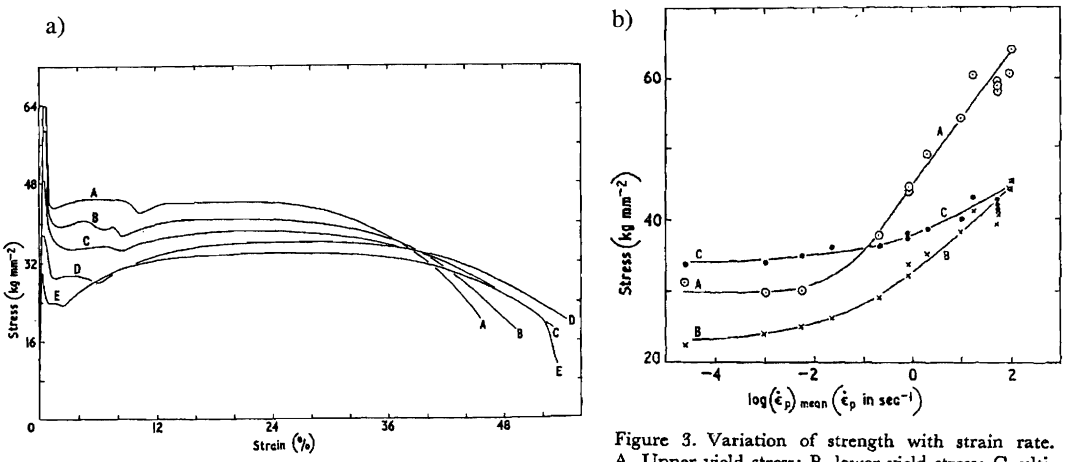


Figure 2. Tensile stress–strain curves. Mean plastic strain rates ($sec^{-1}$): A, 106; B, 55; C, 2; D, 0·22; E, 0·001.

Figure 3. Variation of strength with strain rate. A, Upper yield stress; B, lower yield stress; C, ultimate tensile stress.

**Figure 2.3:** Tensile mechanical properties of EN 2A mild steel, Campbell and Cooper (1966)

Chatfield and Rote (1974) conducted a test program to measure the dynamic mechanical properties of hot rolled sheet steels, including high strength low alloy (HSLA) steels, with yield strengths ranging from 275 MPa to 550 MPa. Target strain rates ranged from 0.008 to 80 $s^{-1}$. Their Results showed that for all the ferrous alloys tested, both yield and ultimate tensile stress increased substantially with strain rate, whilst the 6061-T6 aluminium alloy exhibited no strain rate sensitivity. Chatfield and Rote also found that for the group of HSLA steels tested, strain rate sensitivity decreased with increasing static strength. A comparison of the results at the two extreme strain rates showed a significant reduction in uniform strain at the highest rate for all materials except the highest strength HSLA steel and the aluminium. However, the results for uniform strain at the intermediate rates did not fit a clear trend. No apparent relationship existed between total elongation and strain rate.

Davies and Magee (1975) recognised a lack of material data applicable to low speed vehicle accidents (8 to 48 km/hr), and conducted an extensive testing programme to determine the tensile strength of seventeen materials including steels, Al alloys and fibre reinforced plastics, at strain rates from $10^{-3}$ $s^{-1}$ to $10^{3}$ $s^{-1}$. Stainless steel exhibited no strain rate dependence; the Al alloys were only slightly sensitive to strain rate; the hot rolled steels showed significant strain rate dependence and the reinforced plastics were the most sensitive. Results for the steel specimens showed that: yield stress was more rate-dependent than the flow stress at higher strains; strain rate sensitivity decreased with prior cold work; and strain rate sensitivity also decreased with increasing static

strength (as per Chatfield and Rote (1974)). No significant influence of strain rate on uniform strain was found.

More recently Langseth et al. (1991) tested ST 52-3N mild steel plate (8mm and 25 mm) in tension and torsion at strain rates from $10^{-4}$ $s^{-1}$ to $10^{3}$ $s^{-1}$. Specimens were cut both parallel and normal to the rolling direction, however no systematic variation between the results for the two directions was found. A small increase in the ultimate strain was observed at the lower strain rates, no increase was observed at strain rates between $0.01s^{-1}$ and $20s^{-1}$, and at the higher strain rates a reduction in the ultimate strain was observed. The influence of strain rate on yield stress, yield strain, ultimate tensile stress and flow stress was consistent with the general findings summarised below in Section 2.3.2.3.

Kassar and Yu (1992) also investigated the effect of strain rate on the material properties of sheet steels. Three sheet steels, one hot-rolled and two cold-rolled, were tested in tension and compression at 3 strain rates between $10^{-4}$ and 1.0 $s^{-1}$ and different amounts of prior cold stretching, Figure 2.4. Specimens were cut parallel and normal to the direction of sheet rolling.

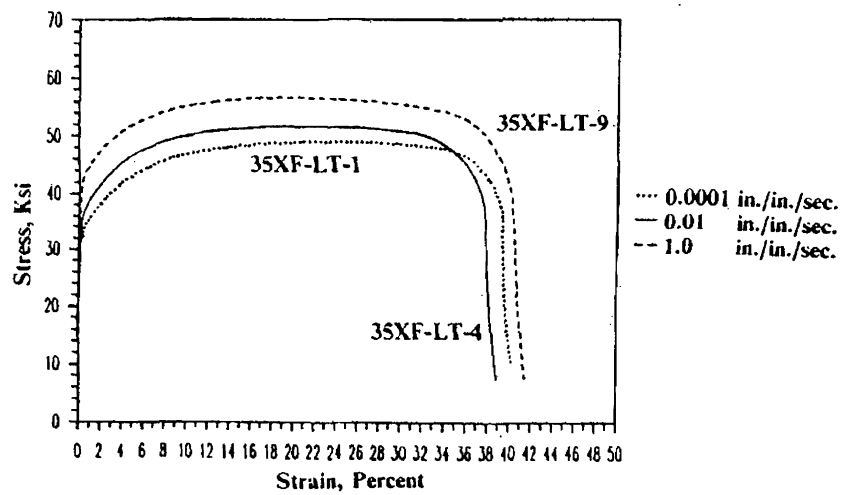


**Figure 2.4:** Stress-strain curves for 35XF sheet steel, Kassar and Yu (1992)

The results conformed to the trend for steels i.e. yield and ultimate tensile strengths increased with strain rate and yield strength was the more sensitive. The strain rate sensitivity of yield stress decreased as the static yield strength and/or the amount of cold stretching increased. The strain rate sensitivity of tensile yield stress, tensile ultimate strength and compressive yield stress were independent of the specimen orientation. The

### 2.3.2.4 CONSTITUTIVE MODELS OF STRAIN RATE SENSITIVITY

For analysis purposes, it is appropriate to describe the strain rate sensitivity of a material in functional form.

Davies and Magee (1975) found that dynamic flow stress was dependent on the logarithm of strain rate. For the materials they tested, the ratio of UTS at the higher strain rate to UTS at the lower strain rate obeyed the equation, $R = 1 + K_r \log\left(\frac{V_2}{V_1}\right)$. The test results of Langseth et. al. (1991) also indicated a linear relationship between stress and the logarithm of strain rate. They defined the ratio of dynamic stress to static stress by the function $1 + C\log\left(\frac{\dot{\varepsilon}}{\dot{\varepsilon}_0}\right)$. Two separate values of C were used, one for lower yield and one for the strain-hardening region.

The results of Marsh and Campbell (1963), at the higher strain rates, (> ≈ 0.1 $s^{-1}$), showed that dynamic flow stress, for a given strain, varied approximately linearly with the logarithm of strain rate. However, the fitted slopes were dependent on strain.

Chatfield and Rote (1974) fitted the function, $\sigma = c\dot{\varepsilon}^m$, to the measured yield stress of various HSLA steels. However, Figure 11 in their paper would suggest that for the majority of the steels, yield stress was linearly related to the logarithm of strain rate, as was found by Davies and Magee (1975) and Langseth et al. (1991).

Kassar and Yu (1992) fitted a quadratic function to plots of tensile yield stress Vs the logarithm of strain rate and suggested that this function might be used to extrapolate the yield stress at higher strain rates. However, since they only tested at 3 strain rates there was no evidence to support this claim. However, the results did show a consistent increase in strain rate sensitivity with increasing strain rate, which suggested that the relationship between tensile yield stress and the logarithm of strain rate was not linear.

A commonly used model to describe the strain rate sensitivity of mild steel is the so-called Cowper-Symonds relation, Equation 2.1, (Bodner & Symonds 1962).

$$\frac{\sigma_{dyn}}{\sigma_{stat}} = 1 + \left(\frac{\dot{\varepsilon}}{D}\right)^{\frac{1}{q}} \tag{2.1}$$

### 2.3.3 Areas Identified for Investigation

1. It has been noted that, qualitatively, the mode shape of the local buckle is the same under quasi-static and impact loading. The quantitative influence of inertia on hinge *moment – rotation* response has not been studied.

2. Whilst there are published experimental studies into the strain rate sensitivity of steels at large strains, the author is unaware of any published test data for the strain rate sensitivity of the material in cold-rolled tube walls, at small or large strains. This is despite a large body of research into the impact response of tubular sections. Given the significant amount of cold work that is done during the manufacture of RHS (see the discussion in Section 2.6.2.1 below), it is possible that the strain rate sensitivity of RHS wall material could be different to that of the steels tested in the studies reviewed above. What then, is an appropriate definition of strain rate sensitivity for the material in cold-rolled hollow sections?

## 2.4 NUMERICAL MODELLING

Recently the application of detailed finite element (FE) analysis to the design of safety structures has become common practice. This has come about due to the increased accuracy of codes and significantly increased computational power and reduced cost of computer hardware. Most commonly explicit dynamic solvers are used, although some impact analyses are conducted using implicit solvers. An example of a detailed explicit crashworthiness analysis is Zaouk et al. (2000b). Zaouk et al. discussed the development and validation of a full-scale FE model of a 1996 Plymouth Neon. They emphasised the advantages of component-wise testing and the importance of verifying the material properties of all vehicle components, especially of the major load bearing members.

While numerical analysis can be a rapid and efficient tool for optimising the crashworthiness of structures, numerical models often require validation by experimental testing (Hashemi et al. 1996; Zaouk et al. 2000a, 2000b). Drazetic et al. (1994) described a procedure where scale models, rather than full size prototypes, were used to validate a numerical model, which was then used to investigate prototype behaviour.

The application of interest in this discussion is the use of FE analyses to derive the crash characteristics of components, for use in the hybrid modelling of a global structure. An important issue when analysing or testing components, is the appropriate modelling of the loading and restraint conditions of the component *in-situ*. (In this case "appropriate" does not necessarily mean exact). Some examples of the successful application of explicit dynamic analysis to the analysis of component impact response are given below.

Vignjevic and Cavalcanti (1997) conducted a crash analysis of components from a Lynx helicopter with the intention of developing a detailed component model for use in a FE model of the entire helicopter. The failure modes predicted by the analysis were consistent with those observed in physical tests, and the analysis gave an acceptable prediction of the maximum load.

Langseth et al. (1999) conducted an explicit dynamic analysis of the axial crush of square aluminium extrusions. They used a very fine mesh to capture the complex progressive folding of the section. The predicted and measured mean crushing loads were typically within 10%. The shape of the force – displacement curves also compared well. Their validated model was then used to study the effect of projectile mass and impact velocity on the collapse response.

Sheh and Khalil (1991) studied numerically and experimentally the impact collapse of a vehicle mid-rail. They achieved good correlation between predicted and measured barrier force and vehicle deceleration time histories. Understandably, there was less correlation for local accelerations on the mid-rail member.

Hashemi et al. (1996) investigated the impact response of an airframe fuselage component under simulated belly crash landing. The measured impact load lay within the predicted upper and lower bands. The predicted collapse behaviour also compared well with the results of impact tests.

### 2.4.1 Bending Collapse of RHS

Just as there have been few experimental studies into the deep bending collapse of RHS, there also appears to be few published detailed numerical studies into the deep bending collapse of RHS under quasi-static or impact loading.

Wierzbicki et al. (1994) modelled the quasi-static pure bending of RHS. Their mesh was suitably refined to capture the local buckling mode, Figure 2.5.

accuracy and solution time. Drazetic et al. (1994) used a coarse mesh to study the local buckling/indentation of hollow sections. Kormi et al. (1995) used a medium density mesh to model the axial crush collapse of square tubes with axial stiffening. Han and Park (1999), (see Figure 2.6 below) and Langseth et al. (1999) used a very fine mesh because the axial and bending collapse under investigation involved complex buckling. A graded mesh, with high element density in the region of local buckling, was used by Wierzbicki et al. (1994), Figure 2.5.

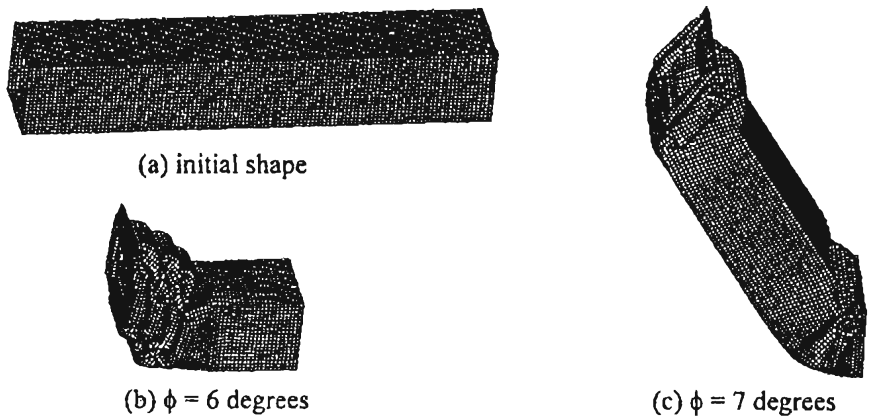


**Figure 2.6:** Typical deformation of a square column under oblique load.
PAMCRASH analysis, Han and Park (1999)

## 2.4.3 Material Definition

In an impact analysis, the strain rate sensitivity of material mechanical properties must be defined. The ideal situation is when material *stress-strain* curves are available for various strain rates (Zaouk et al. 2000b). More commonly, the strain rate sensitivity of steel is accounted for using the Cowper-Symonds model with coefficients $D = 40.4s^{-1}$ and $q = 5$ (Kormi et al. 1995; Jing & Barton 1998). As was discussed in Section 2.3.2.4, these coefficients are generally inappropriate for use in crashworthiness analyses because they represent the strain rate sensitivity of the lower yield stress of mild steel and can significantly over predict flow stress at larger strains. Drazetic et al. (1994) and Harrigan et al. (1999) encountered this problem.

Aluminium is relatively insensitive to strain rate and therefore impact analyses of aluminium structures often use quasi-static material properties.

#### 2.4.5.3 EMPIRICAL MODELS

The models described above were developed by theoretical analysis of the collapse mechanism. An alternative approach is to derive an empirical model of collapse response by applying non-linear multivariable regression analysis to the results of extensive experimental testing (or FE analysis). Wallentowitz and Adam (1995) applied this approach to the prediction of vehicle component crashworthiness. They tested section geometries typical of vehicle front side members, made from various materials, with different joining methods. Axial and oblique quasi-static crush tests and impact crush tests were conducted. Kecman et al. (1990) applied regression analysis to derive equations for the bending *moment – rotation* response of thin-walled, single cell sections, typical of vehicle front side members.

### 2.4.6 Specialised Design Tools

Some of the analytical collapse models discussed above have formed the basis of specialised computer based design tools. These computer codes are typically much more cost-effective than FE analyses, but lack flexibility. Examples are CRASH-CAD for the bending and axial collapse of RHS (Wierzbicki & Abramowicz 1990; Impact Design Inc. 1993) and the Cranfield Impact Centre (CIC) codes WEST and SOUTH for the bending and torsional collapse of RHS and the bending collapse of single cell arbitrary section tubes, respectively (Kecman 1997). Through experience the CIC have determined that it is not necessary to conduct detailed FE analysis of bus and coach structural members because they typically have relatively simple joints and can be analysed using more cost-effective codes such as the CIC design suite. However, FE models are used by the CIC to predict the performance of complex car body members.

Although these specialised codes do not calculate inertial forces or material strain rates they have been used to predict impact response by scaling the material input data to account for material strain rate sensitivity. This approach is an example of the quasi-static scaling design approach discussed below.

### 2.4.7 Areas Identified for Investigation

Most numerical crash studies employ either an explicit or implicit dynamic solver. It is uncommon for numerical crash studies to be conducted using a static solver. However, if the influence of inertia can be neglected, it may be possible to successfully analyse an impact event using a static solver. In the present case the question is, if the inertia of the material in the local buckle has a negligible effect on the *moment – rotation* response of the buckle mechanism, can a quasi-static numerical approach be adopted, that still correctly accounts for material strain rate sensitivity?

One advantage of FE analysis is that FE solutions give thorough insight into material and structural response. Quantities can be output that could not be measured experimentally. The need is identified below for insight into typical strain rates within the buckle, for use in quasi-static scaling design schemes. The distribution and magnitude of strains and strain rates within the buckle, during a typical impact event, can be investigated using a detailed FE analysis.

A key factor in the successful use of FE analysis to predict the impact response of structures is the definition of appropriate dynamic material properties. To date the nature of RHS wall material strain rate sensitivity has not been published. There is therefore a clear need to determine these properties so that the accuracy of FE analyses involving the impact loading of RHS can be improved.

## 2.5 QUASI-STATIC DESIGN SCHEMES

Quasi-static design schemes have been proposed as a means of simplifying impact analyses, in circumstances where the influence of inertia on the collapse response is negligible. The approach is to predict impact response on the basis of known quasi-static performance taking some account of the influence of material strain rate sensitivity.

A review of the literature indicted that there were essentially two quasi-static design schemes, both involving the use of a "dynamic scaling factor". The two schemes were similar but differed in their approach to accounting for the spatial and temporal variation of dynamic flow stress.

## 2.5.1 Theoretical Scaling of Flow Stress

This is the approach commonly used to extend the application of static analytical models to the analysis of impact loading. This approach predicts impact response by substituting dynamic flow stress for static flow stress, in a static analysis. Dynamic flow stress is calculated by scaling static flow stress by a factor $f$, $\sigma_{dyn} = f \times \sigma_{stat}$. Examples of this approach applied to simple "structures" are Grzebieta and Murray (1986), Jones (1989a) and Zhu et al. (1994). Examples of this approach applied to more complex collapse modes are Kecman and Tidbury (1982) and Abramowicz and Jones (1984a, 1984b). These analytical calculations assume a single value of $f$. This approach is appropriate in simple "structures" where there is limited spatial variation of dynamic flow-stress. However, the variation of dynamic flow stress throughout a collapse mechanism can be complex. In these cases the accuracy of the predicted impact response is dependent on the appropriate choices of a material model and strain rate, to calculate $f$.

### 2.5.1.1 Choice of Material Strain Rate Sensitivity Model

It is commonly, indeed almost exclusively, assumed that the scaling factor $f$ is independent of strain, and that material strain rate dependence is given by the Cowper-Symonds function, Equation 2.1, with coefficients of $D = 40.4s^{-1}$ and $q = 5$ (Perrone 1965; Duffey & Karpp 1979; Kecman & Tidbury 1982; Perrone & Bhadra 1984; Zhu et al. 1994). As discussed in Section 2.3.2.4, in large strain crashworthiness design calculations Wierzbicki and Akerstrom (1977) and Jones (1983) questioned the use of the Cowper–Symonds model with these coefficients. The coefficient set $D = 6400$ and $q = 3.91$, which fits the experimental data for the ultimate stress of the steel specimens examined by Campbell and Cooper (1966), has been commonly used by Abramowicz and Jones in their joint and individual publications.

### 2.5.1.2 Choice of Strain Rate

Once an appropriate model to describe material strain rate sensitivity has been determined, it remains to derive an appropriate value for the strain rate parameter in that model. Various approaches have been used for estimating this single strain rate.

Perrone (1965) considered the problem of a strain rate sensitive massless wire supporting an impulsively loaded mass. In this problem, dynamic flow stress varied

temporally. Perrone significantly simplified the theoretical analysis by using the initial strain rate in the wire to calculate a time-independent dynamic flow stress. He justified this approach on the basis that the bulk of the initial kinetic energy would be dissipated before the dynamic flow stress decreased significantly below its initial value. Initial strain rate has been used to calculate dynamic flow stress in the analysis of a number of "structures", including: impulsively loaded fully clamped hemispherical shells and cylindrical shell panels (Jones 1989a), impulsively loaded rings and annular plates (Perrone 1965; Perrone & Bhadra 1984), ring systems (Reid 1983) and cylindrical vessels (Duffey & Karpp 1979). In all these cases, the influence of finite displacements or geometry changes was not important, and there was essentially a single mode of energy absorption.

Perrone and Bhadra (1979) considered an impulsively loaded mass suspended between two massless wires. In this problem there was a change in the deformation mode, in particular the development of membrane forces. Their analysis led to a new approximation, where dynamic yield stress was evaluated using an average strain rate taken as half the maximum strain rate. Perrone and Bhadra (1984) further noted that the maximum strain rate condition occurred at the point in the response corresponding to 2/3 of maximum deflection. This strain rate estimate has been used to study the response of impulsively loaded fully clamped beams, rectangular plates and circular membranes (Jones 1989a) and fully clamped plates impacted by a wedge (Zhu et al. 1994).

Tam (1990) studied "Type II" structures, characterised by quasi-static *load-deflection* curves that have an initial high "peak" followed by a sharp decline. Measurements of surface strain indicated that strain rates during the initial collapse phase were approximately ten times larger than the average strain rate during the second collapse phase. Tam concluded that the use of the initial strain rate to predict dynamic material flow stress was not appropriate in Type II structures, because the initial strain rate was not representative of the strain rate in the dominant second phase of the response.

Grzebieta and Murray (1986) tested a Type II specimen similar to that of Tam. They estimated strain rate for each test from measurements of surface strain. Details of how the strain rates were derived are not given, but it is suspected that the estimated strain rates were applicable to the initial phase of collapse, where strain rates were at their highest. Predicted responses compared well with experimental results, despite the fact

### 2.5.3 Areas Identified for Investigation

The accuracy of the impact response predicted using the flow stress scaling scheme, is dependent on the choices of material model and strain rate used in the calculation of the flow stress scaling factor $f$.

While there is a logical argument against using the Cowper-Symonds model, with coefficients $D = 40.4s^{-1}$ and $q = 5$, for large strain analysis, many still use this material strain rate sensitivity definition in crashworthiness calculations. On the other hand, the two coefficient sets, proposed by Abramowicz and Jones (1986) as being more appropriate in crashworthiness calculations, predict different increases in flow stress. Abramowicz and Jones remark that, *"the disparity between the predictions ... emphasises the lack of adequate experimental data on the dynamic plastic behaviour of materials with large strains which are encountered in the dynamic progressive crushing of square tubes."* Once again, the question is raised as to what is an appropriate definition of strain rate sensitivity for the material in cold-rolled hollow sections.

A second question, given the complex spatial and temporal variation of strain and strain rate within the buckle, is what is an appropriate choice of strain rate to use in the calculation of the single flow stress scaling factor $f$? Further questions are: is this strain rate necessarily representative of strain rates in the buckle and what are typical strain rates in the buckle during collapse?

While the gross response scaling scheme proposed by Kecman will produce a "correct" scaling factor with respect to total hinge energy, there still remains the questions of the extent to which the scaling factor is dependent on the conditions of the test and is it appropriate to scale buckle response using a factor derived by comparing gross specimen energy?

The prediction of impact response by scaling a quasi-static response tacitly assumes that the deformed mode shape is equivalent under quasi-static and impact loading and that the impact response has the same form as the quasi-static response, and hence that inertial effects are negligible. Are these conditions met in the case of the local buckle under investigation, and what are the implications if these conditions are not met?

## 2.6 RELATED AREAS OF LITERATURE REVIEW

### 2.6.1 Special Considerations for Elevated Strain Rate Material Tests

Many different apparatus and techniques have been used to test the mechanical properties of materials at elevated strain rates. One important concern in the design of apparatus and the interpretation of test data is the influence of inertia and stress waves. Elevated strain rate tests are categorised as slow, medium or fast depending upon the relative influence of these effects.

#### 2.6.1.1 LOW STRAIN RATES

The most versatile test equipment for low and intermediate strain rates is a system employing hydraulic actuators to generate the desired loading history. Marsh and Campbell (1963) used an open loop control system and obtained some control over loading rate by incorporating a resizable orifice in the outlet flow. Servo-hydraulic testing machines capable of closed loop control at crosshead speeds above 5 $ms^{-1}$ have been used (Chatfield & Rote 1974) and high-speed hydraulic machines capable of combined axial and torsional loading have also been developed (Lindholm 1974).

In this strain rate class the loading time, whilst relatively short, is still large compared to the time taken for a stress wave to travel the length of the specimen. Consequently, the test piece remains in a state of quasi-equilibrium and wave propagation effects can be neglected, however the strain rates that can be attained are limited. Goldsmith (1960) suggested that wave propagation effects become significant when the strain rate exceeds approximately $10s^{-1}$ for a specimen with a gauge length of 50 to 75 mm. Davies and Magee (1975) encountered problems due to reflected stress waves at strain rates above $80s^{-1}$ with specimens of 19 mm gauge length.

If stress waves are not a concern, then stress and strain in a test specimen can be recorded directly by means of a load transducer in series with the test coupon and an extensometer attached to the coupon. However, as noted by Goldsmith (1960), the strain rate in the specimen is not directly dependent on crosshead velocity but also depends upon the stiffness of the test apparatus and the applied stress-rate. If the stiffness of the test apparatus can be represented by a linear spring with stiffness, $k$, in series with the specimen, the conventional strain rate is given by $\frac{d\varepsilon}{dt} = \frac{v_0}{L_0} - \dot{\sigma}\frac{A_0}{kL_0}$ where $v_0$ is the

crosshead velocity, and $A_0$ and $L_0$ are the original cross-sectional area and length of the specimen, respectively. Depending on the specimen size and machine stiffness, the second term $\dot{\sigma}\frac{A_0}{kL_0}$ may not be negligible. Theoretically, this means that test results cannot be reported in terms of a constant strain rate, but only as a function of crosshead speed. However, in practice the error in the estimate of strain rate is insignificant compared to the range of strain rates under investigation, usually several orders of magnitude. One of the main concerns when designing testing machines in this strain rate range is avoiding system resonance. Thus, another advantage of a stiff test system is its high fundamental natural frequency.

#### 2.6.1.2 MEDIUM STRAIN RATES

Above strain rates of 100 $s^{-1}$, it becomes increasingly difficult to avoid resonance and inertia effects in typical hydraulic and mechanical systems (Lindholm 1974). Since the loading time is now comparable to the transit time of waves in the coupon, large variations in stress, strain and strain rate exist along the coupon. Consequently, force measurements obtained from a load transducer in series with the coupon and extension measurements from an extensometer give only average values, and cannot be directly used to construct a dynamic *stress-strain* relationship. However, meaningful results can be obtained if wave propagation effects are properly considered during data reduction. Ideally, transient stress and strain at a single point in the coupon should be recorded. To minimise these difficulties and retain the assumption of stress equilibrium within the deforming specimen, the coupon must be kept small and attachments to the coupon must be capable of rapid acceleration and be of such geometry that wave propagation effects can be controlled or accounted for.

#### 2.6.1.3 HIGH STRAIN RATES

Various testing apparatus have been designed that overcome the problems of wave propagation by measuring the stress pulse, as in the Hopkinson split pressure bar apparatus. This basic technique has been used, with many modifications, for testing materials under dynamic compression, tension, shear and combined loading (Lindholm 1974; Wulf 1974; Harding 1979). Strain rates up to $10^5 s^{-1}$ have been measured using apparatus of this nature. Still higher strain rates have been achieved using explosive charges to apply the loading.

## 2.6.2 Quasi-Static Mechanical Properties of RHS Material

### 2.6.2.1 RHS MANUFACTURE

The C350LO 50x50x2 hollow sections tested in this study were manufactured by Tubemakers Australia. The section is produced from semi-killed steel strip with a nominal yield stress of 250 MPa, which is supplied in roll form. During manufacture the strip is uncoiled, levelled, formed into a circular section and electric resistance welded in a continuous process. This circular section is finally rolled into the desired rectangular section. The whole process is performed "cold", with no post-forming stress-relieving heat treatment. The significant cold working of the material increases the yield stress to a nominal value of 350 MPa. A complex residual stress state is also developed.

### 2.6.2.2 PROPERTY VARIATION AROUND THE SECTION

As a result of the manufacturing process described above, the amount of cold work experienced by the wall material varies around the section, and consequently the mechanical properties of the tube wall material also vary around the section. A representative picture of these property variations has come from extensive research, conducted at the University of Sydney, into the structural use and performance of cold-rolled hollow sections. Details of the material mechanical properties measured by these researchers will now be discussed.

**Wall properties Vs Corner properties**

Zhao and Hancock (1990) tested C350 102 x 51 RHS and 102 x 102 SHS subjected to both bending and concentrated loading. Tensile coupons were taken from the flat walls and corners of the sections and tested according to AS1391-1974. Because all coupons exhibited gradual yielding, yield stress was measured as a 0.2 percent proof stress. The average yield stress and ultimate tensile strength for the corner coupons were 33% and 23% higher, respectively, than for the wall coupons. The engineering strain at UTS for the corner coupons was 53% of the average for the wall coupons.

Sully and Hancock (1996) tested coupons cut from the corners and flats of 125 x 125 x 6 C350 RHS. The results showed that the average yield stress for the corner coupons was 29% higher than that for the wall coupons and that the average ultimate tensile strength for the corner coupons was 20.5% higher than that for the wall coupons.

The elastic modulus was calculated to be approximately 208 GPa for the wall material and 195 GPa for the corner material.

Zhao and Hancock (1991) report a similar series of material tests on a range of C450 RHS and SHS. The average 0.2% proof stress for the corner coupons was 30.3% higher than that for the wall coupons and the average ultimate tensile strength for the corner coupons was 21.4% higher than that for the wall coupons. These results are very similar to those for the grade 350 material tested by Zhao and Hancock (1990) and Sully and Hancock (1996). The engineering strain at UTS for the corner coupons was 15% of that measured for the flat coupons. This surprisingly large reduction in ductility of 85% for the C450 material is twice as high as the average reduction in ductility for the C350 coupons reported in Zhao and Hancock (1990) and Zhao and Hancock (1992). This result is most likely explained by the fact that the sheet material in the C450 RHS is more heavily cold worked during manufacture.

**Wall opposite seam weld Vs Wall adjacent to seam weld**

Zhao and Hancock (1995) conducted material tests on C350LO RHS and SHS coupons cut from the faces adjacent to the seam weld and from the face opposite the seam weld. The 0.2% proof stress and tensile strength of the opposite face were 7.8% and 3.3% higher, respectively, than those for the adjacent faces. It was concluded that this variation was due to the forming process.

**Tension Vs Compression**

Tensile and compressive tests on coupons cut from C350 RHS and SHS are reported in Zhao and Hancock (1992). Before testing, the "raw" tube was strain-aged at 170°C for 30 minutes. As in other studies, coupons were cut from the walls and corners of each section and tested according to AS1391-1974. For most of the coupons, the *stress-strain* curves exhibited a yield plateau, probably a result of strain ageing. The 0.2% proof stress was used as the yield stress for those coupons exhibiting gradual yielding. The average measured yield stress for the wall coupons was 3.5% lower in compression than in tension. The average tensile yield stress of the corner coupons was 16.8% higher than that for the wall coupons. The average measured yield stress and ultimate strength were 12.2% and 11.2% higher, respectively, than those reported by Zhao and Hancock

(1991). This increase was attributed to the strain ageing of the sections tested in this study.

**Longitudinal Vs Transverse directions**

Tests on RHS wall material reported by Johnson (1990) provide insight into the nature of anisotropy in cold-formed hollow sections. The average yield stress in the longitudinal direction was approximately 5% higher than in the transverse direction. Ultimate tensile stresses were essentially the same. Uniform strain was approximately 5% higher in the longitudinal direction.

**Detailed variations**

Key et al. (1988) reported on some detailed tensile tests to determine the magnitude and distribution of material properties around a series of RHS and SHS. In these tests the "raw" tube was strain-aged at 150°C for 15 minutes prior to testing. The tensile coupons cut from the walls of the sections generally displayed a distinct, though limited, yield plateau in their *stress-strain* behaviour, while the corner regions displayed the gradual yielding typical of highly worked material. A typical distribution of yield stress and ultimate tensile strength around a section is shown in Figure 2.8.

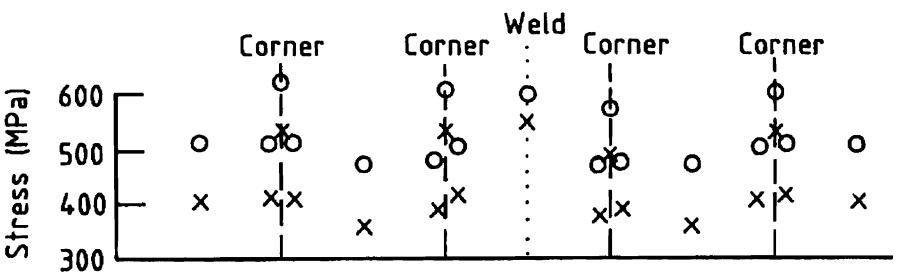


**Figure 2.8:** Variation of tensile properties around a RHS. X = Yield Stress, O = UTS Key et al. (1988)

Figure 2.8 shows the same trends as reported above, that is, yield stress and ultimate tensile strength are significantly higher for the corner material and yield stress and ultimate tensile strength are higher for the material in the face opposite the seam weld compared to material in the faces adjacent to the seam. Figure 2.8 also shows that the increase in strength at the corners is localised and that the strength of material along the seam weld is similar to that at the corners.

**Residual stress distribution around the tube section**

A feature of cold-formed hollow sections is the presence of residual stresses that result from the forming process. These residual stresses can approach the yield stress of the material and are distributed in a complex manner around the section and through the wall thickness. Key and Hancock (1993b) conducted a thorough study into the nature of residual stresses in cold-formed hollow sections, with the aim of developing representative analytical models for both the magnitude and distribution of the residual stresses. Two separate experiments were performed to measure the residual stress state:

1. A three-stage spark erosion process to measure longitudinal and transverse through-thickness residual stress variation.
2. Strip sectioning to measure the variation of longitudinal bending and membrane residual stress components around the section.

The complete residual stress state was assumed to be a summation of membrane, bending and layering stress components in both the longitudinal and transverse directions. The through thickness variations of these components are shown in Figures 2.9 and 2.10.

Key and Hancock investigated the influence of these components of residual stress on the stub column behaviour of square hollow section (SHS) specimens by progressively including the components in a non-linear finite strip analysis. (Details of the finite strip analysis are given in Key and Hancock (1993a)). This analysis showed that:

- the longitudinal membrane component had a negligible influence on section behaviour;
- the longitudinal bending component reduced the ultimate load by up to 5.4% and reduced the axial stiffness of the column by up to 9.1%;
- the longitudinal layering stress component had a small influence on ultimate load and reduced the axial stiffness from an early stage; and
- the transverse components reduced the ultimate load by up to 1.2% and reduced the axial stiffness from an early stage of loading by up to 9%.

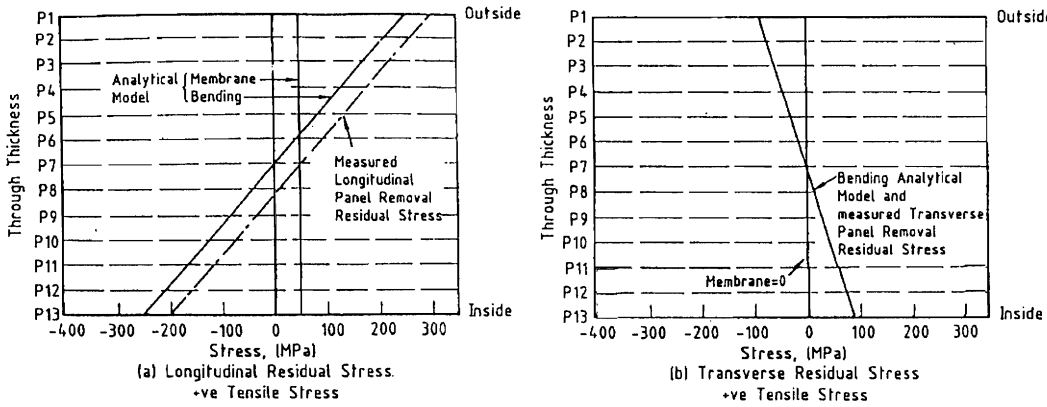


**Figure 2.9:** Analytical model for panel removal residual stress, Key and Hancock (1993b)

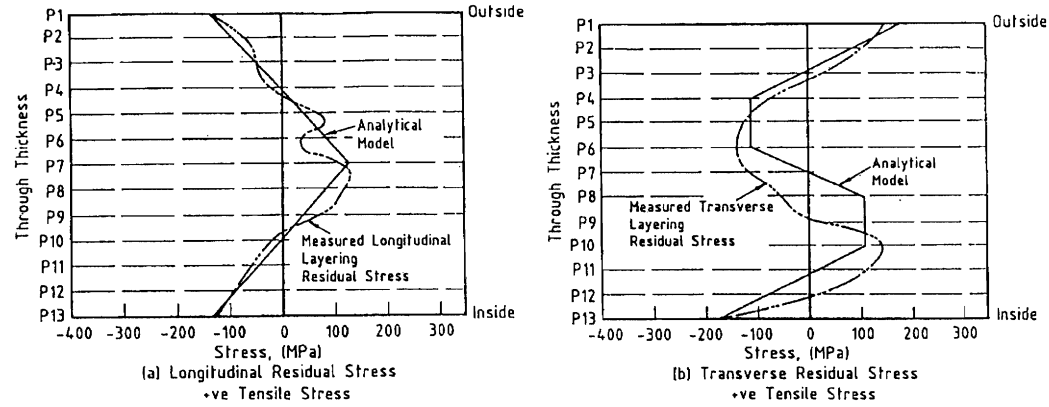


**Figure 2.10:** Analytical model of layering residual stress, Key and Hancock (1993b)

### 2.6.2.3 SUMMARY OF QUASI-STATIC PROPERTIES

- Yield stress and UTS are higher for the corner material compared to the face material.
- Uniform strain for the corner material is approximately half that of the face material.
- Yield stress and UTS are higher for the material in the face opposite the seam weld compared to material in the faces adjacent to the seam weld.
- The increase in strength at the corners is localised; the properties of the material near the corners are similar to those of the face opposite the seam weld and the properties of the material along the seam are similar to those at the corners.

The bend specimens tested in this thesis were designed to represent this joint. Plate 3.3a shows a bend test specimen before and after testing. The specimen consists of a 1300 mm length of 50x50x2 grade C350LO RHS welded to a 16 mm thick mild steel base plate. It was appropriate to test the specimens as cantilevers because *in situ* the joint in Plate 3.2 is loaded by a combination of a bending moment and a shear force. Kecman (1994) recommended this loading arrangement as being "*most suitable in terms of representative loading and boundary conditions*". The similarity between the joint in Plate 3.2 and the specimen in Plate 3.3b is clearly evident.

Initial tests on specimens of this design demonstrated that the buckle location was repeatable, typically to within ± 10 mm. The specimens were mounted so that the predicted buckle location was on the axis of the specimen mount pivot.

Internal plugs to "force" the buckle location were not used, due to the possibility of an unpredictably altered $M$-$\theta$ response. Additionally, a plugged specimen no longer represented a typical bus frame joint and a proper FE model of a plugged specimen would be complicated by contact. Cimpoeru (1992) found that neat fitting inserts could significantly change the pre-collapse response. Cimpoeru therefore adopted loose fitting inserts. Cimpoeru also found that the boundary conditions imposed by inserts could cause an outward buckle, rather than an inward buckle, to develop.

In summary, the chosen specimen design was representative of a real bus frame joint, buckled at a relatively predictable location, was simple to manufacture and could be modelled using a finite element code without the complication of contact.

## 3.3 RIG DESIGN

Quasi-static and impact bend test arrangements for testing the cantilever specimen were required. It was decided that a single rig was needed which would be capable of providing for both loading conditions with no change to the general arrangement or instrumentation and it was necessary to design and build a bend test rig specifically for this study.

Two common impact apparatus were considered, a drop tower and a single axis pendulum.

### 3.4.1 General Specifications

- Pendulum Radius: 1.0 m
- Max Air Spring Pressure: 700 kPa.
- Max. Pendulum Energy: 4 kJ.
- Pendulum Mass: 33 - 90 kg.
- Max. Impact Velocity: 70 km/hr.

### 3.4.2 Measurement of Plastic Hinge Response

Whilst comparisons of gross specimen response could have been made using parameters such as pendulum rotation, contact force and pendulum work (Kecman 1979; Kecman 1993a; Vignjevic et al. 1993), the impact pendulum used in this study was specifically designed and instrumented so that plastic hinge $M$-$\theta$ response could be measured directly. This approach had not previously been reported in the literature for impact tests, although quasi-static tests have been conducted by McIvor (1977a), Cimpoeru (1992) and White et al. (1993) where, in essence hinge $M$-$\theta$ was measured by limiting the deformable length of the specimen. As will be discussed in Chapter 4, the direct measurement of hinge response, without limiting the deformable length of the specimen, required additional instrumentation to measure hinge rotation. Furthermore, as acknowledged by Kecman (1993a, 1993b), the influence of specimen inertia had the potential to significantly complicate the processing of impact test results. Despite these difficulties, the measurement of hinge $M$-$\theta$ response was pursued for the following reasons:

1. The specimen response investigated had two basic geometric phases, pre-buckle and post-buckle. A true assessment of the influence of material strain rate sensitivity on plastic hinge $M$-$\theta$ response could only be made by comparing similar phases of the response. Because comparisons of gross specimen performance combined pre-buckle and post-buckle phases they could only give an indication of the gross influence of material strain rate sensitivity, whereas measurement of hinge $M$-$\theta$ gave a complete picture of the influence of material strain rate sensitivity on impact:static ratios for all rotations.
2. Hinge $M$-$\theta$ responses were less sensitive to the test rig loading arrangement than gross specimen response. (It is shown in Chapter 5 that post-buckle hinge $M$-$\theta$ response was independent of the test rig loading arrangement).

3. Due to the influence of specimen inertia, comparisons of gross specimen response were specific to the geometry of the specimen tested, whereas comparisons of hinge $M$-$\theta$ response were specific to the section tested and independent of specimen geometry.
4. A more comprehensive validation of finite element models was possible by using the complete hinge $M$-$\theta$ response in addition to the gross specimen response.

Because the approach to be used to calculate hinge moment influenced the design of the pendulum, it was appropriate to review the various options for calculating hinge moment. The approach used to calculate hinge rotation is discussed in Section 4.3.1.3.

#### 3.4.2.1 Derivation of Hinge Moment from Pendulum Moment

The methods for calculating hinge moment from measurements of contact force, pendulum acceleration or pendulum work are essentially similar, in that they all use various measures of pendulum moment to derive hinge moment. The three basic problems with this approach were:

1. Pendulum moment was significantly affected by specimen inertia and therefore pendulum moment could not be used to derive the true time history of hinge moment.
2. Contact force was measured remotely from the hinge site and therefore did not strictly represent the response at the hinge at any given instant in time, particularly when the specimen was vibrating. The effect of specimen vibration on the measurement of hinge response is discussed in Sections 4.5.5.1 and 4.5.5.3.
3. To derive hinge moment, specimen tip rotation had to be known.

The limitations imposed by specimen inertia on the calculation of hinge moment using contact force, pendulum acceleration or pendulum work are discussed below.

**Calculation of Hinge Moment from Contact Force**

The influence of specimen inertia on pendulum to specimen contact force was most significant in the early stages of loading. Figure 3.1 shows the transfer of energy from the pendulum to the specimen during the initial pre-buckle response. Also shown is the status of contact between the pendulum and the specimen. Figure 3.2a compares the true hinge moment and the hinge moment derived from contact force. The results are from

the dynamic beam FE model described in Section 7.2. The following observations are noted.

- In the period immediately following initial contact, and before the significant period of lost contact, the majority of energy lost by the pendulum was absorbed as specimen kinetic energy, not strain energy. Large positive contact forces existed during this time and yet the true hinge moment was negative.
- The pendulum and specimen lost contact for a significant period between t = 3 and 7 msec. During this period contact force was equal to zero, however hinge moment was non-zero because the specimen continued to be loaded by the action of its own inertia, converting kinetic energy to strain energy.
- Contact force could only be positive, whereas the initial response of true hinge moment was negative.

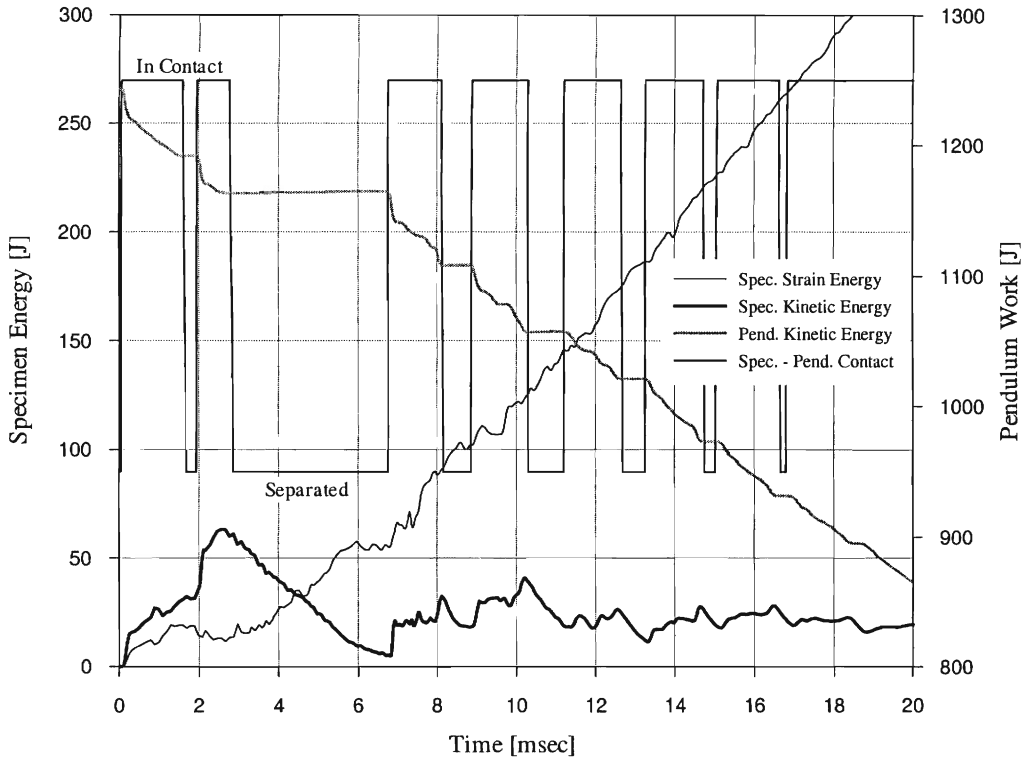


**Figure 3.1:** Pendulum – Specimen energy transfer during the initial stages of an impact test

When contact force was filtered, as is a common procedure for processing impact data, the periods of lost contact caused significant distortion of the signal. This is demonstrated in Figure 3.2b using results from a FE analysis, where in the pre-buckle phase the filtered contact force signal bears little resemblance to the true hinge moment. Figure 3.3 shows *moment-rotation* traces from quasi-static and pendulum impact tests

conducted at the Cranfield Impact Centre on an unknown specimen (Kecman 1993a). Moment was derived from filtered contact force. The nature of the impact trace is remarkably similar to that shown in Figure 3.2b.

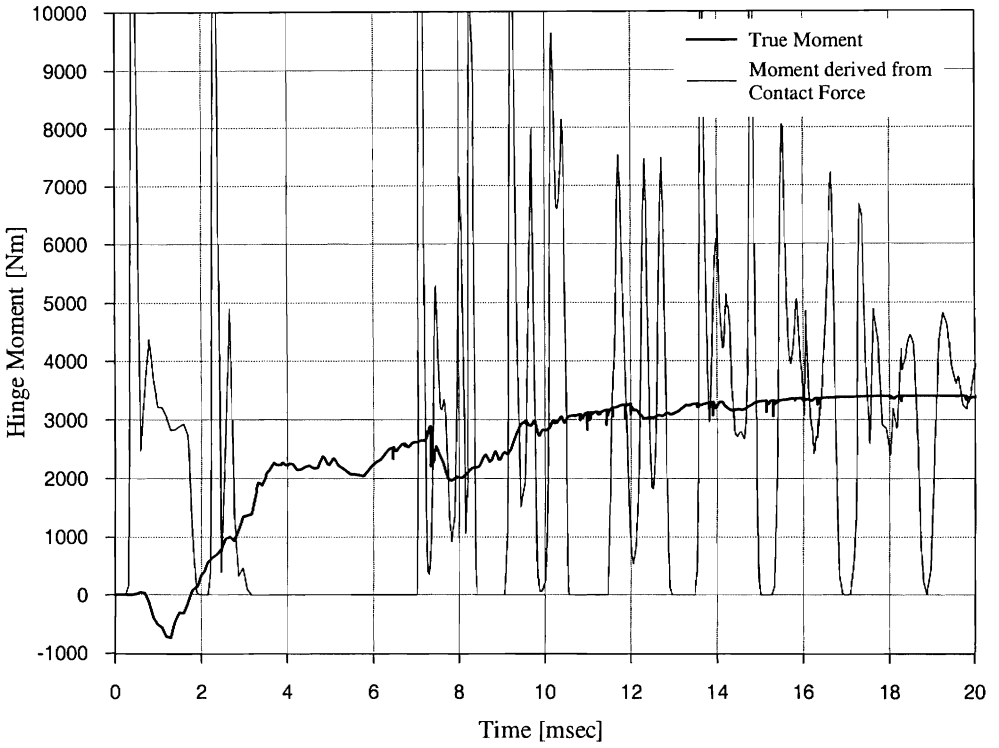


**Figure 3.2a:** Hinge moment from FE analysis – true and derived from contact force

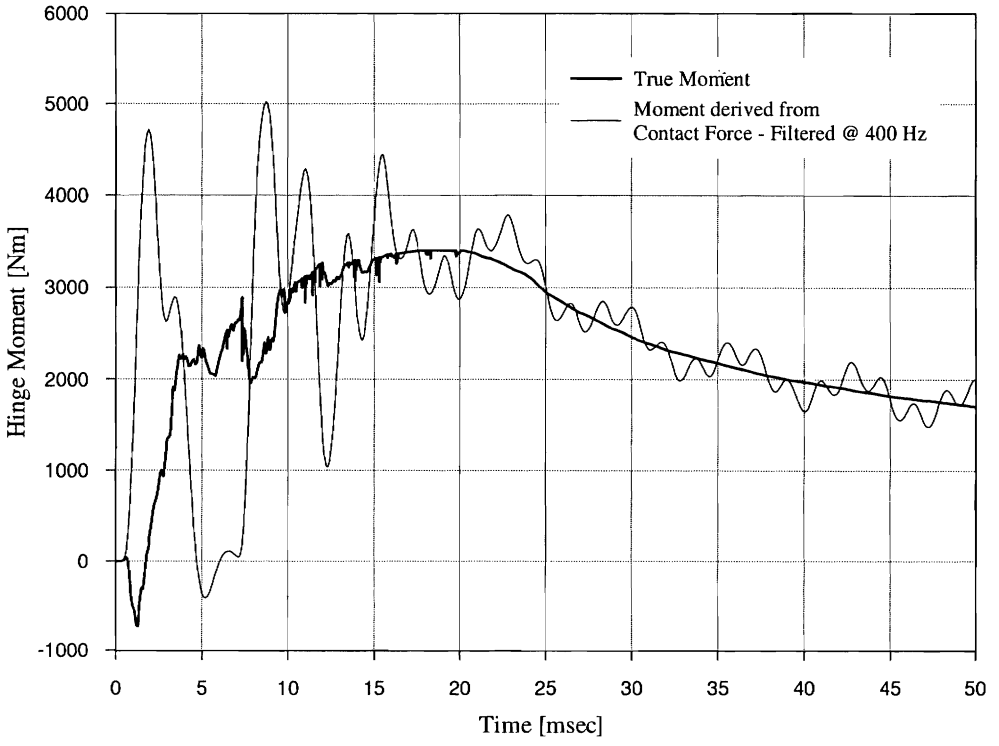


**Figure 3.2b:** Hinge moment from FE analysis – true and derived from filtered contact force

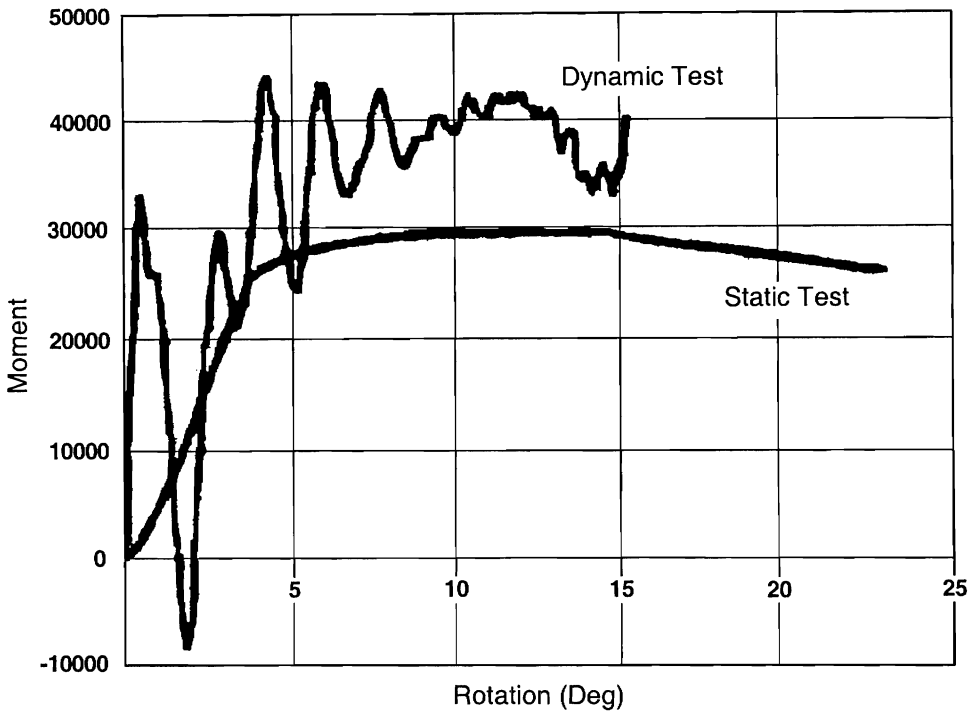


**Figure 3.3:** Moment-rotation traces from quasi-static and pendulum impact tests –Kecman (1993a)
Impact moment was derived from filtered pendulum contact force

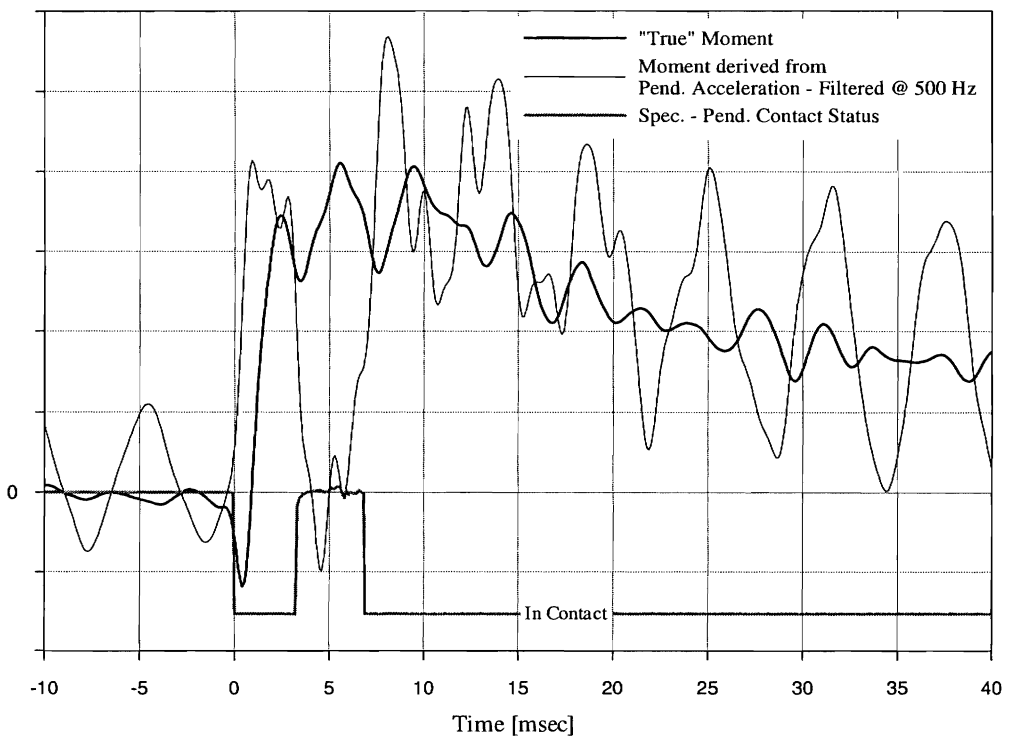


**Figure 3.4:** Unscaled pendulum acceleration and reaction force –
physical impact test

### Calculation of Hinge Moment from Pendulum Acceleration

Measurement of pendulum acceleration was essentially the same as measuring contact force. Figure 3.4 compares unscaled pendulum acceleration and specimen mount reaction force from an actual impact test (both signals have been filtered at 500 Hz using a $4^{th}$ order Butterworth filter). The signals show a distinct similarity to the FE results shown in Figure 3.2b (note that the pendulum acceleration signal was coloured by a frequency corresponding to the vibration of the pendulum).

### Calculation of Hinge Moment from Pendulum Work

In this approach hinge moment was derived from pendulum moment, which was derived from pendulum work. This approach was subject to the same limitations as described for the use of contact force. Theoretically, pendulum moment could have been derived from pendulum work by simple differentiation. Vignjevic et al. (1990) investigated the application of this approach to dynamic FE results. Vignjevic had moderate success predicting post-buckle response using a non-trivial differentiation and filtering procedure. As expected, the procedure could not predict peak moment. It is expected that the procedure would also have had difficulty predicting the true pendulum moment during initial loading.

### Post-buckle Hinge Response

The limitations imposed by the influence of specimen inertia and vibration are most significant during the pre-buckle phase of the specimen response. After buckle formation the pendulum and specimen remained in contact and specimen vibrations were greatly attenuated. Strictly speaking pendulum work (or contact force or pendulum deceleration) still could not be used to calculate post-buckle hinge moment, because of the kinetic energy stored in the specimen.

$$\Delta \text{ pendulum work} = \Delta \text{ specimen strain energy} + \Delta \text{ specimen kinetic energy}$$

At buckle formation, the RHS specimen tested in this study had approximately 20 J of kinetic energy, which was 2.5% of the post-buckle specimen plastic strain energy. If this kinetic energy was neglected and it was assumed that after buckle formation:

$$\Delta \text{ pendulum work} = \Delta \text{ specimen strain energy}$$

then hinge strain energy could have been derived from post-buckle pendulum work, after accounting for the recovery of elastic strain energy in the remainder of the specimen .

### 3.4.2.2 CALCULATING HINGE MOMENT FROM A REACTION FORCE

Because of the significant limitations associated with calculating hinge moment from measures of pendulum moment, an alternative approach was sought. The approach adopted in this study was to calculate hinge moment from a measured reaction force. The advantages of this approach were:

1. The reaction force measured was not affected by specimen inertia. Therefore the true hinge moment could be calculated during pre-buckle and post-buckle response phases.
2. The chosen reaction force was a more direct measure of hinge moment, and accurately reflected hinge moment fluctuations caused by specimen vibration.
3. Measurement of specimen tip rotation was not required to derive hinge moment.

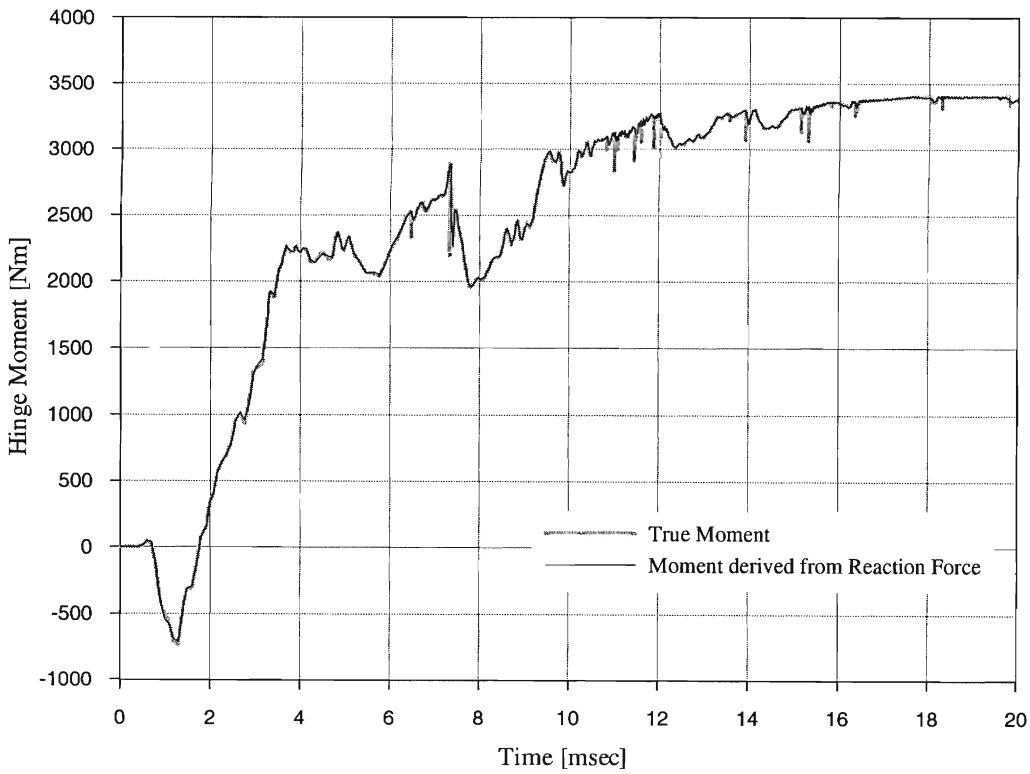


**Figure 3.5:** Hinge moment from FE analysis – true and derived from reaction force.

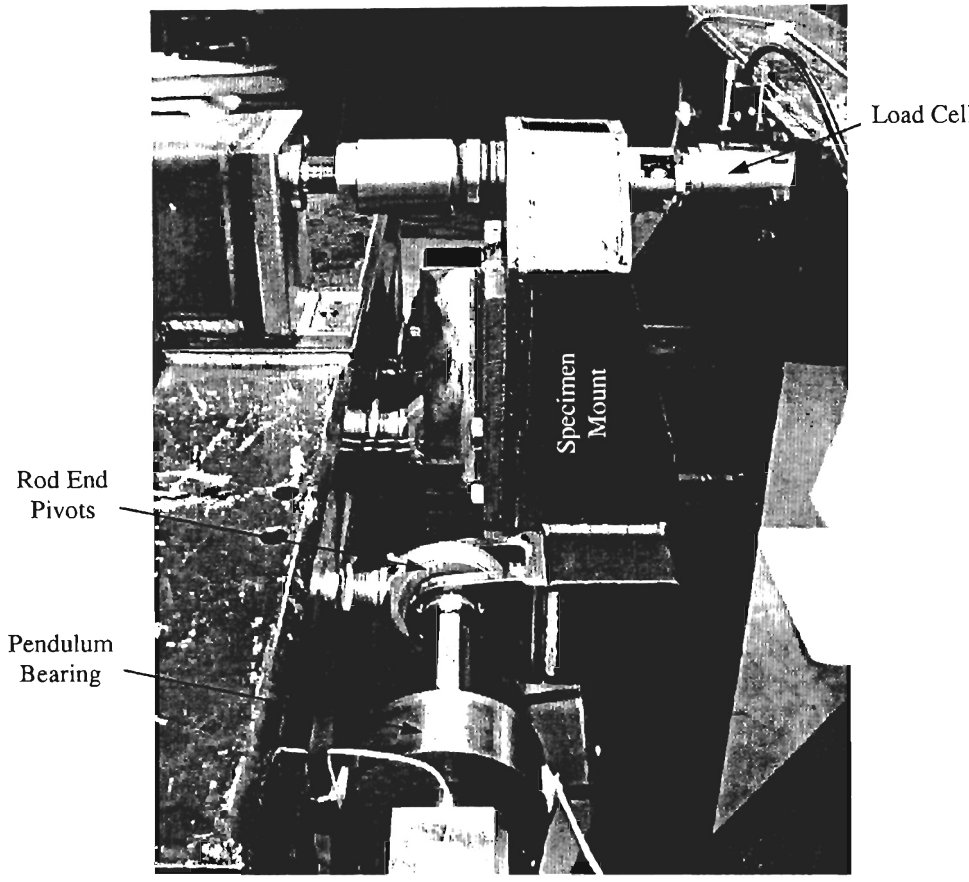


**Plate 3.6:** Physical specimen mount

### 3.4.3 Pendulum Acceleration

The radius of the impact pendulum from pivot to impact nose was 1,000 mm. The centre of mass of the pendulum was typically 700 mm from the pivot, so the maximum impact velocity attainable under free fall was 5.2 $ms^{-1}$. The intended impact velocity for this study was 7 to 8 $ms^{-1}$, therefore some means of accelerating the pendulum was required.

The high speed pendulum at the Cranfield Impact Centre, Plate 3.4, is accelerated using a pressurised air spring. An air spring arrangement is a compact, repeatable and relatively simple means of imparting energy to the pendulum in a controlled manner. For these reasons an air spring was chosen over coil springs and bungee cords as the means of accelerating the pendulum to higher impact velocities.

The air spring arrangement is shown in the compressed and expanded states in Plates 3.7a and 3.7b. To maintain an approximately constant pressure in the air spring as it expanded, thus maximising the energy imparted to the pendulum, a large air reservoir

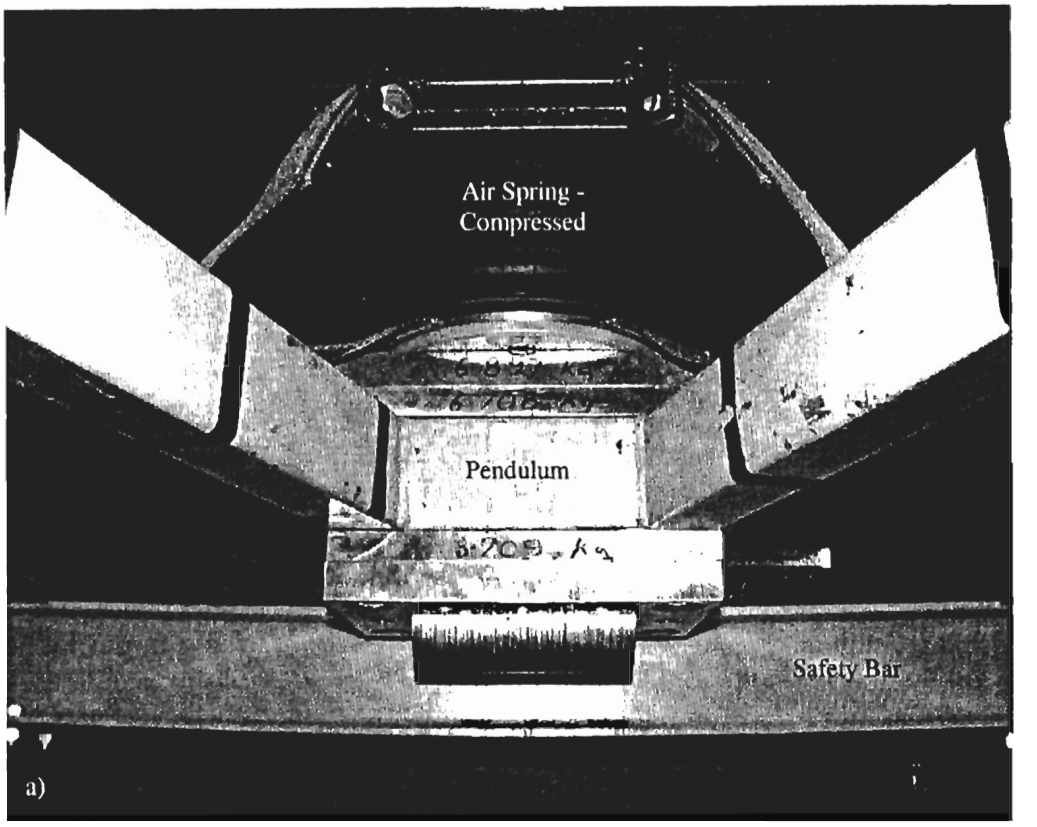


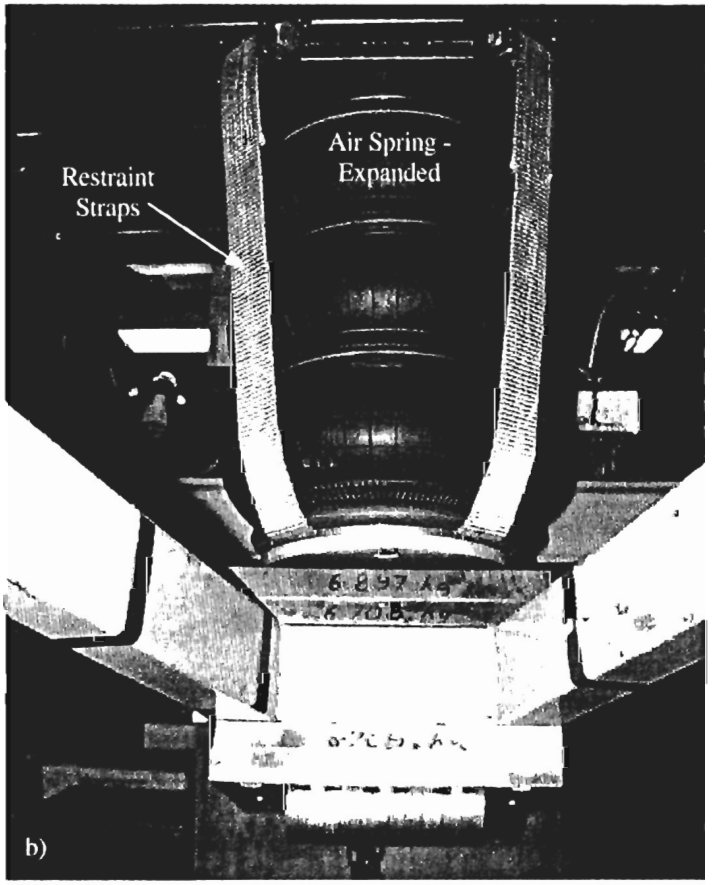


**Plate 3.7:** Air spring arrangement a) air spring compressed by the pendulum and b) air spring expanded and restrained by straps

Initial bend tests exhibited a residual offset in reaction force of approximately 4% of the peak force and 13% of the reaction force at peak rotation. This offset introduced a level of uncertainty that could not be neglected. An investigation suggested that the impact was disturbing the load cell pre-load.

*Modified Design #2*

A new arrangement was installed using the Kistler load washer, pre-loaded via a short 14 mm diameter steel bolt. The relatively stiff pre-load bolt caused the effective sensitivity to drop by approximately 7%. While this pre-load arrangement was less complicated, unfortunately impact test results indicated that the residual offset actually increased with this arrangement.

*Modified Design #3*

A completely new approach for pre-loading the load cell was designed. The pre-load bolt was replaced by a heavy-duty die spring. This die spring was so soft, relative to the load cell, that no re-calibration was necessary. Additionally, lateral restraint was provided for the specimen mount and the strain gauge load cell again replaced the piezoelectric load washer. The strain gauge load cell had a true DC response and therefore the level of pre-load was always known. The load cell could also be used for long duration quasi-static tests.

Some improvement was noted with this arrangement. However, the results were still unsatisfactory.

*Modified Design #4*

Further investigation and testing indicated that the load offset might be due to the transfer of shear loads into the load cell. To minimise shear loading on the load cell a simple "spherical element" coupling was designed, see Plate 3.10. The installation of this coupling reduced the residual reaction force to the negligible level shown in Figure 3.7.

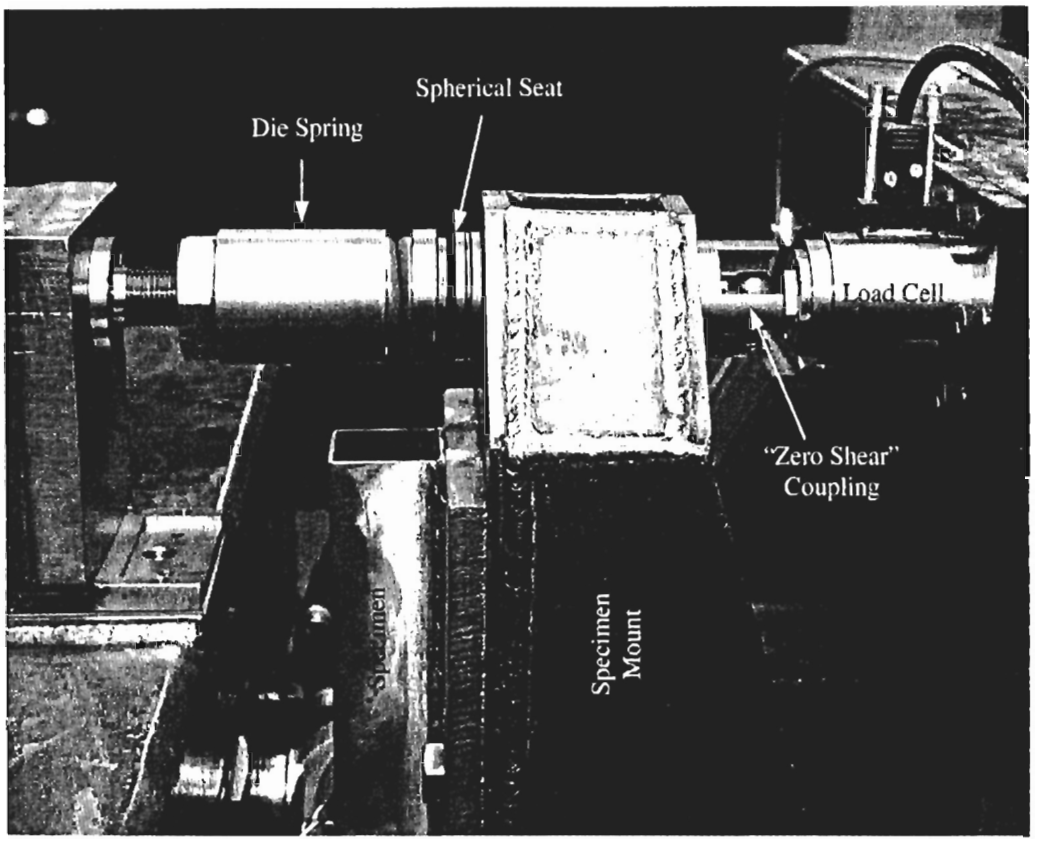


**Plate 3.10:** Final load cell and pre-load arrangement with "zero shear" coupling

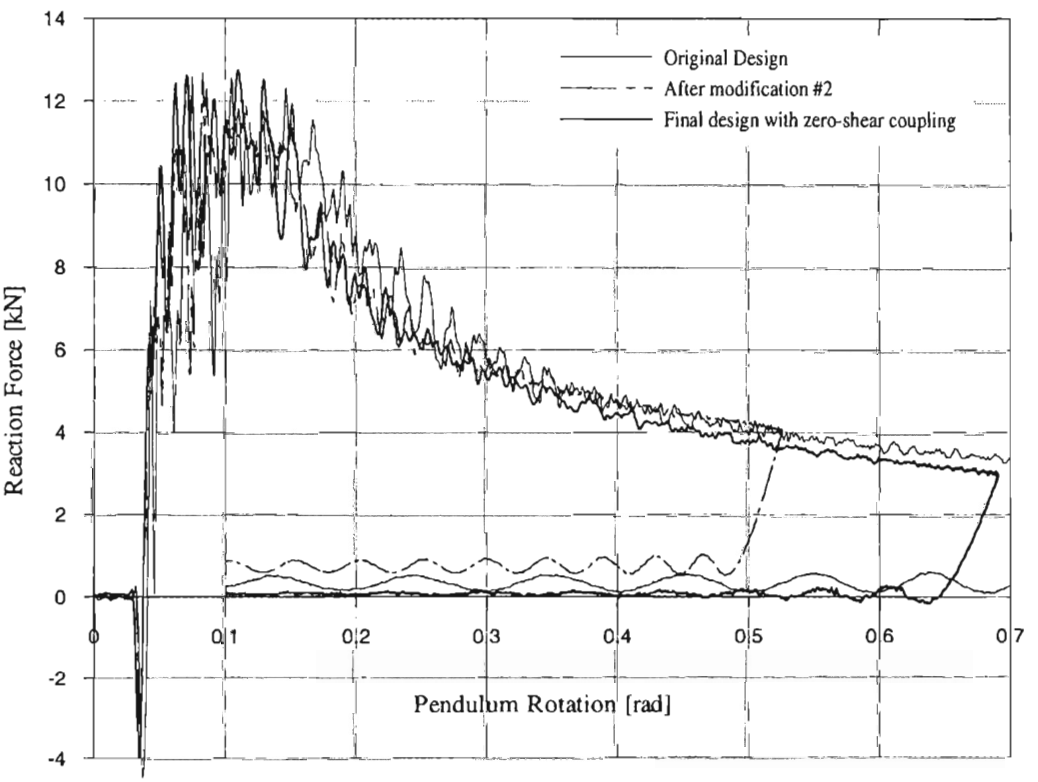


**Figure 3.7:** Residual reaction force - Original, after modification #2 and final

### 3.5.3.1 FREQUENCY RESPONSE OF THE STRAIN AMPLIFIER

The frequency response of the load cell strain amplifier is shown in Figure 3.8. The frequency range of interest in this study is shown in Section 4.5.5 to be from 0 to 200 Hz. Over this frequency range the magnitude attenuation of the amplifier was only 0.004 dB or 0.05%, whilst the phase deviation was essentially linear and corresponded to a 0.02 millisecond delay. No correction of the measured reaction force signal to account for load cell frequency response was considered necessary.

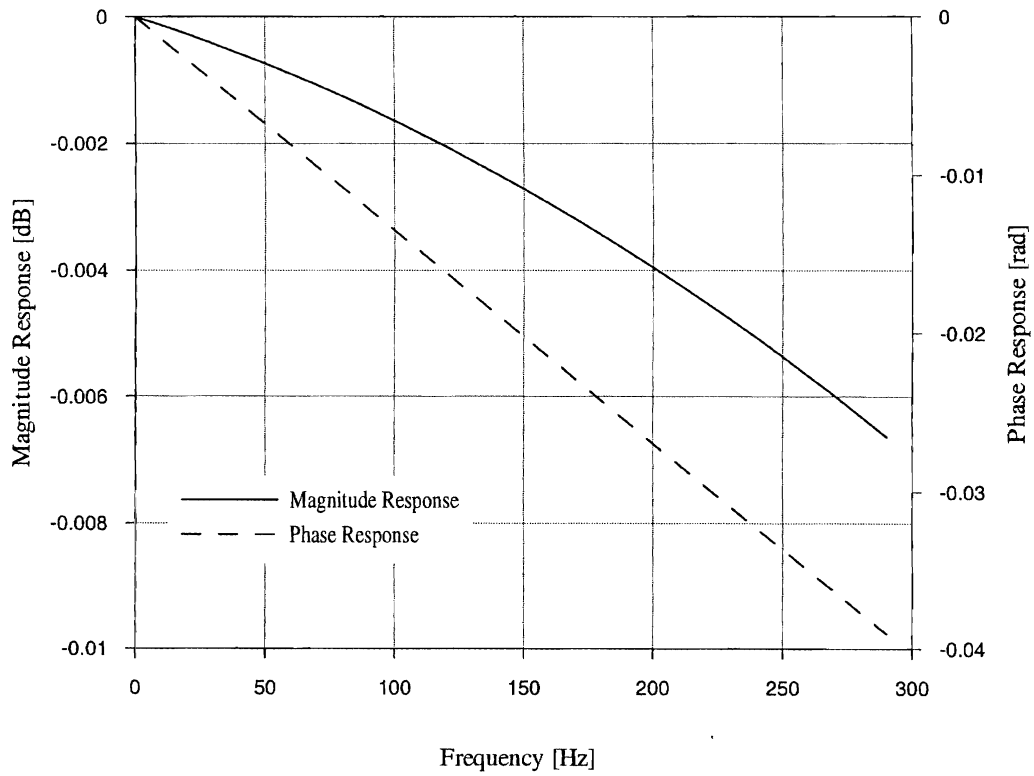


**Figure 3.8:** Frequency Response of Charge Amplifier on 2000με range

## 3.5.4 Air Spring Pressure

Air spring pressure was measured using a pressure transducer and displayed on the control bench. Although pendulum impact velocity could not be derived directly from air spring pressure, adjusting the air spring pressure to a pre-determined value before releasing the pendulum ensured repeatability between tests.

## 3.5.5 Specimen - Pendulum Contact

In the impact tests it was necessary to be able to identify the exact instant of contact between the pendulum and the specimen. The true instant of contact could not be

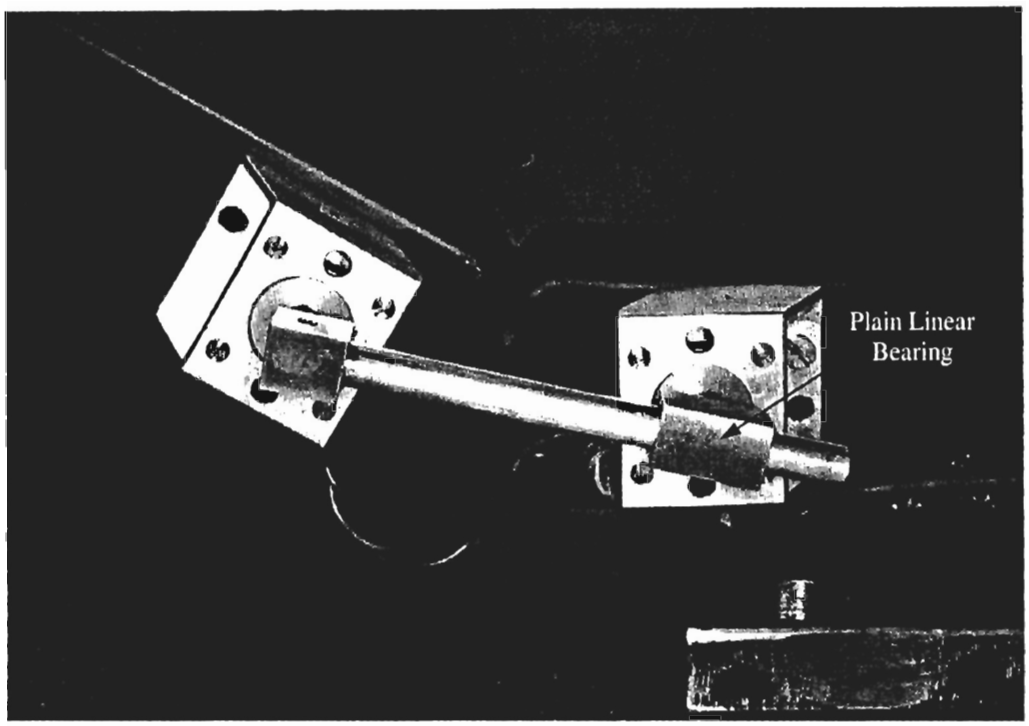


**Plate 3.11b:** Hinge zone rotation device attached to a specimen after testing

### 3.5.7 Surface Strains

Compression flange longitudinal strains were measured and were used to:

- estimate the elastic strain rate at the hinge site before buckle formation;
- identify buckle initiation; and
- investigate buckle strains and strain rates during deep collapse for comparison with FE results.

Because the exact location of buckle formation was unknown prior to testing, a strip gauge, consisting of ten individual strain gauges spaced over a length of 20 mm with a pitch of 2.03 mm, was used to measure longitudinal strain. Measurements Group strip gauges type EP-08-062MW-120 were used and were attached using Measurements Group A-12 high elongation adhesive. These gauges were very successful in capturing buckle strain history, however the common supply terminal on this gauge caused imbalance, cross-talk and sensitivity problems as discussed below.

**Figure 3.9:** Strip gauge used to measure compression flange longitudinal strain

approximately 4.2% from gauge 1 to gauge 10. Gauge imbalance increased steadily from gauge 1 to gauge 9. Only gauge 1 could be balanced and gauge 9 was 1 V out of balance (gauge 10 was not recorded).

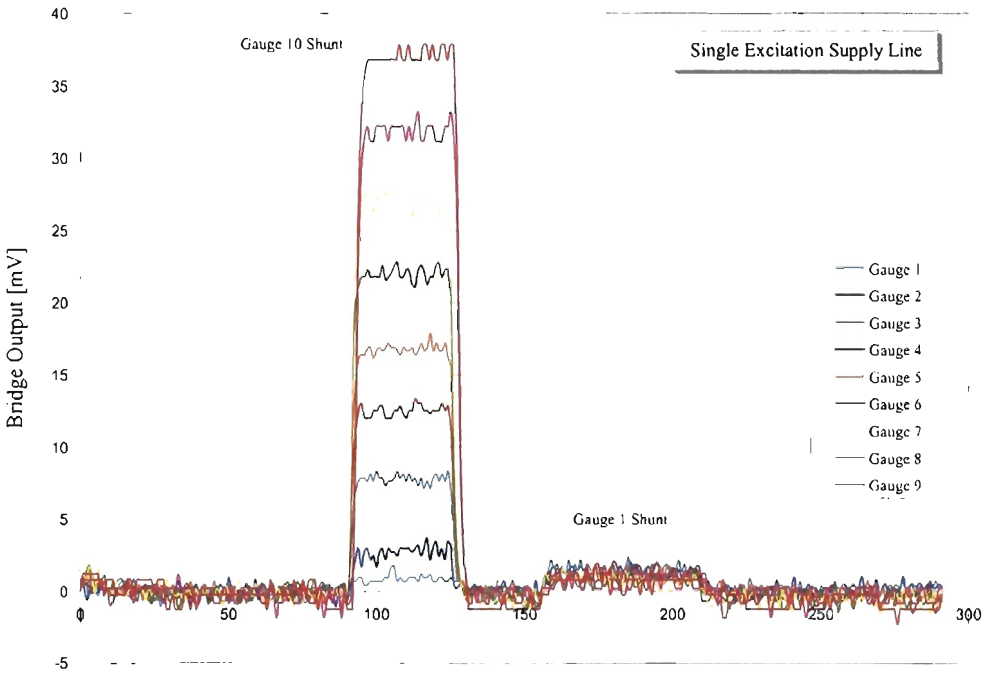


**Figure 3.10:** Cross-talk sensitivity with a single excitation supply line

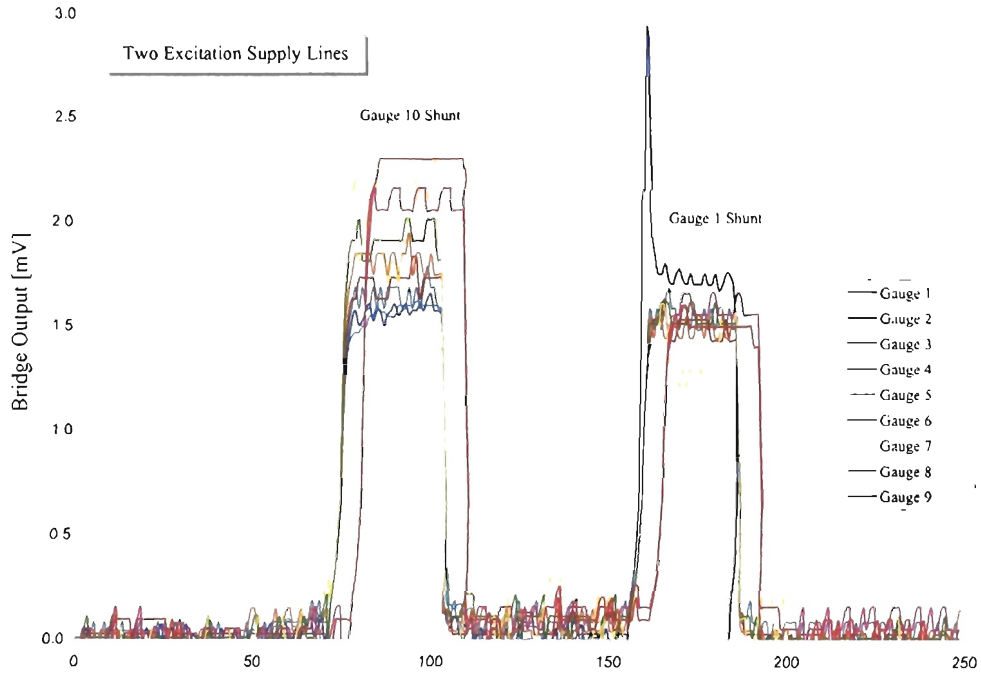


**Figure 3.11:** Cross-talk sensitivity with two excitation supply lines

#### 3.5.7.2 MINIMISING CROSS-TALK, DESENSITISATION AND IMBALANCE

Cross-talk between gauge arms can be reduced by ensuring that the voltage across each gauge remained as constant as possible. Desensitisation and imbalance are also reduced by minimising voltage drop along excitation supply lines. A simple remedy, which addressed these two requirements, was to connect a second excitation line to the far end of the common terminal. This action successfully reduced cross-talk, desensitisation and imbalance in the strip gauge installation.

In this configuration the worst-case gauge arms were at the centre, i.e. gauges 5 and 6. The voltage drop along the common supply line from one end to the middle became 39.7 mV. Figure 3.11 shows the results of the same shunt calibration as performed above but with the additional supply line connected. Significant reductions in cross-talk, from 50% to 90%, were recorded. The maximum imbalance was approximately 0.3 V at gauges 5 and 6. Individual shunt calibration showed only a slight reduction in sensitivity moving from both end gauges towards the centre gauges. The maximum desensitisation was 1.5% at gauge 6 and typical desensitisation was less than 0.5%.

### 3.5.8 Data Acquisition

In total, fourteen channels of data were recorded during each test as outlined in Table 3.1. Two Yokogawa analysing recorders, (a model AR1200 and a model AR1100), were required to provide fourteen channels of acquisition. To ensure channel synchronisation, both units were triggered from the same trigger signal. These recorders were capable of sampling rates from 0.1 Hz to 100 kHz per channel and had in-built anti-aliasing filtering and low-pass filters.

**Table 3.1:** Data acquisition channels

| Channel | Signal Description |
|---|---|
| 1 | Pendulum travel |
| 2 | Specimen mount reaction force |
| 3 | Hinge zone rotation potentiometer #1 |
| 4 | Hinge zone rotation potentiometer #1 |
| 5 | Specimen – pendulum contact |
| 6-14 | Compression flange longitudinal strains 1-9 |

## 3.6 CONCLUSIONS

The test rig and instrumentation described above were specially designed to measure the $M$-$\theta$ response of the local buckle, in addition to the gross response of the specimen. Measurement of buckle $M$-$\theta$ response enabled more detailed validation of FE models and the direct assessment of the influence of material strain rate sensitivity.

The majority of the difficulties in measuring impact *moment-rotation* responses are associated with specimen inertia. The novel test rig and instrumentation described in this chapter were specifically developed to properly treat and, where possible, minimise the influence of specimen inertia on the measurement of impact *moment-rotation* responses. The most significant features of the rig design were the direct measurement of hinge rotation and the calculation of hinge moment from measurements of a reaction force rather than impact force.

# CHAPTER 4 PROCESSING RAW TEST DATA

## 4.1 INTRODUCTION

Chapter 3 described the unique aspects of the test rig design and instrumentation that minimised the influence of specimen inertia on the measurement of impact *moment-rotation* responses. Of equal significance to the accurate measurement of hinge response under impact loading was the proper treatment of "impact effects" in the raw signals. This chapter describes in detail the development and validation of the procedures used to calculate hinge moment and hinge rotation from raw test data.

The first issues discussed apply equally to quasi-static and impact tests. They were:

1. the appropriate definition of hinge moment and hinge rotation in a cantilever bending rig and,
2. the derivation of corrections to hinge moment and hinge rotation to account for offset buckle formation, since the basic calculation of hinge moment assumed that the hinge buckle formed on the pendulum axis.

For the impact tests, hinge moment was calculated and corrected in the same manner as for the quasi-static tests, however the additional aspect of dynamic calibration or frequency response had to be addressed. The system formed by the specimen, the specimen mount, load cell and reaction structure had a specific frequency response. This frequency response distorted, in both magnitude and phase, the reaction force measured during impact tests. The problem was how to retrieve the true force signal. Two approaches for processing the reaction force signal from an impact test were investigated, inverse analysis and low-pass filtering. Dynamic effects also complicated the derivation of hinge rotation in the impact tests. These difficulties were largely overcome by local measurement of hinge rotation.

## 4.2 CHOICE OF ROTATION AND MOMENT MEASURES

In Section 3.4.2 it was argued that the best response to directly assess the influence of material strain rate sensitivity on the impact bending collapse of RHS was the hinge $M$-$\theta$ response rather than gross specimen response represented by *pendulum moment Vs pendulum rotation.*

As discussed in Section 1.3, the plastic hinge that forms in an isolated thin-walled RHS member under flexural loading is a localised buckle similar to that shown in Plate 1.6. The structural performance of this hinge is characterised by a plot of *hinge moment Vs hinge rotation*, Figure 1.2 and 1.3 (The essence of Figure 1.3 is summarised below in Figure 4.1). The following section describes the definitions of hinge moment and hinge rotation adopted in this thesis.

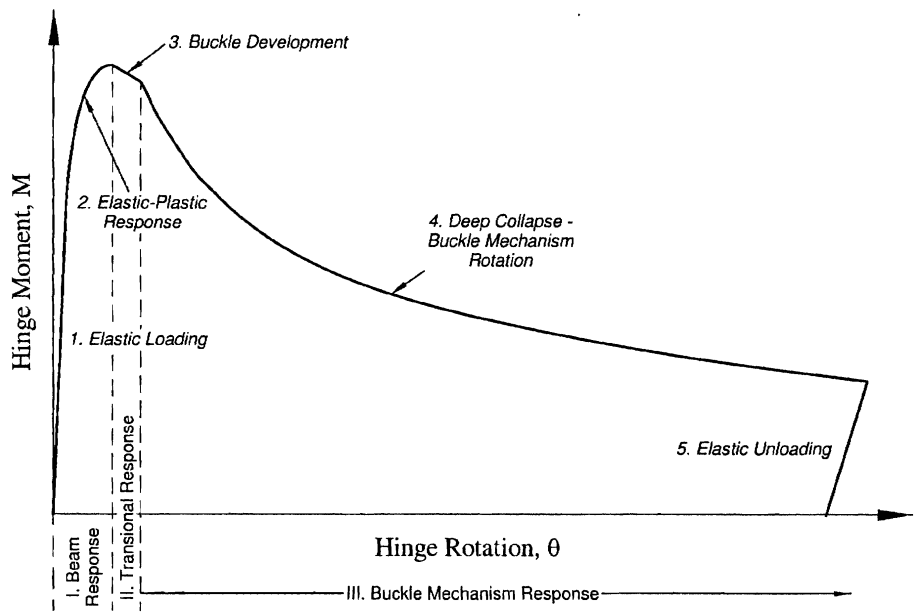


**Figure 4.1:** Plastic hinge characteristic $M$-$\theta$ response (Fig. 1.3)

### 4.2.1 Hinge Zone Rotation

To be consistent with Kecman (1979) hinge rotation was defined as the relative rotation between the two essentially undeformed cross-sections that bound the buckle. These planes can be visualised on the model of the buckle mechanism proposed by Kecman shown in Figure 4.2. In this figure hinge rotation is the relative rotation between lines GK and EL. Typically, for the 50x50x2 RHS tested in this study, the initial length of

section between the two bounding planes was 50 to 60 mm. This was consistent with the mechanism length identified by both Kecman (1979) and Cimpoeru (1992).

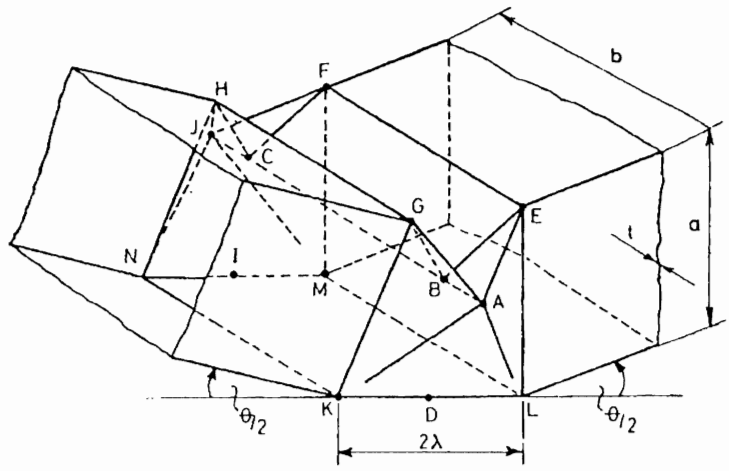


**Figure 4.2:** Buckle mechanism as modelled by Kecman (1979)

Although the buckle geometry shown in Figure 4.2 was only defined during the collapse phase of the response, the same definition of hinge rotation could be used during the pre-buckle or continuous curvature phase of the response. The relative rotation between the two planes was then a measure of the curvature along the length of section that was to develop into the local buckle.

Because the exact location of the buckle was not known before testing, it was difficult to site the instrumentation needed to measure hinge rotation. To overcome this problem, instrumentation was placed so that it measured the relative rotation between the root of the cantilever and a plane 85 mm from the root. This distance was sufficient to ensure that the buckle formed within the measurement zone, without interfering with the instrumentation. Henceforth this length has been referred to as the "hinge zone". Whilst this length was similar to the 90 mm length defined by Cimpoeru (1992) as the "finite mechanism length" associated with a 50x50x2 section (see the comments below), it was not chosen for the reasons proposed by Cimpoeru.

While hinge rotation was not measured directly, if necessary hinge rotation could be calculated from measured hinge zone rotation as follows.

*Pre-Buckle*

FE modelling of the 50x50x2 specimen confirmed that during the pre-buckle phase of the specimen response (continuous curvature phase), hinge rotation and hinge zone rotation were approximately in the same proportion as the ratio of buckle mechanism length and hinge zone length.

*Post-Buckle*

After buckle initiation, during the collapse phase, the moment capacity of the buckle decreased and all further specimen plastic rotation was due to plastic rotation of the buckle mechanism. Additionally the elastic unloading that occurred in the hinge zone was dominated by the buckle mechanism. It could therefore be assumed that after buckle initiation:

$$\Delta \text{ hinge rotation} = \Delta \text{ buckle mechanism rotation} = \Delta \text{ hinge zone rotation}$$

#### 4.2.1.1 A COMMENT ON CIMPOERU'S FINITE MECHANISM LENGTH

Cimpoeru (1992) claimed that by testing a 90 mm deformable length of section in pure bending "*one will obtain a moment-rotation curve that directly gives the angle of rotation at which collapse occurs*". Cimpoeru called this 90 mm the "finite mechanism length" and suggested that it was a fundamental quantity that "*is important for modelling purposes as it defines the length of tubing that directly contributes to the mechanical properties of a local plastic collapse mechanism*".

In the author's opinion the true mechanism length is the length that becomes the buckle mechanism, approximately 50 to 60 mm for a 50x50x2 RHS, because this is the minimum length that directly contributes to collapse response of the buckle mechanism. Two arguments for this interpretation are:

1. There is no single "angle at which collapse occurs" for a particular section, because, as acknowledged by Cimpoeru, the angle at which collapse occurs i.e. the angle at peak moment, depends on the length of section over which $\theta$ is measured. Rotation at collapse will also be dependent on the loading arrangement of the test, which can influence the amount of pre-buckle plastic curvature that develops in the specimen.

2. The significance of the 90 mm deformable length identified by Cimpoeru was that under pure bending it gave the minimum collapse angle that could be obtained experimentally, without the collapse response being influenced by the boundary conditions of the specimen. A deformable length equal to the buckle length would give the minimum collapse angle. Whilst this collapse angle cannot be determined directly by experiment, it can easily be scaled from the collapse angle measured for longer deformable lengths.

### 4.2.2 Hinge Moment

In the pure bending rig of Cimpoeru (1992) section moment was constant. However, in the cantilever bend rig used in this study, section moment varied by approximately 9% along the hinge zone. Therefore the hinge moment to be associated with hinge zone rotation was not uniquely defined. Typically the definition of hinge moment to associate with hinge zone rotation will be influenced by how the hinge zone is modelled in a subsequent hybrid analysis. If the hinge zone is modelled with a constant moment along a finite length then there is a compromise to be made between representing the correct hinge strength or the correct hinge energy. An alternative approach, which avoids this compromise, is to consider the hinge zone as a point at the effective hinge centre[†]. The appropriate and natural choice of moment is the moment at this physical point. As shown below, the combination of hinge zone rotation and moment at the effective hinge centre integrate to give the energy absorbed in the hinge zone. This choice of moment can therefore be described as an "energy consistent moment" which is defined by Equation 4.1.

$$\int_0^{\theta_{pb}} M_{EC}(\theta_{pb})\, d\theta_{pb} = E(\theta_{pb}) \tag{4.1}$$

The energy consistent definition of hinge moment was adopted in this study because this definition avoids a compromise and because representing the hinge zone as a point is the hybrid modelling approach recommended in Chapter 8.

---

[†] Effective hinge centre was defined in Section 1.3.3 to be the point about which the length of specimen beyond the hinge zone appears to rotate during the collapse phase of the $M$-$\theta$ response.

#### 4.2.2.1 CIMPOERU'S CHOICE OF HINGE MOMENT

Cimpoeru (1992) conducted a series of cantilever bend tests and was also faced with the question of how to calculate hinge moment. Cimpoeru took the approach that *"the moment at the root of the cantilever accurately represents the moment capacity of the local plastic collapse mechanism to moderate deflections"*. Cimpoeru also acknowledged that the approach adopted by Kecman (1979) of calculating hinge moment at the centre of the collapse mechanism is correct once collapse occurs. This contradiction is easily resolved by recognising the three phases of the $M$-$\theta$ response shown in Figure 4.1.

In Phase I, prior to buckle formation, the $M$-$\theta$ curve represents the response of a continuous beam to cantilever bending. Section moment can be calculated at any location, the root being a natural choice. In Phase II, the geometry of the plastic hinge is in a transitional state, changing from the continuous curvature of Phase I to the local buckling of Phase III. The $M$-$\theta$ curve is neither that of an elastic-plastic beam nor that of the buckle collapse mechanism. In Phase III the geometry of the local buckle develops and the *moment-rotation* response of the cantilever is dominated by the collapse mechanism. It is now appropriate that hinge moment be calculated at a location associated with the buckle mechanism, such as the effective hinge centre. Kecman and ADR 59/00 Code of Practice Part B adopt this approach.

#### 4.2.2.2 CALCULATING ENERGY CONSISTENT HINGE MOMENT

The beam and shell FE models described in Chapter 7 were used to derive a relationship whereby the energy consistent hinge moment described by Equation 4.1 above could be calculated from the measured reaction force on the specimen mount. Because the energy absorption mechanism was different during the pre-buckle, transitional and post-buckle phases of the hinge response, the derivation of energy consistent hinge moment was considered separately for each phase. The dominant post-buckle phase is considered first, then the pre-buckle and transitional phases.

**Post-Buckle Response**

The post-buckle response was investigated using results from a detailed shell FE model. $E(\theta)$, in Equation 4.1, was taken to represent the total strain energy associated with the formation of the buckle and $d\theta$ was calculated as described in Section 4.2.1. It

transpired that the energy consistent hinge moment was a function of buckle location and could be approximated by the moment at a point corresponding to the original location of the effective hinge centre on the undeformed specimen. (Due to the rotation of the buckle the effective centre moved towards the cantilever root by approximately 5 mm during the test).

An alternative way of arriving at this result is to consider the relationship between pendulum work and hinge energy.

Pendulum work can be calculated as the integral of *pendulum moment Vs pendulum rotation* at the pendulum axis, or the integral of *equivalent pendulum moment Vs equivalent pendulum rotation* at some other location P, not on (but near) the pendulum axis.

$$E_{Pend.} = \int M_{Pend.}\, dPr = \int EM_{Pend.}\, dEPr$$

where $EM_{Pend.}$ = equivalent pendulum moment at the location P

$EPr$ = equivalent pendulum rotation at the location P

Total equivalent pendulum rotation can be divided into two components 1) $EPr$ due to hinge zone rotation and 2) $EPr$ due to curvature of the length of specimen outside the hinge zone.

$$EPr = EPr_{Hinge\ Zone} + EPr_{Specimen}$$

The total work done by the pendulum is stored in the specimen as 1) strain energy in the buckle and 2) strain energy in the length of specimen outside the hinge zone. The strain energy within the buckle is given by $\int EM_{Pend.}\, dEPr_{Hinge\ Zone}$ and is also equal to the integral of *energy consistent hinge moment Vs hinge zone rotation.* That is:

$$\int EM_{Pend.}\, dEPr_{Hinge\ Zone} = \int M_{EC}\, d\theta$$

Therefore if the point P is chosen such that $dEPr_{Hinge\ Zone} = d\theta$, then the energy consistent hinge moment must equal the equivalent pendulum moment at the point P. If point P is located at the effective hinge centre the definition of effective hinge centre ensures this condition is met for post-buckle rotations. Therefore the post-buckle energy consistent hinge moment is the moment at the effective hinge centre.

This result is consistent with the approach adopted by Kecman (1979), where hinge moment was defined as the moment at the centre of the buckle, with the location of the buckle centre being identified after a test.

The relation for energy consistent moment discussed above was derived from FE models of a 50x50x2 C350LO RHS. Although the relations have not been verified for other sections they should be applicable as long as $EPr_{Hinge\,Zone}$ calculated at the original location of the effective hinge centre equals the measured hinge zone rotation. By the same argument Equation 4.1 holds in an impact test as long as post-buckle specimen vibrations are small.

**Pre-Buckle Moment**

Hinge moment prior to buckle formation was derived using results from a beam FE model, in a similar manner to Post-Buckle hinge moment. $E(\theta)$ and $d\theta$ in Equation 4.1 were respectively taken to represent the total strain energy and rotation over the 85 mm hinge zone. The energy consistent hinge moment so derived was approximately equal to the moment at a point near the pendulum axis (the actual point was offset 3 mm from the pendulum axis). A similar definition of energy consistent hinge moment was derived for the impact tests despite the slight differences in the distribution of strain energy along the hinge zone.

**Transitional Hinge Moment**

In the initial stages of collapse, before the buckle had fully developed into the classic mechanism shown in Plates 1.6 and 3.3b, the $M$-$\theta$ response was in a transitional phase and neither calculation of moment, pre-buckle nor post-buckle, was strictly appropriate. In this phase of the response hinge moment was calculated as the weighted average of the two moment measures.

$$M_{EC}^{Trans} = (1-\lambda)\times M_{EC}^{Pre} + \lambda \times M_{EC}^{Post} \tag{4.2}$$

where $\lambda$ varied linearly from 0 to 1 over the transitional phase.

## 4.3 CALCULATING HINGE MOMENT AND HINGE ZONE ROTATION FROM QUASI-STATIC TEST DATA

Pre-buckle and post-buckle hinge responses are again considered separately here. For the remainder of this thesis, hinge moment $M_h$, is assumed to be the energy consistent hinge moment described above, either pre-buckle or post-buckle as appropriate.

### 4.3.1 Buckle Forming on the Pendulum Axis

#### 4.3.1.1 POST-BUCKLE HINGE MOMENT

Post-buckle hinge moment has been defined as the moment at the original location of the effective hinge centre, therefore when the buckle formed on the pivot axis of the specimen mount as intended, hinge moment could be calculated quite simply using Equation 4.3.

$$M_h = R \times d \tag{4.3}$$

where $R$ = Specimen mount reaction force (referred to as reaction force), Figure 4.3.

$d$ = Moment arm from reaction force to specimen mount pivot axis.

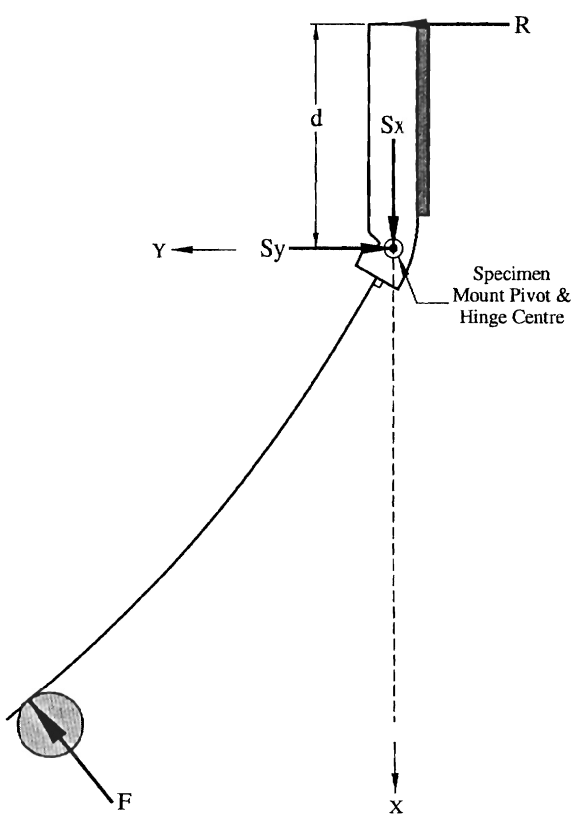


**Figure 4.3:** Bend test reaction forces and rotations - Plastic hinge formed on specimen mount pivot axis

### 4.3.1.2 PENDULUM ROTATION

Pendulum travel was measured using the optical displacement encoder described in Section 3.5.1. Pendulum rotation $\beta$, was calculated as:

$$\beta = \frac{s_p}{r_{op}} \tag{4.4}$$

where $s_p$ = Measured pendulum travel (arc length) [mm] = 0 at impact.

$r_{op}$ = Optical radius of encoder = 1000 mm.

### 4.3.1.3 HINGE ZONE ROTATION

To develop the relationship between pendulum rotation and hinge zone rotation the detailed geometry of Figure 4.4 is considered.

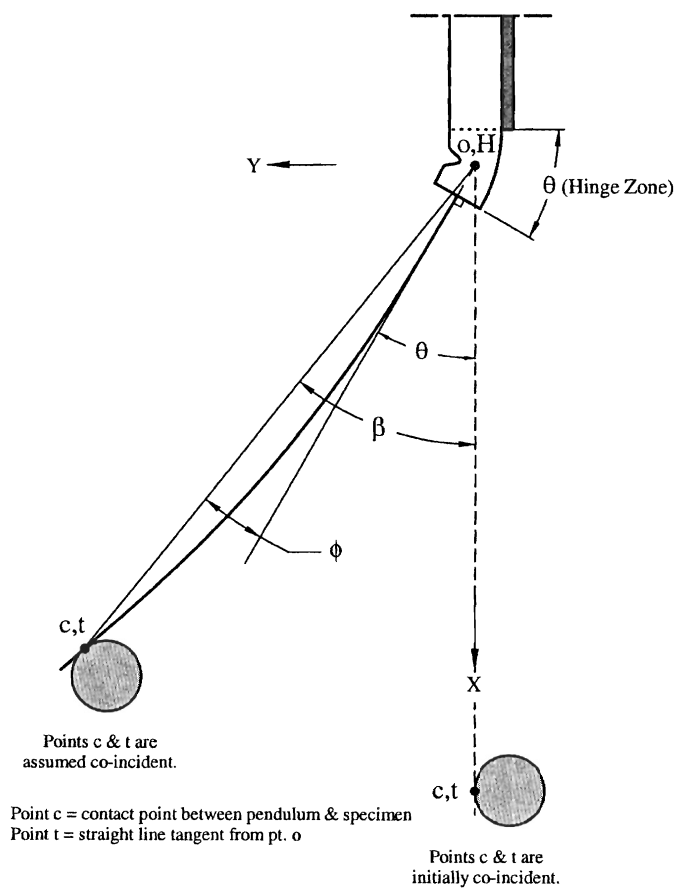


**Figure 4.4:** Bend test geometry detailing specimen and pendulum contact - plastic hinge formed on specimen mount pivot axis

Pendulum rotation can be divided into two components.

$$\beta = \theta + \phi \tag{4.5}$$

where $\phi \approx$ Pendulum rotation due to elastic + plastic curvature of the length of specimen beyond the hinge zone. The approximation symbol is used since $\phi$ also compensates for the fact that rotation $\theta$ is not concentrated at the pendulum axis but is distributed over the hinge zone.

Pendulum rotation can also be divided into elastic and plastic components.

$$\begin{aligned}\beta &= \beta^{elas} + \beta^{plas} \\ &= (\theta^{elas} + \theta^{plas}) + (\phi^{elas} + \phi^{plas}) \\ &= (\theta^{elas} + \phi^{elas}) + (\theta^{plas} + \phi^{plas})\end{aligned} \tag{4.6}$$

Prior to peak moment, the two components of $\beta_{plas}$ cannot be separated. However because no further plastic curvature developed in the specimen after peak moment i.e. after buckle initiation, $\phi_{pb}^{plas} = 0$ and $\beta_{pb}^{plas} = \theta_{pb}^{plas}$ (where the subscript pb stands for post-buckle). Therefore after buckle initiation:

$$\beta_{pb} = \theta_{pb} + \phi_{pb}^{elas}$$

$$\theta_{pb} = \beta_{pb} - \phi_{pb}^{elas} \tag{4.7}$$

(An equality sign can now be used since hinge zone rotation $\theta$ is considered to be concentrated at the effective hinge centre, which is assumed to be on the pendulum axis).

Equations 4.6 and 4.7 indicate that pendulum rotation can only be used to derive post-buckle hinge zone rotation. Therefore hinge zone rotation must be measured directly to obtain pre-buckle hinge response. The device described in Section 3.5.6 was developed for this purpose.

### 4.3.2 Buckle Formation "off" the Pendulum Axis

The previous discussion has assumed that the local buckle formed on the specimen mount pivot axis. However in practice the buckle formed up to 15 mm either side of the specimen mount axis.

The distance from the specimen mount pivot axis to the effective hinge centre is defined as the hinge offset, *a*, Figure 4.5. The implications of this hinge offset on the accuracy of the calculated hinge moment and pendulum rotation are now explored.

#### 4.3.2.1 POST-BUCKLE MOMENT CORRECTION

If the local buckle forms at some distance, *a*, from the specimen mount pivot axis, then the expression for hinge moment becomes;

$$M_h \approx R\times(d+a)-S_y\times a \tag{4.8}$$

Pivot reaction $S_y$ is unknown. Rearranging Equation 4.8:

$$M_h \approx Rd\left[1+\frac{a}{d}(1-\frac{S_y}{R})\right] \tag{4.9}$$

The ratio $\frac{S_y}{R}$ is unknown. An expression for the ratio $\frac{S_y}{R}$ can be derived from the geometry of Figure 4.5 below.

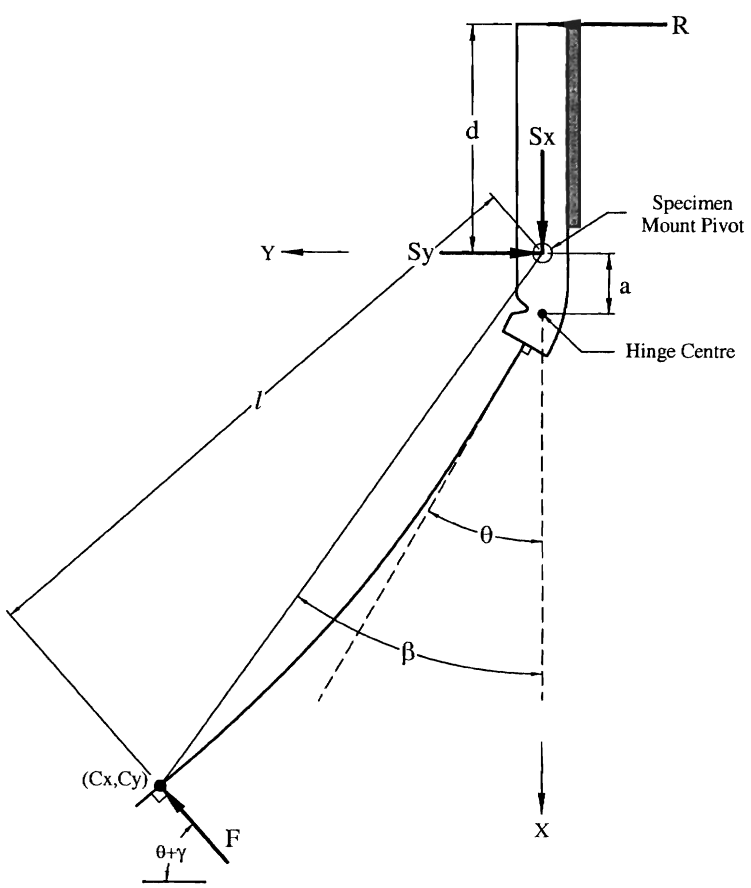


**Figure 4.5:** Bend test reaction forces and rotation - plastic hinge formed offset from the specimen mount pivot axis

An alternative approach was to ignore the reaction $S_y$ and calculate hinge moment at the offset location using Equation 4.12.

$$M_h \approx R \times (d + a) \tag{4.12}$$

The use of Equations 4.11 and 4.12 to calculate hinge moment at an effective hinge centre located +17 mm from the specimen mount pivot axis is compared in Figure 4.6. Figure 4.6 shows that the prediction of hinge moment given by Equation 4.12 is not adequate and that the reaction $S_y$ should not be ignored. Although $S_y$ was not measured, Equation 4.11 provided a good estimate of the true hinge moment when the hinge formed off the specimen mount pivot axis.

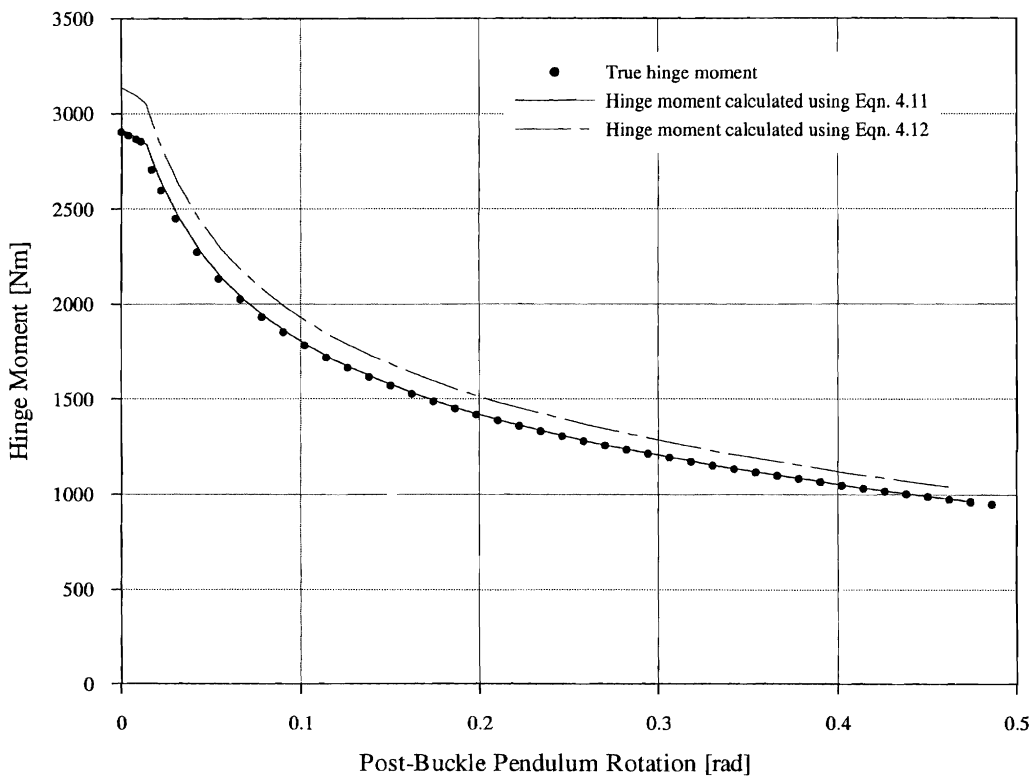


**Figure 4.6:** Hinge moment corrected for offset buckle location. Hinge offset (a) = +17 mm

### 4.3.2.2 PENDULUM ROTATION CORRECTION

Referring to Figure 4.7, it is apparent that measured pendulum rotation $\beta$, was dependent upon the location of the local buckle. Therefore to compare pendulum rotation between specimens it was necessary to define a measure of pendulum rotation that was independent of buckle location. This measure termed "normalised" pendulum rotation, $\beta'$, is given by Equation 4.13 and approximately represents the pendulum rotation that would be measured if the pendulum pivot axis were at the effective hinge

initiation. After buckle initiation, the elastic stiffness of the specimen began to decrease and continued to decrease as the buckle developed.

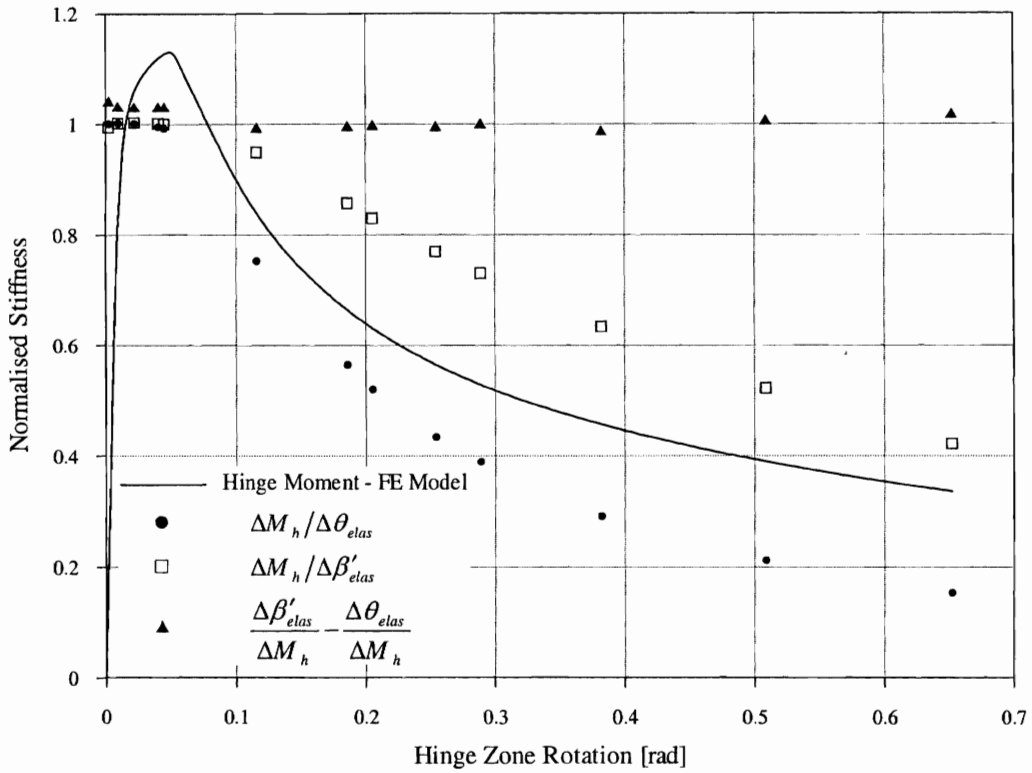


**Figure 4.8:** Specimen elastic stiffness ($\Delta M_h/\Delta\beta'_{elas}$) Vs Hinge zone rotation

The decrease in specimen elastic stiffness after buckle initiation was approximated by the following function:

$$\frac{\Delta M_h}{\Delta\beta'_{elas}} = F(\theta_{pb}) \times \left(\frac{\Delta M_h}{\Delta\beta_{elas}}\right)_0 \tag{4.15}$$

where; $F = 0.4663\theta_{pb}^2 - 1.273\theta_{pb} + 1.018$ and $\left(\frac{\Delta M_h}{\Delta\beta_{elas}}\right)_0$ is the pre-buckle stiffness.

Note that pendulum rotation was not normalised since pre-buckle measured and normalised pendulum rotation are approximately equal.

In a similar manner, the elastic stiffness of the hinge zone alone was approximated by the following function:

$$\frac{\Delta M_h}{\Delta\theta_{elas}} = F(\theta_{pb}) \times \left(\frac{\Delta M_h}{\Delta\theta_{elas}}\right)_0 \tag{4.16}$$

where; $F = 2.544\theta_{pb}^4 - 7.401\theta_{pb}^3 + 7.874\theta_{pb}^2 - 4.006\theta_{pb} + 0.9944$ and

$\left(\frac{\Delta M_h}{\Delta\theta_{elas}}\right)_0$ is the pre - buckle stiffness.

The elastic flexibility of the length of specimen beyond the hinge zone, $\Delta\phi'_{elas}/\Delta M_h$, was then given by:

$$\frac{\Delta\phi'_{elas}}{\Delta M_h} = \frac{\Delta\beta'_{elas}}{\Delta M_h} - \frac{\Delta\theta_{elas}}{\Delta M_h} \tag{4.17}$$

which was essentially constant for all $\theta_{pb}$. Substituting into Equation 4.14, hinge zone rotation after peak moment was calculated as:

$$\begin{aligned}\theta_{pb} &= \beta'_{pb} - \left(\left(\frac{\Delta\phi_{elas}}{\Delta M_h}\right)_0 \times M_h - \left(\frac{\Delta\phi_{elas}}{\Delta M_h}\right)_0 \times M_h^{peak}\right) \\ &= \beta'_{pb} - \left(\frac{\Delta\phi_{elas}}{\Delta M_h}\right)_0 \times \left(M_h - M_h^{peak}\right)\end{aligned} \tag{4.18}$$

(Note: Kecman (1979) assumed that the specimen elastic unloading stiffness was approximately equal to the specimen elastic loading stiffness, for all hinge rotations. This approach tends to overestimate plastic rotations, since the elastic unloading stiffness of the specimen is actually much less than the elastic loading stiffness, due to the presence of the buckle).

## 4.5 CALCULATING HINGE MOMENT AND HINGE ZONE ROTATION FROM IMPACT TEST DATA

### 4.5.1 Identification of Buckle Initiation

Distinction has been made above and in Section 4.2 between the pre-buckle and post-buckle responses of the specimen. It was therefore important to identify the point of buckle initiation during a bend test. Buckle initiation caused a sudden drop in section moment capacity. Therefore, in a quasi-static test, it was a simple matter to identify buckle initiation as the point of moment drop off. However, in an impact test, the point of moment drop off was more difficult to identify consistently, due to the presence of significant oscillations on the measured force trace. One means of identifying buckle initiation was from a record of the compression flange strain. Figure 4.9 is a plot obtained from a detailed finite element analysis (Section 7.3.2) showing compression flange longitudinal strain versus hinge zone rotation. Strain traces at locations spanning 10.8 mm either side of the buckle centreline are shown.

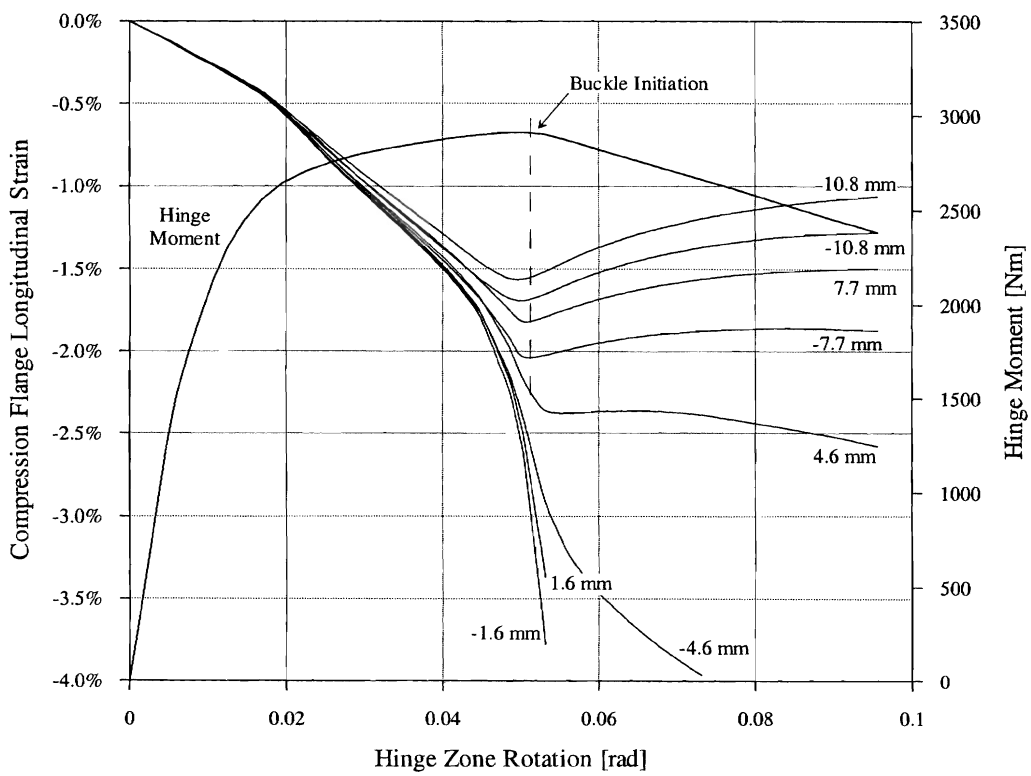


**Figure 4.9:** Compression flange longitudinal strain Vs Hinge zone rotation.

Note: The distances given indicate the location of the strain trace w.r.t. the buckle centreline

From Figure 4.9 it is clear that the longitudinal strains away from the buckle centreline began to reduce at the time of buckle formation, whereas the strains at or near the buckle centreline increased significantly. Either of these features, the local maximum or the rapid increase in strain rate, could have been used to identify buckle initiation, however the local maximum was considered the more precise indicator. It was also noted that the closer the gauge was to the buckle centreline the more the local maximum was delayed. In Figure 4.9 a gauge located approximately ±7.7 mm from the hinge centreline had a local maximum at approximately the same time as the buckle formed and the hinge moment peaked.

Because peak moment was easily identified in a quasi-static test, quasi-static test results were also used to test the reliability of using longitudinal strains to identify the point of moment drop off. Traces of strain and hinge moment from quasi-static test A5 are shown in Figure 4.10. (Cimpoeru (1992, p. 83) measured similar traces.) In this case the gauge located approximately 12 mm from the hinge centreline best predicted the instant of peak moment. The location of the gauge that most closely predicted moment drop off varied between tests. Note also that the hinge centreline could sometimes only be located to within ± 5 mm and the pitch of the strip gauge was 2.03 mm. (See Section 3.5.7 for strip gauge details.)

Typically, the signal from a strain gauge 11 mm from the buckle centreline was a maximum at approximately the point of peak moment. Therefore, using interpolation and extrapolation when necessary, the signals from the strain gauges nearest this location were used to identify the "instant" of buckle initiation/moment drop off in all impact tests. As an example, the hinge moment and strain traces from impact test A2 are shown in Figure 4.11.

surface strains could be used to provide a linear estimate of section moment at the expected hinge site over the frequency range 0 to 500 Hz.

For simplicity, a system of two gauges attached on the centreline of the tension and compression flanges was used. Section moment was calculated from the weighted sum of the individual strain signals. This summation was achieved in real time by wiring the two gauges in a ½ bridge configuration. Thus, a signal could be measured directly that was representative of section moment.

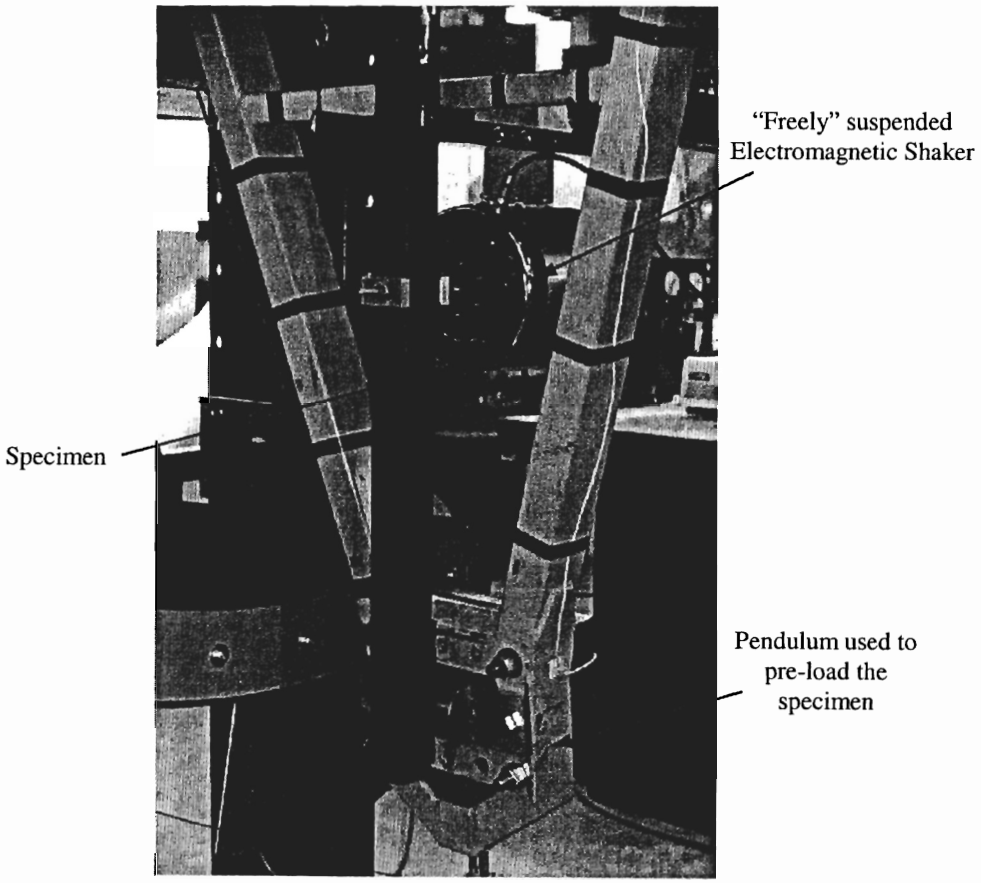


**Plate 4.1:** Unbent specimen with electromagnetic exciter attached. Note pre-load has not yet been applied

A Hewlett Packard spectrum analyser, model 35665A, was used to perform a stepped sine frequency response analysis over the frequency range 65 to 600 Hz. The ½ bridge strain signal was used as the reference. Excitation was provided by an electromagnetic exciter "freely" suspended behind the specimen (see Plate 4.1) and connected to the specimen using a short, small diameter rod (Ewins 1984).

In the frequency range 0 to 65 Hz the specimen was excited using a "soft" impact. No pre-load was applied to the specimen in this case. This form of excitation replaced the electromagnetic shaker because the shaker was only rated down to 20 Hz and because the arrangement used to pre-load the specimen, added low frequency resonances to the system. However, because the "soft" impact only had sufficient energy to excite the 1st natural frequency of the cantilevered specimen, the measured FRF in this frequency range may have been unrepresentative of the system during an impact test.

The combined FRF from 0 to 600 Hz was normalised with respect to 5 Hz (it was assumed that the FRF at 5 Hz was approximately equal to the FRF at 0 Hz). Finally, the measured FRF was corrected to remove the influence of the strain amplifiers that were used during measurement of the FRF but were not present during an impact test.

#### 4.5.4.2 THE MEASURED SPECIMEN MOUNT FRF

**Magnitude Correction**

The frequency dependent hinge moment correction factor, obtained by inverting the magnitude response of the FRF, is shown in Figure 4.13.

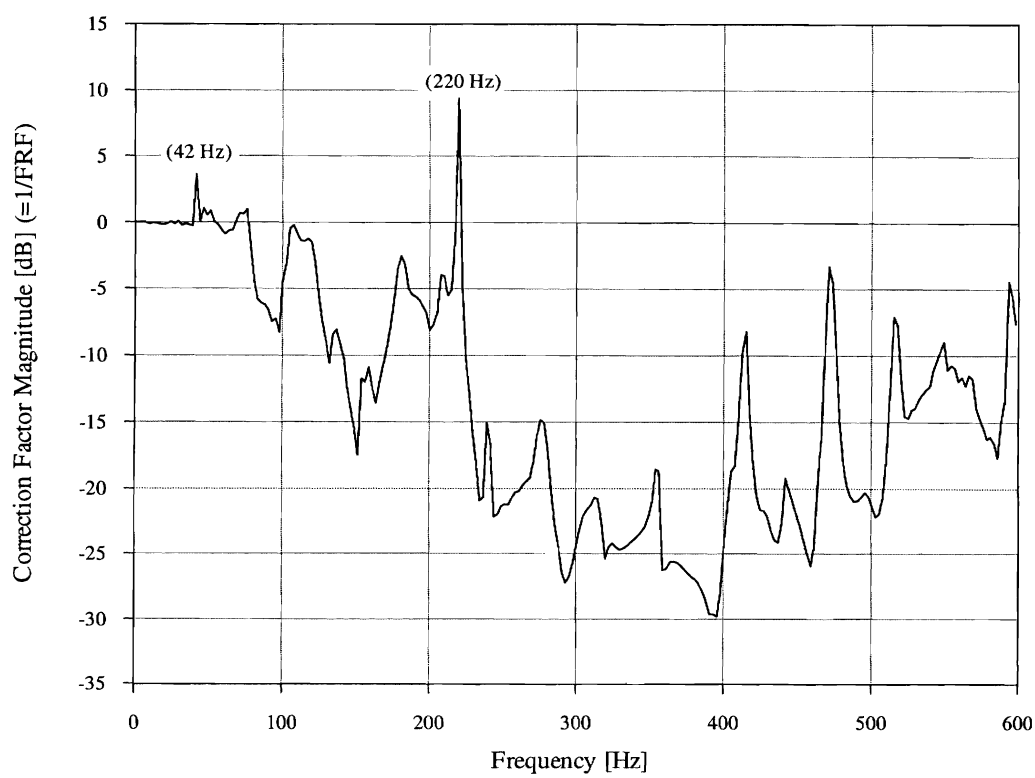


**Figure 4.13:** Hinge moment correction factor
=1/(Normalised FRF of the reaction measurement system)

oscillations in the moment signal were over corrections due to poor characterisation of the FRF at these frequencies. Note also that the FRF correction removed the initial negative response that was present in the raw moment signal.

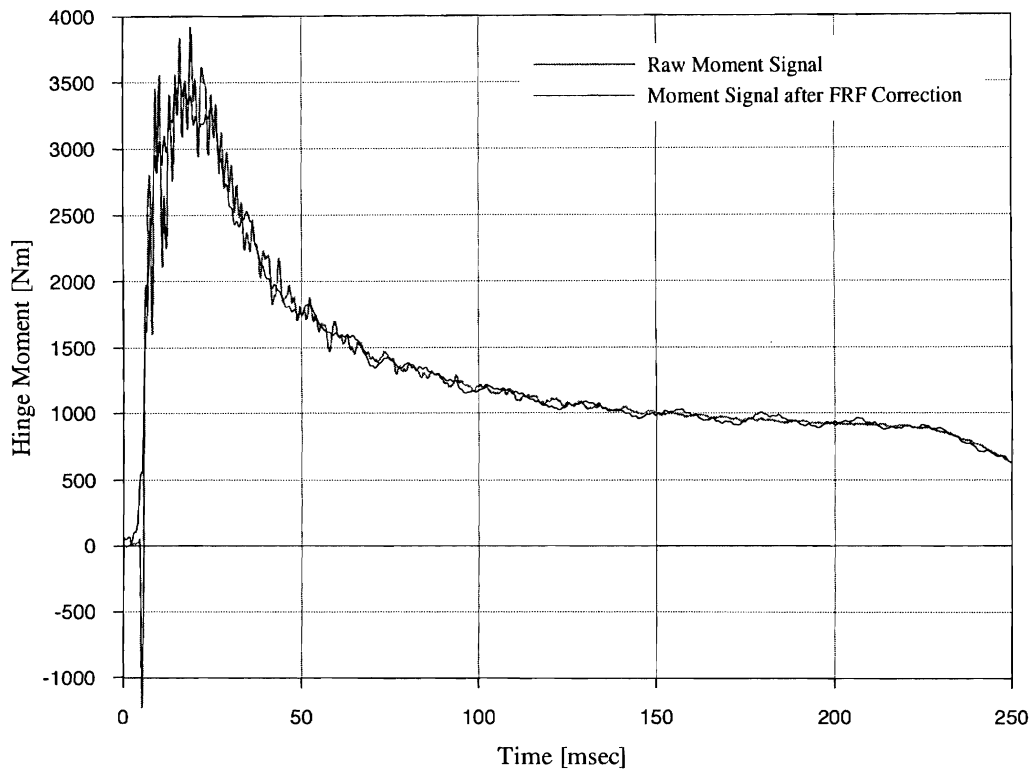


**Figure 4.14:** FRF corrected hinge moment from impact A2

The alternative technique considered for processing the impact moment signal, is now discussed.

## 4.5.5 Low-Pass Filtering

Low-pass filtering is often used to process impact test data. Unlike inverse analysis, the aim of low-pass filtering is to smooth a measured signal by limiting its frequency content. The filter cut-off frequency is typically set at the minimum frequency required to adequately describe the transient to be measured. Determining this frequency may be non-trivial and can only be done once the sources of the signal frequency content have been identified. (This is not required of the inverse analysis technique, instead the FRF must be known.) If the filter cut-off frequency is set too low, a smooth signal, free of measurement system resonances may be obtained, however frequency content that is required to describe the true signal will have been attenuated. Low-pass filtering will be quite successful if the 1$^{st}$ natural frequency of the measurement system is above the

chosen filter cut-off frequency. However, if this is not the case, the filtered signal may contain oscillations that are related to measurement system behaviour rather than true structural behaviour. In this situation, the true response is best derived using a technique that can properly treat measurement system resonance, such as the inverse analysis technique described above.

By transforming a quasi-static *moment-rotation* response into a *moment-time* plot, the frequency range required to adequately describe the moment signal in an impact bend test was estimated to be 0 to 150 Hz. The initial rise time of the moment signal and the drop in moment capacity at buckle initiation dictate the upper frequency of 150 Hz. The frequency content of the deep collapse region was approximately 0 to 50 Hz. These frequency ranges were only initial estimates and neglected the inertial response of the specimen.

In this test arrangement the inertial response of the specimen to the pendulum impact caused two significant effects, an initial negative moment response followed by specimen vibrations. The initial negative response was caused by a bending wave that travelled along the specimen immediately after impact. This initial wave and subsequent specimen vibrations caused oscillations in hinge zone rotation, which in turn significantly affected the moment at the hinge site. The influence of specimen vibration on the measurement of hinge moment will now be discussed.

#### 4.5.5.1 THE INFLUENCE OF HINGE VIBRATION ON HINGE MOMENT

(The following discussion assumes that the hinge moment signal was not corrupted in any way by measurement system frequency response.)

The impact of the pendulum against the specimen excited the natural frequencies of the specimen. These specimen vibrations were most severe during the period between initial contact and peak moment, after which plasticity associated with buckle formation significantly dampened vibrations. Specimen vibrations imposed oscillations upon the gross hinge zone rotation, which was driven by pendulum rotation. Depending on the frequency and magnitude of specimen vibration, hinge zone rotation rate may be 1) always positive or 2) negative for short periods. When hinge zone rotation rate is negative, the hinge moment is unloading elastically. Due to the relatively large elastic stiffness of the hinge, small hinge vibrations can lead to large drops in hinge moment.

As can be seen in Figure 4.15, sudden changes in the hinge moment signal are associated with hinge unloading. A consequence of these sudden changes was that the frequency bandwidth required to correctly describe the moment response was increased above the frequency of the underlying specimen vibration. To avoid distortion of the true $M$-$\theta$ response, similar to that shown in Figure 4.16, it was important to be mindful of this effect when low-pass filtering the impact moment signals. A second consequence of specimen vibration was that to obtain the true $M$-$\theta$ response, both measured hinge moment and hinge zone rotation had to reflect specimen vibration and be "complementary" to each other.

The need to capture hinge oscillations and the corresponding hinge moment fluctuations, including possible unloading, dictated the cut-off frequency of any low-pass filtering applied to the hinge zone rotation and hinge moment signals.

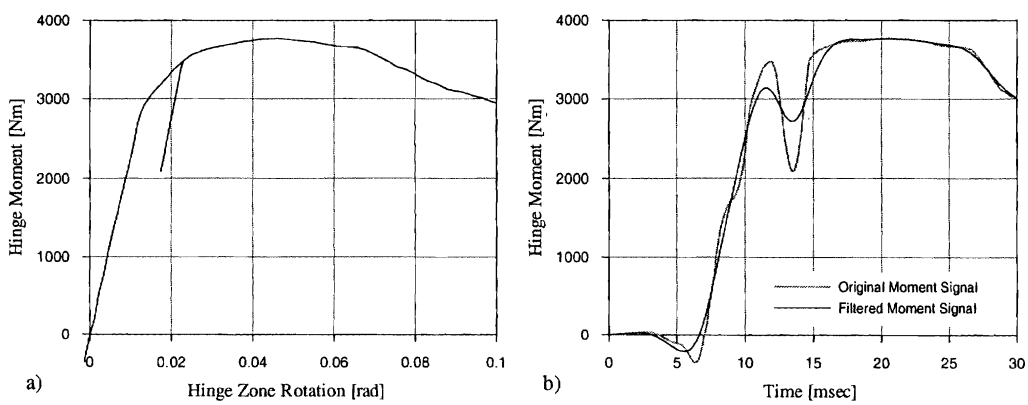


**Figure 4.15:** Effect of hinge elastic unloading on hinge moment signal

a) Hinge $M$-$\theta$ curve with unloading b) Corresponding moment signal

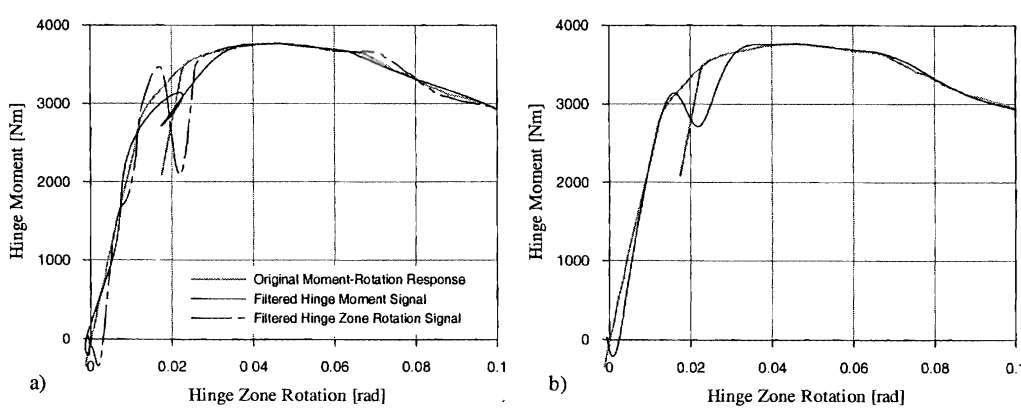


**Figure 4.16:** $M$-$\theta$ signal showing distortion due to;

a) Filtered moment signal or filtered rotation signal and b) both moment and rotation signals filtered

#### 4.5.5.2 POSSIBLE SPECIMEN NATURAL FREQUENCIES

Before deciding upon a low-pass filter cut-off frequency, a spectral analysis of four impact tests was conducted to identify dominant frequencies representative of specimen vibration. The results are given in Table 4.1. This frequency investigation was complicated by the fact that the signals were non-stationary, primarily due to buckle formation. Thus the natural frequencies of the specimen after buckle formation were lower than in the initial stages of impact. For this reason the complete time signal was analysed in two parts, part 1) from initial impact to peak moment and part 2) from just after peak moment to well into the deep collapse region. Before windowing the time signal in this manner, the complete signal was band-pass filtered between 75 Hz and 750 Hz to "de-trend" the signal thereby clarifying interpretation of the frequency spectrum. While this procedure also removed natural frequencies less than 75 Hz, the aim was to identify higher frequency specimen vibrations that might dictate the required low-pass cut-off frequency.

To further investigate the vibration behaviour of a specimen during an impact test a FE model was analysed that accounted for: the continuous change in elastic stiffness; plastic strain; buckle formation; and the influence of specimen contact with the pendulum. Refer to Section 7.2.2 for further details. Dominant frequencies in the predicted response are as given in Table 4.1 below.

The FE analysis also predicted the 1$^{st}$ and 2$^{nd}$ natural frequencies of the specimen before impact to be 42 Hz and 268 Hz and after testing to be 26 Hz and 252 Hz. These frequencies matched those measured experimentally. The stepped sine excitation discussed above gave estimates of the 1$^{st}$ and 2$^{nd}$ natural frequencies of a straight specimen in contact with the impact pendulum as being at 130 Hz and 283 Hz.

**Table 4.1:** Dominant frequencies in impact tests and FE analysis

| Signal Source | Dominant Frequencies [Hz] | | | |
|---|---|---|---|---|
| | Impact B2 | Impact A2 | Impact A4 | Impact A6 |
| ***Initial Response*** | | | | |
| Hinge Zone Rotation | 325, 425 | 316, 435 | 332, 435 | 336, 435 |
| Strain | 132, 250, 460 | 121, 225, 440 | 130, 210 | 122, 225, 442 |
| Hinge Moment | 115, 320, 690 | 122, 312, 695 | 318, 130, 695 | 122, 310, 700 |
| ***Deep Collapse Response*** | | | | |
| Hinge Zone Rotation | 151, 93 | 213, 96 | 146, 215, 88 | 132 |
| Strain† | 151 | - | - | - |
| Hinge Moment | 149, 313, 254 | 260, 307, 138 | 263, 141 | 141, 264, 295 |
| ***Finite Element Model*** | | | | |
| Signal | Initial Response | | Deep Collapse Response | |
| Hinge Zone Rotation | 127, 218, 401 | | 148, 85, 560 | |
| Hinge Moment | 120, 265, 435 | | 155, 560 | |

† These results were obtained from the 1st element of the longitudinal strip gauge attached to the surface of the specimen at the expected hinge location. Due to the formation of the buckle at this location, this signal could not be used to investigate deep collapse frequency content. For this reason separate gauges were attached to specimen B2 below the expected hinge location. Unfortunately, the significant amount of plastic strain in the region immediately below the hinge reduced the resolution with which post-buckle vibration could be measured using these gauges.

## Spectral Analysis Conclusions

1. The dominant frequency components of the FE response compared well with the dominant frequency components of the test signals.
2. Of the three test signals, strain was the most reliable indicator of specimen vibration frequencies.
3. The frequency component in the initial hinge zone rotation signal at an average frequency of 327 Hz and the frequency component in the initial hinge moment signal at approximately the same average frequency of 315 Hz were not reflected in the strain signal or FE results. It is possible that these components reflected contamination of the hinge zone rotation signal by reaction structure vibration.

4. FE natural frequencies in the initial response at (120 & 127), 218 and 435 Hz and FE natural frequencies in the deep collapse response at (148 & 155) and 85 Hz were reflected in the test signals. The reduction in natural frequency between the initial and deep collapse response was due to the formation of the buckle.

5. The dominant frequency components in the FE results and in the test strain signal suggested that in the initial phase of the response, the low-pass filter cut-off frequency ($f_c$) should be approximately 220 Hz and that in the deep collapse phase $f_c$ could be reduced to approximately 150 Hz. However, these cut-off frequencies may have been too low if specimen vibrations caused elastic unloading of the hinge moment.

#### 4.5.5.3 ASSESSMENT OF HINGE UNLOADING DUE TO SPECIMEN VIBRATION

The FE *hinge moment Vs hinge zone rotation* response, Figure 4.17, shows that specimen vibrations before peak moment are sufficient to cause at least one period of significant hinge unloading. Note also the initial negative response. After buckle formation, specimen vibration is damped to the extent that no further unloading occurs.

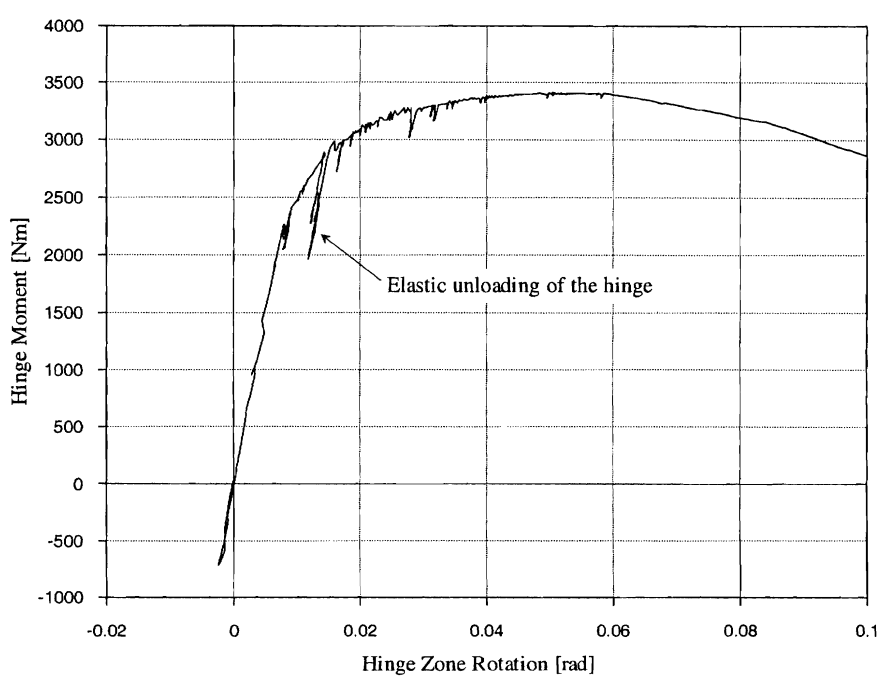


**Figure 4.17:** Hinge $M$-$\theta$ response from impact FE analysis

It was difficult to identify instances of elastic hinge unloading in the raw impact $M$-$\theta$ plots, therefore to investigate hinge unloading the "theoretical" $M$-$\theta$ response shown in Figure 4.18a was constructed. This curve was derived using the as-measured hinge zone

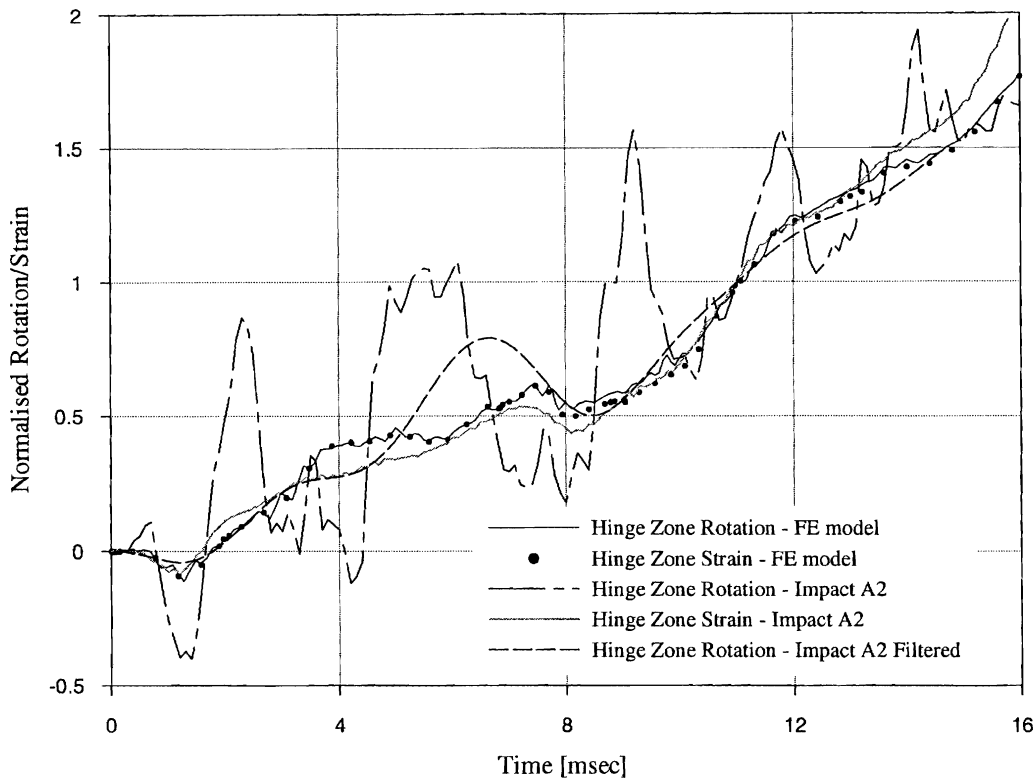


**Figure 4.19:** Comparison of hinge zone rotation and longitudinal strain from impact test A2 and the dynamic FE analysis of Section 7.2.2

#### 4.5.5.4 LOW-PASS FILTER CUT-OFF FREQUENCY ($f_C$) SELECTION

It has been demonstrated that the hinge zone rotation signal should be filtered at approximately 200 Hz. (This frequency was not inconsistent with that suggested by the spectral analysis). However, for the reasons outlined above, the hinge moment signal in the pre-buckle response phase where hinge unloading occurs should be low-pass filtered at a frequency greater than 200 Hz. The $M$-$\theta$ plot shown in Figure 4.20a was obtained after low-pass filtering both the moment and rotation signals at 350 Hz. The filtered moment signal was also shifted in time -0.4 msec, to correct for signal propagation delay. The highlighted peaks are not typical of moment unloading. They are caused by oscillations in the moment signal, which are not representative of real specimen vibration.

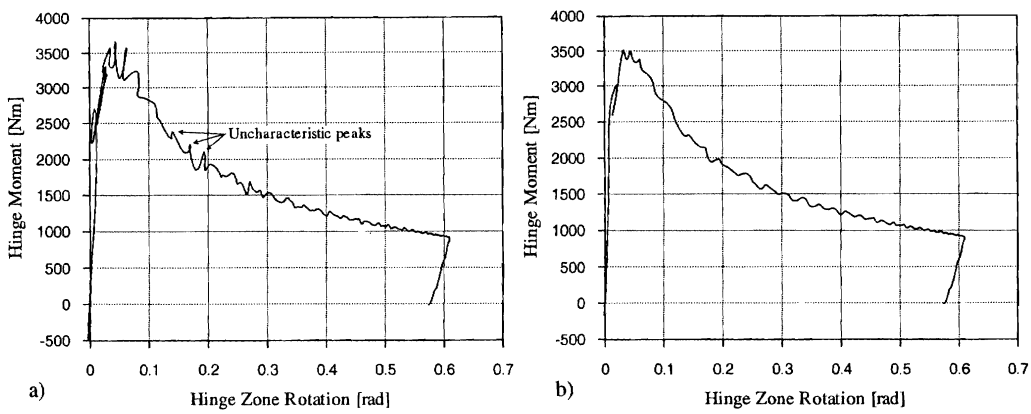


**Figure 4.20:** Hinge moment Vs hinge zone rotation response

a) Impact A2 low-pass filtered at $f_c$ = 350 Hz b) Impact A2 low-pass filtered at $f_c$ = 200 Hz

Figure 4.20b was obtained after low-pass filtering both the moment and rotation signals at 200 Hz and again shifting the filtered moment signal. The following features of the signal after filtering at 200 Hz were noted:

- The initial negative response and apparent unloading before peak were retained although attenuated.
- The deep collapse response was relatively smooth and the atypical peaks in Figure 4.20a were attenuated.
- A 150 Hz signal component is apparent in the deep collapse region. This frequency was also identified in the $M$-$\theta$ responses predicted by the beam and detailed shell-element FE analyses. However, 154 Hz was also a resonance of the reaction structure and it was possible that oscillations in the deep collapse region of the $M$-$\theta$ trace were exaggerated by this resonance.
- The filtered signal compared very well with the FE predictions shown in Figures 7.4a, 7.5a, 7.21 and 7.22.

It was concluded that a low-pass filter cut-off frequency of 200 Hz was appropriate for the majority of the $M$-$\theta$ trace. While this frequency caused some distortion of the true $M$-$\theta$ trace in the region of the large unload that occurred before peak moment, this was considered acceptable given the uncertainty that existed in this region of the $M$-$\theta$ response due to the significant vibrations excited by the initial impact. The use of different cut-off frequencies before and after peak moment to avoid this problem was not warranted.

The ideal condition, that the first natural frequency of the measurement system, (specimen mount, load cell and reaction structure), be greater than the filter cut-off frequency did not hold for the present case, as the reaction structure had natural frequencies of approximately 29, 57, 98, 154, 202 and 297 Hz. Although it has been shown that these resonances had the potential to corrupt the filtered moment signal, this does not appear to have happened.

### 4.5.6 Inverse Analysis or Low-Pass Filter

Finite element analysis confirmed that the initial negative loading and elastic unloading of the hinge before peak moment were features of the real $M$-$\theta$ response. These features of the true hinge moment response were severely attenuated by the FRF corrected curve, however they were retained by the low-pass filtering procedure described above. The FRF approach also appeared to "over correct" at 40 and 220 Hz.

The advantage of the inverse analysis procedure, over low-pass filtering, is that ideally the frequency content of the measured signal is selectively attenuated or amplified, rather than simply band limited. Thus, in theory, the FRF correction procedure is able to derive the true signal with all real frequency components intact. In this situation the FRF correction procedure failed to realise this aim.

The performance of the inverse analysis approach was dependent on the validity of the assumptions that 1) the true frequency response of the system could be represented by an equivalent linear and time-invariant FRF and that 2) this FRF was accurately represented by the measured FRF. The poor performance of the inverse analysis approach in this study would suggest that one or both of these requirements was not met. It was difficult to determine the validity of the first assumption because the extent to which the true FRF of the system was non-linear and time-variant was not known. However, it was suspected that the procedures used to measure the FRF were not capable of properly linearising the complex frequency response of the specimen mount/reaction measurement system.

Comparison of the processed $M$-$\theta$ responses shown in Figure 4.21 suggested that low-pass filtering was an acceptable and indeed the preferred means of processing the moment signal obtained from impact tests in this study. (As explained above, the hinge zone rotation signal was filtered at approximately 200 Hz. To compensate for the phase

shift incurred by filtering the hinge zone rotation signal, the FRF corrected moment signal was also filtered at 200 Hz, with negligible affect other than the intended phase compensation.) The success of low-pass filtering as a means of processing the raw hinge $M$–$\theta$ response was primarily due to the fact that little or no hinge unloading occurred in the deep collapse region, the region of most interest in this study.

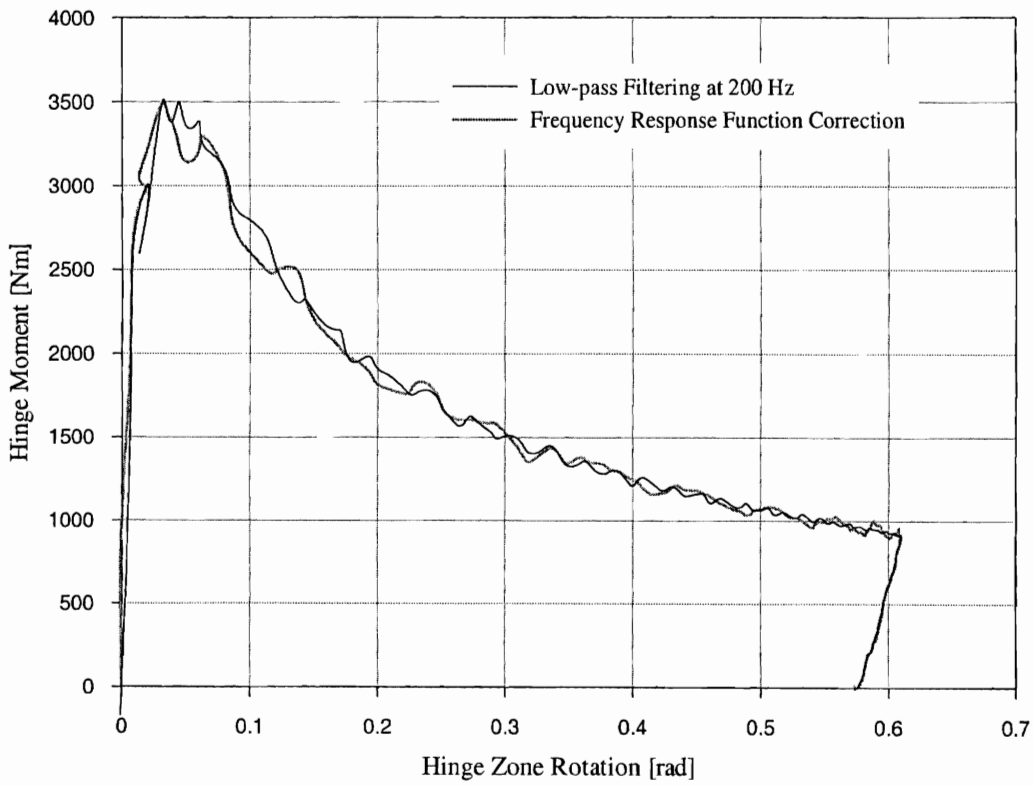


**Figure 4.21:** Comparison of FRF correction and low-pass filtering of impact $M$-$\theta$ response

## 4.6 SUMMARY OF DATA PROCESSING PROCEDURES

### 4.6.1 Quasi-Static Procedures

**Hinge Zone Rotation, $\theta$**

Hinge zone rotation has been defined here as the relative rotation over a 85 mm length of RHS spanning the hinge buckle. The term hinge zone rotation will continue to be used to avoid possible confusion with hinge or buckle rotation, which is the relative rotation between the two undeformed cross-sections that bound the buckle mechanism. The distinction is only really significant prior to buckle formation, as the post-buckle hinge zone rotation is effectively equal to the buckle rotation.

Since it has been shown that no significant vibrations occur after buckle formation, the smooth monotonic pendulum rotation signal could have been used to derive hinge zone rotation beyond peak moment. However it was preferred to use the hinge zone rotation signal measured locally at the buckle, using the device described in Section 3.5.6.

**Hinge Moment, $M$**

Energy consistent hinge moments have been defined for the three phases of the $M$-$\theta$ response. These moments are calculated using Equation 4.11 with values of hinge offset as given below.

$$M_h \approx R \times d \times \left[1 - \frac{a}{1002}\cos(\beta)\right] \quad \text{[Nm]} \qquad \text{(Eqn. 4.11)}$$

Where; $R$ = measured reaction force [kN]
$\beta$ = measured pendulum rotation
$d$ = 298.65 mm
$a$ = hinge offset from pendulum axis [mm]

*Pre-Buckle*

$a$ = -3 mm.

*Post-Buckle*

$a$ = the distance from the pendulum axis to a point corresponding to the original location of the effective hinge centre. The effective hinge centre was identified at the conclusion of testing. The original location of the effective hinge centre was approximately 5.5 mm closer to the tip of the specimen than the final location.

*Transition*

In the initial stages of collapse, before the buckle had fully developed into the classic mechanism, hinge moment was calculated as the weighted average of the pre-buckle and post-buckle moments.

$$M_{EC}^{trans} = (1-\lambda)\times M_{EC}^{Pre} + \lambda \times M_{EC}^{Post} \qquad \text{(Eqn. 4.2)}$$

where $\lambda$ varied linearly from 0 to 1 over the transitional phase. The transitional phase began at buckle initiation and concluded at the point at which the $M$-$\theta$ response began to be dominated by the response of the buckle mechanism. This point was identified as the point at which the power-law curve fit for the collapse phase began to significantly deviate from the $M$-$\theta$ response, see Sections 5.4.3 and 5.4.4.

**Pendulum Rotation, $\beta$**

Pendulum rotation was calculated from measured pendulum travel using Equation 4.4.

$$\beta = \frac{s_p}{r_{op}} \qquad \text{(Eqn. 4.4)}$$

Post-buckle pendulum rotation was normalised to account for offset buckle formation using Equation 4.13.

$$\beta' \approx Tan^{-1}\left(\frac{Sin\beta}{Cos\beta - a/1002}\right) \qquad \text{(Eqn. 4.13)}$$

$a$ = the distance from the pendulum axis to the original location of the effective hinge centre.

**Hinge Zone Elastic Stiffness**

For the purposes of calculating hinge zone plastic rotation, the elastic flexibility of the hinge zone was defined by the reciprocal of Equation 4.16.

$$\frac{\Delta\theta_{elas}}{\Delta M_h} = F(\theta_{pb})\times\left(\frac{\Delta\theta_{elas}}{\Delta M_h}\right)_0$$

where; $F = 23.63\theta_{pb}^4 - 30.02\theta_{pb}^3 + 19.00\theta_{pb}^2 + 3.261\theta_{pb} + 1.009$

$\left(\frac{\Delta\theta_{elas}}{\Delta M_h}\right)_0$ was the pre - buckle flexibility.

### 4.6.2 Impact Procedures

#### Hinge Moment and Hinge Zone Rotation

Hinge moment and rotation were calculated in accordance with the quasi-static procedures above, with additional treatment to account for dynamic effects; specifically specimen vibration and measurement system frequency response. The additional treatment involved low-pass filtering the moment and hinge zone rotation signals using a $4^{th}$ order Butterworth filter with a –3 dB cut-off frequency of 200 Hz. The filtered moment signal was also shifted in time -0.4 msec, to correct for signal propagation delay.

#### Peak Moment and Buckle Initiation

The "instant" of peak moment, corresponding to buckle initiation, was associated with the minimum in the signal from a longitudinal surface strain gauge located ≈11 mm from the buckle centreline on the compression flange.

## 4.7 CONCLUSIONS

The procedures developed in this chapter, most significantly the judicious use of low-pass filtering, were successfully used in Chapter 5 to derive impact hinge $M$-$\theta$ responses from raw test measurements. The major issues relating to proper treatment of test data were:

- In a cantilever bending rig, the choice of a moment to associate with measured hinge rotation is somewhat arbitrary. For the purposes of this study an energy equivalent hinge moment has been defined.
- To minimise the influence of specimen vibrations on the measured hinge $M$-$\theta$ response, hinge rotation and hinge moment signals should be "complementary". This required that hinge rotation be measured directly. A device incorporating two rotary potentiometers was designed for this purpose and was used successfully.
- Low-pass filtering should generally be used with caution. However, it was determined that low-pass filtering was an acceptable means of removing the effects of measurement system resonance from the $M$-$\theta$ response in this series of tests, essentially because no significant hinge unloading occurred post buckle formation. If more significant and frequent hinge unloading were to occur, "inverse analysis"

using a reliable FRF might be the only option to remove the effects of measurement system resonance.

## 4.8 RECOMMENDATIONS FOR FUTURE WORK

The difficulties in processing the test results in this study were due to 1) the complex nature of the reaction mount system and 2) severe specimen vibration and hinge unloading. It is recommended that future rig designs should aim to 1) minimise or eliminate specimen vibration and hinge unloading and 2) use a more direct and structurally simple means of measuring hinge moment.

Loose tolerances in the system and the need therefore to pre-load the system, significantly complicated the system FRF and the measurement thereof, particularly at low frequencies. Re-design of the specimen mount and hinge moment measurement system could improve this situation to the extent that the FRF of the system could be accurately measured and the "inverse analysis" technique successfully used to process impact test signals.

The accuracy of the reaction mount FRF measured in this study could have been improved, although not necessarily to the full extent required, by using a different excitation method. Ramsey (1976) compared five excitation methods and concluded that pure random and periodic random stimuli provided the best means of measuring the linear approximation to a non-linear FRF. This was due to their ability to effectively use ensemble averaging to remove the distortion components from the measurement. The swept sine analysis, used in this study to derive the FRF of the reaction structure, does not average system non-linearities. Therefore, if non-linearities remained in the pre-loaded system, the measured FRF was potentially a poor linear representation of the reaction mount system.

# CHAPTER 5 BEND TEST RESULTS

## 5.1 INTRODUCTION

This chapter presents the results of quasi-static and impact bend tests conducted on 50x50x2 grade C350LO RHS specimens using the novel pendulum rig described in Chapter 3. While experimental studies that characterise the plastic hinge $M$-$\theta$ response of RHS under quasi-static flexural loading have been published, to the best of the author's knowledge, no previously published studies show the plastic hinge $M$-$\theta$ response of RHS under impact flexural loading. The experimental results reported in this chapter therefore constitute an original contribution to the understanding of RHS plastic hinge response. Key features of this test programme were:

- a meticulous attention to detail in the measurement of the various physical parameters and,
- the use of finite element analysis to examine and identify in detail, the effects of the various physical issues influencing the measurement and processing of *moment-rotation* responses.

It is argued that because of this approach to the experimentation, confidence in the integrity of the test results has been maximised.

Quasi-static *moment-rotation* response curves for the buckle mechanism, the local hinge region and for the entire specimen are presented first. Comparisons are made with a published experimental result and analytical model. The quasi-static results are followed by the corresponding response curves measured under impact loading. Finally the direct and effective influence of material strain rate sensitivity is assessed by comparison of quasi-static and impact responses. The measurement of buckle mechanism response enables a more direct assessment of the influence of material strain rate sensitivity than would be possible if only the gross response of the specimen were recorded.

The experimental results from this chapter are used in the following chapters to validate and "calibrate" FE models and to assess the performance of impact design schemes that predict impact response by "scaling" a known quasi-static response.

## 5.2 TEST PROCEDURE DETAILS

### 5.2.1 RHS Specimens

Grade C350LO 50x50x2 RHS was tested. Eight metre lengths of RHS were cut into six specimens, three quasi-static and three impact. To minimise the effects of any variation of material properties along the 8m length, specimens were alternately designated as quasi-static and impact specimens. Specimen geometry was given in Chapter 3.

Each specimen was identified by a letter designating the length of RHS from which it was cut followed by a number indicating the position along the original length. Odd numbered specimens were tested quasi-statically and even numbered specimens were impacted. Sufficient confidence in the repeatability of results was obtained after five quasi-static and four impact tests.

Both quasi-static and impact specimens were tested as cantilevers, subject to an enforced tip displacement applied by a rotating pendulum. All tests used the same specimen geometry and instrumentation, as described in Chapter 3.

### 5.2.2 Loading Rate

#### 5.2.2.1 QUASI-STATIC LOADING RATE

The quasi-static tests were conducted over a period of 15 minutes at a loading rate of approximately 2.3° of pendulum rotation per minute. This loading rate was approximately $10^{-4}$ times the initial loading rate in an impact test.

#### 5.2.2.2 PENDULUM IMPACT VELOCITY AND ENERGY

The pendulum impact velocity was chosen so as to produce a hinge rotation rate typical of what might be experienced by a plastic hinge forming in a bus structure subjected to the rollover test described in ADR 59/00.

The collapse mode of the bus shown in Plates 1.1 – 1.5, with plastic hinges forming at the waist and cant rail, is one of the most common (Kecman & Tidbury 1985). This mode also accommodates the largest hinge rotations before the frame intrudes into the passenger survival space. A standard ring frame, which is required to collapse in this manner, is defined in the National Code of Practice – Part B, Profile B (see Figure 5.1 below). It is accepted that in a typical rollover accident the cant rail of a bus frame

impacts the ground at a velocity of between 3 and 8 $ms^{-1}$ (Australian Design Rule 59/00 1989 Annex 5) and at an angle $\alpha$ of between 15° and 25°. (ADR 59/00 Annex 5 specifies 20° < $\alpha$ < 25°, the associated National Code of Practice sets $\alpha$ = 15°). Thus a plastic hinge forming at the waist rail of Profile B will experience an initial rotation rate $\dot{\theta}$ of between 2.6 and 7.7 $rads^{-1}$. The average impact velocity used in this study of 7.54 $ms^{-1}$ is at the upper end of this range.

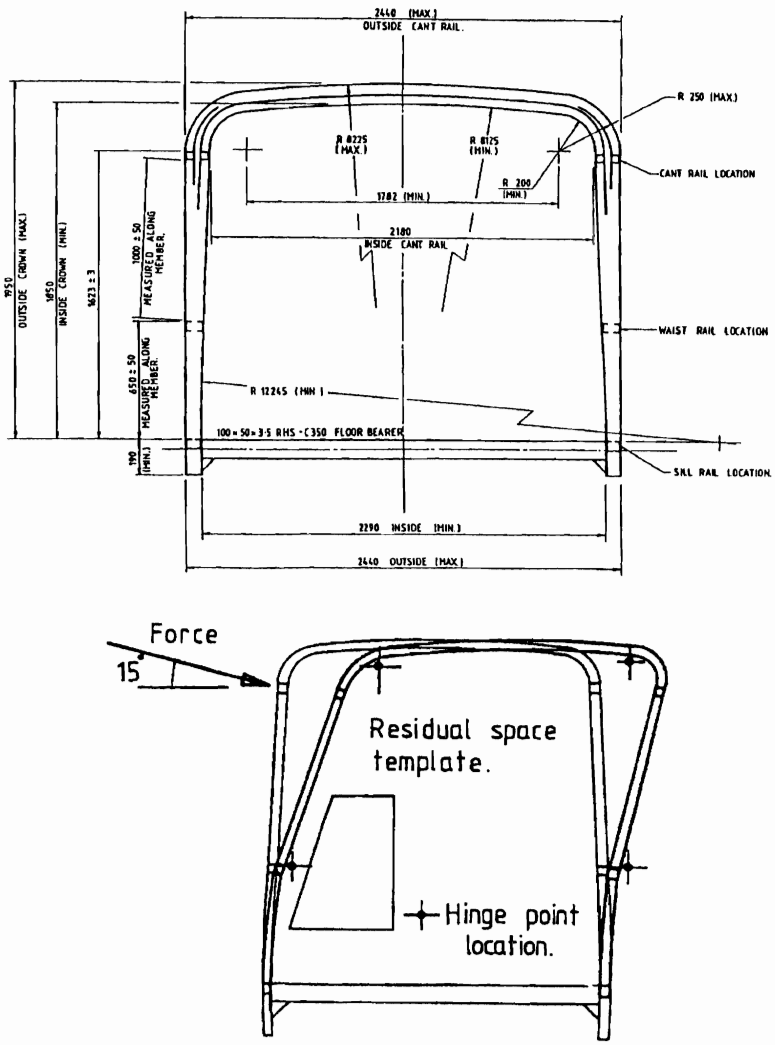


**Figure 5.1:** ADR 59/00 National Code of Practice – Part B, Profile B
a) Allowable roll cage cross section and b) Standard hoop deflection collapse mechanism
(National Code of Practice 1992)

Pendulum inertia was adjusted so as to produce hinge zone rotations of nominally 35°. (This is approximately the rotation of a waist rail hinge in Profile B when the survival space is intruded). The average energy imparted to the specimen was 1185 J.

Finally it is worth noting that the ratio of shear to bending loads at the specimen hinge site are similar to those at the waist rail hinge in Profile B.

### 5.2.3 Data Acquisition

In total fourteen channels of data were recorded during each test. The quasi-static sampling rate was 5 Hz with automatic low-pass filtering at 40 Hz. The impact test sampling rate was 10 kHz with automatic anti-alias low-pass filtering at 4 kHz.

## 5.3 General Results

### 5.3.1 Material Failure, Pre-Buckle Plasticity and Collapse

No external signs of material failure were evident after testing.

While it was difficult to measure the extent of the material plasticity that developed before peak moment, permanent curvature of the specimen extended approximately 300 mm from the root of the cantilever after quasi-static loading and approximately 360 mm after impact loading.

Under both loading conditions, specimen collapse was caused by the formation of an inward compression flange buckle. The fully developed buckle is shown in Plate 5.1. The geometry of the buckle was essentially identical under both quasi-static and impact loading.

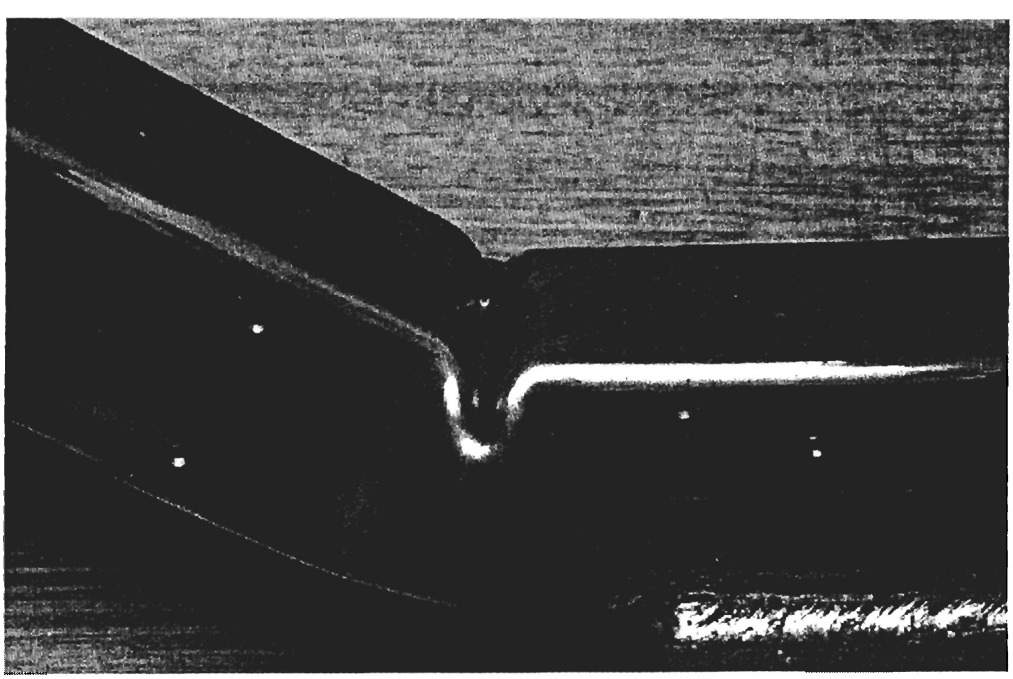

**Plate 5.1:** Typical buckle forming in quasi-static and impact specimens

- that all rotation at buckle initiation is accommodated by the rotation of the mechanism;
- that buckle mechanism geometry is more developed than it actually is at this point; and
- that the same mechanism model geometry will be associated with different physical buckle geometries depending on the amount of pre-buckle rotation.

The rotation at buckle initiation is influenced by loading conditions, boundary conditions, initial imperfections and, most directly, by the length of section over which rotation is measured. Therefore, if the mechanism rotation measure includes pre-buckle rotation, i.e. is absolute rotation, then the buckle mechanism *moment-rotation* response will also be affected by these factors. However, if mechanism rotation is defined from the point of buckle initiation, the influence of pre-buckle rotation is removed (the effect of different pre-buckle responses is to shift, but not alter, the collapse response) and the buckle mechanism *moment-rotation* response becomes a characteristic unique to the section. It is therefore argued that rotation "relative" to buckle initiation is the correct basis for $M$-$\theta$ characterisation of the buckle mechanism. This conclusion is supported by the following observations. (In each case the collapse response was plotted against post-buckle rotation).

1. For $\theta$ measured over different lengths: the collapse phase responses measured by Cimpoeru (1992) for various deformable lengths were all coincident.
2. For different boundary conditions: the collapse phase responses measured by Cimpoeru (1992), for specimens where the buckle formed against a rigid insert, were coincident with the collapse phase responses of specimens where the buckle formed freely.
3. For different loading and boundary conditions: there was excellent agreement between the collapse phase response measured by Cimpoeru and that measured in this study, Figure 5.8.
4. For different loading conditions and initial imperfections: finite element models of the buckle have demonstrated that the collapse phase responses are similar between single and double symmetry models of the buckle, between pure moment and cantilever loading, and between a buckle forming "freely" and one deliberately

### 5.4.4.1 COMPARISON WITH $M$-$\theta$ RESPONSE OF CIMPOERU

Cimpoeru (1992) tested in pure bending the same RHS section as tested in this study. Material mechanical properties reported by Cimpoeru indicated that the majority of the RHS tested was stronger than that tested in this study. The average peak moment measured by Cimpoeru, scaled to account for the difference in material strength, was 2,933 Nm. This compared well with the average peak moment of 2,917 Nm obtained in this study and indicated that the influence of the shear force associated with cantilever loading was minimal. This is consistent with the findings of Mamalis et al. (1992) who investigated the influence of shear forces on the bending collapse of cantilevered circular tubes. Their experiments covered diameter:thickness ratios from 30.8 to 66.5 and length:diameter ratios of 5 to 17.8. In general, Mamalis et al. found little influence of shear on the overall collapse characteristics of each tube size.

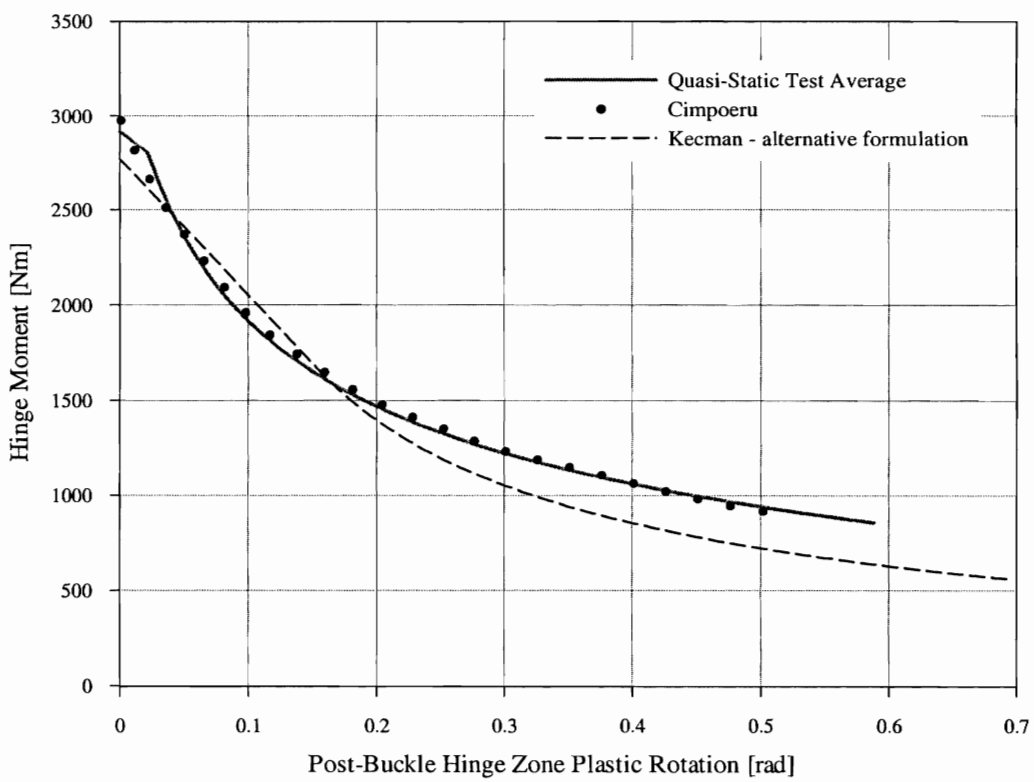


**Figure 5.8:** Comparison with experimental $M$-$\theta$ obtained by Cimpoeru and analytical model developed by Kecman

The average rotation at buckle initiation for the 90 mm deformable length specimens tested by Cimpoeru was 5.95°. In this study the average rotation over the 85 mm hinge zone at buckle initiation was 2.54°. This difference was to be expected given the different loading and boundary conditions between the two test arrangements. The

collapse phase response measured by Cimpoeru and that measured in this study were in excellent agreement when plotted against post-buckle rotation, see Figure 5.8.

#### 5.4.4.2 COMPARISON WITH AN ANALYTICAL MODEL OF BUCKLE $M$-$\theta$ RESPONSE

Kecman (1979) derived a relatively simple analytical model to predict the $M$-$\theta$ collapse response of RHS in bending. Kecman's yield line model of the buckle mechanism is shown in Figure 5.9. The model is applicable for a wide range of section sizes and now forms the basis of the commercial software program WEST which is part of the CIC – SIM family of programs (Kecman & Randell 1996). (This software suite has been approved for ECE 66 type approval by calculation.)

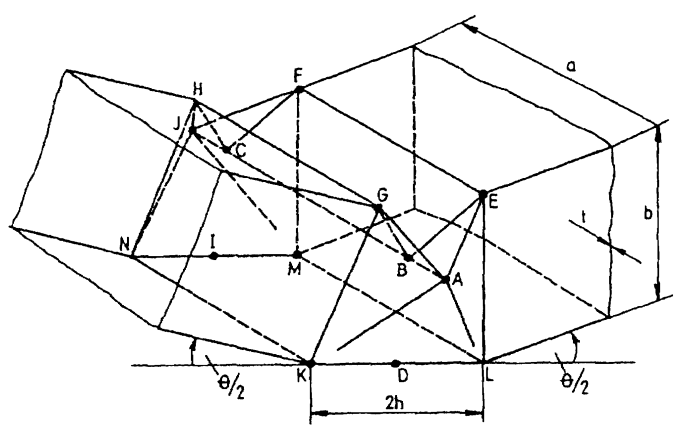


**Figure 5.9:** Yield line model of the buckle mechanism, Kecman (1979)

Kecman's model predicts the $M$-$\theta$ response of the local buckle mechanism forming in a RHS section in bending. Input parameters to the model are the width, depth and thickness of the RHS section together with the yield and ultimate tensile stresses of the RHS material. The model defines buckle rotation $\theta$, as the relative angle between the two yield lines bounding the mechanism and assumes $\theta = 0$ at buckle initiation.

Close study of the model derivation given in Kecman (1979) identified two issues that warrant discussion and a possible typographical error that has been overlooked. Details are given in Appendix A. The alternative formulation of Kecman's model derived in Appendix A was used here to predict the $M$-$\theta$ response for the 50x50x2 RHS tested in this study. This prediction, termed "Kecman – alternative formulation", is compared with the average quasi-static $M$-$\theta$ test response in Figure 5.8. The model performed well up to a buckle rotation of approximately 0.2 radians at which point the analytical model and test results began to diverge. At buckle rotations greater than 0.2 radians the model

underestimated the measured moment capacity of the buckle. The underestimation was 10% at 0.25 radians, 20% at 0.4 radians and 25% at 0.56 radians.

Cimpoeru (1992) compared the collapse response of a 90 mm deformable length specimen with the collapse response predicted by Kecman's analytical model. Cimpoeru treated Kecman's mechanism $\theta$ as an absolute quantity, whereas Kecman derived his model on the basis that $\theta$ was a relative quantity. Cimpoeru noted the good agreement and concluded that the correct treatment of mechanism rotation in Kecman's model was as an absolute quantity. (There is less agreement between Cimpoeru's test results and the alternative formulation of Kecman's model). Cimpoeru also implied that the agreement confirmed the significance of the 90 mm deformable length as being the "finite mechanism length" for a 50x50x2 section.

The choice of deformable length is arbitrary and in the author's opinion, the fact that the collapse response for a deformable length of 90 mm compared well with the response predicted by Kecman's model, imparts no special significance to this 90 mm length. Nor does the comparison justify treating $\theta$ in Kecman's analytical model as an absolute quantity. It was just a coincidence that the collapse angle for a 90 mm deformable length of 50x50x2 RHS tested in pure bending compensated for the inaccuracy of Kecman's model.

### 5.4.5 Gross Specimen Response

Specimen response can be assessed on a gross level by considering pendulum moment, pendulum work and pendulum rotation. Just as plastic hinge response should be treated differently prior to and following buckle formation, so too should the gross specimen response be treated differently. Prior to collapse the specimen deformed as a continuous beam and pendulum moment and pendulum rotation were suitable measures to compare responses from different specimens.

Following buckle formation, the specimen essentially rotated about the effective hinge centre. The kinematics of this situation meant that measured pendulum rotation was dependent upon the location of the buckle. To compare pendulum rotation between specimens it was therefore necessary to derive a measure of pendulum rotation that was independent of buckle location. "Normalised" pendulum rotation was defined in Section 4.3.2.2 as approximately the pendulum rotation that would be measured if the pendulum

pivot axis were at the effective hinge centre. While pendulum rotation should theoretically be normalised, pendulum rotations measured in this study were not normalised because for the hinge locations recorded the correction was a maximum of 1%. The work conjugate to normalised pendulum rotation, "normalised pendulum moment" was equal to the energy consistent hinge moment defined by Equation 4.11.

Pre-buckle and post-buckle gross specimen response were combined on a single plot by defining a transitional pendulum moment, as was done for hinge moment in Section 4.2.2.2. A combined plot of *normalised pendulum moment Vs pendulum rotation* for the five quasi-static tests is shown in Figure 5.10.

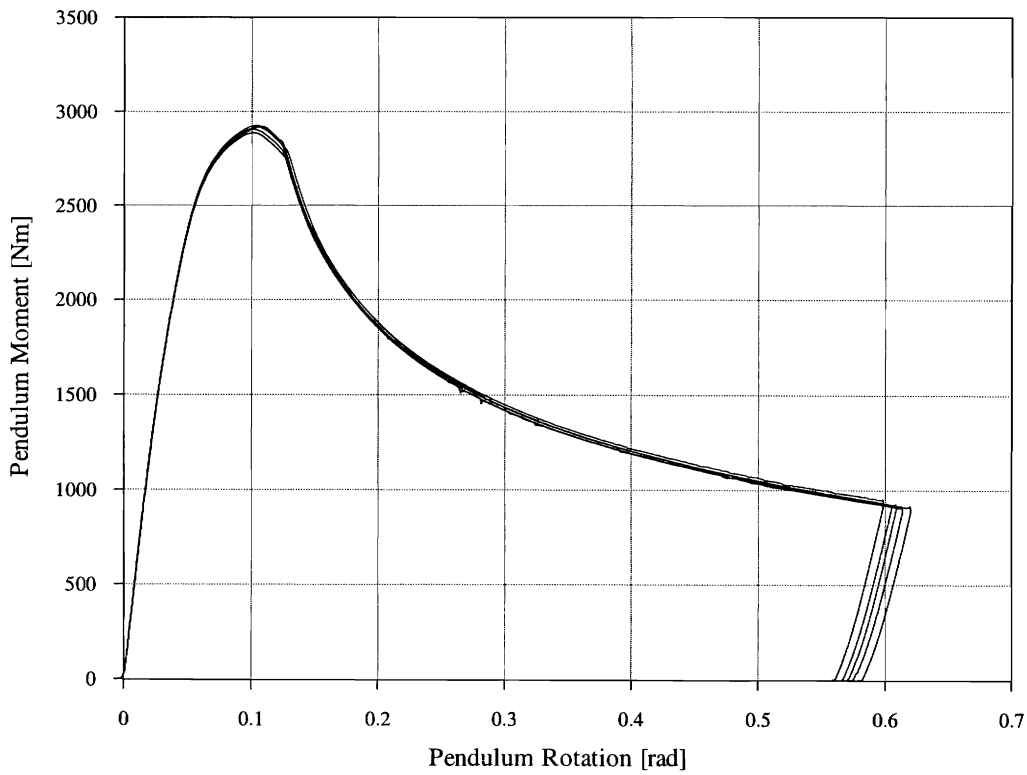


**Figure 5.10:** Gross specimen response – pendulum moment Vs pendulum rotation
Quasi-static tests A1, A3, A5, C1 and C3

This concludes the presentation of the quasi-static test results. The results from the series of impact tests are now presented.

## 5.5.2 Filtered Hinge Zone $M$-$\theta$ Response

As discussed in Chapter 4, the raw hinge moment and hinge zone rotation signals were low-pass filtered to reduce the influence of measurement system frequency response.

Figure 5.13 shows a plot of filtered pre-peak hinge zone $M$-$\theta$ response, with hinge zone rotation derived from the rotary potentiometer device and from longitudinal compression flange strains. Also shown in Figure 5.13 is the average curve, derived as described below. There is no difference of any real consequence between the signals, except for the initial slope. The response derived from compression flange strain suggested that the initial slope of the average response should have been increased by approximately 40%. This increase was difficult to justify on the grounds of material behaviour because the Young's modulus of the material was strain rate insensitive. Furthermore, no increase in initial elastic stiffness was predicted by the detailed FE analyses in Chapter 7. Therefore, the initial stiffness of the average impact $M$-$\theta$ curve was assumed to be equal to that derived from the quasi-static results.

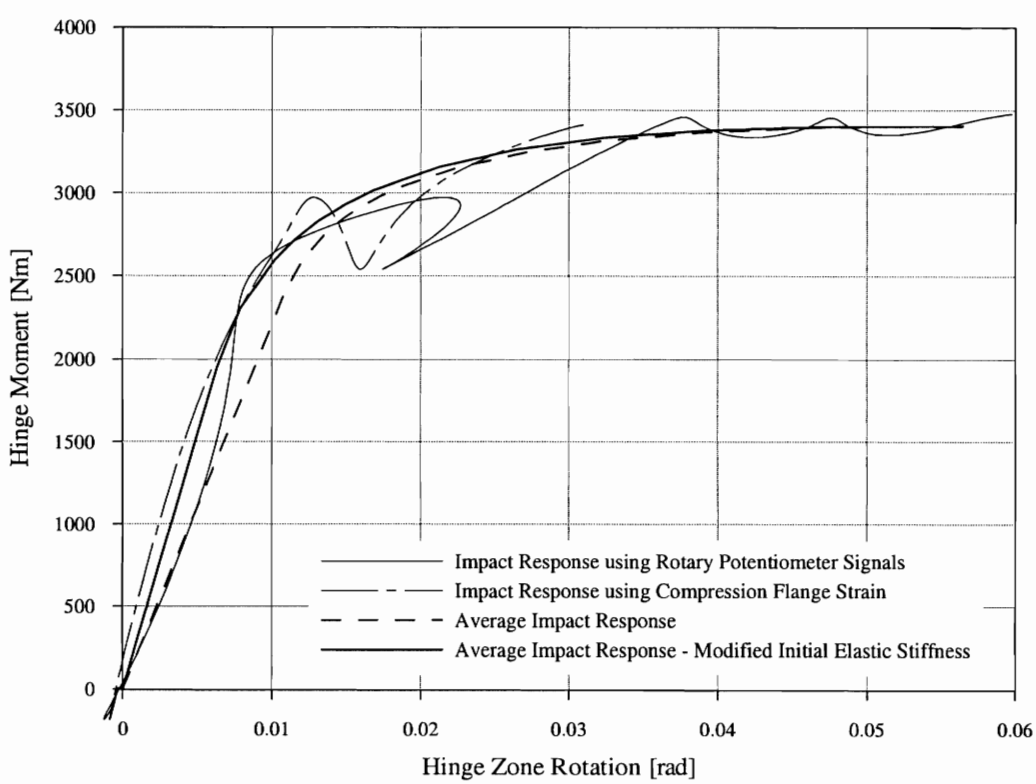


**Figure 5.13:** Filtered hinge zone $M$-$\theta$ response, Impact test A4 – hinge zone rotation derived from the rotary potentiometer device and longitudinal compression flange strains

Combined filtered hinge zone $M$-$\theta$ response curves are shown in Figure 5.14. The repeatability of the traces was again excellent.

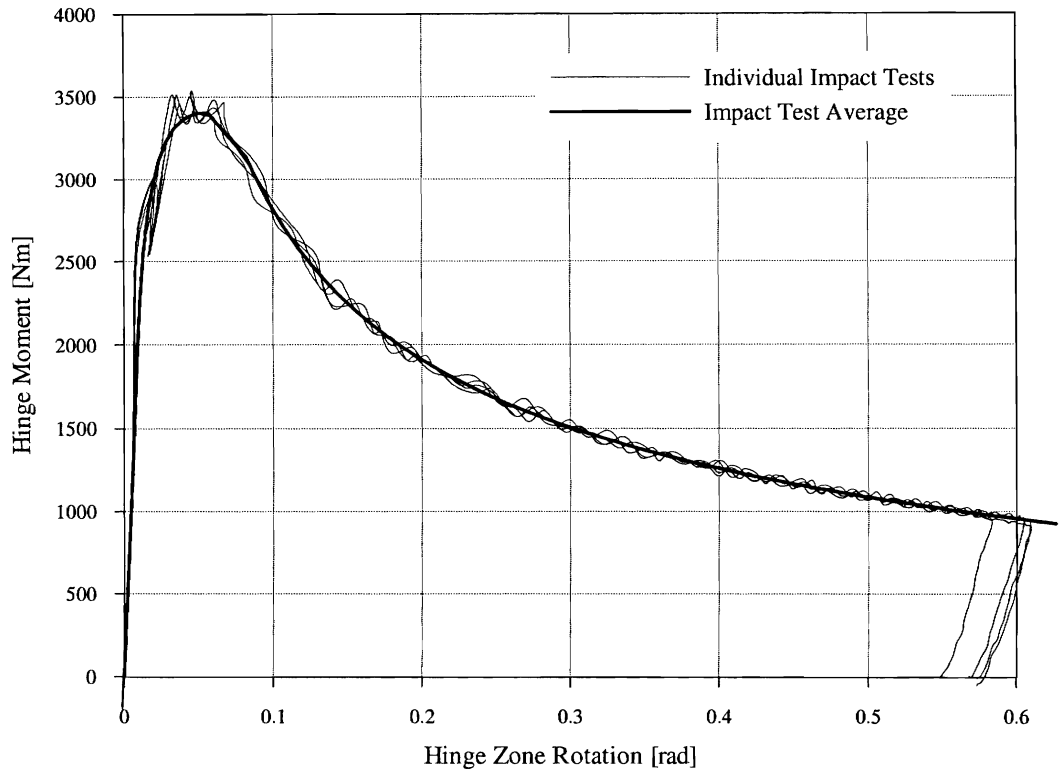


**Figure 5.14:** Filtered hinge zone $M$-$\theta$ response - Impact tests A2, A4, A6 and B2

It is evident in Figure 5.14 that the average moment at buckle initiation slightly underestimated the average peak moment that might have been identified by visual inspection. Note, however, that the load oscillations make the visual estimation of average peak moment a very subjective process. The procedure for identifying the point of buckle initiation using longitudinal compression flange strain, involved taking a "snapshot" of an oscillating signal. Therefore, the moment at buckle initiation was dependent on the timing of the "sample" with respect to the load oscillation. Some averaging would occur over a number of specimens, however, the repeatability displayed in Figure 5.14 suggested that the underestimation was inherent in the relationship between peak moment, specimen vibrations and longitudinal compression flange strain. Kecman (1993a) noted that dynamic "... *signals are very fluctuating, often even after the lowest-pass filtering that may still make sense (e.g. 100 Hz). The dynamic failure moment ... is very difficult or impossible to determine*". The combination of test rig design and data processing procedures used in this study, have yielded a hinge

*moment-rotation* curve from which peak moment was estimated with much less ambiguity than the pendulum *moment-rotation* curves referred to by Kecman.

### 5.5.3 Buckle Mechanism $M$-$\theta$ Curves

Filtered post-buckle hinge zone $M$-$\theta$ responses are shown in Figure 5.15. These curves essentially represented the $M$-$\theta$ response of the buckle mechanism. The limited accuracy with which the point of buckle initiation could be identified affected the degree to which these curves are co-incident.

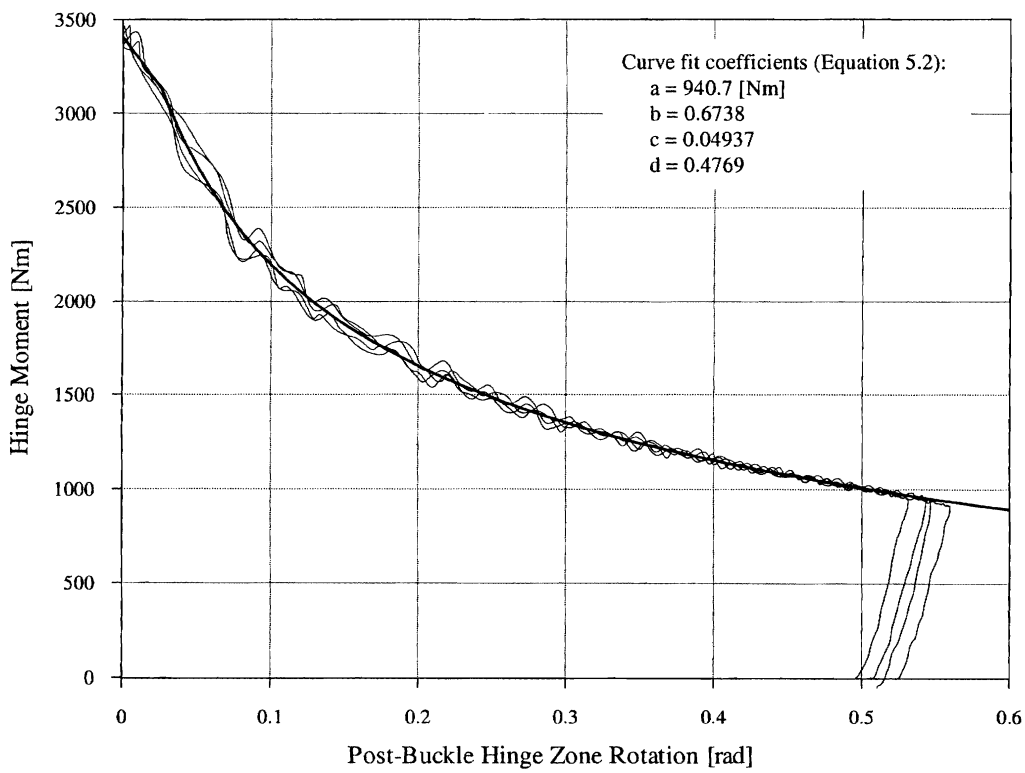


**Figure 5.15:** Filtered buckle mechanism $M$-$\theta$ responses - Impact tests A2, A4, A6 and B2

### 5.5.4 Buckle Mechanism Collapse Curve Fits

The power-law function given by Equation 5.2 was used to fit the collapse phase of the filtered buckle mechanism $M$-$\theta$ responses shown in Figure 5.15. Essentially identical curve fits were obtained by fitting the raw $M$-$\theta$ responses. The average fitted collapse curve and transitional phase is shown in Figure 5.15.

## 5.5.5 Average Combined $M$-$\theta$

The average impact $M$-$\theta$ response curve was derived in the same manner as for the quasi-static case, using the key result quantities summarised in Table 5.3. The initial elastic stiffness was assumed to be equal to that determined from the quasi-static tests. The resulting curve was plotted in Figure 5.14 above.

**Table 5.3:** Summary of key result quantities from impact hinge zone $M$-$\theta$ responses

| Specimen ID | Result Quantity | | |
|---|---|---|---|
| | 1 [Nm] | 2 [rad] | 3 [rad] |
| A2 | 3361.5 | 0.0499 | 0.0776 |
| A4 | 3480.2 | 0.0614 | 0.0825 |
| A6 | 3360.5 | 0.0519 | 0.0873 |
| B2 | 3420.2 | 0.0626 | 0.0825 |
| Average | 3405.6 | 0.0564 | 0.0825 |
| Std. Dev. | 49.4 | 0.0056 | 0.0034 |

1. Hinge moment at buckle initiation.
2. Hinge zone rotation at buckle initiation.
3. Hinge zone rotation at the end of the transitional phase.

## 5.5.6 Gross Specimen Response

In an impact test gross specimen *moment-rotation* response can be determined with or without the influence of specimen inertia (or specimen kinetic energy). Strictly speaking, the reaction force signal measured in these tests could not be used to derive the true time history of either measure of gross specimen response. However, an implicit dynamic FE analysis, discussed in Chapter 7, showed that an approximate measure of specimen strain energy was:

$$E_{spec.} = \int M_{pend}\, d\beta$$

where: $M_{pend}$ = pendulum moment = scaled reaction force

$\beta$ = measured pendulum rotation

Thus, plots of $M_{pend}$ *Vs* $\beta$ were used to compare gross specimen response under impact and quasi-static loading. This same FE analysis confirmed that an acceptable measure of pendulum work could be derived from measurements of impact velocity and pendulum displacement. Pendulum work and specimen strain energy derived from the results of impact test A2 are plotted in Figure 5.16. The difference between the two traces

To illustrate the repeatability of the impact tests, *reaction force Vs pendulum rotation* is plotted in Figure 5.17. Because raw rather than normalised quantities are plotted, the comparison beyond peak moment is affected by the location of the buckle with respect to the pendulum axis.

This concludes the presentation of the impact test results. The following section compares the quasi-static and impact response of the buckle mechanism, hinge zone and specimen as a whole.

## 5.6 COMPARISONS AND DISCUSSION

A direct assessment of the influence of material strain rate sensitivity on plastic hinge $M$-$\theta$ response can only be made by comparing phases of the response with similar hinge geometry. The plastic hinge $M$-$\theta$ response under investigation had two basic geometric phases, pre-buckle and post-buckle, which were compared separately. Comparisons of gross specimen or gross hinge performance combined these two phases and therefore could only provide an indication of the total influence of material strain rate sensitivity.

Since the material Young's modulus is strain rate insensitive, the elastic component of an impact response is often assumed to be strain rate insensitive. Therefore, to assess the influence of material strain rate sensitivity, plastic responses are compared. All the comparisons presented below are between the average impact response and the average quasi-static response. Ratios of impact response to quasi-static response are presented to support the discussion in Chapter 8 on the prediction of impact response by quasi-static scaling.

### 5.6.1 Post-Buckle Hinge Response

Comparisons of post-buckle response were essentially comparisons of the buckle mechanism response. Buckle mechanism response was principally governed by buckle geometry and material properties and, as demonstrated in Section 5.4.2.1, was insensitive to the specific testing conditions. Conclusions regarding impact performance drawn from the cantilever tests conducted in this study are therefore also applicable to RHS tested in pure bending.

### 5.6.1.1 COMPARISON OF HINGE MOMENT

Figure 5.18 compares impact and quasi-static buckle mechanism $M$-$\theta$ responses. The increase in hinge moment under impact loading was due to the strain rate enhancement of material properties. The decrease in the ratio of impact moment to quasi-static moment during the collapse phase was due to the reduction in material strain rates that occurred as a consequence of changes in the geometry of the buckle and the reduction in loading rate. The strain rate enhancement of buckle mechanism moment capacity was a maximum of $\approx$ 1.16 at buckle initiation and decreased to a value of $\approx$ 1.05 at peak rotation, when $\theta_{pb}^{plas} \approx 0.54$ (31°).

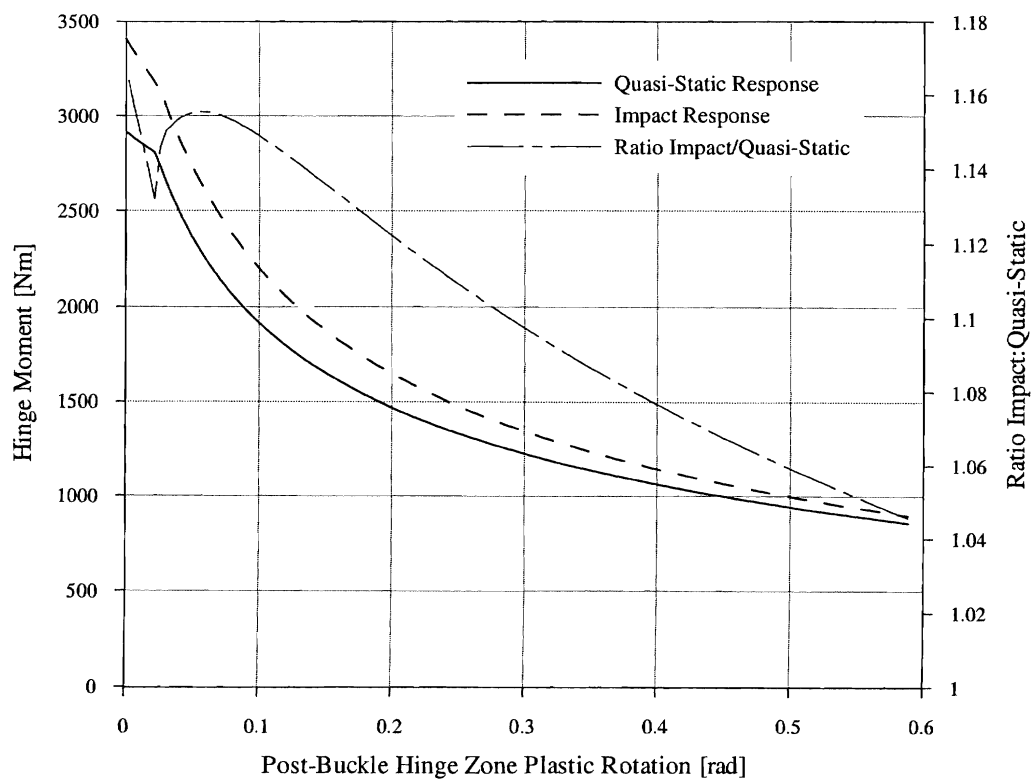


**Figure 5.18:** Quasi-static and impact comparison of buckle mechanism plastic $M$-$\theta$ response

Figure 5.19 compares plots of cumulated buckle mechanism energy. The decrease in the ratio of impact:quasi-static buckle mechanism energy with increasing $\theta$ was a reflection of the decrease in the ratio of impact:quasi-static hinge strength. In the transition phase, immediately after buckle initiation, the average ratio of impact:quasi-static buckle energy capacity was approximately 1.16. This ratio decreased almost linearly to approximately 1.12 at $\theta_{pb}^{plas} \approx 0.54$ (31°).

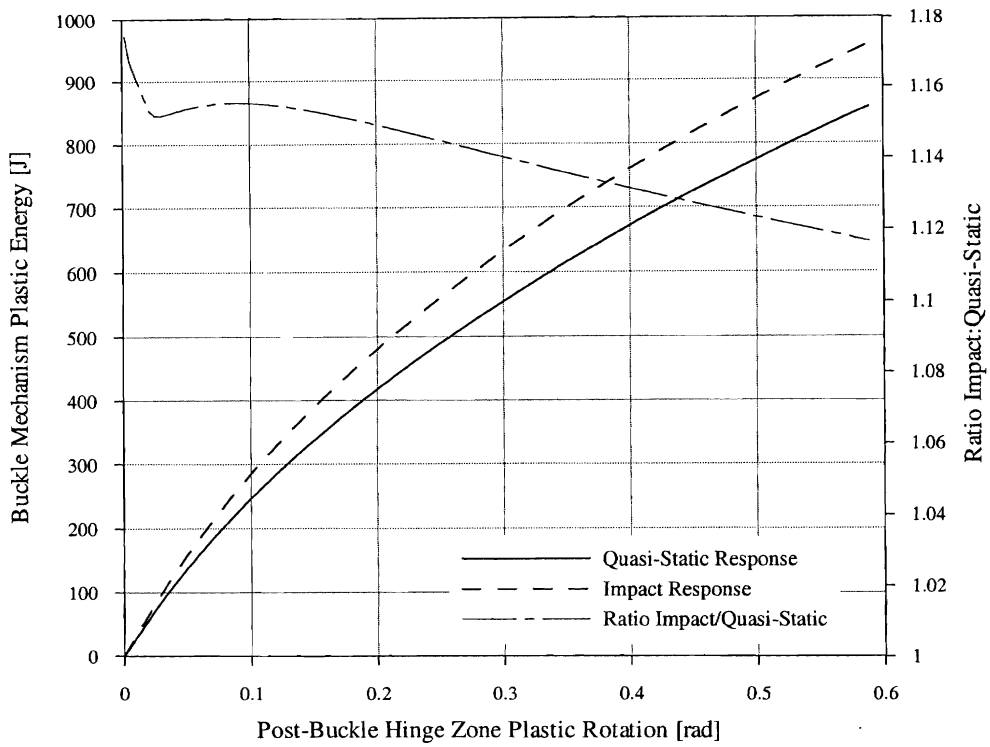


**Figure 5.19:** Quasi-static and impact comparison of buckle mechanism energy Vs plastic rotation

## 5.6.2 Pre-Buckle Hinge Response

A comparison of pre-buckle hinge $M$-$\theta$ response was essentially a comparison of the elastic-plastic beam response of the 85 mm hinge zone. For completeness, the pre-buckle responses are presented below, however, limited significance should be placed on the comparisons because of the difficulties involved in deriving pre-buckle impact response. The symbols mark the "instant" of buckle initiation. The average hinge zone plastic rotation at buckle initiation was 0.0409 radians, which was approximately 35% larger than measured under quasi-static loading.

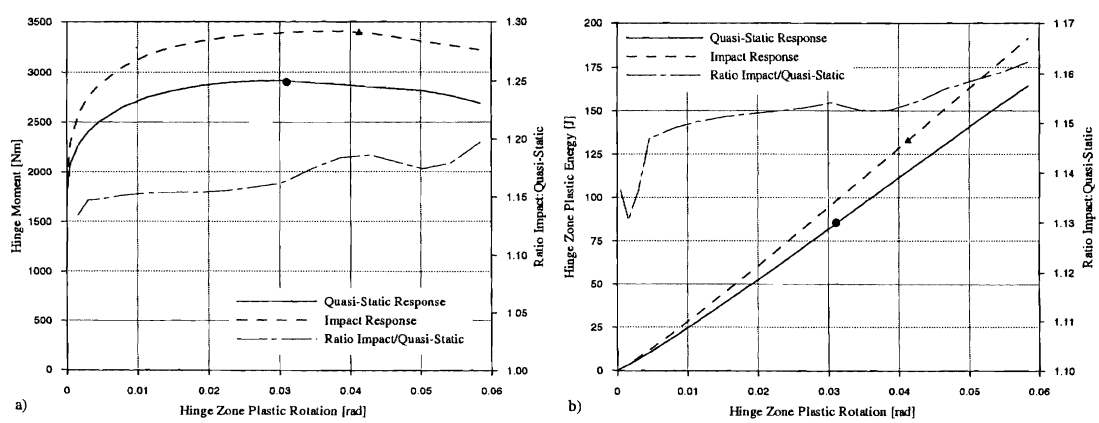


**Figure 5.20:** Quasi-static and impact comparison of a) hinge moment Vs pre-buckle plastic $\theta$ and b) cumulative hinge zone plastic energy Vs pre-buckle plastic $\theta$

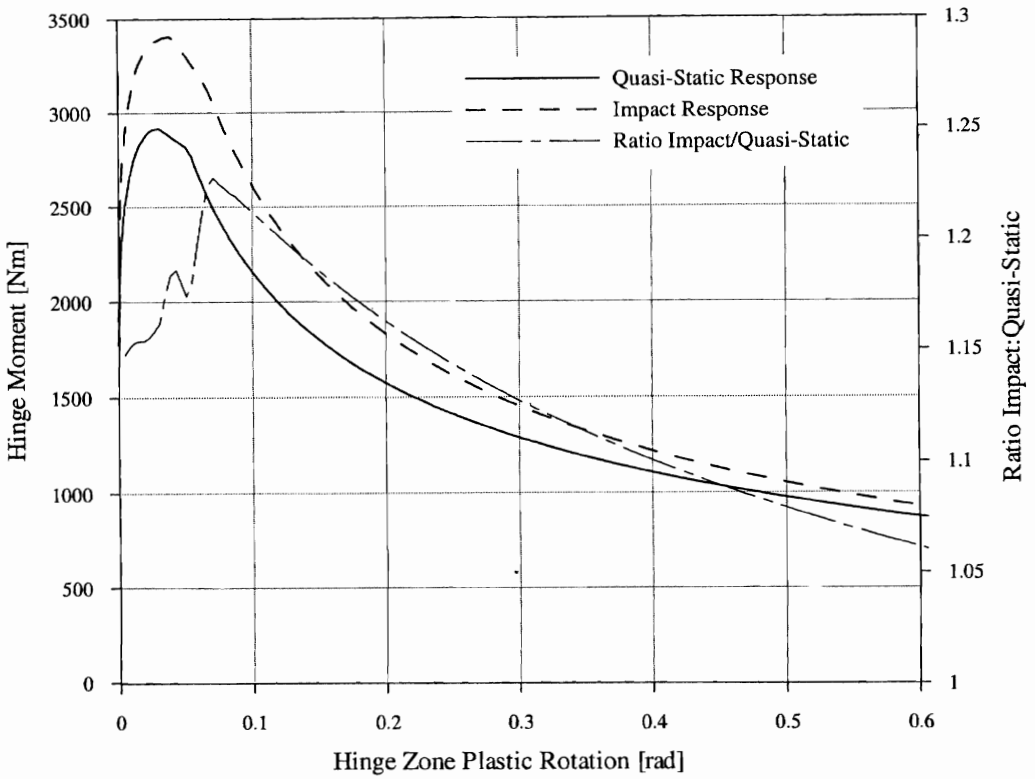


**Figure 5.21:** Quasi-static and impact comparison of hinge moment Vs hinge zone plastic rotation

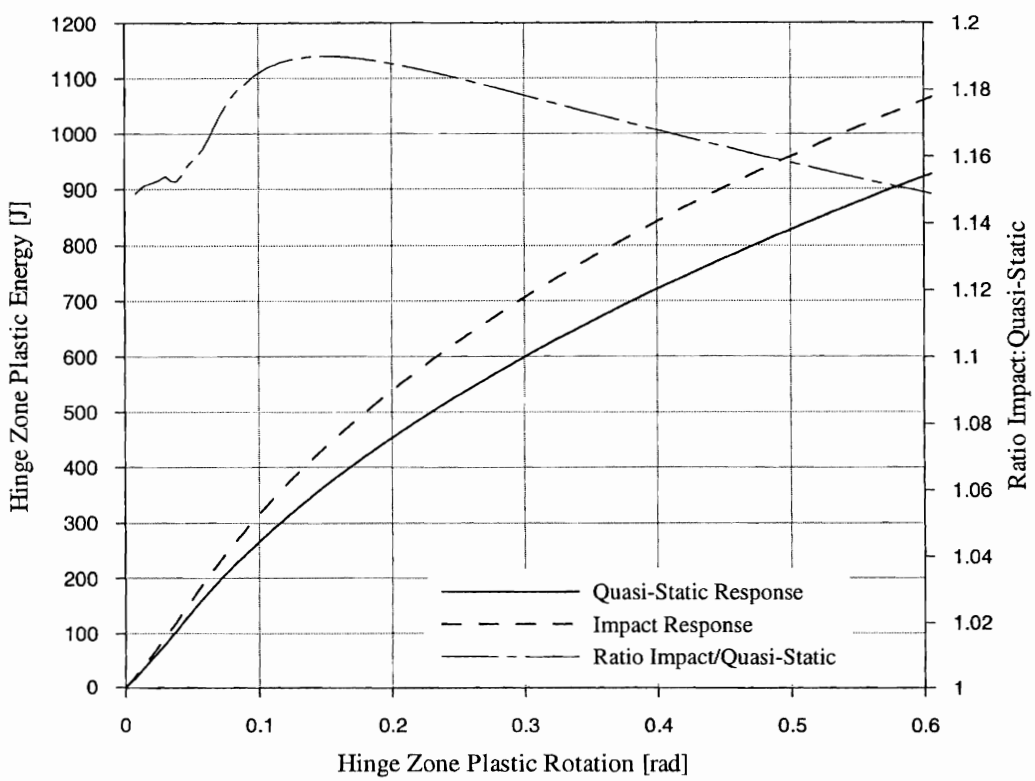


**Figure 5.22:** Quasi-static and impact comparison of hinge zone cumulative plastic energy Vs hinge zone plastic rotation

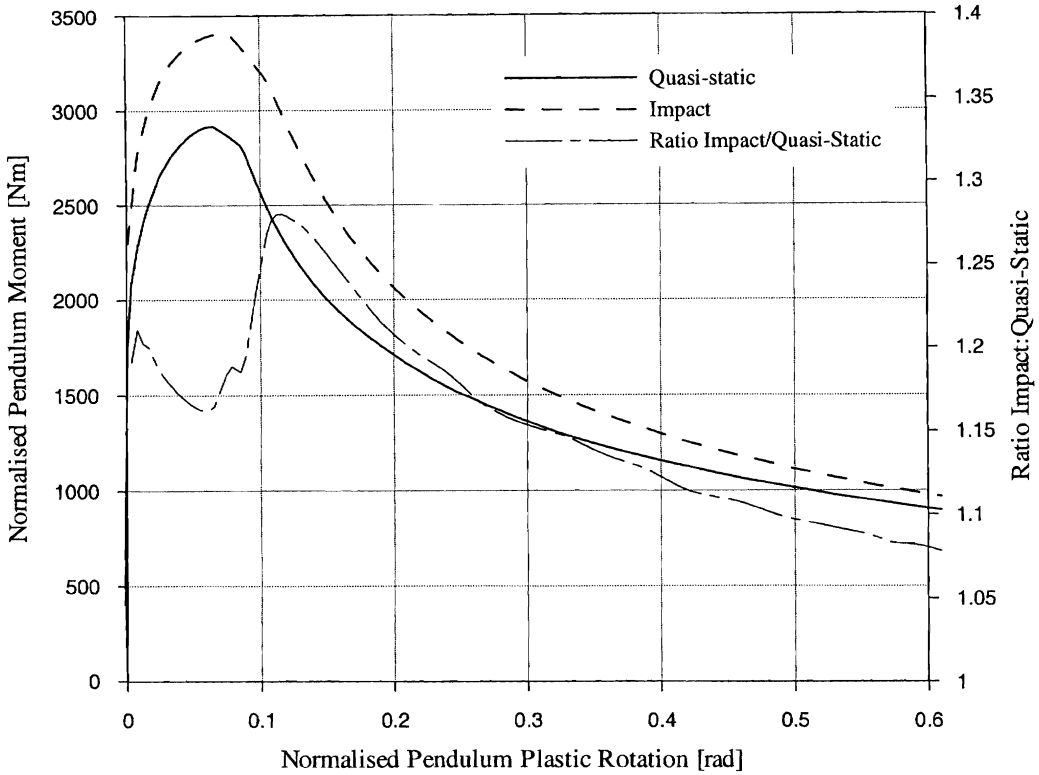


**Figure 5.23:** Quasi-static and impact comparison of pendulum moment Vs normalised pendulum plastic rotation

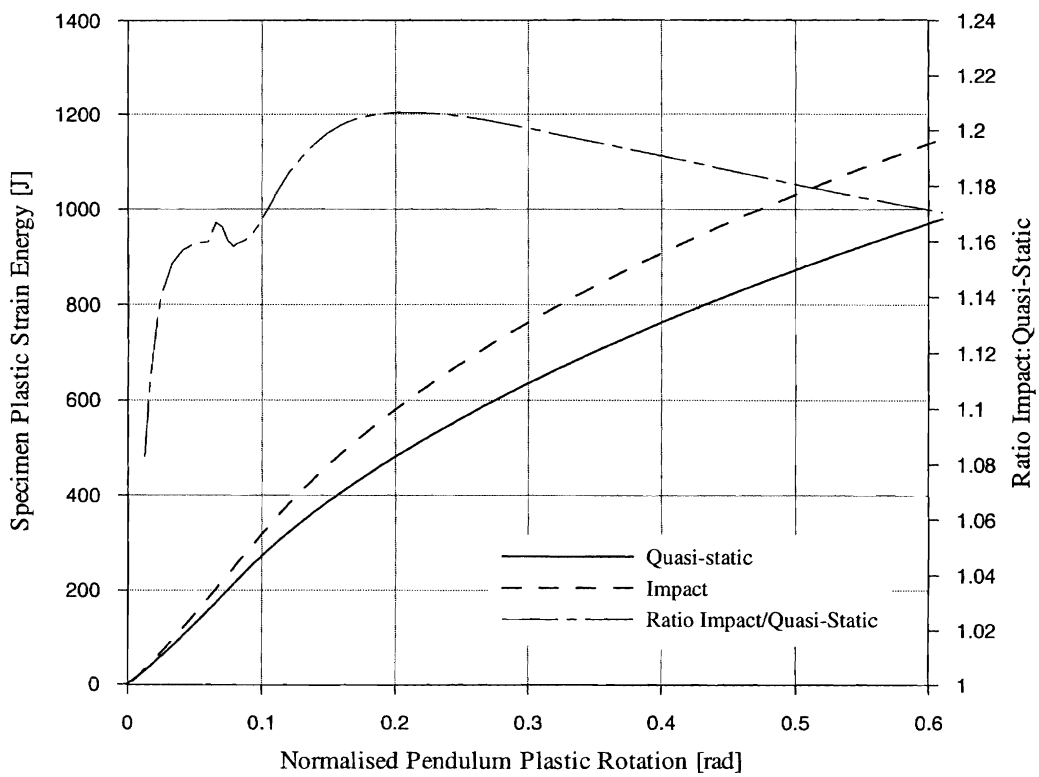


**Figure 5.24:** Quasi-static and impact comparison of cumulative specimen plastic strain energy Vs normalised pendulum plastic rotation

In the impact tests, pendulum moment derived from measured reaction force exhibited oscillations due to specimen vibration. These oscillations caused significant fluctuations in the calculated ratio of impact to quasi-static moment. To avoid these fluctuations pendulum moment in Figure 5.23 was interpolated from the average hinge moment in Figure 5.14. As a consequence, the impact to quasi-static ratio in the pre-buckle region was dependent on the nature of the pre-buckle moment response assumed for the average impact response, see Sections 5.5.5 and 5.4.4. Specimen strain energy in Figure 5.24 was the cumulative integral of the *moment-rotation* response plotted in Figure 5.23.

From Figure 5.24 the impact to quasi-static ratio (or dynamic factor) for specimen plastic strain energy at peak rotation ($\beta'_{plas} = 0.61$) was 1.17. The dynamic factor for pendulum plastic work at $\beta'_{plas} = 0.61$, derived from measurements of impact velocity and pendulum rotation, was 1.21. The value of 1.21 was considered to be the more accurate of the two ratios and is therefore quoted in all subsequent discussion regarding total specimen response.

In Section 5.6.3 the dynamic factor for hinge zone plastic energy, at the peak rotation, was determined to be 1.15. The increase in the dynamic factor when total specimen response is considered is a manifestation of the effect explained in Section 5.6.3. In Section 5.6.3 it was explained how the dynamic factors for response quantities that combine pre and post buckle phases are affected when the impact and quasi-static responses compared have different pre-buckle rotations.

Comparing impact loading to quasi-static loading, pre-buckle normalised pendulum plastic rotation was approximately 23% larger; the specimen material beyond the hinge zone absorbed 21% more plastic strain energy and material plasticity extended approximately 20% further along the specimen.

## 5.7 CONCLUSIONS

While significant difficulties caused by specimen vibrations and measurement system frequency response were experienced in this study, the procedures developed in Chapter 4 were used successfully to derive quasi-static and impact hinge $M$-$\theta$ responses from raw impact data.

A distinguishing aspect of this study was the measurement of plastic hinge $M$-$\theta$ response under both quasi-static and impact loading conditions. This enabled a direct assessment of the influence of material strain rate sensitivity on the strength and energy capacity of the buckle mechanism alone. These detailed test results are used in Chapter 7 to validate and calibrate FE models and in Chapter 8 to assess the performance of impact design schemes that scale a known quasi-static result.

Some specific results for the impact response relative to the quasi-static response of the 50x50x2 C350 RHS specimens tested in this study were:

- Maximum hinge moment increased by a factor of approximately 1.16.
- Total plastic strain energy absorbed by the buckle mechanism, at a mechanism plastic rotation of $\theta_{pb}^{plas} = 0.54$ (31°) increased by a factor of 1.12.
- Total plastic strain energy absorbed in the hinge zone i.e. combined pre-buckle and post-buckle response, at a hinge zone plastic rotation of $\theta_{plas} = 0.59$ (34°) increased by a factor of 1.15.
- Total plastic strain energy absorbed in the entire specimen at a pendulum plastic rotation of $\beta'_{plas} = 0.61$ (35°) increased by a factor of 1.21.

It was noted that the impact to quasi-static ratio (or dynamic factor) for gross energy absorbed by the specimen was larger than the dynamic factor for energy absorbed by the hinge zone, which was in turn larger than the dynamic factor for buckle mechanism energy. This was due to different distributions of plastic strain in the specimen under impact and quasi-static loading and has significant implications, discussed in Chapter 8, for the prediction of impact response by scaling a known quasi-static response.

Two further observations were:

- Hinge mechanism $M$-$\theta$ response was essentially unaffected by the test loading arrangement. Buckle mechanism response can therefore be considered to be a

property of the particular section and can be compared across different loading schemes. However, pre-buckle *moment-rotation* responses are dependent on the loading arrangement.

- Kecman's analytical model for buckle mechanism $M$-$\theta$ response should be assessed by comparison with experimental buckle mechanism $M$-$\theta$ responses using Kecman's original definition of buckle rotation, i.e. with buckle mechanism rotation measured from the point of buckle initiation rather than from the point of initial loading.

# CHAPTER 6 STRAIN RATE SENSITIVITY OF RHS MATERIAL

## 6.1 INTRODUCTION

The enhanced performance under impact loading of the RHS plastic hinge tested in Chapter 5 was primarily due to the effect of material strain rate sensitivity. For impact design purposes it is therefore essential to have an adequate model of RHS wall material strain rate sensitivity. However, whilst there are published experimental studies into the strain rate sensitivity of various steels at large strains (Campbell & Cooper 1966; Chatfield & Rote 1974; Wulf 1974; Davies & Magee 1975; Langseth et al. 1991; Kassar & Yu 1992; Shi & Meuleman 1995), the author could not discover published test data for the strain rate sensitivity of the material in cold-rolled tube walls, at small or large strains. This is despite a large body of research into the impact response of tubular sections. Furthermore, given the significant amount of cold work that is done during the manufacture of RHS, it was concluded that the strain rate sensitivity of RHS wall material would likely be different to that of the steels tested in published studies.

Many researchers and designers use the Cowper–Symonds constitutive model (Bodner & Symonds 1962), to predict the increase in strength and energy capacity of mild steels, including the material in RHS, at elevated strain rates. Commonly the values of 40.4 $s^{-1}$ and 5 are substituted in this model for the coefficients $D$ and $q$, respectively. However, because the values $D$ = 40.4 $s^{-1}$ and $q$ = 5 were derived from a curve fit to lower yield stresses, the use of this coefficient set in crashworthiness applications, where the strains are typically greater than 50%, has been questioned in the literature. Abramowicz and Jones (1986) proposed Cowper–Symonds coefficients of $D$ = 6,844 $s^{-1}$ and $q$ = 3.91 to describe the strain rate sensitivity of mild steel at large strains. Commenting on the appropriate choice of coefficients, Abramowicz and Jones remarked that the disparity between the predictions of different coefficients sets *"... emphasises the lack of adequate experimental data on the dynamic plastic behaviour of materials with large strains which are encountered in the dynamic progressive crushing of square tubes."*. Some eleven years later Jones (1999) again referred to the, *"paucity of available*

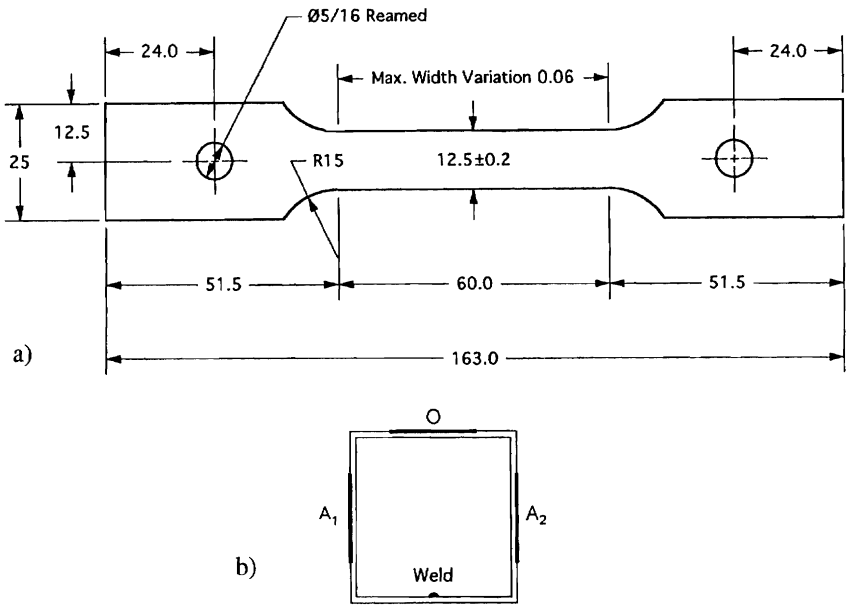


**Figure 6.1:** Uni-axial tensile coupons a) geometry and b) coupon locations around the tube section

## 6.2.2 Choice of Strain Rates and Testing Machines

A detailed finite element model simulating the deep collapse of a local buckle indicated that for an impact velocity typical of the rotation rates experienced in a roll-over accident, the peak strain rate in the buckle was 32 $s^{-1}$ (See Section 7.3.3.5). Based on this information, the desired strain rate range was from nominally quasi-static to 30 $s^{-1}$. However, limitations of the available testing equipment restricted the upper strain rate to nominally 10 $s^{-1}$. This limitation was not considered significant because the same FE analysis also indicated that the strain rate peak was very localised and that by the mid stages of collapse, around $\theta = 20°$, strain rates throughout the buckle were typically less than 10 $s^{-1}$. Furthermore, an energy-weighted average strain rate, calculated over the buckle, had a maximum value of 11.5 $s^{-1}$. The four target strain rates were therefore chosen to be $10^{-4}$, $10^{-2}$, 1 and 10. The actual strain rates achieved were a function of the test equipment and coupon geometry.

For a nominal gauge length of 60 mm strain rates of the order of 10 $s^{-1}$ required a crosshead velocity of approximately 600 $mms^{-1}$. Unfortunately, a tensile testing apparatus capable of this extension rate was not available. Therefore fixtures were designed and procedures developed whereby a servo-hydraulic uniaxial shake table, located in the university's civil engineering laboratories, could be used to perform elevated strain rate tensile tests. Plate 6.1 shows the fixtures in place on the shake table. This apparatus was used to conduct the tests at the two highest strain rates. A hydraulic

50 tonne Shimadzu universal-testing machine was used to conduct the tests at the two lowest strain rates.

## 6.2.3 High Strain Rate Tests – Shake Table

### 6.2.3.1 GRIPS

A pair of special purpose friction grips was machined for these tests. Whilst the grips were intended to transfer load via friction, slip occurred until almost all load was transmitted by bearing against the clamping bolt. Inspection of the coupon after testing revealed only slight plastic deformation over the bearing zone. This slight deformation was considered acceptable because coupon strain was measured using strain gauges attached to the coupon.

One grip was "fixed" and reacted the load to the concrete floor adjacent to the table via a thick walled SHS. This fixed grip also incorporated a pre-loaded piezoelectric load washer that measured the tensile load. The second grip travelled with the shake table, thereby applying an enforced extension to the coupon.

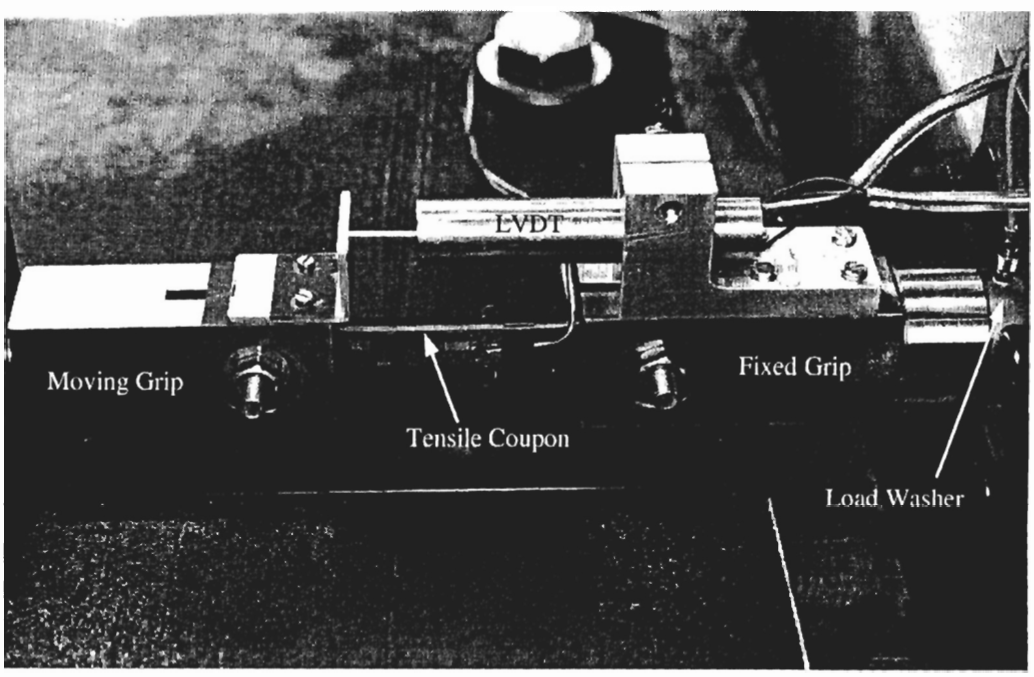


**Plate 6.1a:** Tensile test fixtures in place on the shake table

Close-up before testing

#### 6.2.3.2 LOAD TAKE-UP SYSTEM

The load take-up system designed for this test provided 50 mm free travel of the shake table before loading the coupon. This period of free travel was required to allow the table to accelerate to the programmed test velocity. The load take-up system also provided important guidance for the coupon. Because of the significant initial curvature of the coupon it was important to ensure that the coupon was held straight before the tensile load was applied. If this guidance were not provided, bending vibrations would have been set up in the coupon when the load was suddenly applied.

A thin nylon washer was placed on the contact face to dampen the sudden contact between the steel surfaces, Meyer and Schrödter (1999). However, analysis of the results from the first series of highest rate tests showed that the compressibility of this washer delayed the beginning of the constant loading rate. The washer was therefore replaced in the second series of tests with a thin layer of PVC insulation tape.

#### 6.2.3.3 SHAKE TABLE DRIVE PROFILE

The basic specifications of the shake table installed at UTS are shown in Figure 6.2. The table is controlled by a closed loop dual-stage servo valve system and can be programmed to follow an arbitrary displacement history. The maximum constant table velocity that could be obtained, after 50 mm ramp up travel, was approximately 560 $mms^{-1}$.

The required *displacement-time* drive profiles for the tensile tests were derived by firstly defining the velocity history then integrating to obtain displacement. A typical velocity time history is shown in Figure 6.3. The associated displacement and acceleration histories are also shown.

The test region of the profile consisted of three phases. Phase I was a smooth ramp up to the desired test velocity. The test velocity had to be attained within 50 mm travel, as this was the maximum free travel accommodated by the load take up system. Phase II was a period of constant velocity during which the coupon was loaded. This phase had to extend long enough to ensure that the coupon was strained to failure. Phase III was a ramp down to zero velocity. The total travel for the entire test could not be greater than 125 mm. A short MATLAB script was coded which generated a text drive file from the

following parameters: ramp up travel; test velocity; test travel; ramp down travel; and sample rate. The parameters used for the tests were as follows.

The drive profile defined the relative displacement of the shake table from the table starting or "home" position. The absolute table position, ± 100 mm, was obtained by manually adding an offset using the analogue controller. This offset was adjusted to accommodate the specimen size.

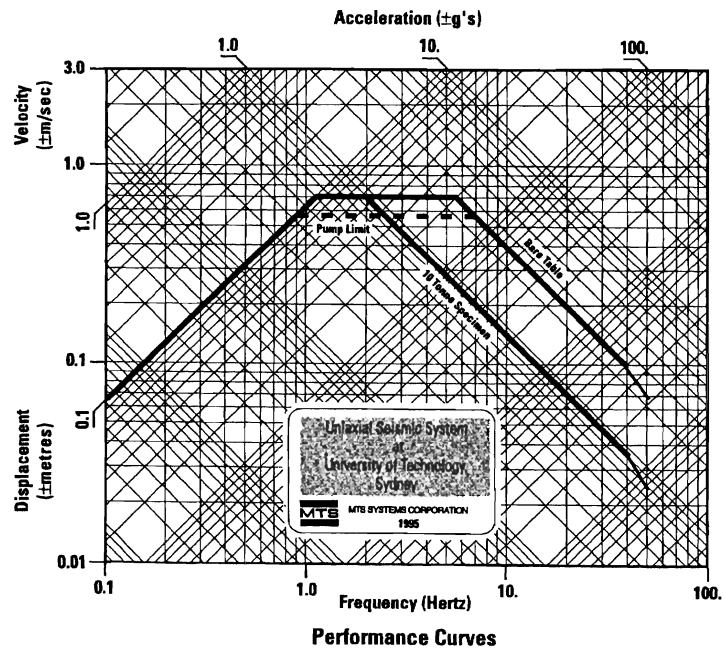


| Table of Specifications | |
|---|---|
| Size | 3.0 m x 3.0 m |
| Maximum Specimen Weight | 10 tonnes |
| Overturning Moment | 100 kNm |
| Displacement | ± 100 mm |
| Maximum Velocity | ± 550 mm/sec |
| Acceleration | 0.9g's (with 10 tonne specimen) |
| Waveform | Regular or irregular |
| Testing Frequency | 0.1 to 50 Hz |

**Figure 6.2:** Shake table specifications

**Table 6.1:** Shake table drive profile parameters

| *Nominal Strain Rate = 10 $s^{-1}$* | |
|---|---|
| Ramp up travel = 48 mm | Ramp Down Travel = 42 mm |
| Test Velocity = 600 mm/sec. | Test Travel = 30 mm |
| Sampling Rate = 1000 samples/sec. | Dwell Time = 5 sec. |
| Return Time = 15 sec. | |
| *Nominal Strain Rate = 1 $s^{-1}$* | |
| Ramp up travel = 48 mm | Ramp Down Travel = 42 mm |
| Test Velocity = 60 mm/sec. | Test Travel = 30 mm |
| Sampling Rate = 100 samples/sec. | Dwell Time = 5 sec. |
| Return Time = 15 sec. | |

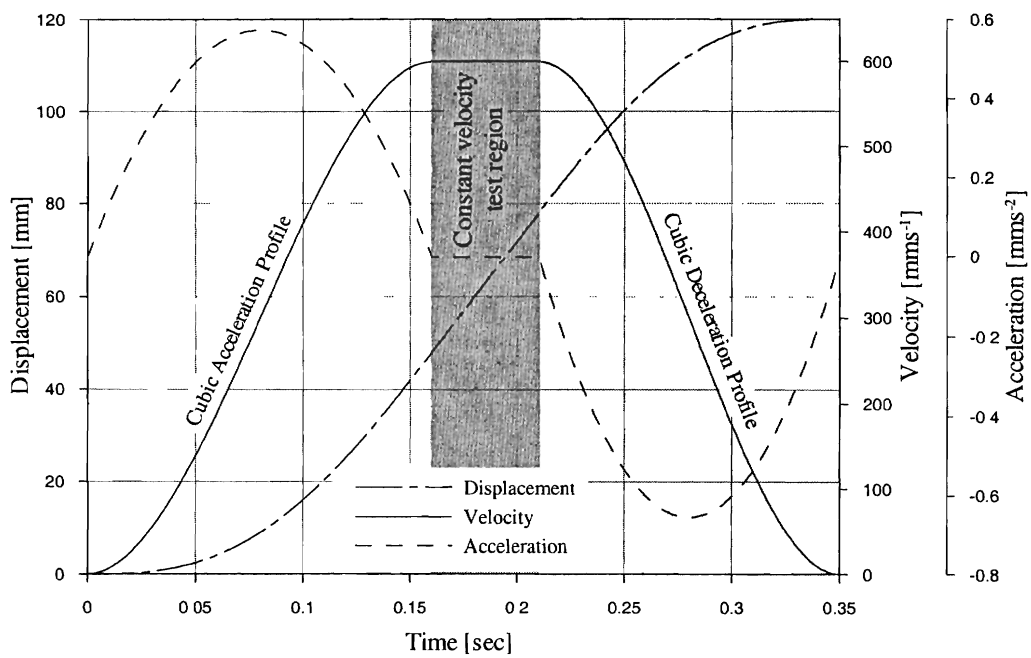


**Figure 6.3:** Displacement-time drive profile, Velocity and Acceleration time histories for highest rate shake table tests

## 6.2.4 Low Strain Rate Tests – Shimadzu Universal Testing Machine

For the low strain rate tests, $10^{-4}$ and $10^{-2}$ $s^{-1}$, a Shimadzu REH 50 universal testing machine was utilised. Although a maximum load capacity of only 2 tonnes was required, the 50 tonne machine was selected for its maximum loading rate. Loading on this machine is manually controlled via a needle valve. Tests were conducted to determine the approximate relationship between control valve position and loading rate. This relationship appeared to be insensitive to load, at least the small loads required for this test, but was affected by oil temperature. The fastest tests were conducted with the

control valve fully open, the slowest tests were conducted with the valve set to give a crosshead rate of approximately 0.9 mm per minute.

## 6.2.5 Instrumentation

### 6.2.5.1 STRAIN

The release of residual stresses when the coupons were cut from the RHS walls caused curvature in the coupons of between 1/750 and 1/1100 $mm^{-1}$. The curvature in a typical coupon is shown in Plate 6.2. This curvature made the use of standard knife-edge extensometers difficult and led to unavoidable inaccuracies in the measured *stress-strain* curve, see Section 6.3.1. To overcome this difficulty and to provide strain signals through to failure, high-elongation uniaxial strain gauges (Measurements Group type EP-08-250BG-120 with no options), were glued to each coupon in its curved state. The gauges were located at the centre of the parallel length and were oriented along the axis of the coupon. Two independent gauges were attached to each coupon, one on each side. In all tests, strain gauge integrity was maintained to beyond ultimate tensile strength (UTS). This often represented strain measurements of 15% and could exceed 20% when the coupon necked on or near the gauge.

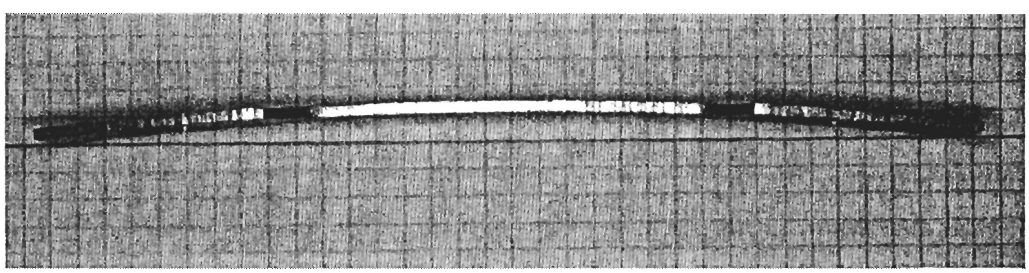

**Plate 6.2:** Initial curvature in a typical tensile coupon

Considerable time was spent testing various techniques before surface preparation and strain gauge attachment procedures were developed that produced reliable strain measurements. These procedures are discussed in Section 6.2.6.

### 6.2.5.2 DISPLACEMENT

Grip displacement was recorded using a Transtek 25 mm stroke DC LVDT. For the shake table tests this transducer was mounted between the two coupon grips, see Plate 6.1a. For the low rate tests conducted in the Shimadzu, the same LVDT measured crosshead travel. This transducer had a stated frequency response of approximately -3 dB at 110 Hz that is limited by the internal low-pass filter circuitry used to remove

separate strain gauged load cell was used to measure load in all the Shimadzu tests. This load cell was mounted in series with the grip fixtures and was loaded in compression.

#### 6.2.5.4 DATA ACQUISITION

The four signals, load, displacement and two strains, were recorded using a Yokogawa Analysing Recorder Model AR1200. This instrument performs 14bit A/D conversion at rates up to 100 kHz per channel. The strain gauges were wired as two independent three wire ¼ bridge circuits. Bridge completion for each strain circuit was provided remote to the strain gauge, within a National Instruments SCXI 1121 module. This module also provided input isolation, amplification and filtering. These modules did not provide bridge balancing, however, because the strains being measured were very high, approximately 15%, balancing was considered unnecessary. Each strain signal was connected to two input channels of the Yokogawa, the second channel having an input range ten times smaller than the first channel. Thus, the initial elastic response of the coupon could be measured at a resolution ten times finer than would have been possible if a single input channel had been used.

The high level LVDT and load signals were also fed through the SCXI 1121 module, with gain set at unity. This was done, in the case of the LVDT signal, to filter out a 13 kHz noise component and in the case of the load signal, to maintain a similar signal path.

The sampling rate and anti-alias filtering used for each strain rate range are given below.

**Table 6.2:** Sampling rate and filter settings used for material tests

| Nominal Strain Rate sec | Sampling Frequency Hz | SCXI 1121 Filter Setting Hz | Anti-alias Cut-off Frequency Hz |
|---|---|---|---|
| 10 | 50,000 | 10,000 | 20,000 |
| 1 | 5,000 | 10,000 | 2,000 |
| $10^{-2}$ | 500 | 10,000 | 200 |
| $10^{-4}$ | 5 | 4 | 40 |

### 6.2.6 High-Elongation Strain Gauging

High-elongation strain measurements place severe demands on gauge installation, and necessitate special gauge and adhesive selection and surface preparation procedures. Several Measurements Group technical notes discuss high-elongation strain gauging installation techniques. These include B-129, TT-605, TT-609 and TT-610, together with the various adhesive instruction bulletins. Considerable time was spent testing the techniques described in the Measurements Group literature before procedures were established that produced reliable results for the current application. The major aspects of these procedures are summarised below. Further details are given in Appendix B.

- Measurements Group EP series high-elongation gauges were selected. To maximise the elongation capability of these gauges, no leadwire attachment options were specified.
- The coupon surface was hand abraded in a cross-hatched pattern using 40 grit aluminium oxide paper.
- Gauges were bonded using Measurements Group A-12 adhesive. This adhesive was cured for 2 hours at a glue-line temperature of 74°C under a clamping pressure of 70 to 85 N/mm$^2$.
- Signal wires were attached to the installed gauges using the wiring recommendations in TT-605 using large strain relief loops and minimal solder.

The final gauge installation is shown in Plate 6.3 below.

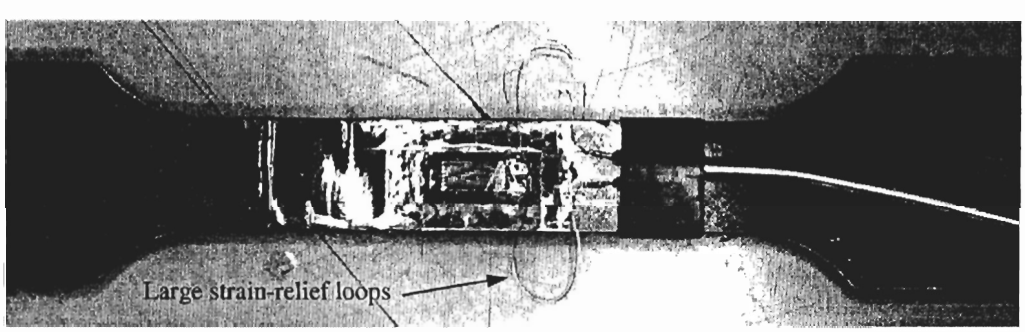


**Plate 6.3:** Large strain relief loops on tensile coupons

An additional concern when measuring strains greater than a few percent was the need to correct for errors and non-linearities in the relationship between measured bridge output voltage and actual strain. The two major sources of non-linearity were Wheatstone bridge and gauge factor non-linearities. These errors and practical

For this investigation into the effect of curvature, an *engineering stress Vs engineering strain* curve was assumed and the *engineering stress Vs engineering strain* curve that would be measured in a test was calculated by integrating stress through the coupon thickness, assuming a linear strain distribution. Figure 6.4 compares the actual material curve with the "measured" curve, assuming an initial radius of curvature of 734 mm and surface strain of 0.13%. These were the worst case values measured for the C350LO material.

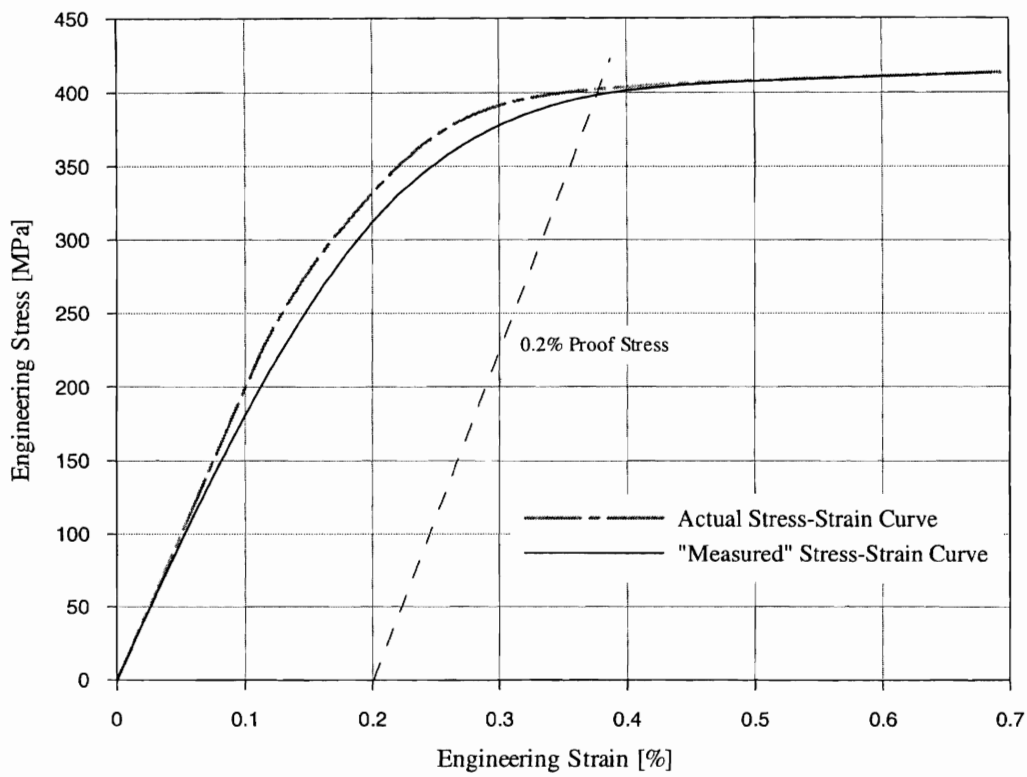


**Figure 6.4:** Effect of coupon curvature on measured engineering stress Vs engineering strain curve

As long as the strains through the coupon thickness were all elastic, the two responses were equal. However, when the tension side of the coupon yielded, the two curves began to deviate. This was because equal increments of strain produce different increments of stress on the compression and tension faces. This deviation gave the appearance of a reduced proportional limit. As the plastic strain increased the *stress-strain* curve could be considered linear over a $\Delta$ strain range of 0.26% (i.e. the strain variation between the two faces of the coupon) and the "actual" and "measured" curves again became coincident.

### 6.3.6 Plastic Log Strain

The majority of the results and discussion below consider plastic log strain. This is because crashworthiness design calculations often neglect elastic strains and because the test data was intended for use in a finite element code which required that material properties be defined as true stress Vs plastic log strain.

### 6.3.7 Plastic Strain Energy Density to UTS

The plastic energy capacity of a material is of fundamental importance in crashworthiness design calculations. The plastic strain energy density at UTS was calculated, for the volume of material over the length of the strain gauge grid, as the area under the *true stress V plastic log strain* curve up to UTS.

### 6.3.8 Strain Rate and Crosshead Velocity

Strain rate was calculated by taking the first order difference of plastic log strain, then low-pass filtering the result. The cut-off frequency for the filter operation was carefully chosen to remove only the high frequencies created by differentiating the digitised strain signal. A similar process was used to calculate crosshead velocity from crosshead displacement.

## 6.4 RESULTS

A total of twelve tensile coupons were tested for each grade of RHS, three coupons (one from each Face $A_1$, $A_2$ and O), at each of four nominal cross head velocities. Test results are presented in Table 6.3a and Table 6.3b for grade C350LO and DuraGal, respectively. Because there was no physical distinction between faces $A_1$ and $A_2$, the results from these faces were averaged to give a singe result for the material in the tube walls adjacent to the seam weld. This averaged result was designated as Face A. Data for coupon C350LO – $A_2$ at the nominal strain rate of $10^{-4}$ was lost. The results quoted for C350LO Face A at the nominal strain rate of $10^{-4}$ therefore represent the results of the single coupon C350LO – $A_1$.

*True stress Vs plastic log strain* curves, derived for use in a detailed finite element model, are shown in Figure 6.5.

**Table 6.3a:** Mechanical properties for grade C350LO RHS wall material

| Location around RHS | Nominal Strain Rate [$sec^{-1}$] | Average Plastic Strain Rate [$s^{-1}$] | Lower Yield [MPa] | UTS [MPa] | Young's Modulus [GPa] | Uniform Strain | Ext. from 3% $\varepsilon$ to Failure [mm] | Strain Energy Density† [$J/mm^3$] |
|---|---|---|---|---|---|---|---|---|
| Face A | 10 | 7.0 | 501.1 | 558.6 | 200.3 | 9.31% | 13.10 | 56.8E-3 |
| | 1 | 0.86 | 464.5 | 533.7 | 202.8 | 9.75% | 13.09 | 53.9E-3 |
| | $10^{-2}$ | 2.1E-02 | **425.0**‡ | 498.4 | 202.1 | 9.53% | 10.91 | 50.4E-3 |
| | $10^{-4}$ | 2.2E-04 | **403.6** | 468.2 | 204.6 | 13.00% | 11.92 | 47.6E-3 |
| Face O | 10 | 7.8 | 528.2 | 575.3 | 213.7 | 7.20% | 10.91 | 58.9E-3 |
| | 1 | 0.80 | 478.8 | 536.6 | 201.8 | 7.05% | 10.19 | 54.9E-3 |
| | $10^{-2}$ | 2.0E-02 | **438.0** | 499.8 | 200.7 | 7.11% | 10.58 | 51.2E-3 |
| | $10^{-4}$ | 2.4E-04 | **425.7** | 475.9 | 205.8 | 5.70% | 9.86 | 49.1E-3 |

† Average plastic strain energy density over gauge grid, at 10% plastic log strain.

‡ Bold indicates 0.2% Proof Stress.

**Table 6.3b:** Mechanical properties for DuraGal RHS wall material

| Location around RHS | Nominal Strain Rate [$sec^{-1}$] | Average Plastic Strain Rate [$s^{-1}$] | Lower Yield [MPa] | UTS [MPa] | Young's Modulus [GPa] | Uniform Strain | Ext. from 3% $\varepsilon$ to Failure [mm] | Strain Energy Density† [$J/mm^3$] |
|---|---|---|---|---|---|---|---|---|
| Face A | 10 | 8.0 | 534.8 | 596.8 | 204.6 | 8.59% | 10.08 | 46.2E-3 |
| | 1 | 0.85 | **498.8**‡ | 581.3 | 202.9 | 8.20% | 8.99 | 44.9E-3 |
| | $10^{-2}$ | 2.2E-02 | **450.2** | 531.6 | 196.4 | 7.86% | 8.12 | 41.1E-3 |
| | $10^{-4}$ | 2.5E-04 | **438.8** | 512.2 | 204.1 | 6.89% | 6.95 | 40.0E-3 |
| Face O | 10 | 8.8 | 594.7 | 629.6 | 210.0 | 5.59% | 8.92 | 49.8E-3 |
| | 1 | 1.0 | **553.6** | 601.6 | 198.0 | 5.70% | 6.27 | 47.5E-3 |
| | $10^{-2}$ | 2.1E-02 | **517.9** | 565.4 | 203.8 | 4.48% | 5.40 | 44.8E-3 |
| | $10^{-4}$ | 2.6E-04 | **504.5** | 545.4 | 184.5 | 4.36% | 5.44 | 43.3E-3 |

† Average plastic strain energy density over gauge grid, at 7.8% plastic log strain.

‡ Bold indicates 0.2% Proof Stress.

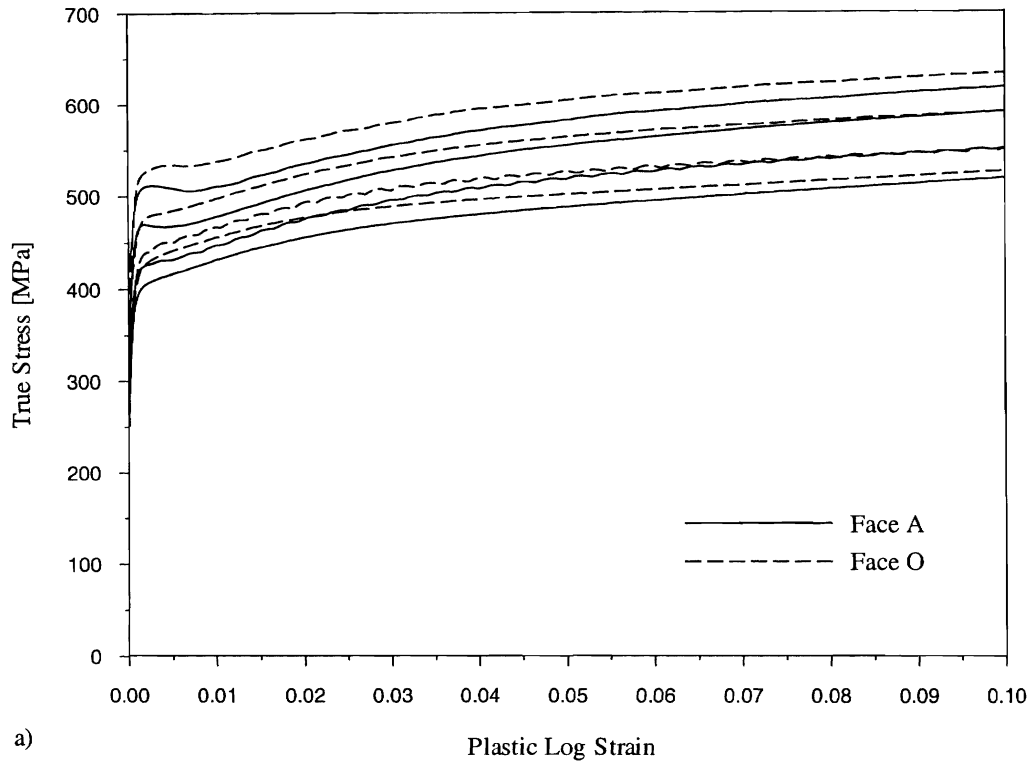


a)

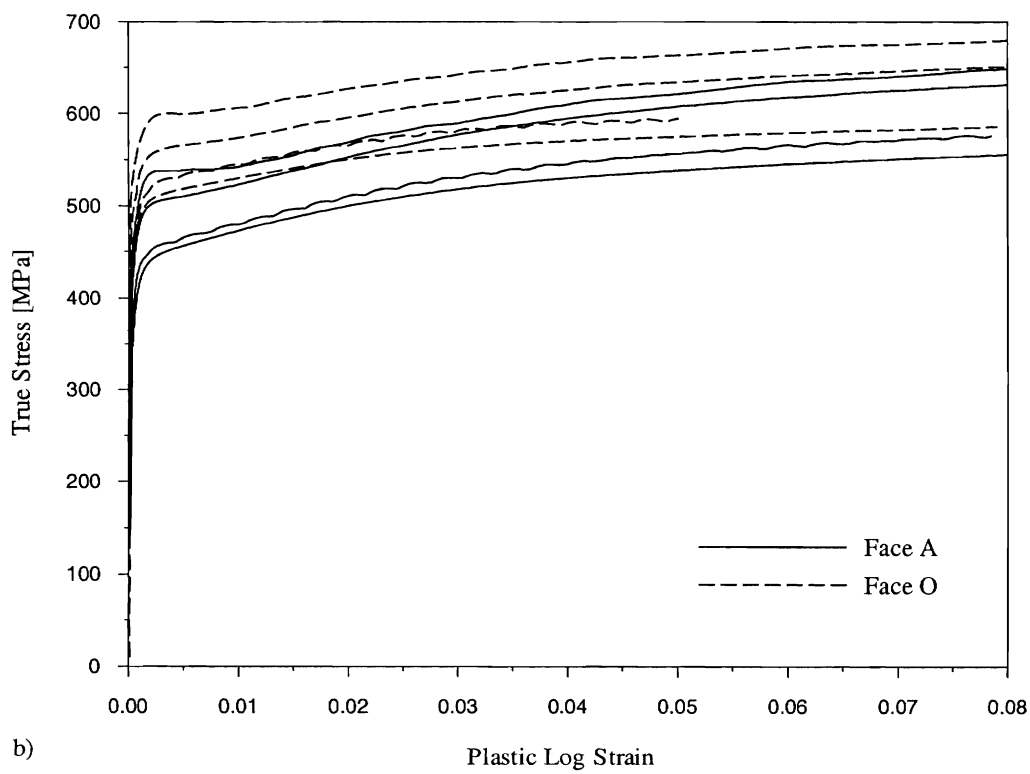


b)

**Figure 6.5:** True stress Vs plastic log strain for RHS wall material

a) Grade C350LO RHS, b) DuraGal RHS

In both graphs, the higher the strain rate the higher the stress-strain curve.

## 6.5 DISCUSSION

### 6.5.1 Coupon Curvature and Residual Stress

As discussed in Section 2.6.2, a feature of cold-formed hollow sections is the presence of residual stresses that result from the forming process. When the coupons were machined out of the RHS the longitudinal and transverse residual stresses were "released". This caused appreciable curvature to develop in the coupons as shown in Plate 6.2. The radius of curvature of each specimen was measured using a co-ordinate measuring machine, to obtain an indication of the magnitude of the longitudinal residual bending stress. These radii are listed in Table 6.4, together with the equivalent surface strain. Table 6.4 also lists the measured surface strain of the clamped "straightened" coupon. It was apparent from the ratio of predicted and measured strains that clamping the coupons did not always fully straighten them and that the shake table fixtures provided greater restraint than the Shimadzu fixtures. Face O for the DuraGal coupons showed consistently less curvature than Face A. No such trend is apparent for the C350LO coupons. Considering Face A only, the predicted residual stresses are approximately 57% of the respective quasi-static lower yield stress for both material grades.

**Table 6.4a:** Grade C350LO coupon curvature and residual stress

| Nominal Strain Rate [$sec^{-1}$] | Location | Measured Radius | Predicted Residual | | Clamped | | Equivalent Radius | Strain Ratio |
|---|---|---|---|---|---|---|---|---|
| | | | Strain | Stress | Strain | Stress | | Measured: Predicted |
| 10 | Face A | 838 | 0.112% | 226.7 | 0.110% | 222.7 | 852 | 0.986 |
| | Face O | 738 | 0.127% | 258.2 | 0.127% | 258.2 | 743 | 1.000 |
| 1 | Face A | 867.5 | 0.107% | 216.5 | 0.108% | 219.6 | 870.5 | 1.012 |
| | Face O | 735 | 0.131% | 266.3 | 0.127% | 258.2 | 758 | 0.969 |
| $10^{-2}$ | Face A | 809.5 | 0.115% | 232.8 | 0.079% | 160.6 | 1173 | 0.692 |
| | Face O | 769 | 0.124% | 252.1 | 0.098% | 199.2 | 974 | 0.790 |
| $10^{-4}$ | Face A | 761 | 0.122% | 248.0 | 0.105% | 213.5 | 882 | 0.861 |
| | Face O | 744 | 0.127% | 258.2 | 0.101% | 205.3 | 933 | 0.795 |

Note: Stresses were calculated from measured strain assuming E = 203.3 MPa.

**Table 6.4b:** DuraGal coupon curvature and residual stress

| Nominal Strain Rate [$sec^{-1}$] | Location | Measured Radius | Predicted Residual | | Clamped | | Equivalent Radius | Strain Ratio |
|---|---|---|---|---|---|---|---|---|
| | | | Strain | Stress | Strain | Stress | | Measured: Predicted |
| 10 | Face A | 750 | 0.125% | 254.0 | 0.124% | 251.7 | 761 | 0.989 |
| | Face O | 1024 | 0.093% | 188.8 | 0.082% | 166.7 | 1159 | 0.883 |
| 1 | Face A | 733 | 0.127% | 258.2 | 0.124% | 252.9 | 749 | 0.980 |
| | Face O | 1146 | 0.083% | 168.6 | 0.072% | 147.4 | 1312 | 0.874 |
| $10^{-2}$ | Face A | 790 | 0.120% | 244.5 | 0.094% | 191.4 | 1028 | 0.778 |
| | Face O | 1034 | 0.092% | 188.4 | 0.072% | 147.0 | 1328 | 0.780 |
| $10^{-4}$ | Face A | 735 | 0.128% | 259.9 | 0.105% | 214.2 | 895 | 0.824 |
| | Face O | 1077 | 0.088% | 179.4 | 0.059% | 120.7 | 1602 | 0.673 |

Note: Stresses were calculated from strain assuming E = 203.9 MPa

## 6.5.2 Variation of Mechanical Properties around the Section

Comparison between the *stress-strain* curves for Faces A and O showed that yield stress and UTS from Face O were consistently higher than from Face A, whilst uniform strain and total extension were much reduced at Face O. This variation of material properties around the tube section suggested that the material opposite the seam weld had undergone more cold work during tube manufacture, and was consistent with previous material tests conducted by Zhao and Hancock (1995).

## 6.5.3 Variation of Strain Rate with Strain

Figure 6.6 shows the variation of strain rate and equivalent crosshead strain rate with engineering strain from a tensile test with a nominal strain rate of $10^{-4}$ $s^{-1}$. Crosshead velocity was approximately constant for the duration of the test, however strain rate peaked sharply in the early stages of the test then increased steadily for the remainder of the test. The peak in strain rate was sharpest at the highest strain rates, while the subsequent increase in strain rate with coupon strain was most significant at the lowest strain rates. This behaviour was also observed in a FE simulation of the tensile test. (The results of this FE investigation are discussed in Section 6.5.6.). It is generally accepted that strain rate sensitivity is an "order of magnitude" effect (see Section 6.5.4.8). Therefore strain rate was plotted on a logarithmic scale, Figure 6.7. It is seen that the logarithm of strain rate was essentially constant over the region from 1% to UTS. Therefore, for the purpose of comparison the average strain rate over this region was quoted as the strain rate for the test.

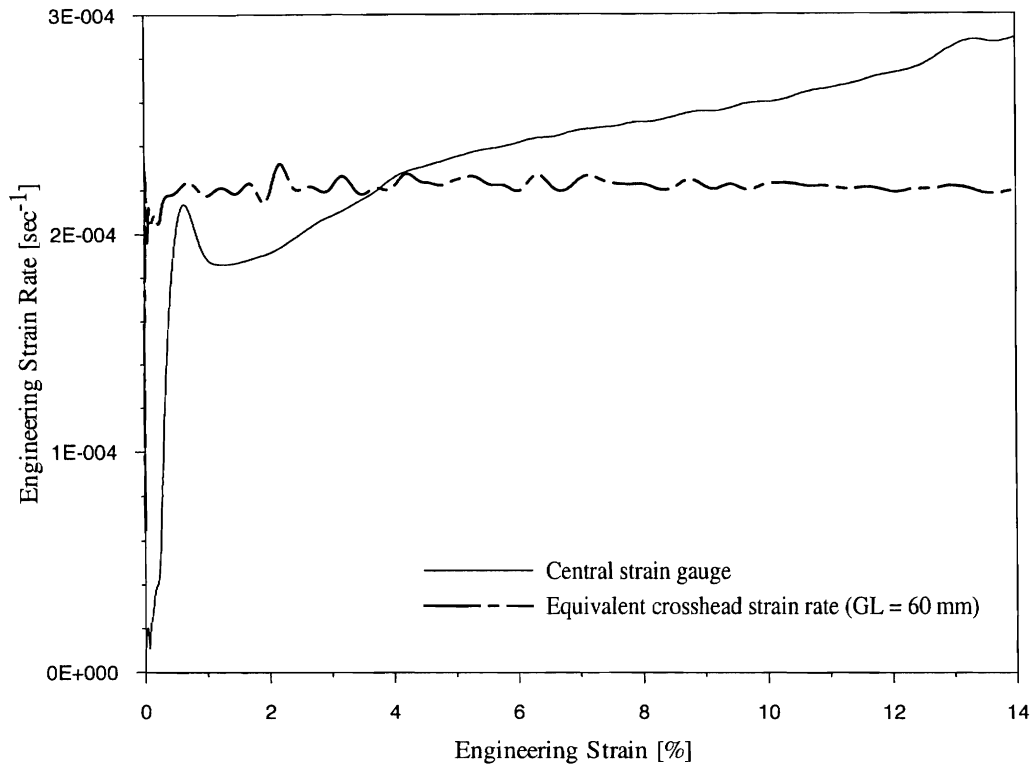


**Figure 6.6:** Engineering strain rate and equivalent crosshead strain rate Vs engineering strain

C350LO RHS Face $A_1$, Nominal $\dot{\varepsilon} = 10^{-4}$ $s^{-1}$

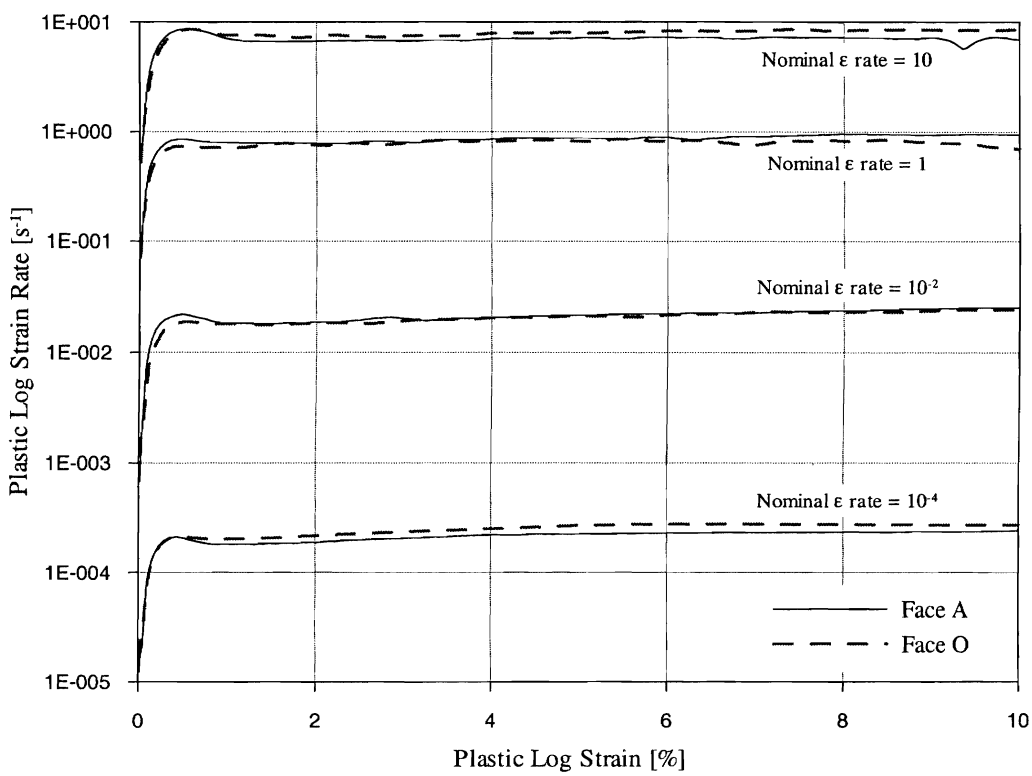


**Figure 6.7:** Plastic log-strain rate Vs plastic log strain, logarithmic scale – C350LO RHS

## 6.5.4 Strain Rate Sensitivity

The strain rate sensitivities of lower yield, UTS and strain energy density at UTS are shown in Table 6.5. The quasi-static reference quantities are those measured at the nominal strain rate $10^{-4}$ $s^{-1}$. The results presented in Table 6.5 are discussed in Sections 6.5.4.1 through 6.5.4.4 below.

**Table 6.5a:** Dynamic mechanical properties of grade C350LO RHS wall material

| Location around RHS | Nominal Strain Rate [$sec^{-1}$] | Lower Yield [MPa] | Ratio Lower Yield Dyn/Q. Stat. | UTS [MPa] | Ratio UTS Dyn/Q. Stat. | Strain Energy Density† [$J/mm^3$] | Ratio Strain Energy Dyn/Q. Stat. |
|---|---|---|---|---|---|---|---|
| Face A | 10 | 501.1 | 1.242 | 558.6 | 1.193 | 56.8E-3 | 1.193 |
| | 1 | 464.5 | 1.151 | 533.7 | 1.140 | 53.9E-3 | 1.132 |
| | $10^{-2}$ | **425.0**‡ | 1.053 | 498.4 | 1.065 | 50.4E-3 | 1.059 |
| | $10^{-4}$ | **403.6** | 1.000 | 468.2 | 1.000 | 47.6E-3 | 1.000 |
| Face O | 10 | 528.2 | 1.242 | 575.3 | 1.209 | 58.9E-3 | 1.200 |
| | 1 | 478.8 | 1.125 | 536.6 | 1.128 | 54.9E-3 | 1.118 |
| | $10^{-2}$ | **438.0** | 1.029 | 499.8 | 1.050 | 51.2E-3 | 1.043 |
| | $10^{-4}$ | **425.7** | 1.000 | 475.9 | 1.000 | 49.1E-3 | 1.000 |

† Average plastic strain energy density over gauge grid, at 10% plastic log strain.

‡ Bold indicates 0.2% Proof Stress.

**Table 6.5b:** Dynamic mechanical properties of DuraGal RHS wall material

| Location around RHS | Nominal Strain Rate [$sec^{-1}$] | Lower Yield [MPa] | Ratio Lower Yield Dyn/Q. Stat. | UTS [MPa] | Ratio UTS Dyn/Q. Stat. | Strain Energy Density† [$J/mm^3$] | Ratio Strain Energy Dyn/Q. Stat. |
|---|---|---|---|---|---|---|---|
| Face A | 10 | 534.8 | 1.219 | 596.8 | 1.165 | 46.2E-3 | 1.155 |
| | 1 | **498.8**‡ | 1.137 | 581.3 | 1.135 | 44.9E-3 | 1.123 |
| | $10^{-2}$ | **450.2** | 1.026 | 531.6 | 1.038 | 41.1E-3 | 1.028 |
| | $10^{-4}$ | **438.8** | 1.000 | 512.2 | 1.000 | 40.0E-3 | 1.000 |
| Face O | 10 | 594.7 | 1.179 | 629.6 | 1.154 | 49.8E-3 | 1.150 |
| | 1 | **553.6** | 1.097 | 601.6 | 1.103 | 47.5E-3 | 1.097 |
| | $10^{-2}$ | **517.9** | 1.027 | 565.4 | 1.037 | 44.8E-3 | 1.035 |
| | $10^{-4}$ | **504.5** | 1.000 | 545.4 | 1.000 | 43.3E-3 | 1.000 |

† Average plastic strain energy density over gauge grid, at 7.8% plastic log strain.

‡ Bold indicates 0.2% Proof Stress.

#### 6.5.4.1 LOWER YIELD STRESS

Many studies, such as (Manjoine 1944; Campbell & Cooper 1966; Marsh & Campbell 1963; Langseth et al. 1991) have found that yield stress, particularly upper yield stress, is very sensitive to changes in strain rate. Figures 6.5a and 6.5b confirm this behaviour. At the lower strain rates the stress-strain curves exhibited gradual yielding typical of cold worked material. As the strain rate increased these curves showed the development of an upper yield stress and a distinct yield plateau. This was considered to be "real" material behaviour rather than an effect caused by the experimental technique. See Section 6.5.7.

#### 6.5.4.2 UTS

Many references (Manjoine 1944; Campbell & Cooper 1966; Davies & Magee 1975; Langseth et al. 1991, Kassar & Yu 1992) have found that UTS was less strain rate sensitive than lower yield stress. This was not consistently the case for the RHS wall material tested in this study. At the highest strain rate, the dynamic to quasi-static ratio (dynamic factor) for lower yield stress quoted in Table 6.5 was higher than the dynamic factor for UTS. However, as the strain rate decreased, the difference between the dynamic factors for lower yield and UTS decreased. At a nominal strain rate of $10^{-2}$ $s^{-1}$, the dynamic factor for UTS was higher than the dynamic factor for lower yield stress, which indicated that UTS was more strain rate sensitive than lower yield stress. The apparent inconsistency between the results obtained in this study and other published studies may be due to the nature of the RHS wall material tested.

#### 6.5.4.3 COMPARISON BETWEEN C350LO AND DURAGAL

The higher strength, more heavily cold worked, DuraGal material was consistently less strain rate sensitive than the grade C350LO RHS wall material. Similarly the material from Face O, which appeared to have undergone more cold work during manufacture, was slightly less strain rate sensitive than material from Face A. This result was consistent with Davies and Magee (1975) and Kassar and Yu (1992).

#### 6.5.4.4 STRAIN ENERGY DENSITY

The results in Table 6.5 showed that the plastic strain energy density at UTS increased with increasing strain rate. It was also seen that the strain rate sensitivity of plastic strain energy density was very similar to that of the ultimate tensile strength.

### 6.5.4.5 YOUNG'S MODULUS

As in previous studies, the results in Table 6.3 showed no sensitivity of Young's modulus to strain rate.

### 6.5.4.6 UNIFORM STRAIN AND TOTAL EXTENSION

For the C350LO material there appeared to be no trend in the results for uniform strain and total extension.

For the DuraGal material, uniform strain and total extension appeared to increase with increasing strain rate. This was in contradiction to other studies (Campbell & Cooper 1966; Chatfield & Rote 1974, Langseth et al. 1991), where uniform strain and/or total extension decreased with increasing strain rate. Still others (Manjoine 1944; Davies & Magee 1975, Langseth et al. 1991) have found no apparent trend in the results for uniform strain and/or total extension.

### 6.5.4.7 FLOW STRESS

Table 6.6 shows the variation of flow stress with plastic strain and strain rate. Above 1% plastic strain, the strain rate sensitivity of the material tested was approximately constant. Additionally, it was only at the highest strain rate that the sensitivity of yield stress was significantly greater than that of flow stresses at higher strains.

**Table 6.6a:** Variation of flow stress with strain rate and plastic strain - C350LO RHS

| Location | Strain Rate [$Sec^{-1}$] | True Stress [MPa] | | | | Dynamic Stress : Quasi-Static Stress | | | |
|---|---|---|---|---|---|---|---|---|---|
| | | Plastic Log Strain | | | | Plastic Log Strain | | | |
| | | 0.3% | 1% | 5% | 10% | 0.3% | 1% | 5% | 10% |
| Face A | 7.0 | 512.1 | 511.0 | 582.5 | 617.8 | 1.249 | 1.184 | 1.194 | 1.191 |
| | 0.86 | 468.0 | 478.4 | 555.1 | 591.0 | 1.141 | 1.108 | 1.138 | 1.140 |
| | 2.1E-2 | 429.1 | 447.8 | 517.8 | 551.7 | 1.046 | 1.037 | 1.061 | 1.064 |
| | 2.2E-4 | 410.1 | 431.7 | 487.9 | 518.6 | 1.000 | 1.000 | 1.000 | 1.000 |
| Face O | 7.8 | 531.4 | 538.0 | 604.2 | 633.3 | 1.225 | 1.179 | 1.205 | 1.204 |
| | 0.80 | 480.9 | 497.5 | 564.3 | 591.0 | 1.108 | 1.090 | 1.125 | 1.124 |
| | 2.0E-2 | 445.7 | 467.0 | 526.2 | 550.7 | 1.027 | 1.023 | 1.049 | 1.047 |
| | 2.4E-4 | 433.9 | 456.3 | 501.5 | 526.0 | 1.000 | 1.000 | 1.000 | 1.000 |

**Table 6.6b:** Variation of flow stress with strain rate and plastic strain - DuraGal RHS

| Location | Strain Rate [Sec$^{-1}$] | True Stress [MPa] | | | | Dynamic Stress : Quasi-Static Stress | | | |
|---|---|---|---|---|---|---|---|---|---|
| | | Plastic Log Strain | | | | Plastic Log Strain | | | |
| | | 0.3% | 1.25% | 5% | 7.8% | 0.3% | 1.25% | 5% | 7.8% |
| Face A | 8.0 | 538.1 | 554.9 | 621.0 | 647.1 | 1.201 | 1.138 | 1.153 | 1.167 |
| | 0.85 | 506.1 | 538.5 | 607.4 | 629.8 | 1.129 | 1.104 | 1.128 | 1.136 |
| | 2.2E-02 | 458.4 | 496.8 | 556.3 | 573.8 | 1.023 | 1.019 | 1.033 | 1.035 |
| | 2.5E-04 | 448.1 | 487.7 | 538.7 | 554.6 | 1.000 | 1.000 | 1.000 | 1.000 |
| Face O | 8.8 | 599.6 | 616.8 | 662.9 | 678.2 | 1.170 | 1.139 | 1.154 | 1.159 |
| | 1.0 | 560.6 | 584.9 | 633.8 | 650.1 | 1.094 | 1.080 | 1.103 | 1.111 |
| | 2.1E-02 | 528.0 | 558.0 | 594.5 | 610.8 | 1.031 | 1.031 | 1.035 | 1.044 |
| | 2.6E-04 | 512.4 | 541.4 | 574.5 | 585.2 | 1.000 | 1.000 | 1.000 | 1.000 |

### 6.5.4.8 ORDER OF MAGNITUDE NATURE OF STRAIN RATE SENSITIVITY

The strain rate sensitivity of steel is often referred to as an "order of magnitude" effect (Perrone 1965; Jones 1989a p. 395; Kecman 1993a; Jones 1999), which implies that significant changes in mechanical properties are only noticed after order of magnitude changes in strain rate. The results in Tables 6.6 and 6.8 support this description. Reading from Table 6.5a, one order of magnitude increase in strain rate, from $10^{-4}$ to $10^{-3}$, resulted in an increase of approximately only 3% in the dynamic factor for strain energy density at UTS for the C350LO – Face A coupons. Similar results are summarised in Table 6.7 below.

**Table 6.7:** Order of magnitude sensitivity of C350LO – Face A strain energy density at UTS

| Change in strain rate from ... | Estimated inc. in ε energy density Dynamic Factor |
|---|---|
| $10^{-4}$ to $10^{-3}$ | 1.023 |
| $10^{-3}$ to $10^{-2}$ | 1.033 |
| $10^{-2}$ to $10^{-1}$ | 1.043 |
| $10^{-1}$ to 1 | 1.051 |
| 1 to 10 | 1.058 |

It is noted that the change in dynamic factor for strain energy density for a given change in strain rate increases as the strain rate increases. The increasing slope of the curves in Figure 6.8, with increasing strain, is another manifestation of this result. From Figure 6.8, it was evident that this result is not specific to strain energy density.

## 6.5.5 Strain Rate Sensitivity Models

For modelling and design purposes, it is convenient to describe the strain rate sensitivity of a material in a functional form. Three commonly used functional forms are:

1. $\frac{\sigma_{dyn}}{\sigma_{stat}} = 1 + \left(\frac{\dot{\varepsilon}}{D}\right)^{\frac{1}{q}}$ Cowper-Symonds (Bodner & Symonds 1962)

2. $\frac{\sigma_{dyn}}{\sigma_{stat}} = 1 + k \times \log\left(\frac{\dot{\varepsilon}_{dyn}}{\dot{\varepsilon}_{stat}}\right)$ (Campbell & Cooper 1966)

3. $\sigma_{dyn} = c \times \dot{\varepsilon}^{m}$ (Chatfield & Rote 1974)

The Cowper-Symonds form gave the best fit to the test results obtained in this study. Least squares fits of the Cowper-Symonds form for engineering lower yield stress, UTS and strain energy density at UTS are shown in Figure 6.8.

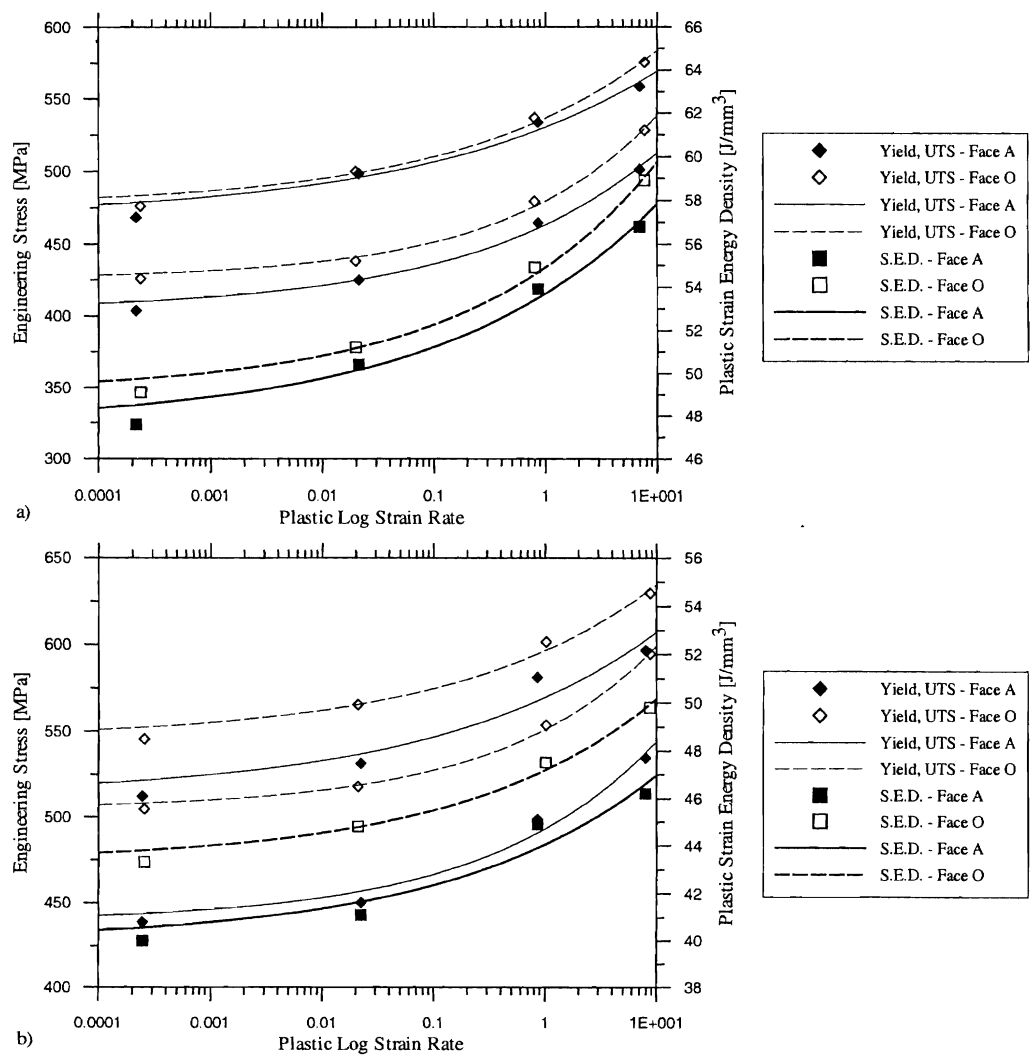


**Figure 6.8:** Strain rate sensitivity of RHS wall material a) grade C350LO and b)DuraGal

Note: UTS results were greater than yield stress results at all strain rates. Symbols (◆◇■□) represent test results. Curves are a least squares fit of the Cowper-Symonds form.

The commonly used Cowper-Symonds coefficients for mild steel of $D$ = 40.4 $s^{-1}$ and $q$ = 5 were derived by fitting the results for lower yield obtained by Manjoine, (1944). Abramowicz and Jones (1986), considered it inappropriate to use these values to predict material strain rate sensitivity at large strains and fitted the same functional form to the results for UTS published by Campbell and Cooper (1966), to obtain $D$ = 6,844 $s^{-1}$ and $q$ = 3.91. Abramowicz and Jones also derived $D$ = 802 $s^{-1}$ and $q$ = 3.585 by fitting the results for UTS from dynamic uniaxial tensile tests conducted at the University of Liverpool. Jones (1983) had previously derived $D$ = 1,300 $s^{-1}$ and $q$ = 5 by fitting the results for flow stress at $\varepsilon$ = 0.05 measured by Marsh and Campbell (1963). The performance of these four coefficient sets is compared in Table 6.8. In Table 6.8 the "Measured Ratio" at each strain rate is the ratio of the strain energy density at UTS measured at that strain rate, divided by the strain energy density at UTS measured at the lowest strain rate. Strain energy density (values are from Table 6.5) was chosen for this comparison because the ability to predict absorbed energy correctly is usually the main concern in crashworthiness applications. The coefficients identified as "GJ" in Table 6.8 were obtained by fitting the Cowper-Symonds form to the results for UTS given in Table 6.3, averaged over Faces A and O.

The Cowper-Symonds model with coefficients $D$ = 40.4 $s^{-1}$ and $q$ = 5 significantly over-estimated the strain rate sensitivity of the RHS wall material tested. It is interesting to note that coefficient sets "AJ1" and "AJ2" both gave good predictions, despite the fact that they were derived from separate tests conducted on materials quite different to the RHS tube wall material tested in this study. The predicted ratios using coefficient set "J1" were not as accurate as those obtained using coefficient sets "AJ1" and "AJ2". It was evident that the best results were obtained when the coefficients $D$ and $q$ were determined by fitting flow stresses at or near UTS.

**Table 6.8a:** Cowper-Symonds strain rate sensitivity predictions for Grade C350LO RHS

| Location around RHS | Strain Rate | *Measured Ratio Dyn.:Q. Stat. | Predicted Ratio/Measured Ratio | | | | |
|---|---|---|---|---|---|---|---|
| | | | GJ | CS | AJ1 | AJ2 | J1 |
| Face A | 7.0 | 1.193 | 1.008 | 1.428 | 0.982 | 1.061 | 1.133 |
| | 0.86 | 1.132 | 0.994 | 1.292 | 0.972 | 1.014 | 1.087 |
| | 2.1E-2 | 1.059 | 0.995 | 1.153 | 0.981 | 0.994 | 1.049 |
| | 2.2E-4 | 1.000 | 1.019 | 1.088 | 1.012 | 1.015 | 1.044 |
| Face O | 7.8 | 1.200 | 1.007 | 1.433 | 0.981 | 1.062 | 1.133 |
| | 0.80 | 1.118 | 1.005 | 1.303 | 0.983 | 1.025 | 1.098 |
| | 2.0E-2 | 1.043 | 1.010 | 1.168 | 0.996 | 1.009 | 1.063 |
| | 2.4E-4 | 1.000 | 1.019 | 1.090 | 1.012 | 1.015 | 1.045 |

Cowper-Symonds coefficients $D$ and $q$:
CS: $D$=40.4s$^{-1}$ and $q$=5 GJ: $D$=7,099s$^{-1}$ and $q$=4.35 AJ1: $D$=6,844s$^{-1}$ and $q$=3.91
AJ2: $D$=802s$^{-1}$ and $q$=3.585 J1: $D$=1,300s$^{-1}$ and $q$=5

**Table 6.8b:** Cowper-Symonds strain rate sensitivity predictions for DuraGal RHS

| Location around RHS | Strain Rate | *Measured Ratio Dyn.:Q. Stat. | Predicted Ratio/Measured Ratio | | | | |
|---|---|---|---|---|---|---|---|
| | | | GJ | CS | AJ1 | AJ2 | J1 |
| Face A | 8.0 | 1.155 | 1.009 | 1.492 | 1.020 | 1.105 | 1.178 |
| | 0.85 | 1.123 | 0.979 | 1.303 | 0.980 | 1.023 | 1.097 |
| | 2.2E-02 | 1.028 | 1.016 | 1.190 | 1.012 | 1.025 | 1.082 |
| | 2.5E-04 | 1.000 | 1.016 | 1.091 | 1.012 | 1.015 | 1.045 |
| Face O | 8.8 | 1.150 | 1.016 | 1.510 | 1.028 | 1.116 | 1.189 |
| | 1.0 | 1.097 | 1.006 | 1.349 | 1.007 | 1.054 | 1.130 |
| | 2.1E-02 | 1.035 | 1.007 | 1.179 | 1.003 | 1.017 | 1.072 |
| | 2.6E-04 | 1.000 | 1.016 | 1.091 | 1.013 | 1.015 | 1.046 |

Cowper-Symonds coefficients $D$ and $q$:
CS: $D$=40.4s$^{-1}$ and $q$=5 GJ: $D$=22,307s$^{-1}$ and $q$=4.41 AJ1: $D$=6,844s$^{-1}$ and $q$=3.91
AJ2: $D$=802s$^{-1}$ and $q$=3.585 J1: $D$=1,300s$^{-1}$ and $q$=5

$$\text{*Measured Ratio}_{\text{Dyn:Q.Stat.}} = \frac{\text{strain energy density at UTS measured at the given strain rate}}{\text{strain energy density at UTS measured at the lowest strain rate}}$$

## 6.5.6 FE Modelling of the Uni-Axial Tensile Test

A finite element analysis of the tensile test was conducted to investigate the relationship between measured crosshead travel and coupon strain over the gauge length.

The coupon, including initial curvature, was modelled using linear shell elements. The coupon grips and clamping bolt were also modelled, using rigid elements, so that the initial stress state caused by clamping the coupon could be replicated. The coupon

model is shown in Figure 6.9. Loading was applied in two stages. Stage one modelled the clamping process and stage two modelled the tensile loading. Contours of surface stress caused by clamping the curved coupon are shown in Figure 6.10.

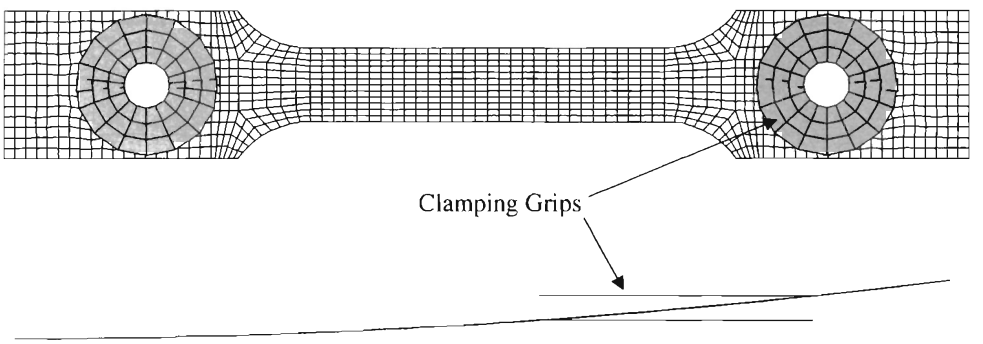


**Figure 6.9:** FE model of the tensile test coupon including initial coupon curvature and grips

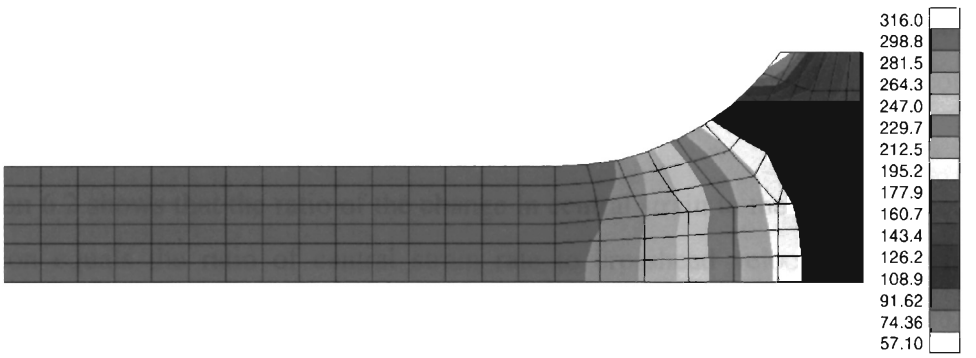


**Figure 6.10:** Tensile surface stresses after clamping the curved coupon

### 6.5.6.1 STRAIN DISTRIBUTION ALONG THE COUPON CENTRELINE

Figure 6.11 shows the profile of longitudinal surface strain along the longitudinal centreline of the coupon. Profiles were plotted at five stages throughout the loading, corresponding to different levels of central strain. Because the absolute strain is not important in this discussion strains were normalised with respect to the strain at the centre of the coupon. It was clear that the distribution of strain along the parallel length was not uniform but instead was a function of strain and also varied for different *stress-strain* relationships.

An implication of this result is that extensometer gauge lengths need to be used with more caution than is commonly found in practice. When using an extensometer to measure engineering strain, it is usually assumed that strain is uniform over the

sizes and grades, at a broader range of strain rates, and loaded under tension and compression.

**Gauge factor variation at large strain**

Enquiries to Measurements Group, the US manufacturer of the strain gauges used in this study, to clarify the procedure for correcting large strain measurements for the variation of gauge factor, revealed that the nature of gauge factor variation at high strains is a subject requiring further study. A study into the variation of gauge factor could follow the general procedure of Huang and Khan (1991), but need not be conducted at elevated strain rates. The aim of this study would be to measure the variation of gauge factor up to strains of 20%, but particularly in the region of 0.1% to 5%. It is in this range that the gauge factor begins to vary significantly from that determined at manufacture.

- Investigate the affect of hinge unloading on hinge moment and hinge rotation. § 4.5.5.3.
- Investigate the strain distribution in a tensile test coupon. § 6.5.6.

The results of the many supporting analyses have been cited and/or presented in previous sections, so details of all these analyses will not be given here. However, since the majority of these investigations were based on the results from a beam element analysis, the details of this model are discussed in this chapter.

## 7.2 BEAM ELEMENT MODEL

### 7.2.1 Analyses

Static, implicit dynamic and eigenvalue analyses were performed. Eigenvalue analyses were performed to determine the natural frequencies of the specimen before loading and after loading at a buckle rotation of 35°. Eigenvalue extraction solutions to determine the vibratory response of the specimen during an impact are complicated by the contact between the specimen and pendulum. This behaviour was therefore investigated using the implicit dynamic solution.

### 7.2.2 Model Details

#### 7.2.2.1 BUCKLE TOPOLOGY

Two beam element models with different treatments of the buckle region were developed. The first modelled the specimen as a continuous beam. This model was used to investigate pre-buckle specimen response. The second modelled the buckle using a single beam element for which *moment-curvature* ($M$-$\kappa$) properties were defined directly using the *BEAM GENERAL SECTION option in ABAQUS. (The reader is referred to Section 15.3.7 of the ABAQUS documentation for a full description and example of how this option can be used to replicate the non-linear *moment–rotation* response of a beam due to local buckling of its section). This model was essentially an example of the hybrid approach used by Kecman (1983), Cimpoeru (1992) and Kecman et al. (1993). Because the $M$-$\kappa$ of the "buckle element" was pre-defined, the hybrid model was not used to predict overall $M$-$\theta$ response. Rather, it was used to derive correction factors for an offset hinge location and to investigate post-buckle specimen vibration.

#### 7.2.2.2 RESTRAINT

Planar beam elements were used to model the length of the RHS specimen from the tip to the welded connection between the RHS and the base plate. The specimen base plate and reaction mount were not modelled. Instead the root of the cantilever was restrained in the $U_x$ and $U_y$ directions and attached to a grounded linear torsional spring in the $R_z$ direction. The torsional spring was included to account for the physical stiffness of the mounting structure. The stiffness of this base spring was determined by "calibrating" the predicted *pendulum moment Vs pendulum rotation* plot against the measured response.

#### 7.2.2.3 CANTILEVER LOADING AND PENDULUM CONTACT

Loading of the specimen by the pendulum was modelled using a rigid surface to represent the pendulum nose. The reference node for this rigid surface was placed on the pendulum axis. Contact was defined between this rigid surface and the specimen tip using a contact node set. To capture slippage of the pendulum nose along the specimen, the mesh density was increased in the contact zone. For the static analysis, an enforced rotation was applied to the pendulum reference node. Pendulum moment was obtained directly as a reaction moment. For the dynamic analysis the pendulum was given inertia, mass and an initial velocity. Pendulum moment was derived from specimen constraint forces $M_x$ and $R_y$.

In both analyses gravitational body loads were defined for the specimen and pendulum.

#### 7.2.2.4 MATERIAL AND SECTION PROPERTIES

The mechanical properties of the RHS wall material vary around the section, as discussed in Section 2.6.2.2. The material properties defined for the beam elements were therefore "equivalent" properties that produced the same gross response of the beam section. Material properties for the beam section were defined up to 2.5% strain and were based on the measured material mechanical properties for Face O (Section 6.4), but were modified such that the *pendulum moment Vs pendulum rotation* response, and the ratio of hinge zone rotation to pendulum rotation, matched those measured experimentally. Material strain rate sensitivity was defined using the power law option within ABAQUS, with constants $D = 950.0\ s^{-1}$ and $q = 4.0$. These values represented the equivalent strain rate sensitivity of the section and were based on the measured strain rate sensitivity of the coupons cut from Face A at 0.3% plastic strain, see Chapter 6.

The $M$-$\kappa$ properties defined on the *BEAM GENERAL SECTION option for the "buckle element", were derived in two parts. To be consistent with the continuous model, the pre-buckle $M$-$\kappa$ properties were derived from the $M$-$\theta$ response of the buckle region in the continuous model. The post-buckle properties were derived from the average experimental $M$-$\theta$ response presented in Chapter 5. Curvature was derived from rotation, assuming an element length equal to the physical buckle length i.e. 50 mm.

To model the variation in elastic stiffness of the buckle region, see Section 4.4, the elastic stiffness of the buckle was separated from the $M$-$\kappa$ properties and was represented by elastic torsional springs, as shown in Figure 7.1. The $M$-$\kappa$ properties now represented *moment Vs plastic curvature*. The variation of elastic stiffness with buckle rotation was modelled by defining the stiffness of the spring elements to be temperature dependent, and controlling the time history of temperature. This detail was modelled in an attempt to capture the true vibratory behaviour of the specimen under impact loading. In the static analysis, where the loading was monotonic, this detail was not necessary.

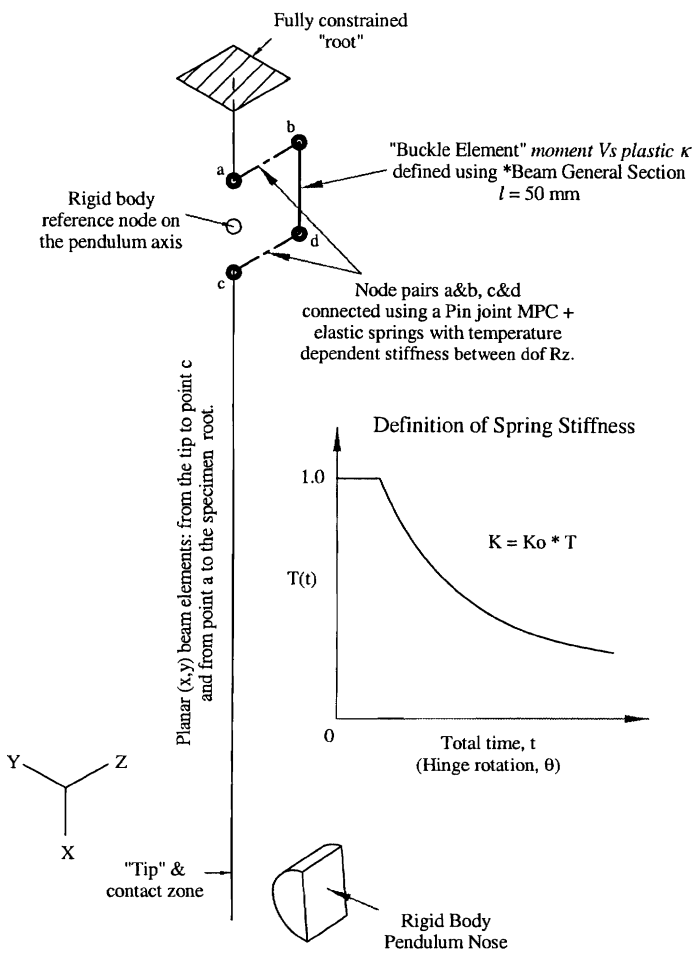


**Figure 7.1:** Modelling the variation in buckle elastic stiffness.

## 7.2.3 Results

### 7.2.3.1 STATIC ANALYSIS

Static analyses were principally used to validate the expression used to calculate hinge moment at locations offset from the specimen mount pivot axis, Section 4.3.2. Static results were also used to derive expressions for energy consistent hinge moment. These results have been presented in previous chapters and will not be discussed here. The comparison between computed and experimental specimen response is shown in Figures 7.2 and 7.3. The excellent correlation in Figure 7.3b is to be expected since the post-buckle $M$-$\kappa$ properties of the "buckle element" were predefined.

### 7.2.3.2 DYNAMIC ANALYSIS

Dynamic analyses were principally used to investigate the effects of specimen inertia and specimen vibrations on the measured $M$-$\theta$ response. The implicit artificial numerical damping factor $\alpha$ (sometimes used to improve solution efficiency) was set to the default value of –0.05. Larger values of $\alpha$ adversely altered the computed response by dissipating too much energy. The specific results from the various analyses have been presented in previous chapters and will not be discussed here. The comparison between computed and experimental specimen response is shown in Figures 7.4 and 7.5. Again, the excellent correlation in Figure 7.5b is to be expected since the post-buckle $M$-$\kappa$ properties of the "buckle element" were predefined.

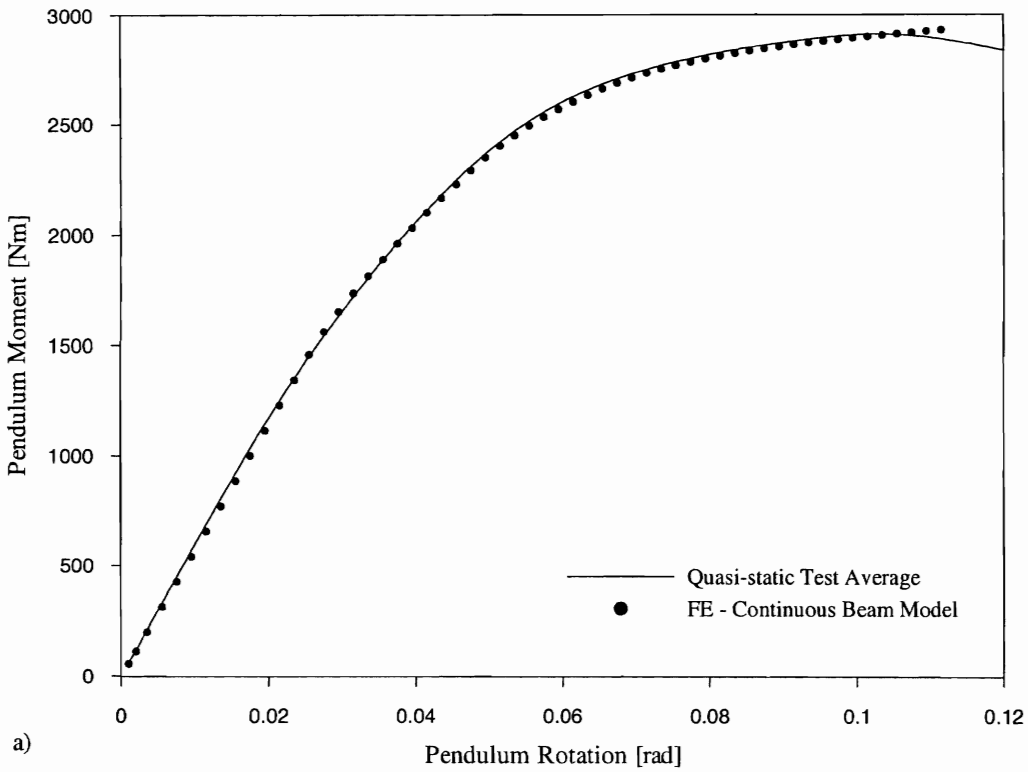


a)

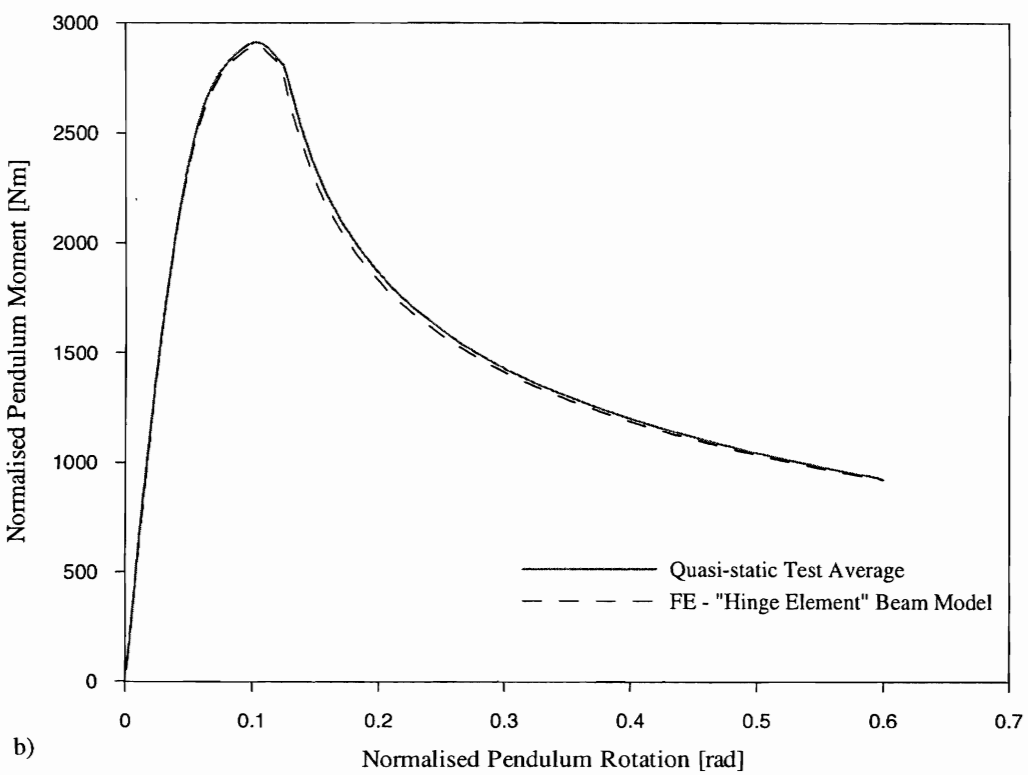


b)

**Figure 7.2:** Static Pendulum moment Vs Pendulum rotation

a) pre-buckle and b) post-buckle

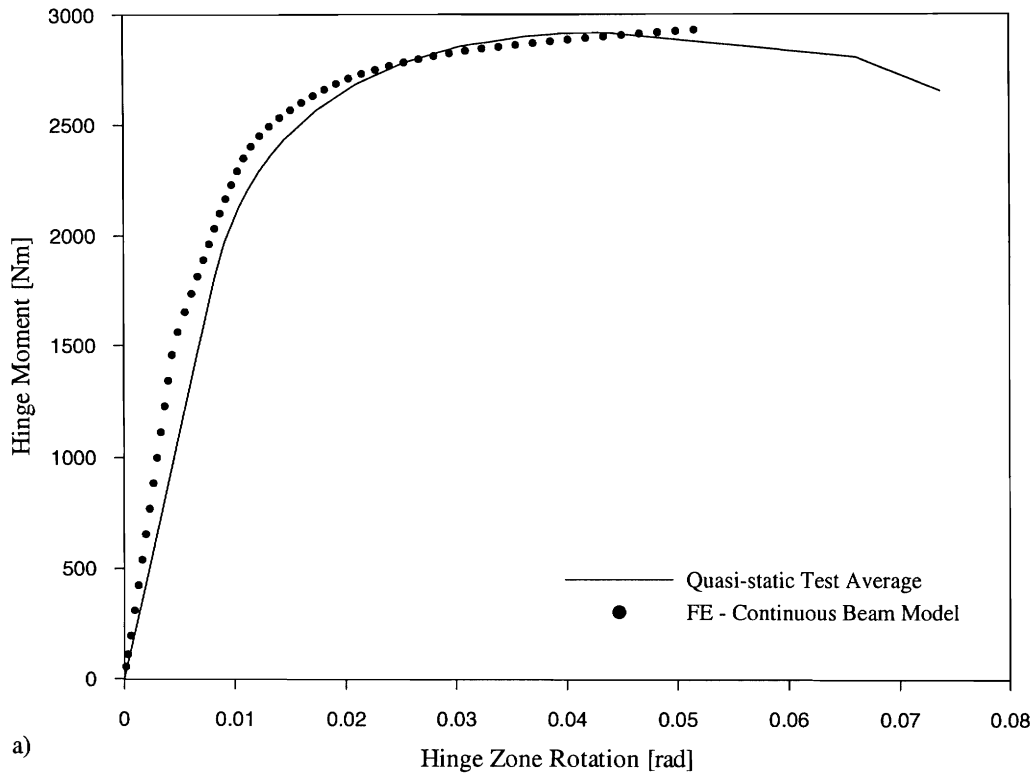


a)

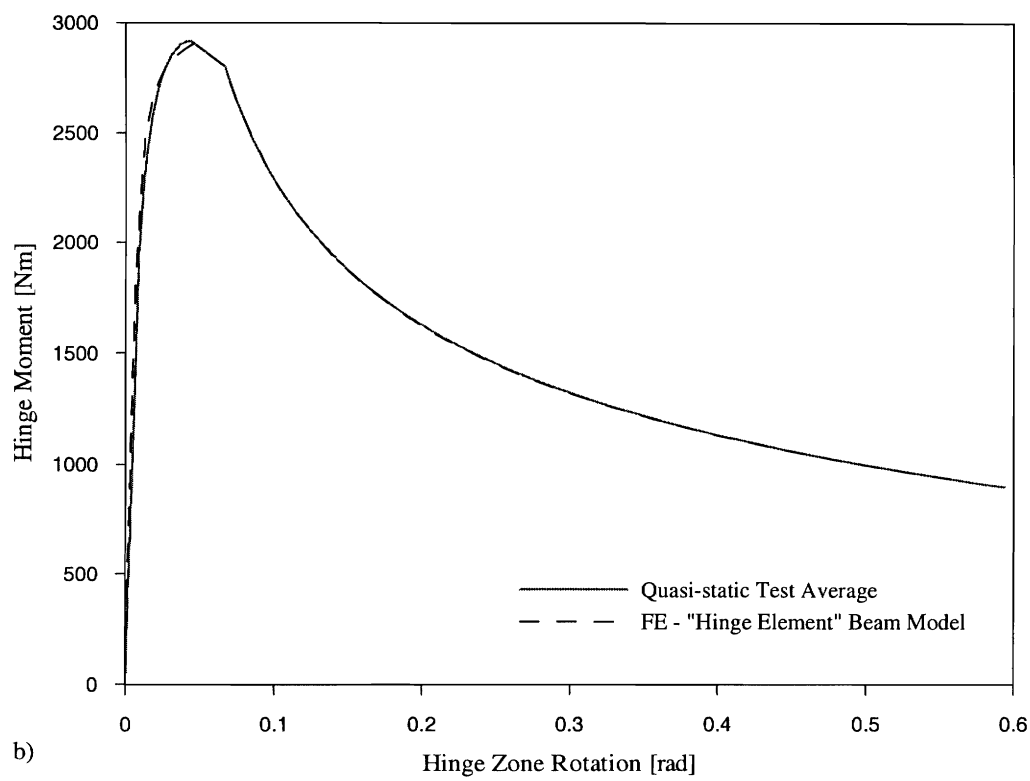


b)

**Figure 7.3:** Static Hinge moment Vs Hinge rotation

a) pre-buckle and b) post-buckle

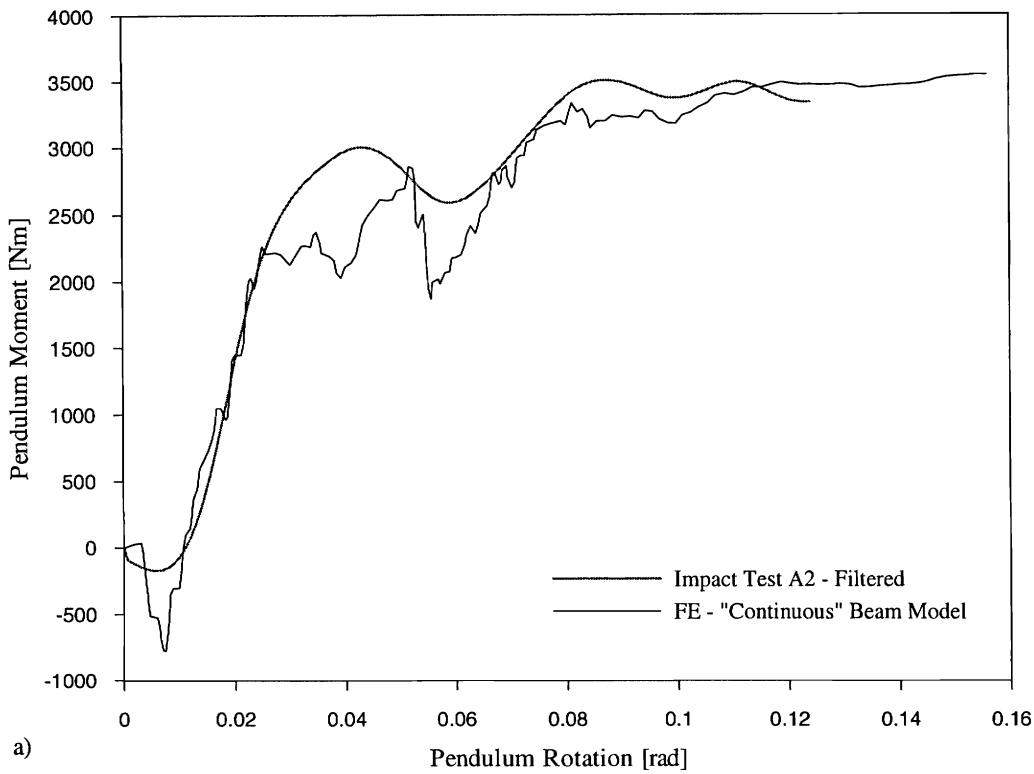


a)

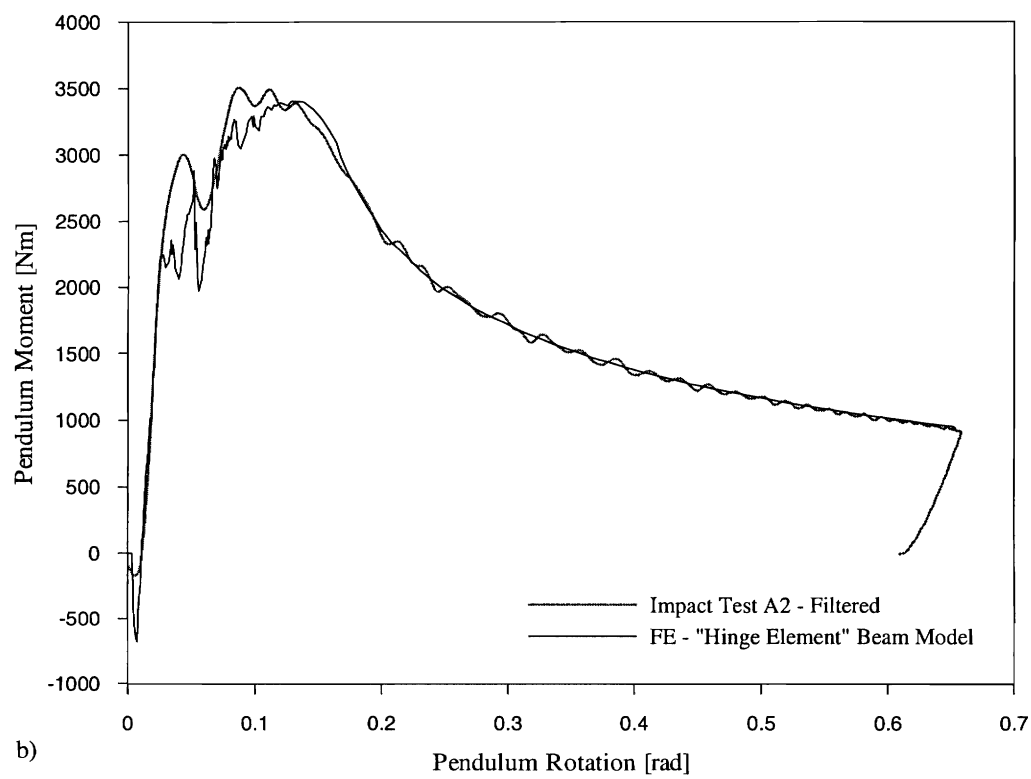


b)

**Figure 7.4:** Dynamic Pendulum moment Vs Pendulum rotation

a) pre-buckle and b) post-buckle

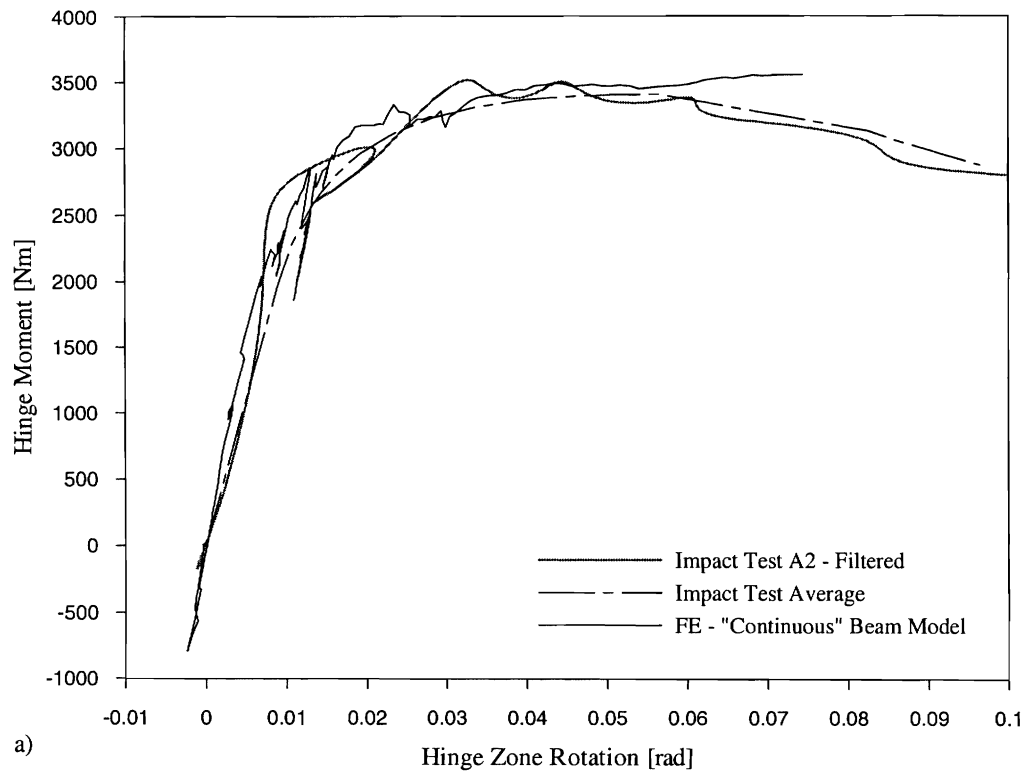


a)

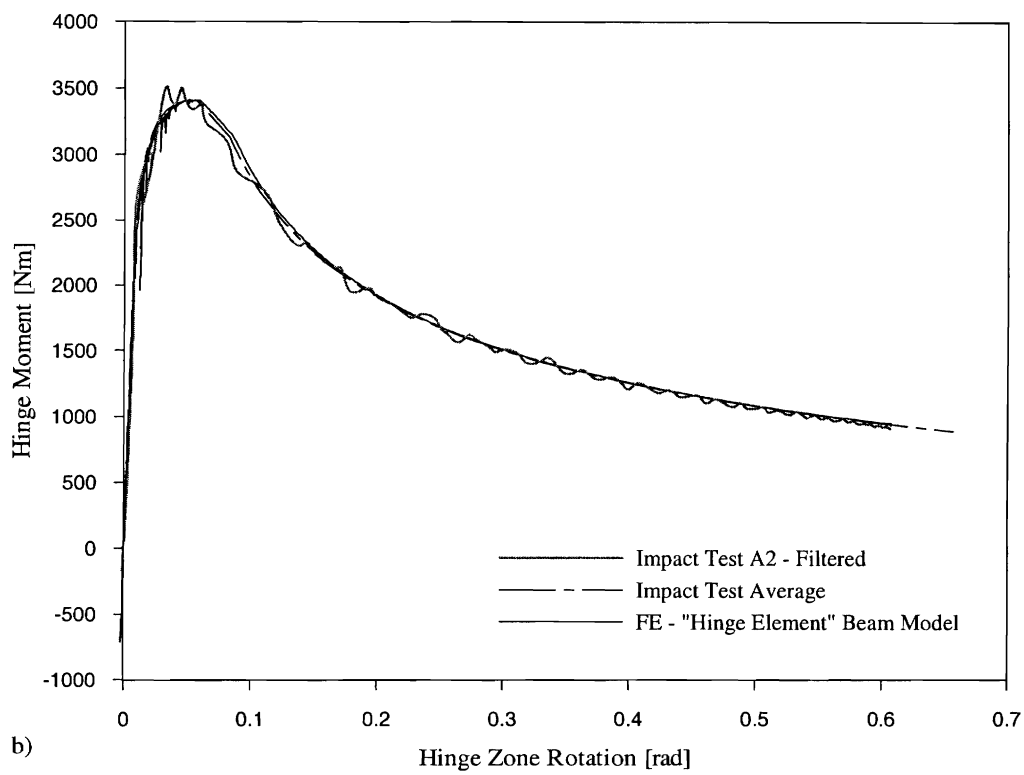


b)

**Figure 7.5:** Dynamic Hinge moment Vs Hinge zone rotation

a) pre-buckle and b) post-buckle

### 7.2.3.3 SOME INTERESTING RESULTS

#### Initial Specimen Response

The initial hinge response to impact by the pendulum was a "negative" rotation. This was mentioned in Chapters 3 and 4 and was clearly evident in the experimental results plotted in Figure 5.11. The implicit beam analysis revealed that this response was caused by a "negative" bending wave that was initiated in response to the contact between the specimen and pendulum and then propagated up the specimen to the hinge zone. Shortly after reaching the hinge zone this "negative" bending wave was overwhelmed by the gross "positive" bending of the specimen. The initiation and propagation of this "negative" bending wave are shown in Figure 7.6a. Figure 7.6b shows the corresponding *hinge moment Vs time* plot.

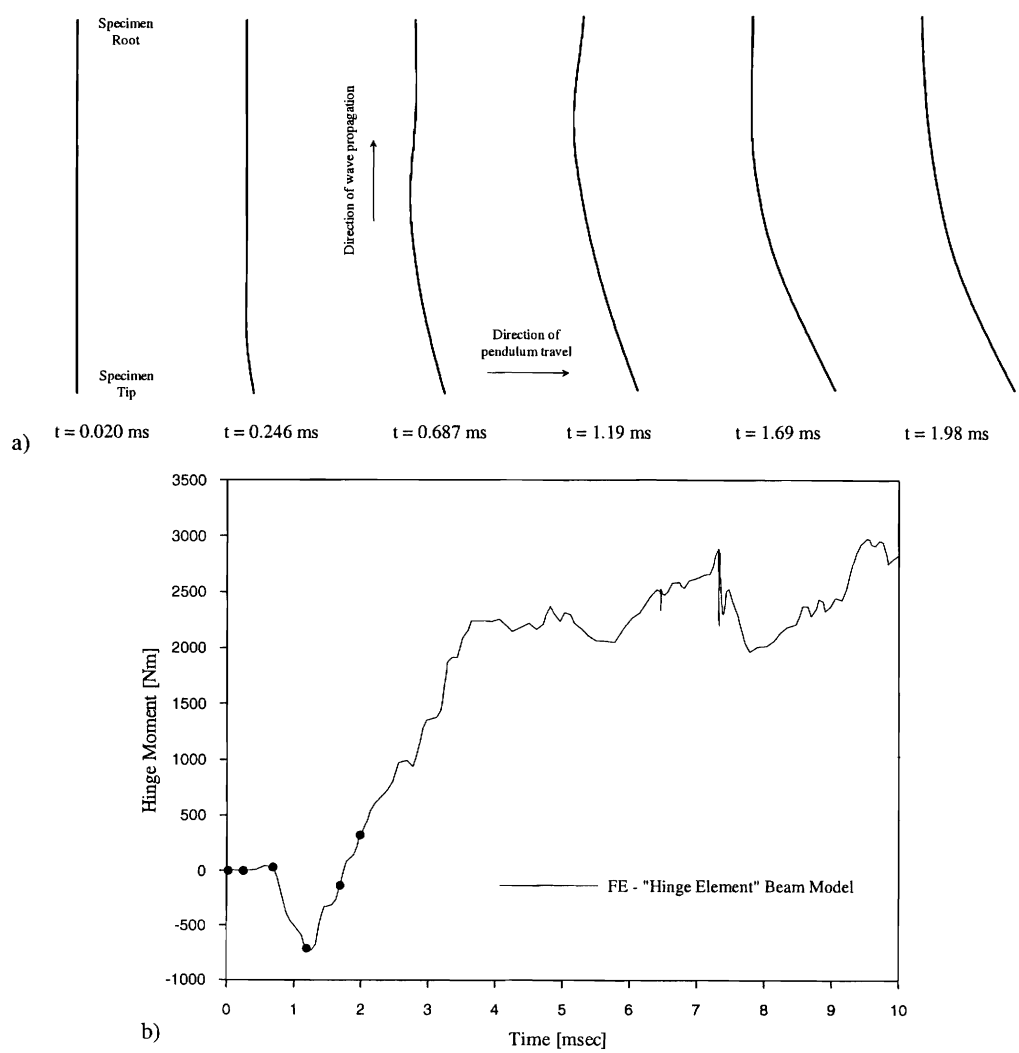


**Figure 7.6:** a) Propagation of a "negative" bending wave in the initial stages of impact
b) Corresponding hinge moment Vs time (• symbols mark the time "snapshots" in Figure 7.6a)

### Hinge Unloading

Specimen vibration and hinge unloading in the period before buckle formation was discussed in Sections 4.5.5.1 and 4.5.5.3. There was only one significant instance of hinge unloading that was evident in the experimental (Figure 4.19 – Impact A2 hinge zone strain and Figure 5.14) and finite element (Figure 4.17) hinge moment responses. It is interesting to note that this unloading occurred just after the pendulum and specimen re-contacted, see Figure 7.7 below. It was likely that the hinge unloading was due to a second "negative" bending wave initiated by the re-contact.

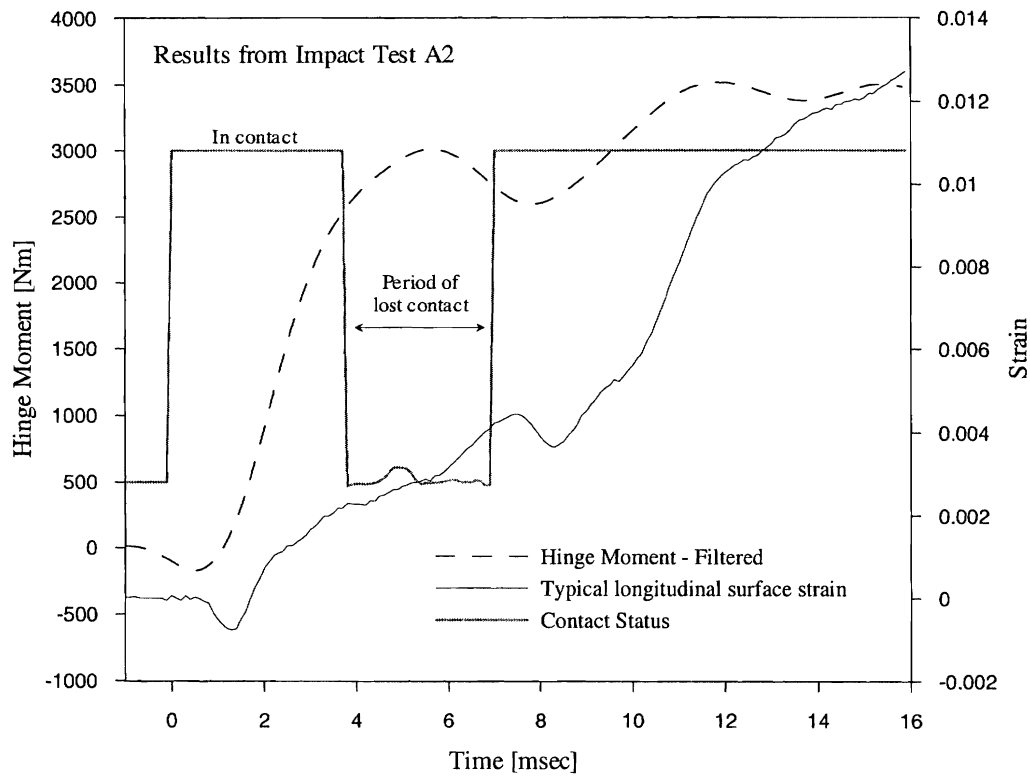


**Figure 7.7:** Hinge "negative" response corresponding to pendulum-specimen re-contact

### Hinge Zone $M$-$\theta$ is not necessarily smooth

The hinge $M$-$\theta$ response measured under impact loading, Figures 5.11 and 5.14, bore little resemblance to the smooth $M$-$\theta$ response measured quasi-statically. This was expected and was due primarily to the dynamic response of the specimen and measurement system as discussed in Sections 4.5.3 to 4.5.6. The $M$-$\theta$ response obtained from FE analyses were expected to be smooth because the analysis was unaffected by measurement system response and other experimental uncertainties. However,

non-smooth hinge $M$-$\theta$ responses were also predicted by FE analyses. The reasons for this were that:

- hinge moment was derived indirectly and remotely using a reaction force;
- hinge zone rotation was calculated over a finite length of 85 mm; and
- specimen vibrations and material strain rate sensitivity interacted in a non-linear manner.

Figure 7.8 shows the non-smooth hinge $M$-$\theta$ response obtained from the beam element analysis under discussion and an implicit dynamic analysis using a detailed shell element model.

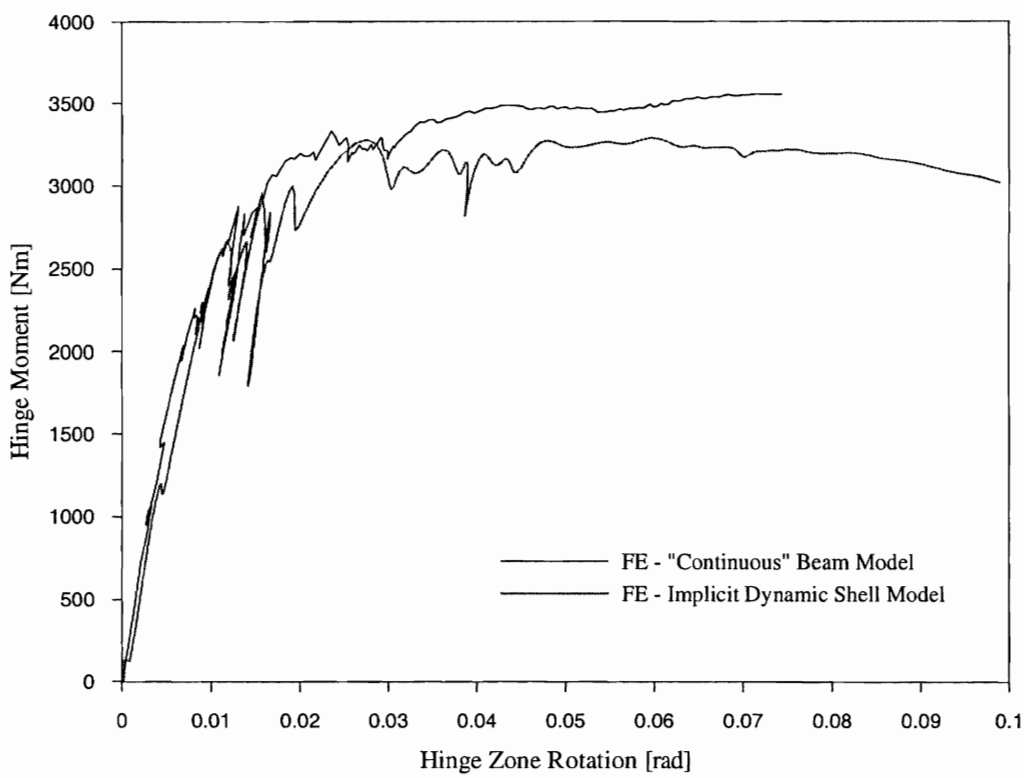


**Figure 7.8:** Non-smooth hinge $M$-$\theta$ responses

## Extent of Material Plasticity

Material plasticity (defined as 0.2% outer fibre plastic strain) extended 170 mm from the cantilever root in the static analysis and 260 mm in the dynamic analysis, an increase of 53%. Experimentally, it was found that permanent curvature of the specimen extended ≈300 mm from the root of the cantilever after quasi-static loading and ≈360 mm after impact loading, an increase of 20%. (Without more extensive measurement of

strains along the specimen, the extent of material plasticity could not be quantified further).

## 7.3 SHELL ELEMENT MODEL

### 7.3.1 Aim

Detailed, shell-element models of the specimen were developed to investigate the spatial and temporal distribution of plastic strain and strain rate within the local buckle and to demonstrate the use of commercial finite element codes as predictive design tools.

### 7.3.2 Model Details

#### 7.3.2.1 MODEL TOPOLOGY

The finite element model shown in Figure 7.9 is composed of shell and beam elements. Shell elements were used to model the RHS specimen in the vicinity of the local buckle. The shell region covered the full length of the mounting plate and extended approximately 285 mm along the specimen from the plate edge. Planar beam elements were used to model the remaining length of the specimen. The beam and shell elements were rigidly connected using non-linear multi-point constraint equations (MPCs). The use of more complex MPCs was not warranted. A linear analysis of a model meshed entirely with shell elements was used to derive an equivalent stiffness for the beam elements. The mounting plate was modelled using shell elements and was attached to the RHS shells using rigid MPCs. A row of solid elements was used to represent the transverse weld between the mounting plate and specimen. These elements were connected to the mounting plate using rigid MPCs. This detail was included to account for the stiffness of the mounting arrangement.

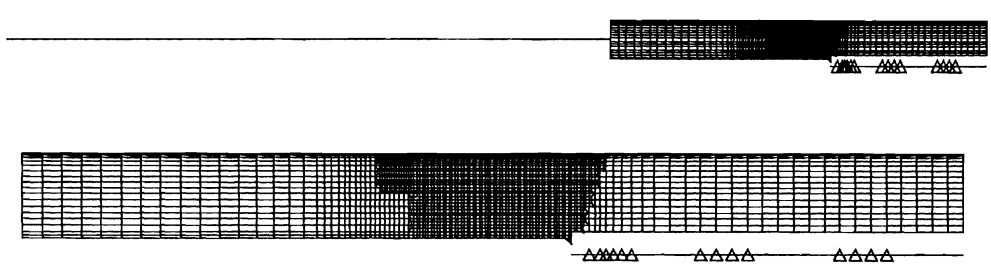

**Figure 7.9:** Detailed model of the RHS specimen using a combination of shell and beam elements

### Mesh Perturbation

In post-buckling (load-displacement) analyses, a difficulty that can arise when loading a model with "perfect" geometry is how to initiate buckling. Also, the sudden change in stiffness at the point of buckling may pose numerical difficulties. One approach that is often taken to overcome these difficulties is to introduce some initial imperfection into the model. This converts the problem into one with a continuous response instead of a bifurcation. Various strategies for perturbing the "perfect" mesh have been used. Vignjevic and Cavalcanti (1997) randomly perturbed their mesh, Langseth et al. (1999) defined a local imperfection, Haug et al. (1983) imposed a mesh perturbation described by the 1$^{st}$ eigenvalue buckling mode and the ABAQUS documentation recommends that a linear superposition of all relevant eigenvalue modes be used. Imperfections can also be introduced simply by perturbations in the loads or boundary conditions.

No form of mesh perturbation was included in the final analyses performed in this study and no numerical difficulties were experienced obtaining the *load-displacement* response during, and beyond, the period of buckle initiation. (A mesh perturbed using the 1$^{st}$ eigenvalue buckling mode was analysed, however the resulting moment peak was too low and was unrealistically "rounded").

### Buckle Symmetry

The longitudinal symmetry of the deformed specimen was exploited. A ¼ buckle model that assumed lateral symmetry at the centre of the buckle was also analysed. Whilst the collapse response predicted by the ½ and ¼ symmetry models were similar, see Figure 7.10, the analyses discussed in this section were conducted using the ½ buckle model for the following reasons. (The ¼ buckle model would be appropriate for parametric studies).

- The stress distribution was not strictly symmetrical, due to the influence of the transverse weld.
- At large rotations the local buckle tended to become asymmetrical.
- The ½ buckle model permitted the derivation of hinge rotation in the same manner as that adopted experimentally.
- The implementation of the pseudo-dynamic loading scheme, developed to simulate pendulum impact in a static analysis, was simplified if only longitudinal symmetry was assumed.

- The manner in which boundary conditions are modelled is a major source of discrepancy between FE model stiffness and experimental stiffness. The ½ buckle model, which incorporated the root of the specimen, mounting plate, welds and mounting bolts, was the most realistic and therefore the most appropriate model for comparison with experimental results.
- ½ buckle solution times were acceptable.

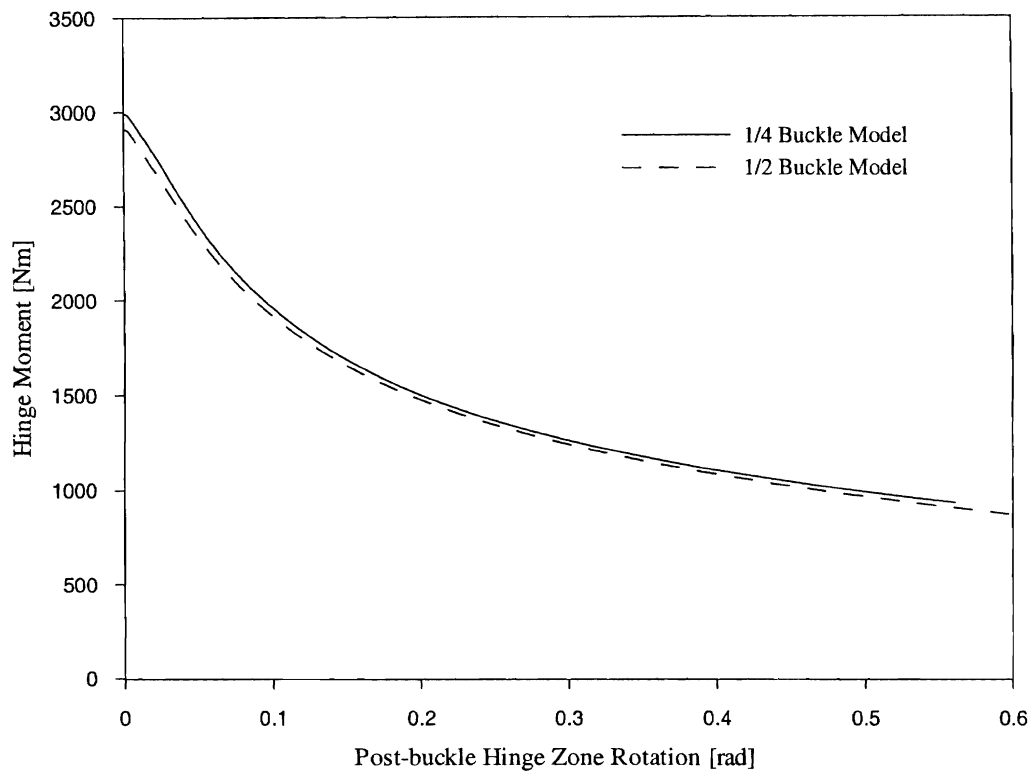


**Figure 7.10:** Collapse response for ¼ buckle model and ½ buckle models

## Mesh Density

Mesh density was dictated by the regions of concentrated plastic strain along the yield and rolling lines of the buckle mechanism (see Kecman's model, Figure 2.7b or 5.9). The most critical region was the corner radius and adjacent material:

- Material originally in the corner radius of the section underwent severe deformation during buckle development. The corner radius was flattened laterally and bent longitudinally to form a "saddle", see Figure 7.16.
- Radii of curvature in the "saddle" were of the order of the material thickness.
- Strain gradients in the "saddle" were high, see Figure 7.27.

- The flattening of the corner and the "rolling" deformation (bending followed by straightening) of the material adjacent to the corner accounted for a significant proportion of the plastic strain energy absorbed in the buckle.

An overly stiff or coarse corner mesh will adversely affect the prediction of $M$-$\theta$ response during the initial development of the buckle.

The mesh in the region of the local buckle is shown in Figure 7.11. To ensure the mesh did not dictate the buckle location, the mesh extended 15 mm behind and 82 mm in front of the lateral weld to the mounting plate. The mesh beyond this region was then transitioned to a coarser mesh.

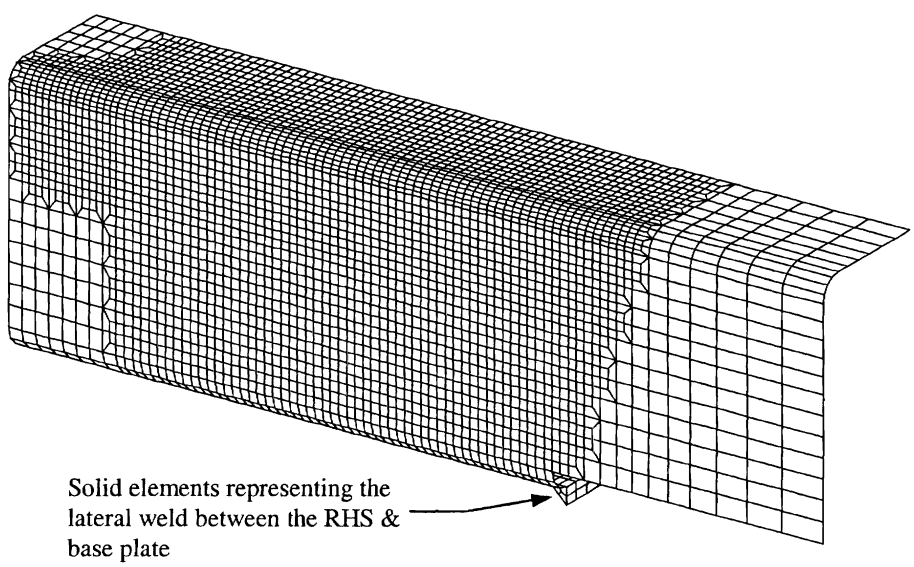


**Figure 7.11:** Mesh density in the region of the local buckle

This mesh was finer than might be practical in a dynamic crash analysis such as (Hashemi et al. 1996; Reid 1996; Vignjevic and Cavalcanti 1997), but the mesh was appropriate for the aims of this study. The mesh density was also finer than in Jing and Barton (1998) but was consistent with that in Ducrocq et. al. (1998).

**Element Type**

The shell elements used in this analysis were bi-linear finite strain elements with reduced integration, (ABAQUS type S4R elements). These elements accounted for transverse shear deformations when the shell was "thick" and became discrete Kirchoff thin elements when the thickness decreased. These elements also accounted for finite membrane strains and allowed for change in thickness due to plastic strain. The shell

section Poisson's ratio was 0.5, which assumed material incompressibility at large plastic strains. Simpson's rule with nine integration points was used to integrate through the shell section. Full integration elements (type S4) were tested. These elements gave essentially identical results but with increased solution times.

#### 7.3.2.2 RESTRAINT

As discussed above attempts were made to represent the stiffness of the mounting arrangement as realistically as possible. Physically the specimen mounting plate was bolted to a reaction structure. This arrangement was modelled using "grounded" linear spring elements to represent the mounting bolts. These elements had stiffness representative of the bolts and were positioned in a pattern similar to the bolt arrangement, Figure 7.12.

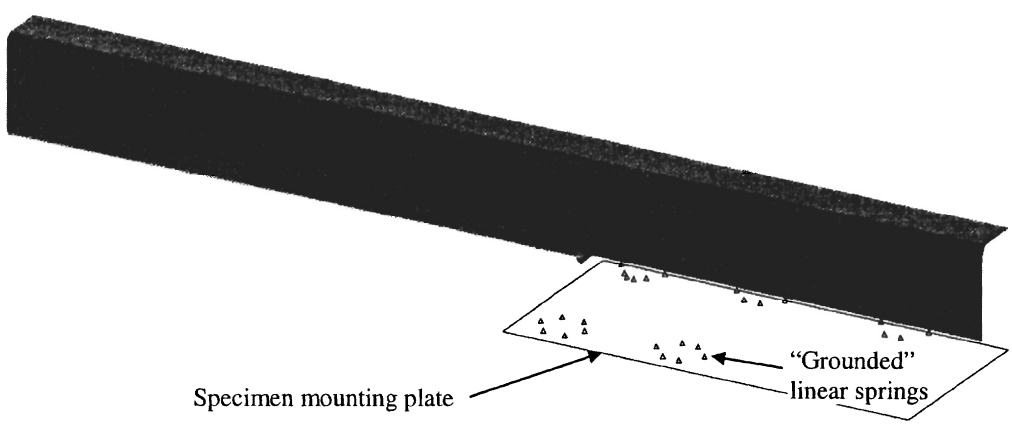


**Figure 7.12:** Specimen mounting plate restraint

A more complex approach incorporating pre-loaded spring elements, and contact between the specimen mounting plate and the reaction structure, was also tested. Both arrangements predicted very similar $M$-$\theta$ responses, however the more complex contact boundary conditions almost doubled the solution time and this approach was therefore abandoned.

#### 7.3.2.3 LOADING

The cantilever loading of the specimen was modelled in the same manner as described for the beam element analysis. The pendulum nose was defined as a rigid surface with the reference node at the pendulum pivot. Contact was defined between this rigid surface and the specimen tip using a contact node set. To capture slippage of the

pendulum nose along the specimen, the mesh density of the beam extension was increased in the contact zone.

For static analyses, an enforced rotation was applied to the pendulum reference node. Pendulum moment was obtained directly as a reaction moment. For dynamic analyses the pendulum was given inertia, mass and an initial velocity. Pendulum moment was derived by summing the action of all "grounded" spring elements and single point constraints.

#### 7.3.2.4 PSEUDO-DYNAMIC ANALYSIS

The two main "dynamic effects" influencing hinge response under impact loading were inertia and material strain rate sensitivity. Results from implicit dynamic analyses, with actual and reduced material densities, indicated that the inertia of material in the buckle had a negligible effect on the $M$-$\theta$ response of the buckle. Further justification for this conclusion is discussed in Section 7.3.3.2, where the results of implicit dynamic and pseudo-dynamic analyses are compared and shown to be very similar, see Figures 7.21 and 7.22. Whilst significant specimen vibrations were excited by the impact loading and specimen inertia, as discussed in Chapter 4, these oscillations did not significantly affect hinge $M$-$\theta$ response. Additionally, specimen vibrations were significantly damped after buckle formation and therefore did not influence buckle $M$-$\theta$ response. Because inertia could be neglected, the influence of material strain rate sensitivity was investigated using a pseudo-dynamic analysis scheme implemented within a static solution. In order to correctly replicate the strain rates within the specimen during an impact test the basic requirement of the pseudo-dynamic scheme was to replicate the loading history imposed on the specimen i.e. to replicate the rotation history of the pendulum.

The physics of the pendulum motion were very simple. The pendulum configured with a certain mass and inertia impacted with the cantilevered specimen at an initial velocity. Deformation of the specimen, specifically the formation and rotation of a plastic hinge, absorbed kinetic energy from the pendulum. The pendulum slowed until it momentary came to rest when all its initial kinetic energy had been converted to strain energy in the specimen plus some pendulum potential energy. Pendulum velocity was thus a function of total specimen strain energy.

The *AMPLITUDE option provided in ABAQUS could have been used to replicate pendulum velocity history from a physical impact test. Unfortunately this approach would not have properly modelled the impact event, as the loading history would not have been solution dependent, i.e. in this case a function of total specimen strain energy. ABAQUS also provided several very general and versatile user subroutines. One such routine, DISP, allowed the user to directly control the magnitude of prescribed boundary conditions. By coding the physics of the impact test into this routine the actual loading history of the impact could be replicated.

The implementation of this pseudo-dynamic loading scheme actually involved the use of two ABAQUS user routines, DISP and URDFIL. An overview of the scheme showing how the two routines interacted is given in Figure 7.13.

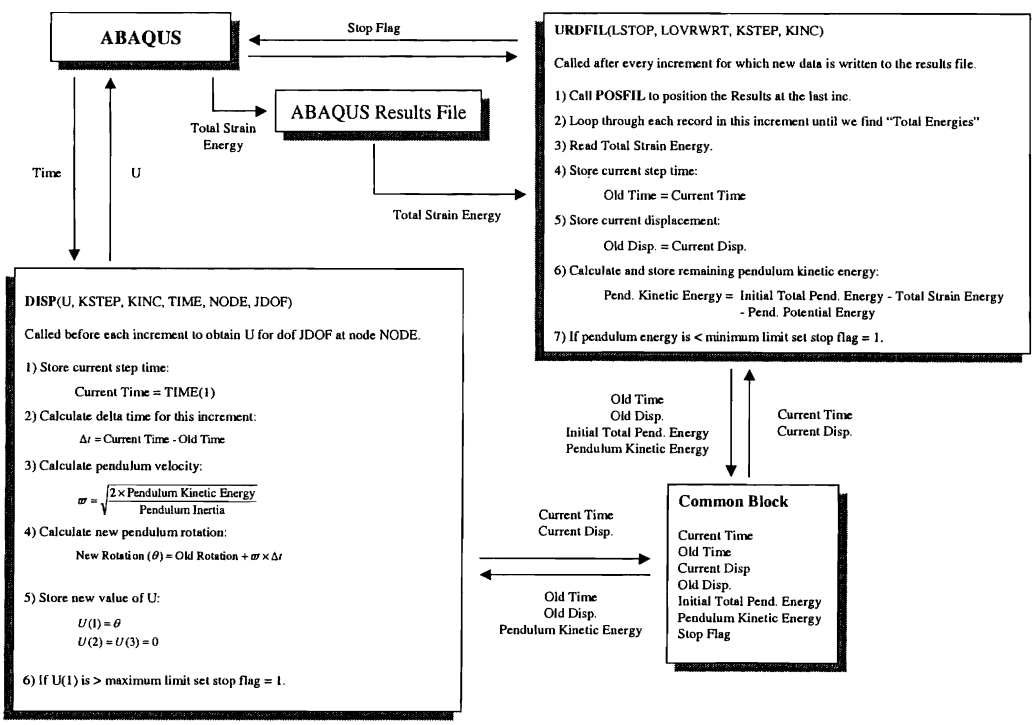


**Figure 7.13:** User routine flow chart

## Function of DISP

ABAQUS calls user routine DISP at the beginning of each increment. This routine calculates the new value of U for the particular node and degree of freedom (DOF) for which it is called. In this example U represents pendulum rotation and DISP is only called for one DOF. The very simple physics of the pendulum impact and the incremental scheme used to calculate U are given by the following equations.

$$KE_{Pend.} = E^{0}_{Pend.} - SE_{Spec.} - PE_{Pend.}$$

where; $E^{0}_{Pend.}$ = Initial Total Pendulum Energy

$KE_{Pend.}$ = Pendulum Kinetic Energy

$PE_{Pend.}$ = Pendulum Potential Energy

$$KE_{Pend.} = \frac{1}{2} I_o \varpi^2$$

where; $I_o$ = Pendulum Inertia

$\varpi$ = Pendulum Angular Velocity

Therefore: $$\varpi^i = \sqrt{\frac{2 \times E^i}{I_o}}$$

Total pendulum rotation = Previous rotation + New increment of rotation

$$\theta^i = \theta^{i-1} + \Delta\theta$$
$$= \theta^{i-1} + \varpi^i \times \Delta t$$
$$U^i = \theta^i$$

After calculating U, the routine checks whether U is greater than a user specified maximum limit and sets the stop flag LSTOP accordingly. If LSTOP is set, ABAQUS will terminate the analysis when URDFIL is next called.

**Function of URDFIL**

At the end of each increment for which new data is written to the results file ABAQUS calls routine URDFIL. The routine URDFIL performs four functions.

1. Looks for a "total energies" record in the current increment of the results file. If a "total energies" record exists, the total strain energy attribute is read. If "total energies" has not been written to the file in this increment, pendulum energy is not updated. It is not necessary for "total energies" to be written every increment, however since pendulum velocity is a function of pendulum energy, the more frequently pendulum energy is updated, the more accurate will be the estimate of U.
2. Calculates the remaining pendulum kinetic energy and stores the result in the common block..
3. Saves the current values of step time and U in the common block..
4. Checks if the remaining energy is less than the user defined minimum limit and sets the flag LSTOP accordingly.

**Function of the Common Block**

A common block is used as a convenient means of passing variables between the two routines DISP and URDFIL.

**Supplementary Notes**

- In a static analysis time is not real. Pseudo time can be chosen as any convenient measure e.g. seconds, milliseconds, however the definition of material strain rate sensitivity must be consistent with the chosen time measure.
- Units must also be consistent within the routines DISP and URDFIL i.e. between energy, inertia, velocity, time and rotation.

#### 7.3.2.5 MATERIAL PROPERTIES

**Anisotropy - Longitudinal Vs Transverse Directions**

Tests on RHS wall material reported by Johnson (1990) indicated only slight anisotropy between the longitudinal and transverse directions. The average yield stress in the longitudinal direction was approximately 5% higher than in the transverse direction. Ultimate tensile stresses were essentially the same in both directions. Uniform strain was approximately 5% higher in the longitudinal direction.

For the purpose of this FE analysis, the RHS wall material was assumed to be isotropic.

**Variation around the Section**

The variation of material properties around the section has been studied by Zhao and Hancock (1990, 1995) and Key et al. (1988). Some consistent trends in the mechanical properties of the RHS material were:

- Yield stress and UTS were higher for the corner material.
- Yield stress and UTS were higher for the material in the face opposite the seam weld, as compared to the material in the faces adjacent to the seam. This is consistent with the results presented in Chapter 6.
- Uniform elongation for the corner material was approximately half that of the face material. Tensile tests, presented in Chapter 6, also showed that uniform elongation was lower for the face opposite the seam as compared to the face adjacent to the seam.

The detailed measurements reported by Key et al. (1988) (see Figure 2.8) of yield stress variation and ultimate tensile strength variation around a section further indicated that:

- the increase in strength at the corners was localised;
- the properties of the material near the corners were similar to those of the face opposite the seam; and
- the properties of the material along the seam were similar to those at the corners.

On the basis of the above results and additional quantitative results presented in Zhao and Hancock (1990, 1991, 1992, 1995) and Sully and Hancock (1996), the following scheme was adopted for defining material properties in the FE model.

*Compression Flange:* Properties as measured for Face O, See Chapter 6.

*Web:* Properties as measured for Face A, See Chapter 6.

*Tension Flange:* Properties as measured for Face O.

*Corner:* Properties scaled from Face A, using a factor that varied exponentially from 1.25 at yield to 1.14 at UTS ($\varepsilon = 0.1$) to 1.0 at $\varepsilon = 1.0$. To reflect reduced ductility, corner strain was set equal to 0.5 times Face A strain.

Additionally, a 3 mm wide strip of web material adjacent to the compression corner was given the properties of Face O.

**Residual Stresses**

The detailed study conducted by Key and Hancock (1993b) revealed a complex combination of membrane, bending and layering residual stresses within the walls of RHS after manufacture. When included in a finite strip analysis of column behaviour, the longitudinal bending residual stresses reduced the maximum load by "*up to 5.4% over the residual stress free case*" and reduced the axial stiffness by "*up to 9.1% at an applied strain of 70% of the nominal yield strain*". The inclusion of transverse residual stresses "*resulted in a decrease in the ultimate load of up to 1.2% and a decrease of up to 9% in the axial stiffness from an early stage of loading*".

Kormi et al. (1995) neglected both residual stresses and imperfections in their FE analysis of axially loaded stiffened square tubes and cite this as a possible reason for the prediction of higher peak loads than they measured experimentally.

Residual stresses were not included in the FE analyses undertaken in this study.

**Uniaxial Tension Properties only**

Although crash deformations involve complex stress states, Davies and Magee (1975) found that tensile results give a proper indication of rate effects in complex bending. Tests conducted by Zhao and Hancock (1992) indicated that uniaxial tensile and uniaxial compressive yield stress differed by only 3.5%.

For the purposes of this study, the mechanical properties of RHS wall material were assumed to be equal in tension and compression.

**Bauschinger Effect**

The Bauschinger effect is characterised by a reduced yield stress upon load reversal, after plastic deformation has occurred during the initial loading. This phenomenon decreases with continued cycling. The cold rolling process by which square and rectangular hollow sections are formed induces a cycle of straining in the wall material. The deformations that occur during buckle development subject the material to further strain reversals. HKS ABAQUS provided two measures of plastic strain 1) PEEQ – the monotonically increasing integral of equivalent plastic strain rate and 2) PEMAG – a scalar measure of the total plastic strain. The difference between these strain measures gave an indication of the amount of reverse yielding. The contours in Figure 7.14 show the difference between these two strain measures over the outer surface at $\theta = 28.4°$. Large areas of reverse yielding are apparent. The largest plastic strain reversals have occurred in the "saddle" and where the flattened corner material is bent longitudinally.

Although the influence of the reverse yielding shown in Figure 7.14 on the true flow stress of the material and on the overall collapse response of the buckle was unknown, the Bauschinger effect was neglected in this study and the evolution of the Mises yield surface was defined to be isotropic. This is the approach commonly taken in crashworthiness studies. The justification for this approach is the fact that the Bauschinger effect is most apparent around yield and that it is reasonable to neglect the Bauschinger effect when plastic strains are large, as is commonly the case in crash deformations. This approach is further supported by the experience of Davies and Magee (1975) which implied that the Bauschinger effect is not significant in complex bending / crash deformations.

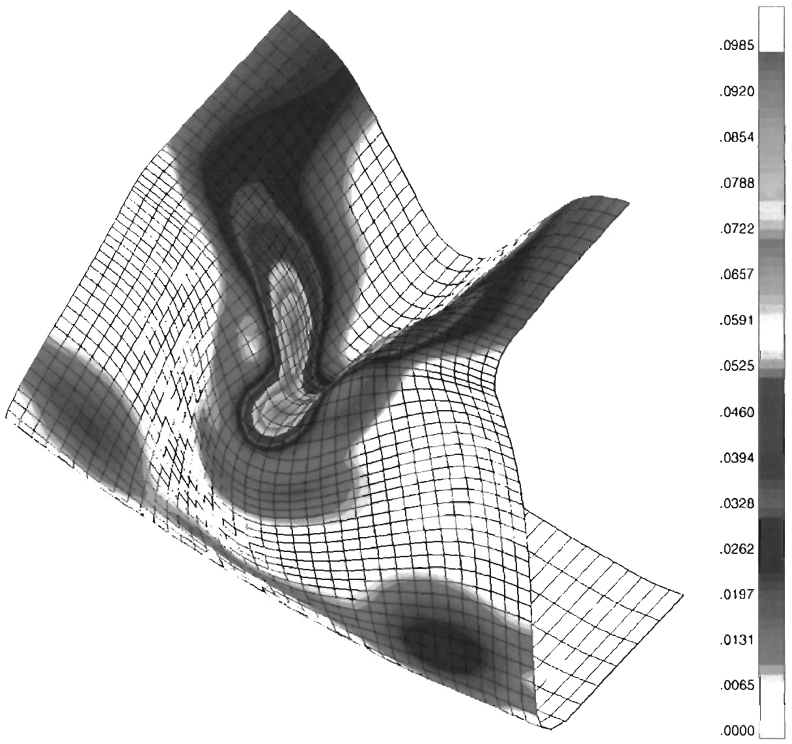


**Figure 7.14:** Reverse yielding in the buckle. (PEEQ – PEMAG)

### Yield Criterion

The classical metal plasticity constitutive models are used by ABAQUS. For isotropic yield these models use the Mises yield criteria with associated plastic flow to define plastic strain. (The reader is referred to Sections 11.2.1 through 11.2.3 of the ABAQUS documentation for further details).

#### 7.3.2.6 "CALIBRATION" OF STATIC MATERIAL PROPERTIES

Figures 7.15a and 7.15b compare the static pre and post buckle *moment-rotation* responses predicted by the detailed shell-element model described above with the corresponding experimental response from Chapter 5. The correlation between the predicted (curves identified as "original material definition") and measured responses was very good. To provide an accurate basis for the comparison of impact responses improved correlation was sought by "calibrating" the FE model. This "calibration" process involved modifying the material definition to obtain the desired level of correlation between the predicted and experimental responses. "Calibration" of the model resulted in an "equivalent" material definition that produced the same gross effect (*Pendulum moment Vs Pendulum rotation* and *Hinge moment Vs Hinge rotation*) as that measured experimentally. This "equivalent" material definition therefore

accounted for differences between the predicted and experimental responses that were associated with all aspects of the model's fidelity and performance e.g. material definition, mesh refinement, element formulation, constraint definition, etc.

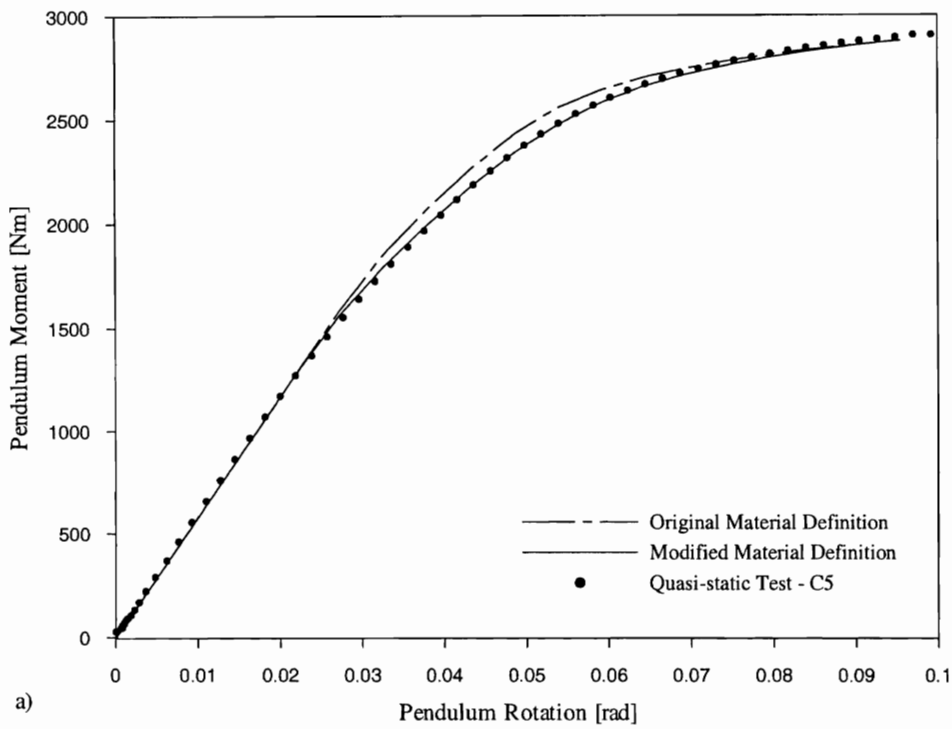


a)

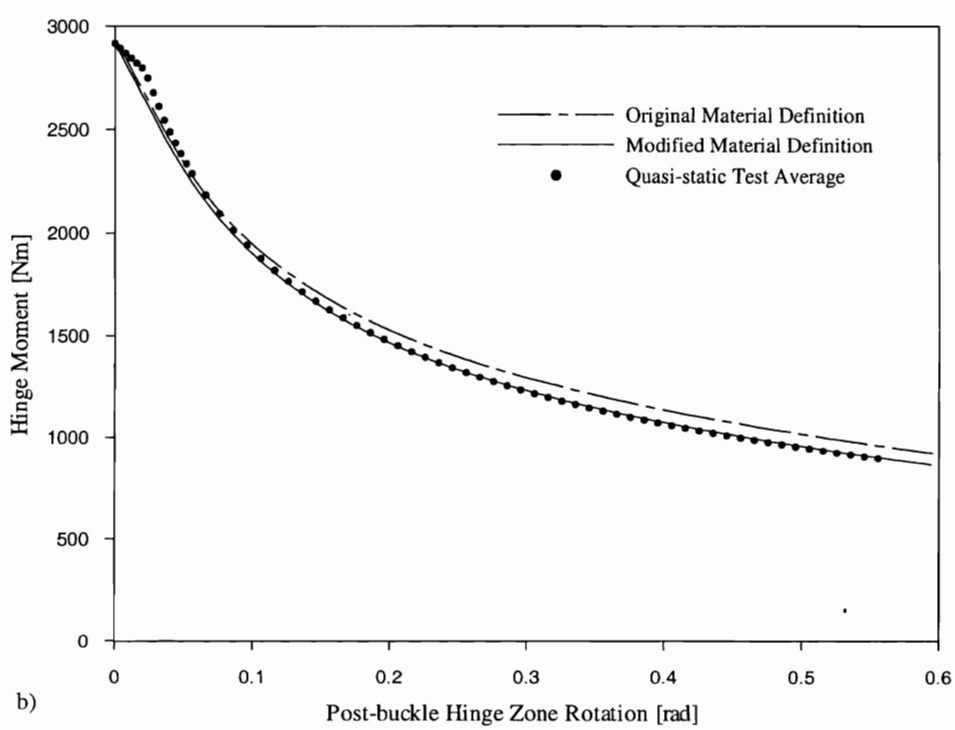


b)

**Figure 7.15:** FE moment-rotation responses before and after modification of material stress-strain curves (Note that the FE responses shown in Figure 7.15a have accounted for the physical flexibility of the specimen mounting arrangement. See Section 7.3.3.2 – Static analysis.)

The early elastic-plastic and deep collapse experimental responses shown in Figure 7.15 were both slightly overestimated by the FE predictions. Therefore it was the regions of the *stress-strain* definition that corresponded to these regions of the $M$-$\theta$ response that were modified.

**Elastic-plastic Region**

Plastic strains in the early elastic-plastic stages of the pendulum *moment-rotation* response were less than 0.5%, therefore to improve the correlation with the experimental result, the measured *true stress Vs log strain* curves for Faces A and O were modified in the region from 0 to 0.3% plastic log strain. The most significant modification, -13%, was in the elastic limit. The modification of measured stress reduced to only +1% at 0.3% plastic log strain. The pre-buckle pendulum *moment-rotation* response predicted using the modified material definition (curve identified as "modified material definition" in Figure 7.15a) compared extremely well with the experimental curve.

**Deep Collapse**

Plastic strains in the deep collapse phase of the buckle *moment-rotation* response were well beyond 10%, i.e. much greater than the strains in the uniaxial tensile coupons at UTS. Therefore the deep collapse response of the buckle was influenced most directly by the stress-strain definition beyond UTS.

Because the tensile mechanical properties of the RHS material were only measured up to UTS, the nature of the *true stress Vs log strain* curve beyond UTS had to be assumed. It is commonly accepted that the true stress continues to rise throughout the test, even after necking, although opinions on the rate of hardening differ. The hardening rate is frequently linear, as measured by Jing and Barton (1998) and assumed by Zaouk et al. (2000b). In other cases the hardening rate decreases continuously until fracture. Experimental measurements of true stress beyond UTS are complicated by the fact that once the geometry of the neck begins to form, the stress state in that region becomes triaxial tension, rather than the uniaxial tension assumed for the tensile test. Voids or cracks can also develop in the necked region as a preface to failure. Bridgman's correction (Dieter 1988; DeGarmo et al. 1984) for the triaxial stress state in a tension neck tends to reduce the measured hardening rate.

Initially it was assumed that the strain-hardening rate of the *true stress Vs log strain* curve beyond UTS was constant and equal to the instantaneous value at UTS. Figure 7.15b shows that the deep collapse response predicted with this post UTS strain-hardening definition (curve identified as "original material definition") compared well with the experimental curve in the early stages of collapse but began to diverge from the experimental response in the late stages of collapse. To improve the correlation in the late stages of collapse the hardening rate beyond UTS was reduced. The excellent correlation shown in Figure 7.15b by the curve identified as "modified material definition" was obtained by exponentially reducing the hardening rate beyond UTS from the instantaneous rate at UTS to 15% of this rate at a log strain of 1.0. Although this modification to the material definition calibrated for all aspects of the model's performance, it was possible that the need to significantly reduce the post-UTS strain-hardening rate in this manner was partly a consequence of the Bauschinger effect in the real material.

The *moment-rotation* responses predicted by the final modified or "equivalent" material definition provided an excellent basis for comparisons of predicted and experimental impact response.

#### 7.3.2.7 DYNAMIC PROPERTIES - STRAIN RATE SENSITIVITY

The Cowper-Symonds and Johnson-Cook material strain rate sensitivity models are commonly used in finite element crashworthiness studies (Kormi et al. 1995; Ducrocq et al. 1998; Jing & Barton 1998). In ABAQUS, strain rate dependency of yield stress can be defined using the Cowper-Symonds model or by defining a family of *true stress Vs plastic log strain* curves at various strain rates. The advantage of the later approach is that the strain dependency of strain rate sensitivity is implicitly defined. Using this approach, the effect of material strain rate sensitivity can be limited.

Since the quasi-static material properties for Faces A and O had been modified as described above, it was appropriate that the material properties measured at elevated strain rates reflect these modifications. *True stress Vs log strain* curves at the four nominal test strain rates ($10^{-4}$, $10^{-2}$, 1 and 10 $s^{-1}$) were derived by scaling the modified quasi-static properties in the same ratio as the measured *stress-strain* curves. These *true stress–log strain* curves were entered directly into the ABAQUS model. The material *stress-strain* curve for the corner material was scaled from the Face A properties in the

same manner as was done for the static properties. Material properties for Face A, Face O and the corner, at a strain rate of 80 $s^{-1}$, were extrapolated from data at the four test strain rates.

## 7.3.3 Results

### 7.3.3.1 BUCKLE MODE SHAPE

Buckle mode shapes obtained from static, dynamic and pseudo-dynamic analyses were all essentially identical. The predicted buckle mode shape at $\theta = 37°$, shown in Figure 7.16, compared extremely well with the buckle geometry obtained experimentally, see Plate 5.1. The average "effective centre" of the numerical buckle was -9.6 mm from the pendulum axis, which was within the range (although near the extreme) of experimental effective centre locations. The progressive development of the buckle is shown in Figure 7.17. The cross-sectional profile of the buckle at $\theta = 36°$, shown in Figure 7.18a, exhibited asymmetry similar to Plate 5.2.

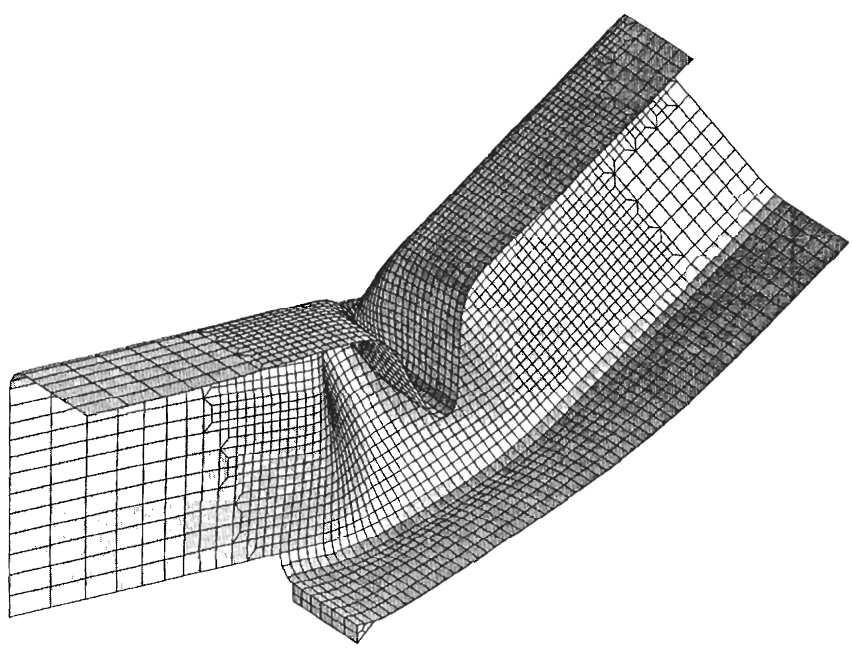

**Figure 7.16a:** FE buckle mode shape, $\theta = 37°$

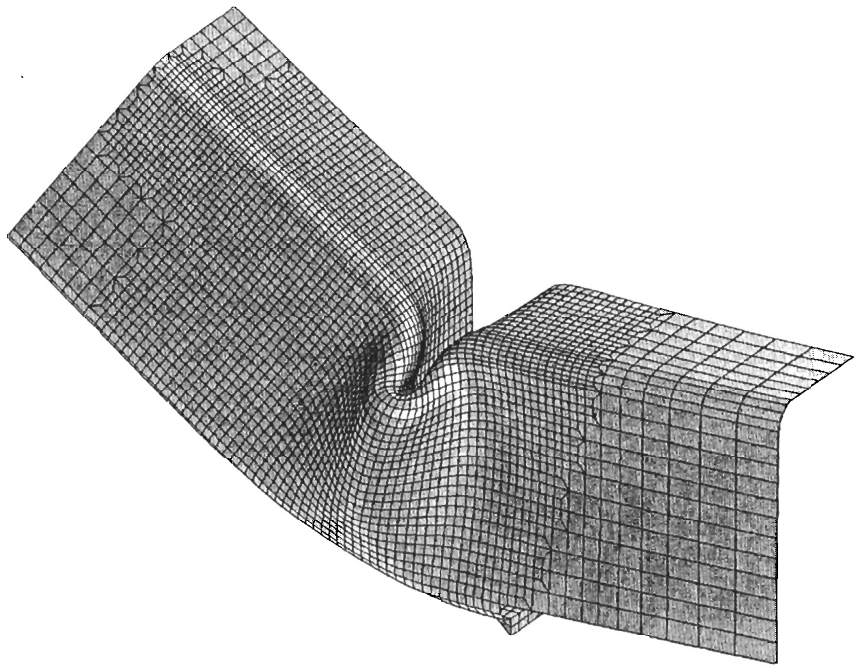

**Figure 7.16b:** FE buckle mode shape, $\theta = 37°$

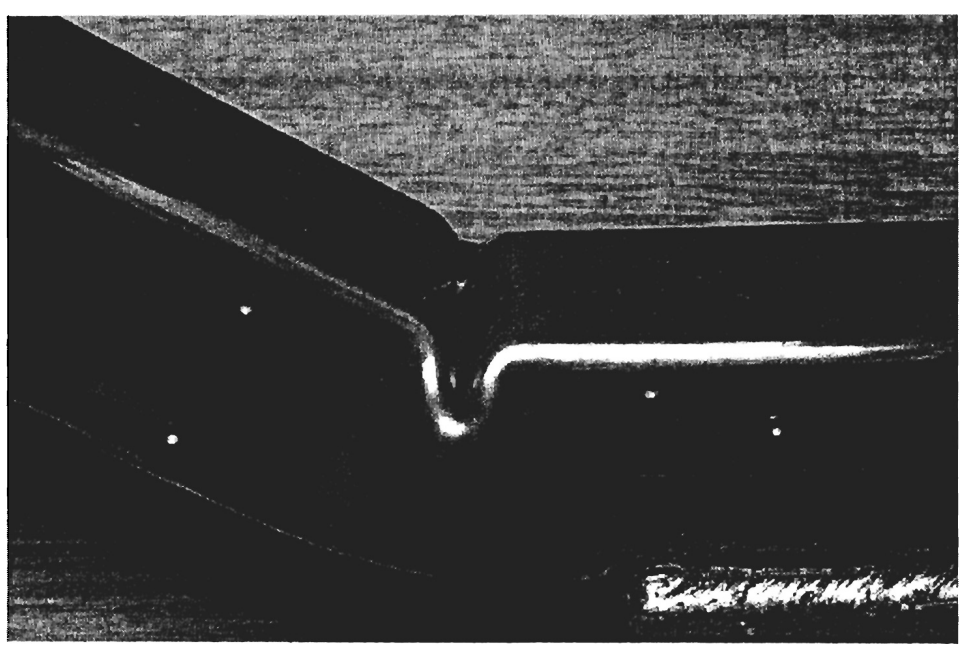

**Figure 7.16c:** Experimental buckle mode shape, $\theta \approx 35°$ (Plate 5.1)

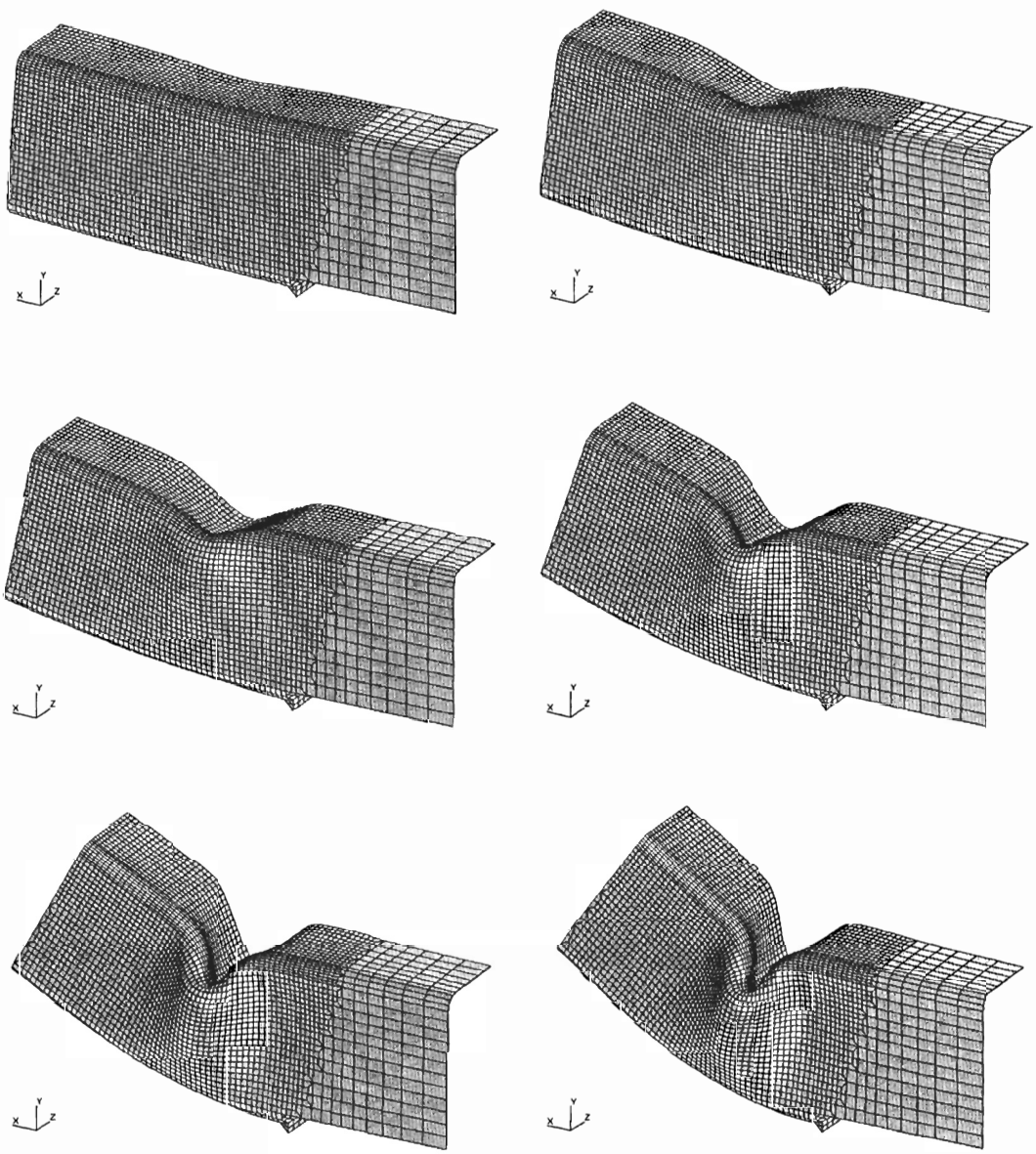

**Figure 7.17:** Progressive development of local buckle. Reading L → R then Top → Bottom; $\theta = 4.18°$, 7.79°, 11.9°, 18.7°, 28.4° and 35.3°

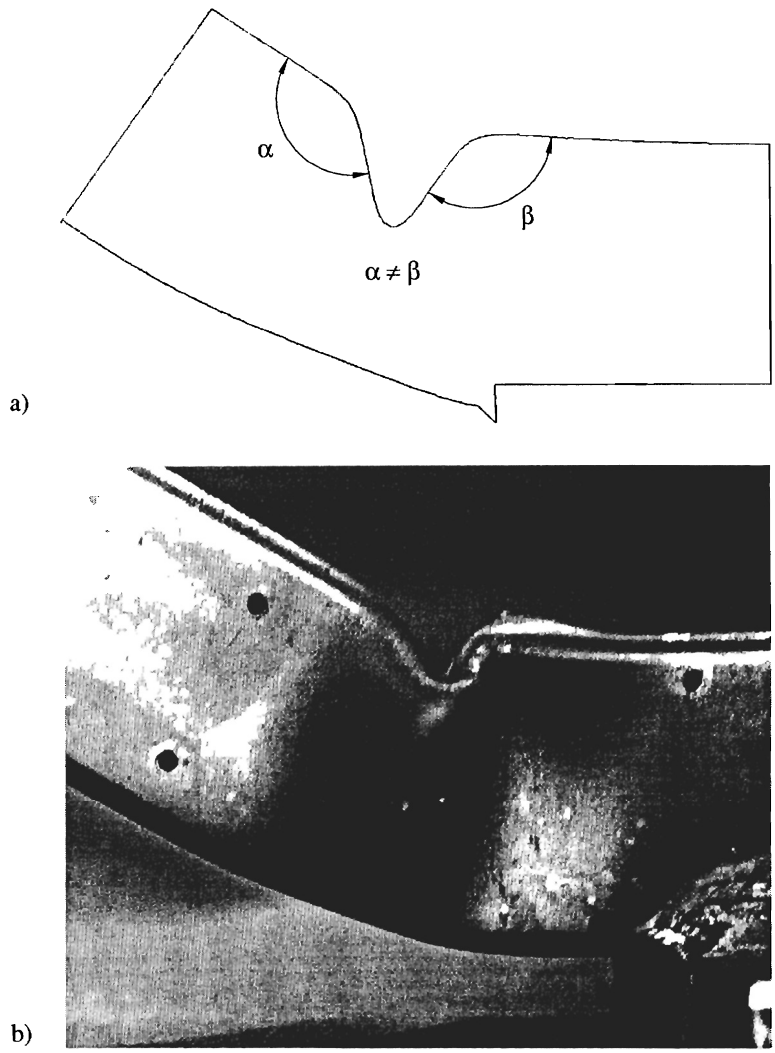


**Figure 7.18:** Buckle asymmetry

a) Longitudinal cross-section of buckle at $\theta = 36°$ - FE result and b) Physical buckle

### 7.3.3.2 MOMENT – ROTATION COMPARISONS

#### Static Analysis

A comparison of predicted and measured gross specimen response, i.e. *pendulum moment Vs pendulum rotation*, is shown in Figure 7.19. As is typical of FE – experimental comparisons, the FE elastic loading stiffness was greater than measured experimentally. To represent the physical flexibility not accounted for in the FE model, an additional component of elastic pendulum rotation was added to the FE results. Predicted gross specimen responses, pre-buckle and post-buckle, compared extremely well with the results from a typical quasi-static test.

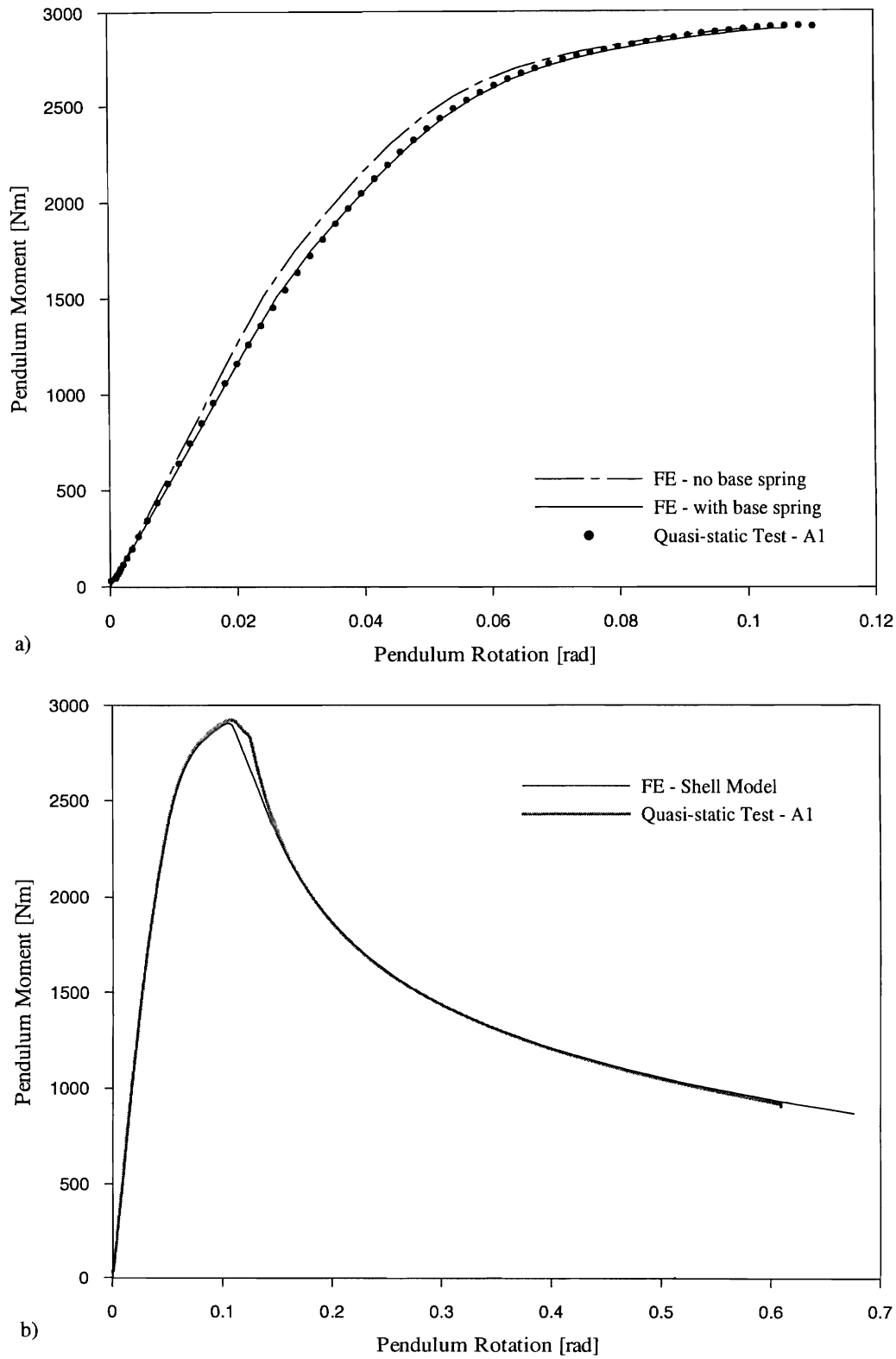


**Figure 7.19:** Comparison of FE and experimental gross specimen response

a) pre-buckle and b) complete

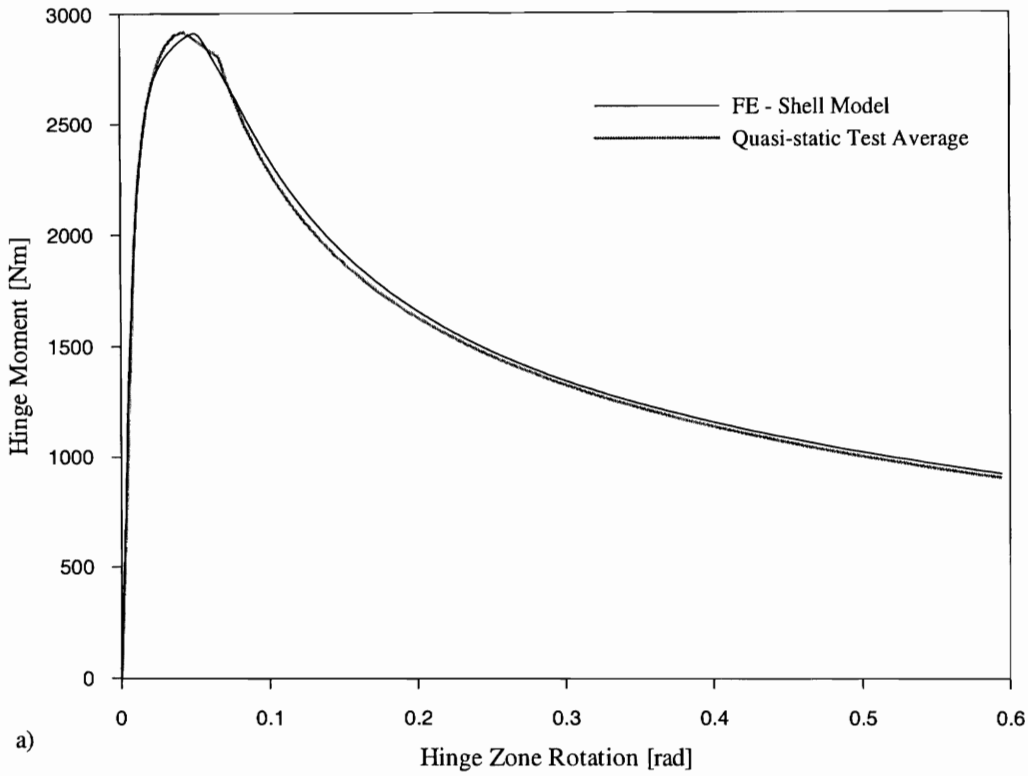


a)

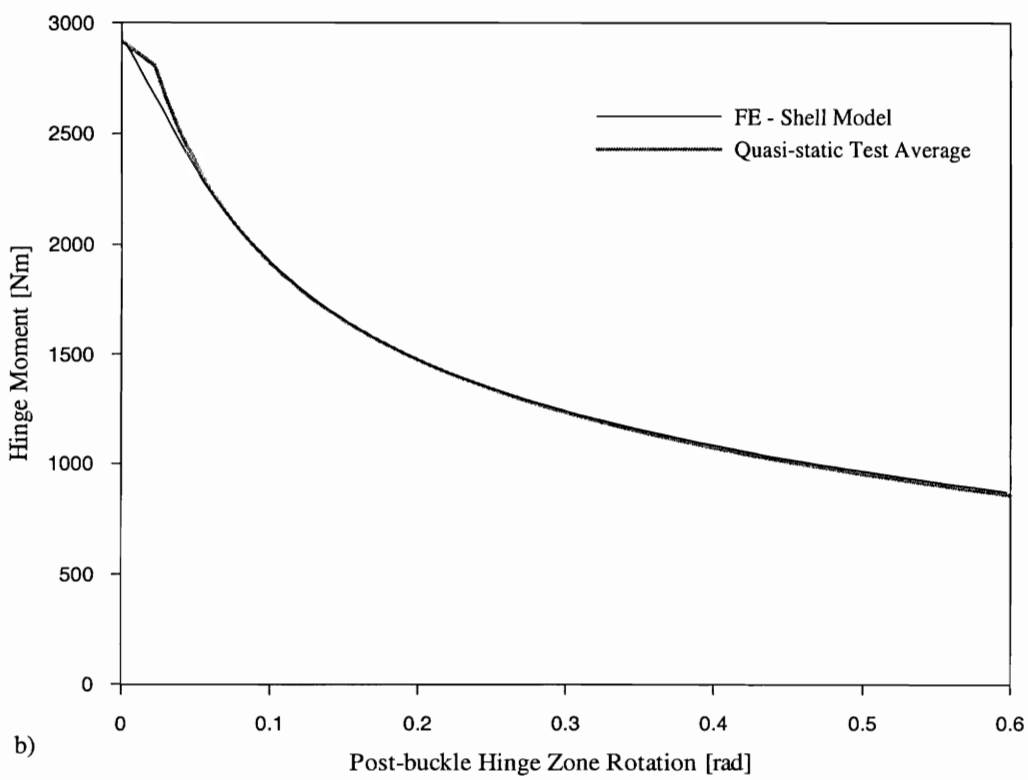


b)

**Figure 7.20:** Comparison of FE and experimental moment – rotation response

a) hinge zone and b) buckle mechanism

Predicted hinge zone $M$-$\theta$ response also compared well with the average experimental response, see Figure 7.20a. However, the FE solution did not predict the same point of buckle initiation. This was not unexpected since the instant of buckle initiation was dependent upon factors such as residual stress and initial imperfection, which were not included in the FE model.

The FE and experimental post-buckle or buckle mechanism responses, shown in Figure 7.20b, compared extremely well.

**Impact Analysis**

Figures 7.21, 7.22 and 7.23 show gross specimen, hinge zone and buckle mechanism responses. In each figure, the results for experimental, implicit dynamic FE and pseudo-dynamic FE are compared.

Generally there was very good agreement between the experimental and predicted responses. In particular the following points were noted.

- Experimental pre-buckle responses were higher than predicted by FE analysis. This was possibly due to underestimated yield stress strain rate sensitivity, particularly for the corner material.
- Apart from the obvious vibrations, the pre-buckle implicit FE hinge zone response was similar to and slightly higher than the pseudo-dynamic FE response. This was possibly due to the influence of buckle material inertia or the interaction between specimen vibrations and material strain rate sensitivity.
- The differences between the implicit and pseudo-dynamic hinge zone response curves were insignificant. This justified the pseudo-dynamic approach and the assumption that the influence of buckle material inertia could be neglected.
- The CPU time of the Pseudo-dynamic solution was ½ the CPU time of the implicit dynamic solution.
- There was excellent comparison between the FE and experimentally measured buckle mechanism responses.

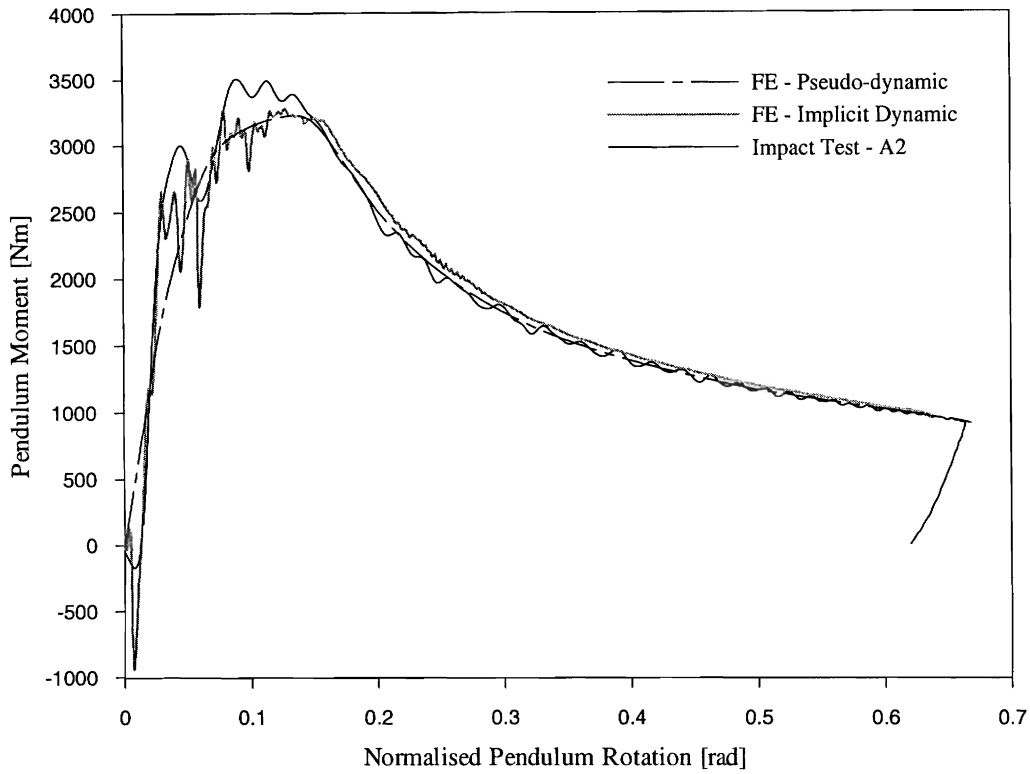


**Figure 7.21:** Normalised pendulum moment Vs Normalised pendulum rotation - Comparison FE and experimental

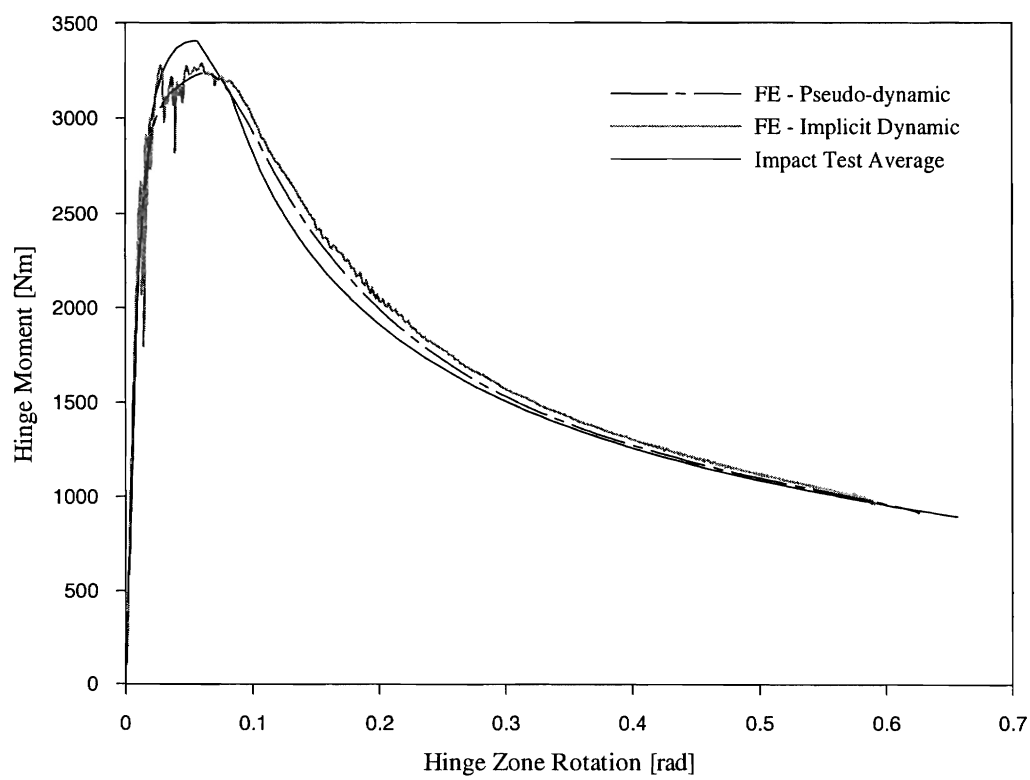


**Figure 7.22:** Hinge zone $M$-$\theta$ impact response – Comparison FE and experimental

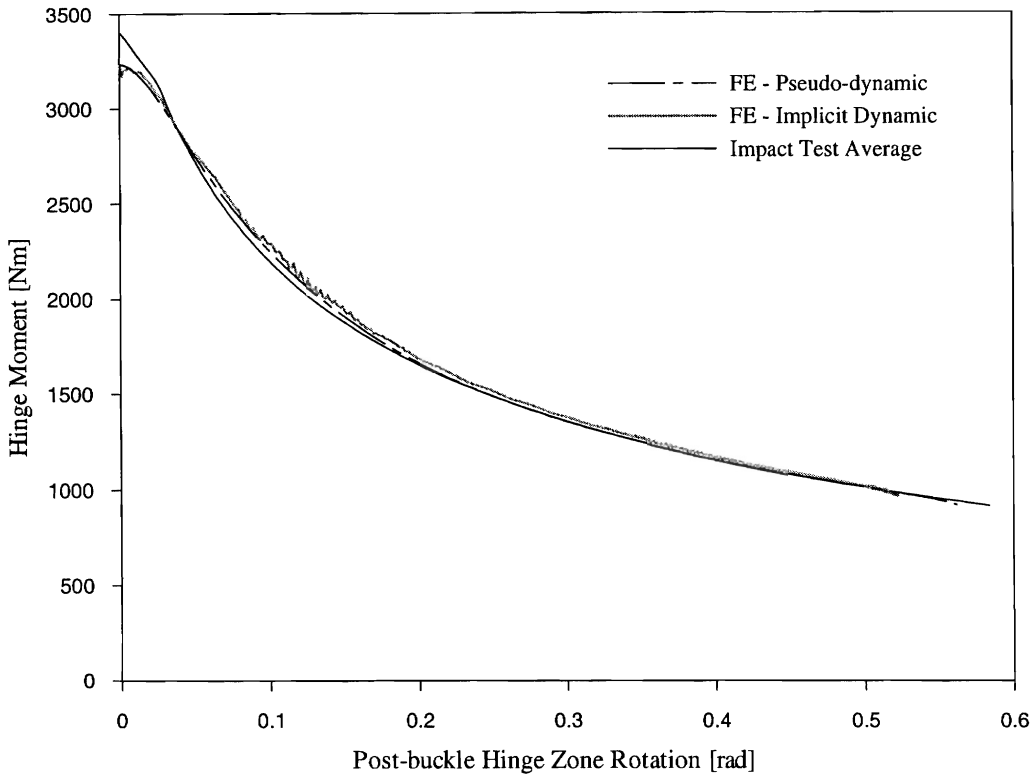


**Figure 7.23:** Buckle mechanism $M$-$\theta$ impact response – Comparison FE and experimental

The results from the implicit analysis were used to validate the derivation of pendulum work and specimen strain energy, from pendulum displacement and reaction force respectively. True and derived responses are compared in Figure 7.24. For clarity, only the initial response is shown. Beyond $\beta' = 0.2$ the true and derived results were equal. The results indicated that:

1. $\int M_{pend}\, d\beta$ (where $M_p$ = scaled reaction force), was an acceptable measure of specimen strain energy.
2. An acceptable measure of pendulum work could be derived from *pendulum displacement Vs time.*
3. At peak rotation, $\int M_{pend}\, d\beta$ was approximately equal to pendulum work derived from pendulum displacement, indicating that the net influence of specimen kinetic energy was negligible.

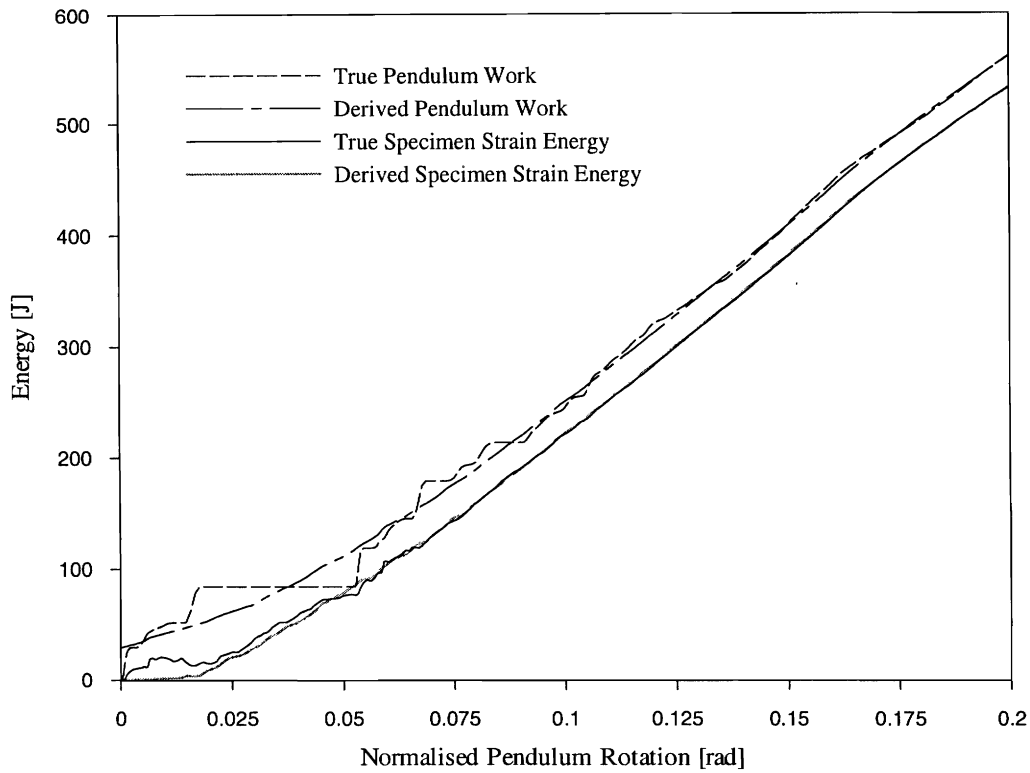


**Figure 7.24:** Pendulum work and specimen strain energy – Comparison true and derived

## Cowper-Symonds Material Strain Rate Sensitivity Model

The Cowper-Symonds material strain rate sensitivity model with coefficients $D$ = 40.4 $s^{-1}$ and $q$ = 5 is commonly used in FE and analytical impact analyses (Kormi et al. 1995; Jing & Barton 1998). The material tests discussed in Chapter 6 showed that this model significantly over estimated the strain rate sensitivity of the RHS wall material tested in this study, particularly at large strains, such as developed in the buckle. This is dramatically demonstrated in Figure 7.25, where the results from a pseudo-dynamic analysis with material strain rate sensitivity defined using this form of the Cowper-Symonds model are compared with the responses shown in Figure 7.22. (Apart from the definition of material strain rate sensitivity, the model was identical to the model that produced the results shown in Figure 7.22).

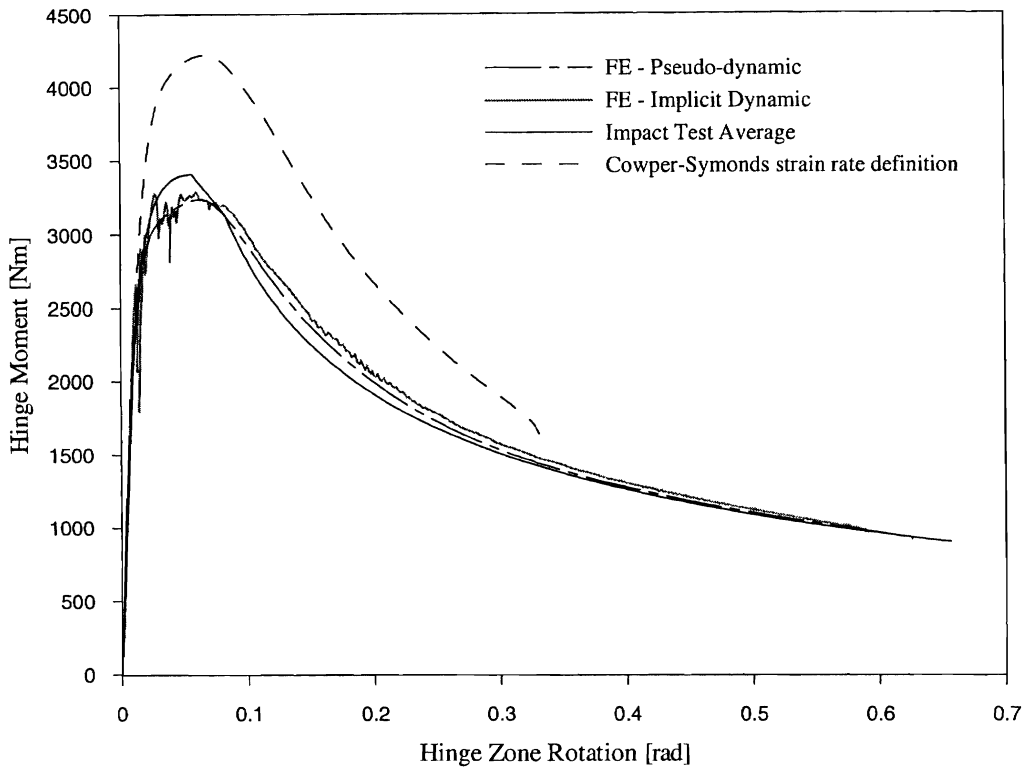


**Figure 7.25:** Hinge zone $M$-$\theta$ response using Cowper-Symonds material strain rate definition

### 7.3.3.3 LONGITUDINAL COMPRESSION FLANGE STRAIN

Longitudinal compression flange strains, measured at the buckle site, can be used to assess the accuracy of FE strain predictions. Figure 7.26a compares the pre-buckle longitudinal compression flange strain history at a location 40 mm from the edge of the specimen base plate. The FE and experimental results were in excellent agreement up to the point of compression flange buckle inception. The average strain rate during initial elastic loading was 0.57 $s^{-1}$, compared to 0.58 $s^{-1}$ measured in impact test A4. Figure 7.26b compares a typical experimental buckle profile with that predicted by FE modelling. The strains plotted were absolute quantities. Again there was good agreement. Strains at the centre of the buckle predicted by the pseudo-dynamic analysis were within 20% of the experimentally measured strains, which was more than adequate agreement in terms of strain rate predictions.

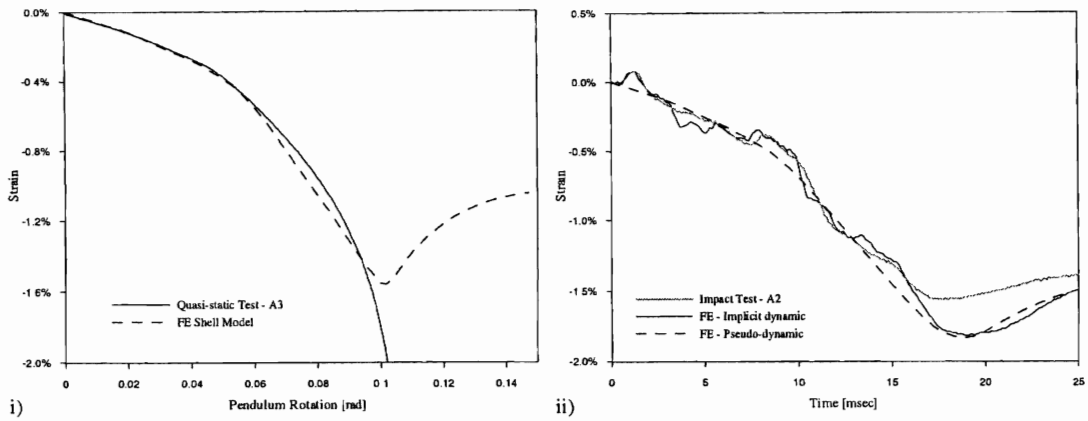


**Figure 7.26a:** Pre-buckle longitudinal compression flange strain (40 mm from base plate edge) - Comparison FE and experimental

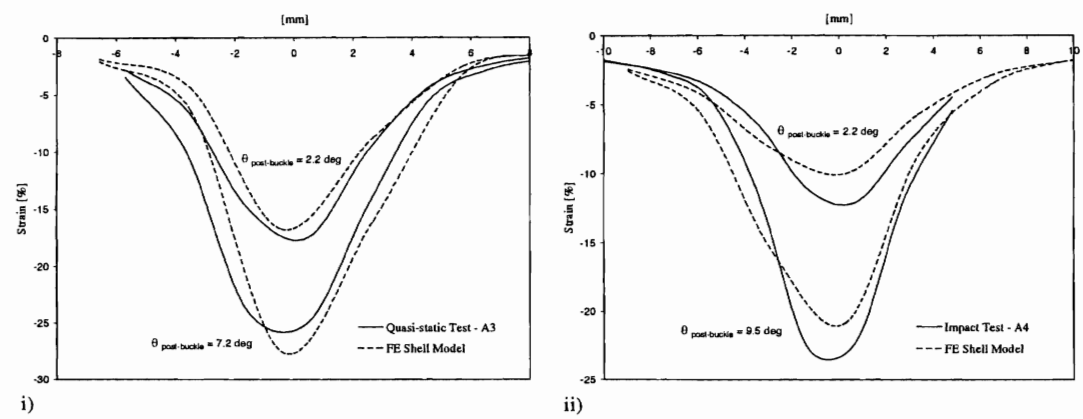


**Figure 7.26b:** Buckle profile – Comparison FE and experimental

### 7.3.3.4 COMPARISON IMPACT VS STATIC

Comparisons between impact and static FE responses would give similar results to those presented in Chapter 5, and are therefore not presented here. Comparisons between FE predictions of impact to static ratios and experimental impact to static ratios are useful. Ratios of impact to static plastic strain energy at peak rotation within the entire specimen, the hinge zone and the buckle mechanism, are given in Table 7.1.

**Table 7.1:** Impact:Static plastic strain energy comparisons at peak rotation

| Plastic strain energy at peak rotation within the ... | Finite Element Shell Model | | Experimental | |
|---|---|---|---|---|
| | Pseudo-Dynamic : Static | Peak Plastic Rotation | Impact : Quasi-static | Peak Plastic Rotation |
| Entire Specimen | 1.18 | $\beta'_{plas} = 0.63$ | 1.21†, 1.17‡ | $\beta'_{plas} = 0.61$ |
| Hinge Zone | 1.15 | $\theta^{plas} = 0.61$ | 1.15 | $\theta^{plas} = 0.59$ |
| Buckle Mechanism | 1.12 | $\theta^{plas}_{pb} = 0.55$ | 1.12 | $\theta^{plas}_{pb} = 0.54$ |

† Dynamic factor derived using $E^{impact}_{pend.}$ calculated from pendulum rotation and impact velocity. This value is considered to be the more accurate, see Section 5.6.4. ‡ Dynamic factor derived using $E^{impact}_{pend.}$ calculated from integration of the pendulum *moment-rotation* response shown in Figure 5.23.

### 7.3.3.5 FULL FIELD RESULTS

#### Equivalent Plastic Strain

Figure 7.27 shows a contour plot of equivalent plastic strain for the inner surface at $\theta \approx 36°$. Plastic strain in the buckle was clearly concentrated in material folding and rolling regions similar to those identified by Kecman (1979) and Seki and Sunami (1978). Localised equivalent plastic strains in the rolling region were as high as 100% to 150%.

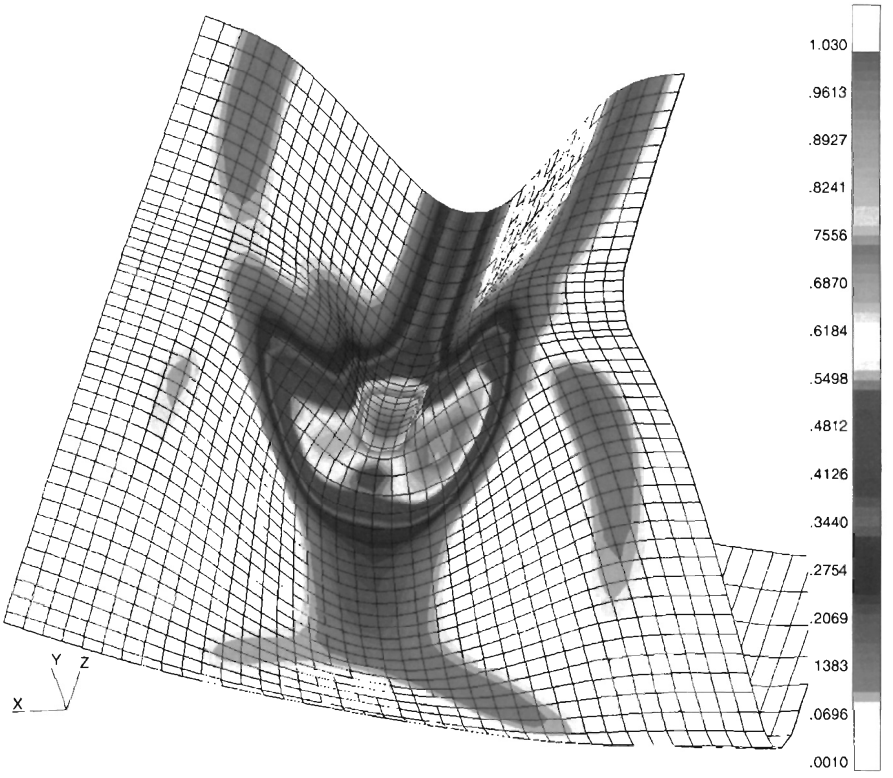


**Figure 7.27:** Equivalent plastic strain, inner surface at $\theta \approx 36°$

(Note: for clarity, displacements have been scaled by 0.8)

### Strain Energy

Figure 7.28 shows a contour plot of element plastic strain energy at $\theta \approx 36°$. Plastic strain energy was concentrated in regions of large plastic strain, i.e. material folding and rolling yield regions. It was notable that the majority of the plastic strain energy was absorbed in flattening the corner and rolling the web material adjacent to the corner. This was consistent with the energy distribution predicted by the analytical model of Seki and Sunami (1978) and Kecman (1979).

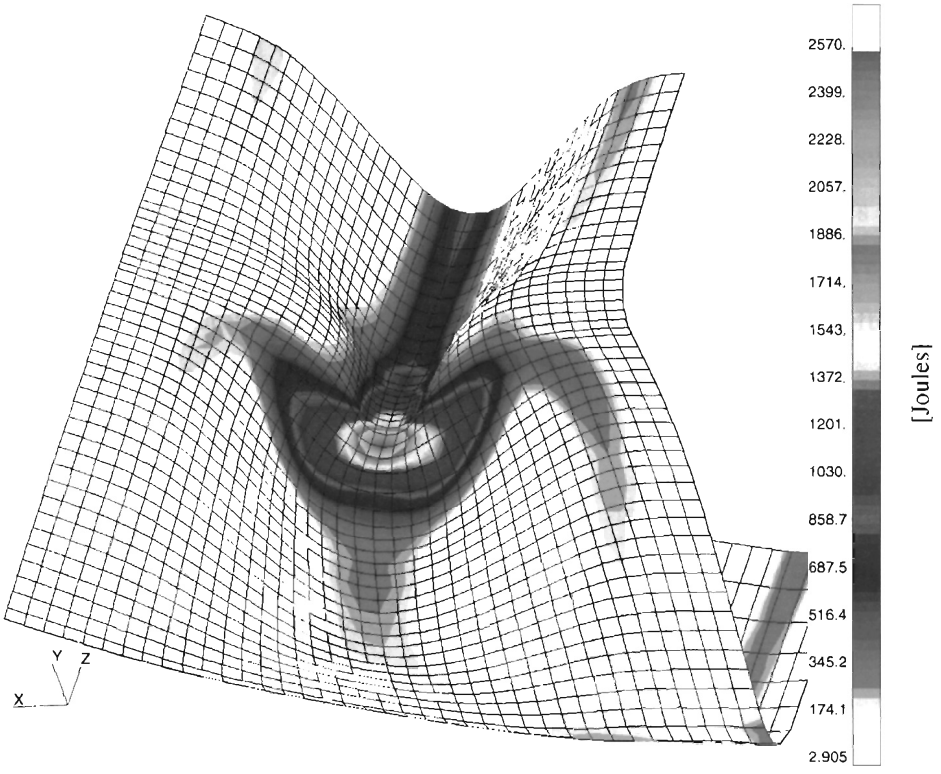


**Figure 7.28:** Element plastic strain energy, $\theta \approx 36°$

(Note: for clarity, displacements have been scaled by 0.8)

### Adiabatic Temperature

In high strain rate plastic deformations, viscoplastic and thermal effects compete. The increase in temperature caused by plastic work tends to reduce material flow stress, whilst high strain rates tend to increase material flow stress. Ducrocq et al. (1998) conducted tensile tests on E24 mild steel to derive parameters for thermo-viscoplastic (assumed adiabatic) and viscoplastic only (assumed isothermal) constitutive models. They then conducted FE analyses of an axially crushed 60x60x1.9 RHS using both constitutive models. The mean strain rate during the development of the first buckle

lobe was 200 $s^{-1}$ and the maximum temperature rise was 155°C. The final crush deformation of the tube obtained with the adiabatic model was 8% more than with the isothermal model.

When the element strain energy distribution shown in Figure 7.28 was scaled to represent adiabatic temperature rise, integration point temperature rises of between 200°C and 300°C were predicted. An analysis that included the thermal dependence of yield stress was not conducted. Such an analysis may have predicted lower temperature rises.

It should be remembered that up to UTS, the dynamic material properties used in this study were derived experimentally, and hence inherently accounted for thermal influences. However the material properties beyond UTS were not measured and therefore the definition of flow stress did not account for thermal influences on yield strength. Beyond UTS the concentration of plastic strain in the neck would have induced localised temperature increases, which at elevated strain rates, may have softened the material and reduced the hardening rate.

**Strain Rate**

In ABAQUS, strain rate sensitive yield stresses are a function of equivalent plastic strain rate. Equivalent plastic strain rate is not available as an output quantity, but is easily computed using backward differences:

$$\dot{\bar{\varepsilon}}_i^{pl} = \frac{\left(\bar{\varepsilon}_i^{pl} - \bar{\varepsilon}_{i-1}^{pl}\right)}{\left(t_i - t_{i-1}\right)} \tag{7.1}$$

where $\bar{\varepsilon}_i^{pl}$ is equivalent plastic strain at increment $i$ and $t$ is step time.

Routines were written to calculate integration point equivalent plastic strain rate and store the results in MSC-Patran for processing. Figure 7.29 shows contour plots of equivalent plastic strain rate for the outer surface. As expected, large equivalent plastic strain rates were associated with localised regions of equivalent plastic strain. Peak localised strain rates were as high as 30 $s^{-1}$ in the initial stages of buckle development and typically less than 2 $s^{-1}$ in the late stages of collapse. In the mid stages of collapse, around $\theta = 20°$, strain rates throughout the buckle were typically less than 10 $s^{-1}$.

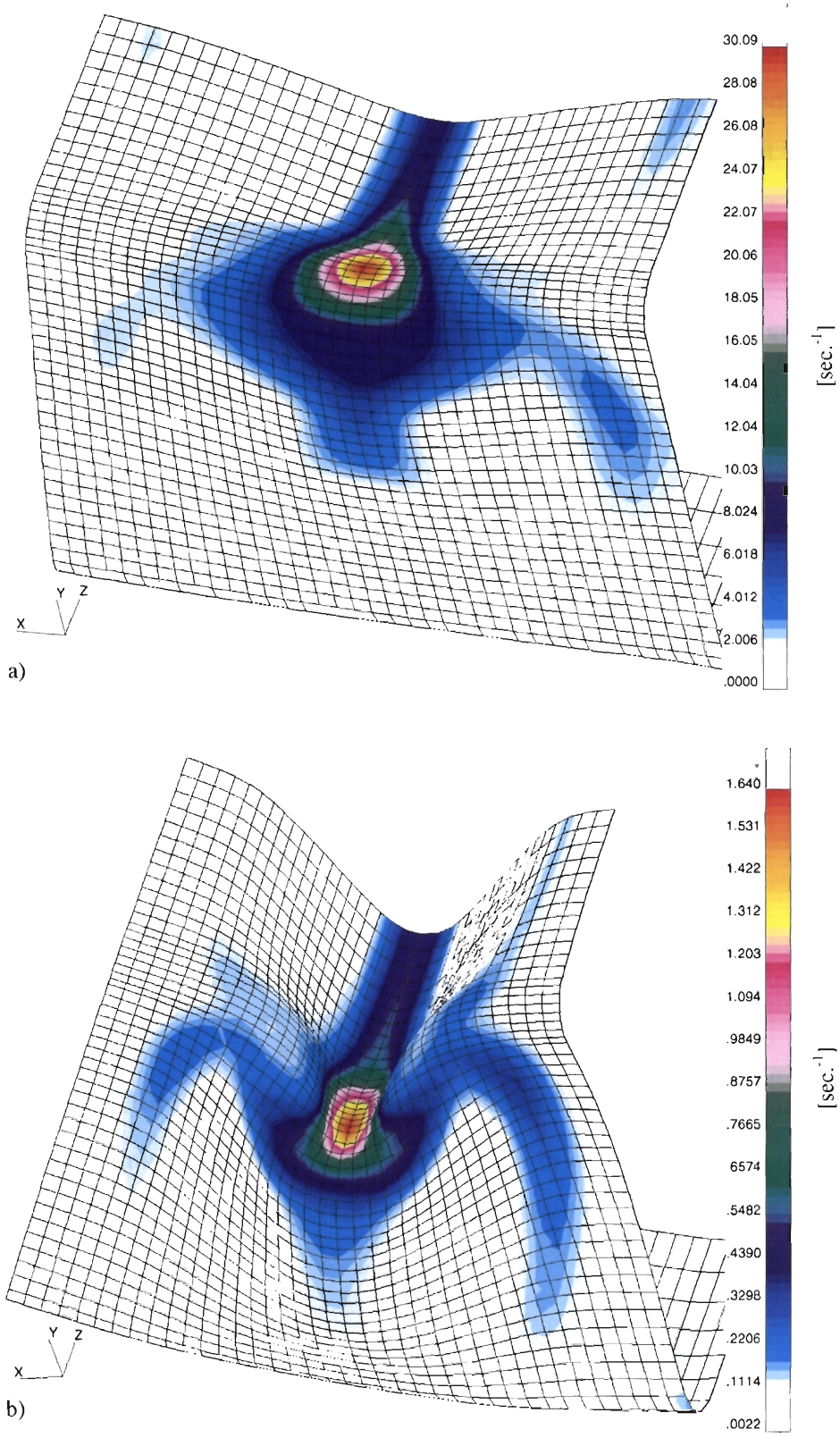


**Figure 7.29:** Equivalent plastic strain rate, outer surface, a) $\theta \approx 7.8°$ and b) $\theta \approx 36°$

(Note: for clarity, displacements have been scaled by 0.8)

A single average strain rate for the buckle region can be derived using a weighted average calculation. The most appropriate weighting quantity is incremental strain energy. Outer surface energy-weighted equivalent plastic strain rate, averaged over the entire buckle region, is plotted in Figure 7.30. The weighting factor in this plot was:

$$w_{i,j} = \frac{(E_{i,j} - E_{i-1,j})}{\sum_j (E_{i,j} - E_{i-1,j})} \tag{7.2}$$

where $i$ and $j$ are the increment and integration point indexes, respectively. This weighting function was calculated for the inner and outer surfaces separately.

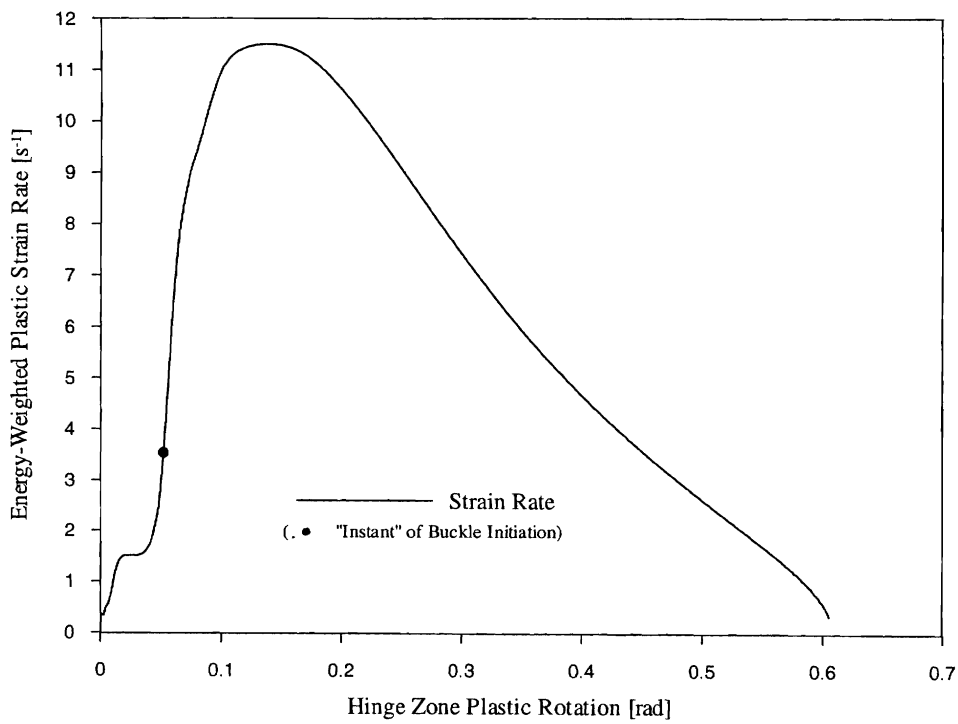


**Figure 7.30:** Energy-weighted equivalent plastic strain rate, outer surface

It is interesting to investigate the respective influences of loading rate and changes in geometry on the energy-weighted average plastic strain rate ($\dot{\varepsilon}_{e.w.avg}$). Defining:

$$\dot{\varepsilon}_{e.w.avg}(\theta) = \dot{\theta}(\theta) \times g(\theta)$$
$$g(\theta) = \frac{\dot{\varepsilon}_{e.w.avg}}{\dot{\theta}} \tag{7.3}$$

where: $\dot{\theta}(\theta)$ represents the influence of loading rate; and

$g(\theta)$ represents the influence of changes in buckle geometry.

The variation of $\dot{\varepsilon}_{e.w.avg}$, $\dot{\theta}$ and $g(\theta)$ throughout an impact event is plotted in Figure 7.31. Each quantity has been normalised to range from 0 to 1.

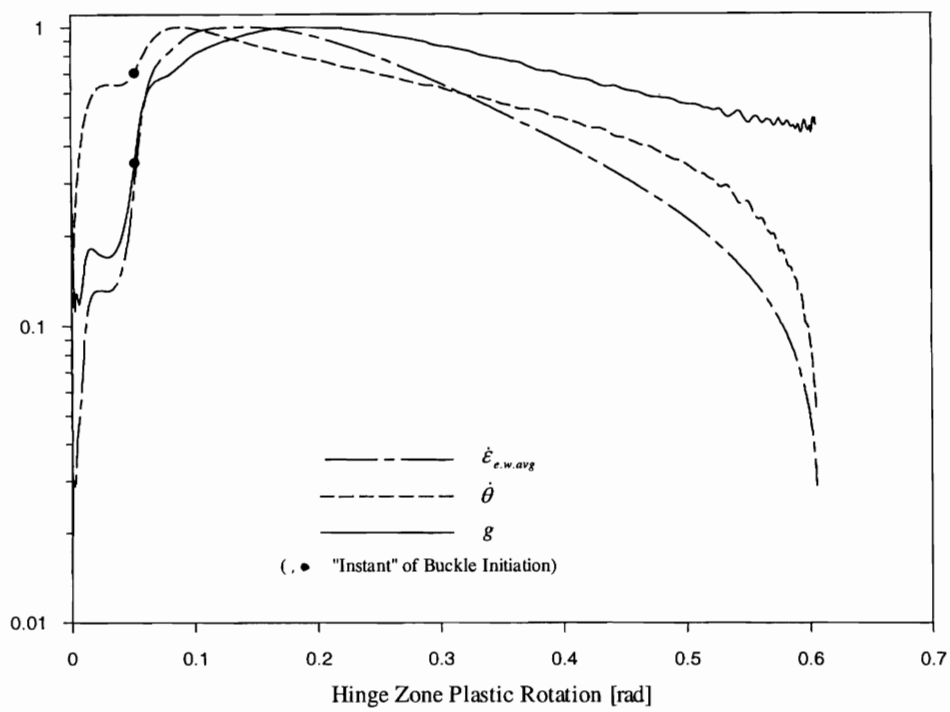


**Figure 7.31:** Relationship between average buckle strain rate, buckle geometry and hinge rotation rate

Some observations from Figure 7.31 are:

1. Geometry changes were the major factor contributing to the rapid rise in $\dot{\varepsilon}_{e.w.avg}$ at buckle initiation.
2. Geometry changes acted to increase the $\dot{\varepsilon}_{e.w.avg}$ up to $\theta \approx 0.2$.
3. For $\theta > 0.2$ geometry changes acted to decrease the $\dot{\varepsilon}_{e.w.avg}$, i.e. the change in $\varepsilon_{e.w.avg}$ for a given change in $\theta$ decreased as the buckle developed. This sensitivity decreased linearly with $\theta$.
4. For $0.2 < \theta < 0.45$ geometry changes and loading rate changes contributed equally to the reduction in $\dot{\varepsilon}_{e.w.avg}$.
5. For $\theta > 0.45$ the reduction in $\dot{\varepsilon}_{e.w.avg}$ was essentially entirely due to the reduction in loading rate.

## 7.4 CONCLUSIONS

Finite element analysis has proven to be an extremely useful investigative tool throughout this study. Relatively simple beam element models were successfully used to investigate specimen response to impact loading and to derive and prove various data processing procedures. This use of FE analysis in experimental design has great potential.

The excellent agreement between the predicted and measured $M$-$\theta$ response of the local buckle clearly demonstrated the predictive capability of modern FE codes for both static and impact loading conditions.

A key factor influencing the accuracy of FE predictions is the definition of material properties. It is important therefore to represent the true variation of material properties within a structure, in this case around the tube section. In impact analyses, it is also essential that material strain rate sensitivity definitions be appropriate to the strain range of the analysis. Ideally material strain rate sensitivity should be defined as a function of strain and strain rate i.e. $f(\varepsilon,\dot{\varepsilon})$, by defining complete $\sigma$–$\varepsilon$ curves at a range of strain rates or by using a material model similar to Jones (1993). If a constitutive model such as the Cowper-Symonds equation is used to define material strain-sensitivity it is essential that appropriate model parameters be used.

Whilst the accuracy of material definitions can be improved by "calibration" of the FE model against experimental results, this procedure would not normally be warranted in a design cycle. For design purposes, the FE predictions obtained using as-measured material properties would be adequate. A "calibration" procedure was conducted in this study to give an accurate base for the impact analysis.

Results from an implicit dynamic analysis indicated that the inertia of the material in the local buckle had a negligible effect on plastic hinge $M$-$\theta$ response. Therefore, the impact response of the specimen was investigated using a novel "pseudo-dynamic" solution procedure. The results from this pseudo-dynamic analysis, using measured material strain rate sensitivities, were in excellent agreement with the impact responses measured experimentally.

This pseudo-dynamic approach correctly accounts for the effect of material strain rate sensitivity within a static solution by appropriate control of the loading rate. The

approach also removes the need for a dynamic solver and can lead to reduced solution times. A pseudo-dynamic analysis of an impact event can be conducted whenever the influence of material inertia in the region of local deformation is negligible. This would typically not be the situation in structures where the initial response is dominated by inertia (Grzebieta & Murray 1986; Tam 1990; Abramowicz & Jones 1997). However the approach may be applicable for components such as vehicle chassis rails, which often contain collapse triggers to minimise the initial inertial response.

FE analysis can give insight into structural behaviour that would be too expensive or even impossible to test or measure. Insight into the temporal and spatial distribution of strain and strain rate within the buckle is summarised in the following key observations.

- Plastic strain in the buckle was clearly concentrated in material folding and rolling regions similar to those identified by Seki and Sunami (1978) and Kecman (1979).
- Localised equivalent plastic strains in the rolling region were as high as 100% to 150%.
- The majority of the plastic strain energy absorbed by the buckle was absorbed in flattening the corner and rolling the web material adjacent to the corner.
- Peak localised strain rates were as high as 30 $s^{-1}$ in the initial stages of buckle development and typically less than 2 $s^{-1}$ in the late stages of collapse. In the mid stages of collapse, around $\theta = 20°$, strain rates throughout the buckle were typically less than 10 $s^{-1}$.
- Strain energy weighted, average equivalent plastic strain rate ($\dot{\varepsilon}_{e.w.avg}$) calculated over the buckle was a maximum of 11.5 $s^{-1}$ at $\theta \approx 8°$, which was twenty times the initial elastic strain rate of 0.57 $s^{-1}$.
- Geometry changes were the major factor contributing to the rapid rise in $\dot{\varepsilon}_{e.w.avg}$ at buckle initiation. For hinge rotations between 0.2 and 0.45 buckle geometry changes and the decrease in loading rate contributed equally to the reduction in $\dot{\varepsilon}_{e.w.avg}$. Beyond $\theta = 0.45$ the reduction in $\dot{\varepsilon}_{e.w.avg}$ was essentially due to the reduction in loading rate.

# CHAPTER 8 ESTIMATION AND USE OF DYNAMIC SCALING FACTORS

## 8.1 INTRODUCTION

Designing for crashworthiness requires an assessment of a structure's response under crash or impact loading. Common approaches to assessing a structure's response to impact loading are full-scale impact testing, numerical analysis or a "hybrid" combination of numerical modelling and component analysis. The "hybrid" design approach is often the most cost effective and is particularly effective in the early stages of design. Treatment of local plastic hinge response separately from the global structure is the key to the simplicity and power of a hybrid analysis. This chapter assumes that the hybrid design approach has been adopted and what remains is to determine the impact response of the local plastic hinges. Three ways to determine these impact responses are by:

- Numerical modelling
- Instrumented impact testing
- Scaling a quasi-static response

This chapter draws on the quasi-static and impact bend tests, material tests, and detailed finite element modelling of Chapters 5, 6 and 7 to provide insight into the proper and successful use of the quasi-static scaling approach for predicting plastic hinge impact response during the design phase. In particular, a critical assessment is made of quasi-static scaling schemes used in the literature to predict RHS impact response.

The issues associated with the use of numerical modelling and instrumented impact testing, to predict and measure component impact response, were investigated in Chapters 5 and 7 respectively, and are not discussed further in this Chapter.

## 8.2 SCALING QUASI-STATIC RESPONSES

Because of the difficulties involved with conducting and interpreting impact tests, and because numerical modelling requires specialised software and expertise, plastic hinge impact responses are commonly predicted by scaling known quasi-static performance by a factor that accounts for the influence of material strain rate sensitivity. Typically the quasi-static response is obtained by testing or analytical modelling. Plastic hinge responses derived from detailed static FE analyses can be scaled, but a better approach to predict impact response would be to conduct a dynamic or pseudo-dynamic FE analysis.

As discussed in Chapter 6, the flow stress of mild steel increases with increasing strain rate and the ratio, $f$, of dynamic flow stress to quasi-static flow stress is a function of both strain and strain rate.

$$f(\varepsilon,\dot{\varepsilon}) = \frac{\sigma_{dyn}(\varepsilon,\dot{\varepsilon})}{\sigma_{stat}(\varepsilon)} \tag{8.1}$$

Therefore to calculate impact response by accounting directly for dynamic flow stress the full strain field must be known. In some "structures" the deformation mode is very simple and the distribution of strain rate can be derived, whereas in a region of local deformation like the buckle under investigation, the spatial variation of strain rate is much more difficult to define. To overcome this difficult requirement two predictive schemes are commonly used. They are similar, and often equivalent, but differ in their approach to accounting for the spatial and temporal variation of dynamic flow stress.

1. Theoretical scaling of flow stress: In this approach, impact response is calculated by scaling quasi-static flow stress in a static analysis.
2. Experimental scaling of response: In this approach, impact response is calculated by scaling a known quasi-static response by a factor $F_{dyn}$.

### 8.2.1 Theoretical Scaling of Flow Stress

This scheme takes a direct approach of accounting for the influence of material strain rate sensitivity and substitutes dynamic flow stress in a static analysis. This scheme is most commonly used to extend the application of static analytical models to the analysis of impact loading. The problem of predicting the variation of dynamic flow stress

throughout the structure is addressed by assuming that the material scaling factor, $f$, is constant spatially and temporally. This follows from the simplified rigid-plastic treatment of quasi-static flow stress in analytical models and the inability of most analytical models to predict instantaneous strain rates. It is interesting to note that, when the static response predicted by the analytical model is directly proportional to flow stress, this approach is equivalent to scaling the static response by a factor $F_{dyn} = f$ (Grzebieta & Dayawansa 1987; Vignjevic et al. 1993).

Because this scheme does not allow for the true spatial and temporal variation of dynamic flow stress, the approach is best suited to predicting the impact response of simple "structures" with limited spatial and temporal variation of strain rate. When the deformation is more complex, the accuracy of the impact response predicted by this approach is dependent on how well the dynamic flow stress throughout the structure is represented by the single scaling factor $f$. The appropriate choice of a material model and strain rate, to calculate $f$, is now discussed.

#### 8.2.1.1 MATERIAL MODEL

It is commonly, indeed almost exclusively assumed, that the scaling factor $f$ is independent of strain (thus strain-hardening and strain rate effects are decoupled) and that material strain rate dependence is given by the Cowper-Symonds function, Equation 8.2.

$$f = \frac{\sigma_{dyn}}{\sigma_{stat}} = 1 + \left(\frac{\dot{\varepsilon}}{D}\right)^{\frac{1}{q}} \tag{8.2}$$

Coefficients of $D = 40.4\text{s}^{-1}$ and $q = 5$ are often used in the Cowper–Symonds model to describe the strain rate sensitivity of mild steel. The Cowper–Symonds model with coefficients $D = 40.4\text{s}^{-1}$ and $q = 5$ was derived from a curve fit to the lower yield stress of an annealed low-carbon steel tested by Manjoine (1944) at strain rates from approximately $1\text{x}10^{-6}$ to 300 $\text{s}^{-1}$. As previously noted in Chapters 2 and 6, the use of the Cowper–Symonds model, with coefficients $D = 40.4\text{s}^{-1}$ and $q = 5$, in large strain crashworthiness design calculations (material strains in the buckle shown in Figure 7.27 are typically > 50%), has been questioned by Wierzbicki and Akerstrom (1977) and Jones (1983). The pseudo-dynamic FE results presented in Figure 7.25 clearly demonstrated that the Cowper–Symonds model, with coefficients $D = 40.4\text{s}^{-1}$ and $q = 5$,

significantly overestimated structural strength and is therefore inappropriate in large strain crash analyses. Wierzbicki and Akerström (1977) obtained a similar result. Abramowicz and Jones (1986) present two alternative coefficient sets that predict different increases in flow stress. They remark that *"the disparity between the predictions ... emphasises the lack of adequate experimental data on the dynamic plastic behaviour of materials with large strains which are encountered in the dynamic progressive crushing of square tubes."*

Whilst there are several studies into the strain rate sensitivity of steels at large strains, the author is unaware of any previously published test data for the strain rate sensitivity of the material in cold-rolled tube walls, at small or large strains. This is despite a large body of research into the impact response of tubular sections. Given the significant amount of cold work that is done during the manufacture of RHS, it was possible that the strain rate sensitivity of RHS wall material would be different to that of the steels tested in published studies. For this reason a series of uni-axial tensile tests were conducted over the strain rate range $10^{-4}$ to 10 $s^{-1}$ to determine the nature of strain rate sensitivity in RHS wall material, see Chapter 6. The study concluded that the strain rate sensitivity of the RHS wall material tested was not atypical, compared to other steels, and in particular:

1. For crashworthiness applications, which involve large plastic strains, material strain rate sensitivity should be defined at strains near UTS.
2. The Cowper-Symonds functional form with coefficients $D$ = 7,099 $s^{-1}$ and $q$ = 4.35 could be used to describe the strain rate sensitivity of the RHS wall material at strains near UTS. These coefficients predicted similar values of $f$ to those predicted by the coefficients of $D$ = 6,844 $s^{-1}$ and $q$ = 3.91 proposed by Abramowicz and Jones (1984a) to describe the strain rate sensitivity of mild steel at large strains.

#### 8.2.1.2 STRAIN RATE

Having determined an appropriate model to describe material strain rate sensitivity, it remains to derive an appropriate value for the strain rate parameter in this model. Various approaches have been used for estimating this single strain rate. The appropriate method will depend on the nature of the collapse under investigation. Some examples of the theoretical scaling approach found in the literature, are reviewed below.

Perrone (1965) proposed using a single dynamic flow stress, calculated using an estimate of the initial strain rate in the structure. Perrone (1965), Jones (1989a), Duffey and Karpp (1979) and Reid (1983) used this approximate approach to analyse simple "structures" in which there was essentially a single region of energy absorption and the influence of finite displacements or geometry changes was not important.

When there is a change in the deformation mode, in particular the development of membrane forces, it is not appropriate to calculate $f$ using the initial strain rate. For this class of problem Perrone and Bhadra (1979) proposed using an average strain rate equal to half the maximum strain rate. The maximum strain rate was noted to occur when approximately half the initial kinetic energy had been absorbed as plastic work, or alternatively, at the point in the response corresponding to 2/3 of maximum deflection (Perrone & Bhadra 1984). Unlike the use of initial strain rate, the implementation of this approximation involves a simple iteration. This approach has been used by Jones (1989a) and Zhu et al. (1994).

The effectiveness of these two strain rate estimates resulted from the fact that for the class of problem considered 1) the dynamic flow stress was essentially constant whilst the bulk of the impact energy was absorbed and 2) the collapse geometry and strain rate field were simple. A single strain rate was therefore sufficient to account for material strain rate sensitivity. Furthermore this strain rate could be derived from analytical analysis of the simple collapse geometry.

In more complex structures, several separate regions of deformation may develop during impact loading. Some account must be taken of the variation of dynamic flow stress between these regions, if an accurate prediction of overall impact response is to be obtained.

Zhu et al. (1994) studied the response of fully clamped rectangular mild steel plates impacted by a wedge. They calculated individual flow stress scaling factors for the two distinct regions of deformation in the plate, and then used an area weighted average to calculate an effective dynamic flow stress for the overall response. Using this approach they achieved good correlation with experiments.

Abramowicz and Jones (1984a) considered the much more complex problem of the dynamic axial crushing of square tubes. A detailed kinematic model of the buckling

mode, indicated that approximately 1/3 of the total energy was absorbed in the regions of rolling deformation. Thus, they considered it reasonable to assume a single dynamic flow stress throughout the structure, based on an estimate of the average strain rate in the rolling region. Values of $F_{dyn}$ derived using this procedure "*agreed reasonably well*" with experimental scaling factors for circular and square tubes. Jones (1989a p. 408) noted that the theoretical scaling factors for the square tubes "*tended towards a lower bound of the experimental values*" and that "*This underestimate may be due partly to the difficulty of calculating a mean strain rate in a square tube...*".

#### 8.2.1.3 SCALING FLOW STRESS – FE MODELS

If a detailed FE analysis is an option, it is preferable that a dynamic or pseudo-dynamic analysis be conducted, as the true variation of dynamic flow stress through the structure will be calculated. Sometimes, static analyses are used to analyse impact events (Smith 1989; Thornton & Yeung 1990). The dynamic material definitions used in these examples were calculated prior to running the analysis by scaling the quasi-static material properties by a single factor *f*. The difference between running this type of analysis and simply scaling the static result arises from the possible variations of the strain distribution due to the increased flow stress.

### 8.2.2 Experimental Scaling of Gross Response

In crashworthy components that crush and buckle, there are many separate regions of folding, rolling and membrane deformation which develop during the impact. In many cases the complex variation of flow stress cannot be accounted for by simple analytical models of these collapse modes, and the quasi-static response must be obtained by experimental testing. By the same argument the complex variation of dynamic flow stress cannot be predicted. Recognising this difficulty, the philosophy of the quasi-static scaling approach applied to this class of structure is that from a design perspective, it is not actual strain rates that are of interest but the overall effect of loading rate on plastic hinge collapse response (Kecman 1993a, 1993b).

A "dynamic factor", $F_{dyn}(\delta)$, can be defined in terms of some chosen response quantity (e.g. hinge moment, absorbed energy), as given below.

$$F_{dyn}(\delta) = \frac{Response_{imp}(\delta)}{Response_{stat}(\delta)} \tag{8.3}$$

Since material Young's modulus is strain rate insensitive, the elastic component of the chosen response quantity will be strain rate insensitive. Therefore, only the plastic component of the response needs to be scaled, and $F_{dyn}(\theta)$ can be defined as the ratio of plastic responses.

$F_{dyn}$, as defined in Equation 8.3, will vary with collapse deformation, $\delta$. The variation of $F_{dyn}$ for hinge moment and $F_{dyn}$ for hinge zone plastic strain energy was shown in Figures 5.21 and 5.22. Figure 5.21 is repeated below.

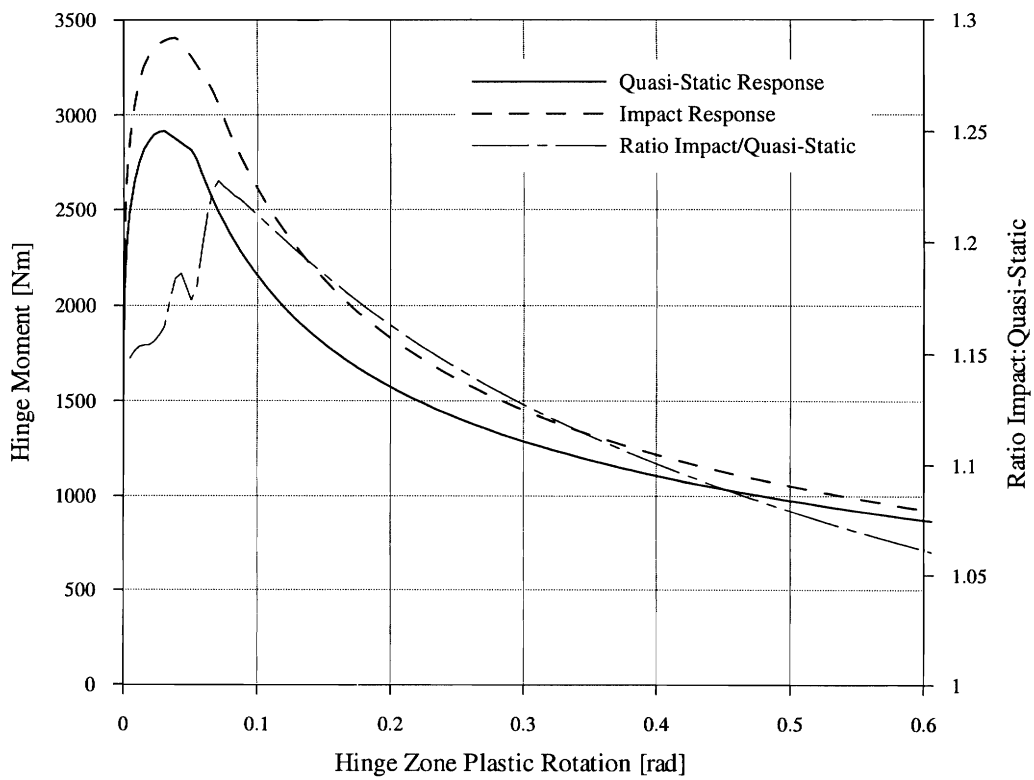


**Figure 8.1:** Comparison of hinge zone $M$-$\theta$ response from quasi-static and impact tests (Figure 5.21)

In practice, for the sake of simplicity, a constant $F_{dyn}$ factor is used and is defined as the impact to quasi-static ratio of a single valued response quantity e.g. total energy capacity, Equation 8.4. This approach implicitly assumes that the deformed mode shape is equivalent under quasi-static and impact loading, that the impact response has the same form as the quasi-static response and that inertial effects are negligible.

$$\text{constant } F_{dyn} = \frac{Response_{impact}}{Response_{static}} \tag{8.4}$$

The factor $F_{dyn}$ is usually obtained directly, or indirectly via an empirical model, from physical quasi-static and impact tests.

Physical impact tests to derive $F_{dyn}$ are usually uninstrumented since the quasi-static scaling approach would not be required if results from an instrumented test were available. For this reason total absorbed energy, which can be determined with a minimum of instrumentation, is commonly used to derive $F_{dyn}$.

Experimentally determined $F_{dyn}$ factors properly account for material strain rate sensitivity because the spatial and temporal variations of dynamic flow stress are "calculated by the component" during the test. Experimentally determined scaling factors also inherently account for the effects of inertia. Therefore, if inertial effects are not negligible, the scaling factor will be appropriate only for the particular combination of quasi-static and impact collapse modes tested and possibly only for the particular impact velocity of the test.

Empirical models defining $F_{dyn}$ as a function of parameters such as material thickness, flow stress, component geometry and loading rate are often derived by applying a regression analysis to a matrix of individual $F_{dyn}$ values. Because in terms of overall component response the concept of a single strain rate is meaningless, empirical $F_{dyn}$ functions are usually defined as a function of loading rate, since loading rate has physical meaning to a designer. Various empirical models have been derived in the literature including linear (Ohkubo et al. 1974), logarithmic (Thornton 1975) and power law functions (Tani & Funahashi 1978). The complexity of structural behaviour modelled using the empirical approach has ranged from the axial crush of "closed-hat" sections (Ohkubo et al. 1974) to the frontal crush of complete vehicles (Prasad & Padgaonkar 1981).

In complex components, because gross response is not linearly related to material behaviour, the form of the $F_{dyn}$ function will not necessarily be the same as the model that defines material strain rate sensitivity. Sometimes, however, the same function is used, e.g. Tani and Funahashi (1978). In this case the strain rate parameter is best described as an equivalent strain rate and, depending on the geometry of the collapse mode, may not be representative of actual strain rates. Additionally, the coefficients of the model will not necessary be the same as determined by material testing. However, in circumstances where a particular deformation region dominates the response, the equivalent strain rate may have some physical meaning.

When available, appropriate empirical $F_{dyn}$ models quickly provide predictions of impact response that are sufficiently accurate for use in the early stages of design. However, the applicability of empirical scaling factors is restricted to the specific class of structure and loading conditions for which they were derived. When a suitable empirical model is not available, a value of $F_{dyn}$ for any component can be obtained directly by conducting quasi-static and impact tests.

## 8.3 SCALING THE PLASTIC HINGE RESPONSE OF RHS

The broader issues associated with the quasi-static scaling approach for predicting impact response have been discussed above with reference to the use of the approach in the literature. The following section focuses on the application of the quasi-static scaling approach to predicting the plastic hinge response of RHS under impact bending loads. There are only two quasi-static scaling schemes used in the literature for this application, both proposed by the same author.

### 8.3.1 Kecman's Theoretical Scaling Scheme

In his Ph.D. thesis, Kecman (1979) proposed a quasi-static scaling scheme to predict the plastic hinge response of RHS under impact flexural loading. The same procedure has subsequently been used by Kecman and Tidbury (1982) and Vignjevic et al. (1993).

Kecman (1979) used a hybrid analysis to study the collapse of a single bus ring frame subjected to quasi-static and impact loading. Quasi-static hinge response was predicted using the analytical model developed by Kecman in his thesis. Impact hinge response was predicted using the same model, with material properties scaled by a single constant factor to account for material strain rate sensitivity. This factor was derived using material models from the literature and an estimate of the initial elastic strain rate at the hinge site. In this respect the approach is in the spirit of Perrone (1965). It was assumed that all hinges in the ring experienced the same loading rate. Comparisons between predicted and measured responses were presented for two ring frames.

Ring A: Conservative predictions of material strain rate sensitivity gave $f$ = 1.226 for yield stress and $f$ = 1.08 for flow stress. Using these scaling factors, and after compensating for a material failure during the impact test, an impact *load-deflection* response for the ring was predicted which was in apparent agreement with the measured

response. The material failure limited the scope of comparisons, therefore a second ring test was compared.

Ring B: In this case a scaling factor of $f$ = 1.31, derived from the Cowper-Symonds model with coefficients of $D$ = 40.4 $s^{-1}$ and $q$ = 5, was used to scale flow stress. For the same energy input, the predicted and measured deflected shapes of the ring compared well.

How can two different scaling factors both predict impact responses for similar ring frames that apparently compare well with experimental results? The following comments are offered.

Ring A: The comparison of predicted and measured pendulum contact force was complicated by the influence of ring inertia, material failure and different amounts of pre-collapse pendulum rotation. It was therefore difficult to make a true assessment of the influence of strain rate sensitivity and to assess the real accuracy of the scaling factor. This test result is therefore disregarded.

Ring B: The theoretical model used by Kecman assumed all energy was absorbed by buckle rotation at concentrated hinge sites, whereas in the physical test it would be expected that some distributed plasticity would develop in the ring members before buckle formation. For a given energy input, the modelling approach used by Kecman would predict larger ring distortions than a model that properly distributed pre-buckle plastic strain. The agreement between predicted and measured deflected shape suggested that this over estimation was compensated for by the choice of scaling factor, i.e. the scaling factor was too high.

The purely theoretical hybrid analysis procedure used by Kecman above was used by Kecman and Tidbury (1982) to predict the rollover response of a complete coach frame. Again, an initial elastic strain rate together with the Cowper-Symonds model ($D$ = 40.4 $s^{-1}$, $q$ = 5) was used to scale material properties, and it was assumed that all hinges in the frame experienced the same rotation rate. The purely theoretical analysis predicted peak deflections that were on average only 5% greater than measured experimentally. The maximum error was 15%. These results did not take into account factors such as:

- equivalence between theoretical ring frame loading and actual impact loading.
- elastic springback of the frame.
- energy absorbed by the real bus structure other than by plastic hinge rotation.

It is not known what percentage of the actual bus kinetic energy was assumed to be absorbed by the framework in the theoretical analysis. It is likely that it was in the order of 75% as specified in ECE regulation 66. More recently, Kecman and Randell (1996) stated that in their experience the theoretical energy absorption could be reduced to 62% of the vehicles kinetic energy, as specified in ADR 59/00. If the analysis was repeated with this reduced energy requirement, the theoretical analysis may under estimate test deflections. Given that the modelling approach tends to overestimate deflections, as explained for Ring B above, it is possible that the scaling factor of 1.32 used by Kecman and Tidbury was too high.

Kecman's analytical model indicated that the moment response of the local buckle was directly proportional to flow stress, hence the flow stress scaling factor derived using Kecman's scheme could be used as an $F_{dyn}$ factor to directly scale a quasi-static moment response.

Vignjevic et al. (1993) used this approach to derive impact $M$-$\theta$ response curves from experimentally measured quasi-static responses. These component responses were used in a dynamic hybrid analysis of a simple framework. A scaling factor of 1.6 was derived for an impact velocity of 11 $ms^{-1}$. This factor was noted as being "*rather high*" and the underestimation of framework displacement in the latter collapse stages, compared to measured displacements, was attributed to the "*high and constant strain rate factor*". Vignjevic et al., suggested that the scaling factor should be determined using a material model for the strain rate sensitivity of maximum flow stress, not yield stress. The appropriate choice of a material model was discussed in Section 8.2.1.1. Abramowicz and Jones (1984a) recommended using the Cowper-Symonds model with coefficients $D$ = 6,844 $s^{-1}$, $q$ = 3.91 to derive impact scaling factors when the collapse involved large strains. For the initial elastic strain rate of 4.07 $s^{-1}$ these coefficients predicted a scaling factor of just 1.15. It is difficult to assess how calculations based on this factor would compare with experimental results, however it is likely that the calculated response would overestimate framework distortion, i.e. the new scaling factor would be too low.

Unfortunately, given the unknowns and uncertainties in the results of Kecman and others presented above, no specific conclusion can be drawn on the accuracy of the theoretical quasi-static scaling procedure proposed by Kecman. However it is possible that the scheme over estimates the strain rate enhancement of plastic hinge response. To better assess the accuracy of the theoretical quasi-static scaling procedure proposed by Kecman, the approach was applied to the bend results obtained experimentally in Chapter 5.

The initial elastic strain rate at the hinge site is easily estimated from a simple linear analysis of a cantilever with point loading at the tip.

$$\delta = \frac{PL^3}{3EI} \tag{8.5}$$

$$\varepsilon_h = \frac{M_h y}{EI} \tag{8.6}$$

Combining Equations 8.5 and 8.6 gave:

$$\varepsilon = \frac{3 \times \delta \times l_h \times y}{L^3} \tag{8.7}$$

$$\delta = V_0 \times t \tag{8.8}$$

Combining Equations 8.7 and 8.8 gave:

$$\dot{\varepsilon} = \frac{3 \times V_0 \times l_h \times y}{L^3} \tag{8.9}$$

Where; $V_0$ = impact velocity at tip of cantilever, $L$ = cantilever length and $l_h$ = distance from impact point to the hinge site.

Substituting the following values from impact test A4 into Equation 8.9, $l_h$ = 1.0 m, $y$ = 0.025 m, $L$ = 1.040 m and $V_0$ = 7.55 ms$^{-1}$, gave $\dot{\varepsilon} = 0.51\,\text{s}^{-1}$. This result compared well with the average initial elastic strain rate measured in impact test A4 of 0.58 s$^{-1}$. Substituting $\dot{\varepsilon} = 0.58\,\text{s}^{-1}$ into Equation 8.2, with coefficients $D$ = 40.4 s$^{-1}$ and $q$ = 5, gave $F_{dyn}$ = 1.43. Multiplying the average measured quasi-static moment response by this factor would increase pendulum work, hinge zone energy and buckle energy by the same factor of 1.43. The corresponding experimental plastic energy ratios, calculated at a deflection corresponding to peak impact deflection, were 1.21, 1.15 and 1.12. Clearly the scaling scheme as proposed by Kecman led to an erroneous prediction of impact

response in the present case. Given this poor result, Kecman's choice of material strain rate sensitivity model and strain rate are reviewed below.

The intent of Kecman's theoretical method was to directly account for material strain rate sensitivity by scaling flow stress. To obtain the dynamic flow stress scaling factor $f$ Kecman's method used a material model that described the strain rate sensitivity of lower yield stress (i.e. the Cowper-Symonds model with coefficients $D$ = 40.4 $s^{-1}$ and $q$ = 5). However, it was concluded in Section 8.2.1.1 that in large strain applications flow stress scaling factors should be derived using the strain rate sensitivity of flow stress at UTS. Using the Cowper-Symonds coefficients derived in Chapter 6 for the flow stress at UTS of RHS wall material, i.e. $D$ = 7,099 $s^{-1}$ and $q$ = 4.35, in Equation 8.2 gave $F_{dyn}$ = 1.115 for $\dot{\varepsilon} = 0.58\,\text{sec}^{-1}$. This was an improved prediction of $F_{dyn}$ for pendulum work and was a good prediction of $F_{dyn}$ for buckle energy. Importantly it was a conservative prediction.

This result is particularly surprising since the initial elastic strain rate was obviously not related to the spatially and temporally varying strain rates within the buckle (see Section 7.3.3.5). Furthermore, rearranging Equation 8.9 gave $\dot{\varepsilon} \approx \frac{3 \times y \times \dot{\theta}}{L}$, which incorrectly suggested that, for a given section geometry and hinge rotation rate, the strain rate would be a function of the cantilever length $L$.

This dilemma regarding the use of the initial elastic strain rate to calculate $f$ can be resolved by considering Kecman's approach as an example of direct $F_{dyn}$ scaling. Thus, rather than being considered representative of actual strain rates within the buckle, the initial elastic strain rate is now considered to be an "equivalent" or an "effective weighted average" strain rate for the combination of actual buckle behaviour and the chosen model for $F_{dyn}$. In this instance, using the Cowper-Symonds model with $D$ = 7,099 $s^{-1}$ and $q$ = 4.35, the "equivalent" strain rate that predicts the measured value of $F_{dyn}$ for buckle plastic energy is approximately equal to the initial elastic strain rate. The reason for this result, and proof that it is generally true for RHS, cannot be demonstrated by rational consideration of the actual strain rates within the buckle. Thus, the success of this combination as an $F_{dyn}$ scaling scheme for different loading conditions and hinge geometry needs further study.

It should be noted that Kecman did not claim that the initial elastic strain rate was in any way representative of actual strain rates in the buckle and he recognised that strain rates reduce as the collapse progresses stating, "*it is sufficient in practice to find the order of magnitude rather than the exact value of strain rate and for that purpose the ... method is adequate*".

It should also be noted that the probability of an estimated strain rate, even an estimate that cannot be supported by rational argument, approximately predicting the measured dynamic scaling factor is increased due to the non-linear nature of material strain rate sensitivity. Realistically, strain rate estimates need only be "correct" to within ½ to 1 order of magnitude. For example, assuming the Cowper-Symonds model with $D$ = 7,099 $s^{-1}$ and $q$ = 4.35, the experimental pendulum work ratio of 1.21 will be predicted to within ± 10% by strain rates in the range 0.09 to 46.3 $s^{-1}$, or to within ± 5% by strain rates in the range 1.2 to 18.5 $s^{-1}$.

### 8.3.2 Abramowicz and Jones' Theoretical $F_{dyn}$ Scaling Factor

Kecman's kinematic model of the flexural buckling mode in RHS predicted that regions of rolling deformation would absorb more than 75% of the total energy. Seki and Sunami (1978) derived a similar percentage. Therefore, it might be possible to assume that $F_{dyn}$ is approximately equal to the value of $f$ for the material in the rolling region. The equations below follow the same derivation as Abramowicz and Jones (1984a, 1984b).

The final rolling radius in the rolling region was estimated using the empirical equation proposed by Kecman (1979, p. 101).

$$r_{\min} \approx 0.06 \times h \tag{8.10}$$

Outer fibre strain and average outer fibre strain rate are given simply by:

$$\varepsilon = \frac{t}{2r} \tag{8.11}$$

$$\dot{\varepsilon}_{\text{avg}} = \frac{\dot{\varepsilon}_{\max}}{T} \tag{8.12}$$

where $T$ is the total period of the impact. $T$ was estimated using an empirical fit to the test results in Chapter 4, as per Abramowicz and Jones.

$$T = \frac{2.7 \times \theta_{\max}}{\dot{\theta}_0} \tag{8.13}$$

Combining Equations 8.10 to 8.13 gave an estimate of the outer fibre strain rate.

$$\dot{\varepsilon}_{avg} \approx \frac{3 \times t \times \dot{\theta}_0}{h \times \theta_{\max}} \tag{8.14}$$

The dependency of average strain rate on section size $h$, material thickness $t$, peak rotation $\theta_{\max}$ and impact velocity $\dot{\theta}_0$ is expected. Due to the variation of strain rate through the thickness, the effective strain rate for the section is $\approx 0.65 \times \dot{\varepsilon}_{avg}$ (assuming no strain hardening and $f(\varepsilon, \dot{\varepsilon})$). Hence:

$$\dot{\varepsilon}_{avg} \approx \frac{1.95 \times t \times \dot{\theta}_0}{h \times \theta_{\max}} \tag{8.15}$$

Substituting $t = 2, \dot{\theta}_0 = 7.5, h = 25, \theta_{\max} = 0.61$ gave $\dot{\varepsilon}_{\text{eff.}} = 1.92\, s^{-1}$. Substitution into the Cowper-Symonds model with $D$ = 7,099 $s^{-1}$ and $q$ = 4.35 gave $f = F_{dyn}$ = 1.151. It should be noted that the averaging of maximum rolling strain over the total impact time does not predict strain rates that are truly representative of the actual rolling process. The theoretical basis for this approach is therefore compromised. Nonetheless the predicted value of $F_{dyn}$ compares well the values of $F_{dyn}$ measured in this study.

### 8.3.3 Kecman's Experimental $F_{dyn}$

Kecman (1993a, 1997) and Kecman and Randell (1996) proposed deriving $F_{dyn}$ experimentally by comparing gross specimen plastic energy from quasi-static and impact tests at a deflection equal to peak impact rotation. The average $F_{dyn}$ derived by applying this method to the impact tests in this thesis is 1.21. This experimental approach is preferred over theoretical estimates of $F_{dyn}$, however, the drawback of experimentally derived scaling factors is that a prototype component must be produced and tested. Fortunately, minimal instrumentation is required to determine energy absorption in an impact test and in fact this scheme does not necessarily require additional testing, since some form of impact test should always be conducted to verify material integrity under impact loading.

While this approach will predict the "correct" scaling factor for gross specimen plastic energy, care should be exercised in the derivation and use of experimental $F_{dyn}$ factors. An issue, reiterated from Chapter 5, is that $F_{dyn}$ derived from pendulum work was greater than $F_{dyn}$ derived from buckle energy. This difference would increase if the ratio

of pre-buckle rotation to post-buckle rotation in the response increased. Therefore, $F_{dyn}$ factors derived from pendulum work should not be used to scale buckle plastic energy. Additionally, $F_{dyn}$ should be derived at a total hinge rotation similar to that which the hinge would experience within the global structure.

#### 8.3.3.1 IMPLICATIONS OF NON-SCALEABLE QUASI-STATIC AND IMPACT RESPONSES

When the quasi-static scaling approach is used to predict impact response usually only the ordinate (e.g. moment or absorbed energy) is scaled. An implicit assumption in this procedure is that the impact response has the same "shape" as the quasi-static response. In the case of the local buckle under investigation, the FE analysis discussed in Chapter 7 showed that the influence of material inertia on the geometry and collapse properties of the local buckle was negligible. Thus, the assumption that the impact and quasi-static responses had the same "shape" was satisfied for the post-buckle *moment-rotation* response. Unfortunately, the assumption was not valid for the pre-buckle *moment-rotation* response of the cantilevered specimens investigated in this study. This was because under impact loading, pre-buckle pendulum rotation increased due to additional plasticity in the specimen beyond the hinge zone. (The same situation applied to the hinge-zone *moment-rotation* curve but to a lesser extent). The consequences of this difference in "shape" between the impact and quasi-static pre-buckle responses were:

1. Predicted rotation at peak moment was less than the actual rotation at peak moment.
2. The predicted moment at small post-buckle rotations was too low, since the predicted pre-buckle rotation was underestimated.
3. As discussed in Section 5.6.3, the additional pre-buckle plastic energy led to larger estimates of $F_{dyn}$ based on gross specimen energy than would have been predicted if both the quasi-static and impact responses had the same pre-buckle rotation.

### 8.3.4 Examples of Predicted RHS Plastic Hinge Impact Response

The significance of issues 1) and 2) above is demonstrated in Figure 8.2 where quasi-static, impact and scaled quasi-static responses are compared. (The *moment Vs plastic rotation* response of the entire specimen is plotted in Figure 8.2 because in the next section it is recommended that this be the response used to define hinge properties in a hybrid model). Clearly the theoretical scaling factor proposed by Kecman was

inappropriate. Much improved results were obtained using scaling factors derived using the Abramowicz and Jones approach or experimentally. Ideally, in a well designed crashworthy structure, the overall collapse mode of the structure would be insensitive to the relative strength of individual plastic hinges. In such a case the errors in predicted moment shown in Figure 8.2 would be acceptable and it would be appropriate for the design priority to be placed on total energy absorption capacity. Of course if the collapse mode of a structure was sensitive to relative hinge strengths then more accurate predictions of hinge response, derived from detailed FE modelling or instrumented testing, may be required.

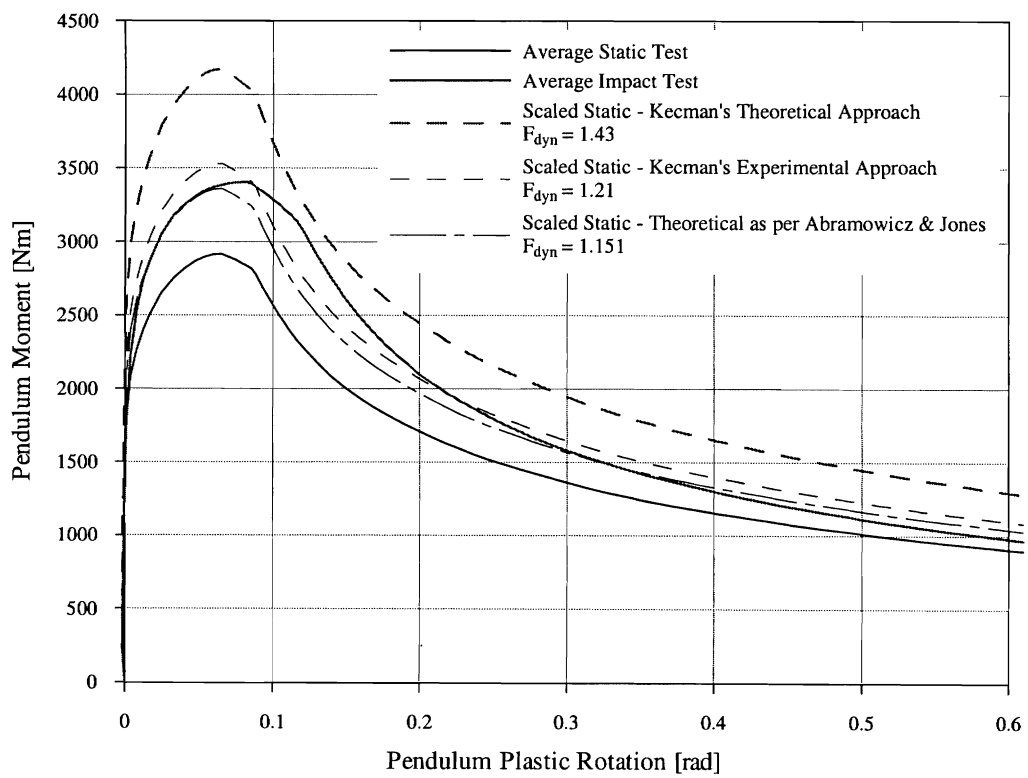


**Figure 8.2:** Performance of various scaling factors compared to the test results from Chapter 5

Figures 8.3a and 8.3b show the true variation in the ratios of impact response to quasi-static response from Figures 5.23 and 5.24, respectively. While a single scaling factor may give an acceptable result for total collapse energy say, it is clear that a single scaling factor cannot predict the true time history of hinge moment. The predicted moment at large rotations will always be too high since the true ratio reduces towards unity. While in the present case the scale factor derived experimentally from gross specimen energy gives a good prediction of peak impact moment, this will not necessarily be so in general. Because specimen strain energy is a cumulative quantity,

the variation of $F_{dyn}^{\varepsilon energy}$ is reduced and a single constant factor can be a reasonable approximation. One advantage of the experimentally derived factor is that total specimen strain energy is, by definition, correctly predicted at peak rotation.

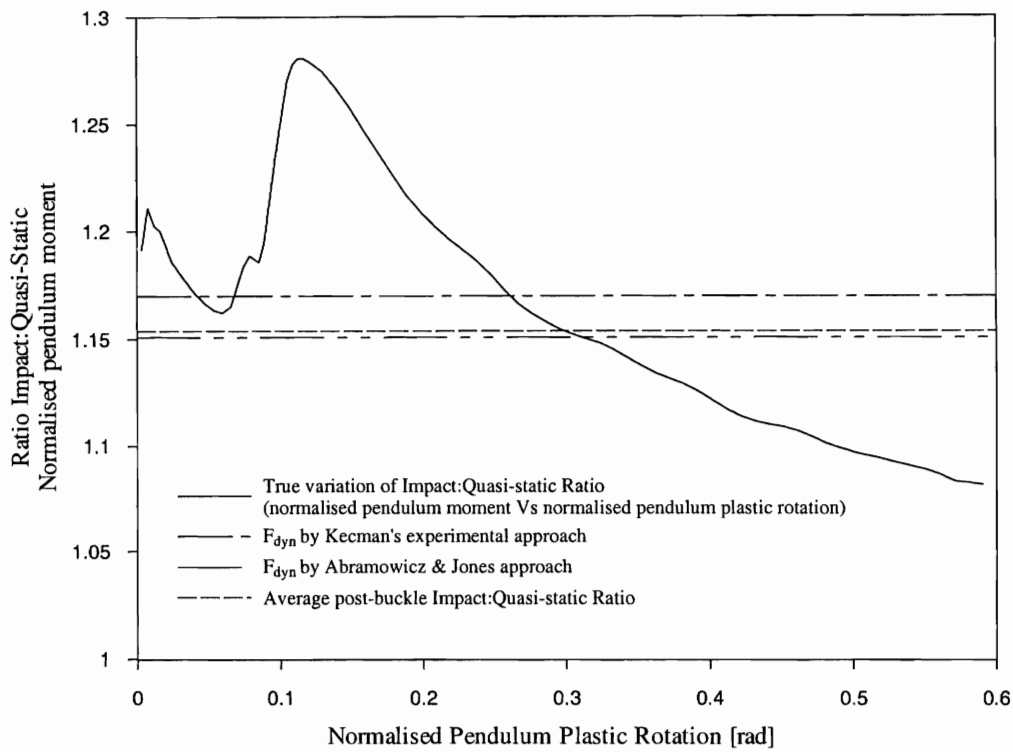


**Figure 8.3a:** Comparison of true and estimated $F_{dyn}$ for pendulum moment Vs pendulum rotation

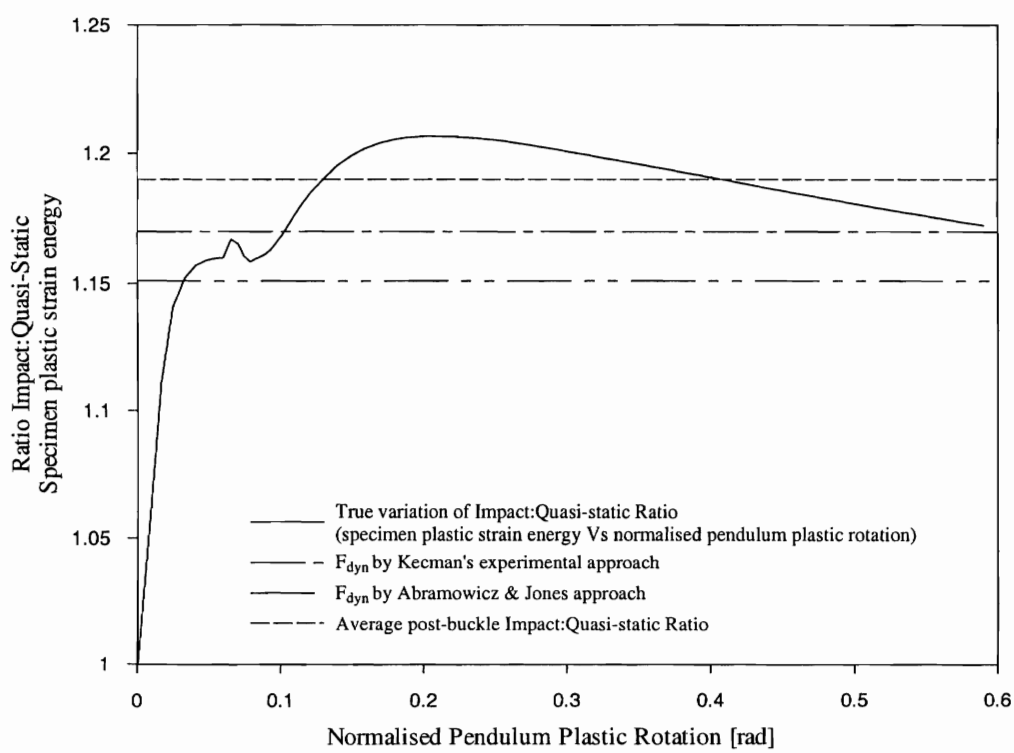


**Figure 8.3b:** Comparison of true and estimated $F_{dyn}$ for specimen strain energy Vs pendulum rotation

### 8.3.5 Possible Developments to Predictive Schemes

Kecman and Tidbury (1982) estimated RHS plastic hinge impact response by scaling the static *moment-rotation* response predicted by Kecman's analytical model. A more direct approach may be to modify Kecman's analytical model to include continuous curvature at bending and rolling yield lines, so that strain rates and thus dynamic flow stress can be predicted. This derivation would be quite complex and would likely involve various empiricisms to define curvature. An alternative would be to derive an empirical model that predicts $F_{dyn}$ for RHS under flexural impact loading.

An empirical model that gives $F_{dyn}$ as defined by Kecman could be developed from a programme of uninstrumented quasi-static and impact bend tests. Alternatively a series of detailed FE analyses could replace physical experimentation. (The spatial and temporal averaging of local strain rates, (actually local dynamic flow stress), that occurs naturally in a physical test is carried out implicitly within the FE analysis). One advantage of using FE analysis to derive "empirical" models is that the detailed results allow more flexibility in the definition of $F_{dyn}$. For example:

By averaging $F_{dyn}(\delta)$ independently of the FE analysis, a rotation-weighted average of $F_{dyn}(\delta)$ can be calculated. $F_{dyn}^{M}$ and $F_{dyn}^{En}$ factors calculated using this definition are shown in Figures 8.3a and 8.3b. It is noted that, the experimental definition of $F_{dyn}$ proposed by Kecman, (the impact:quasi-static ratio of specimen plastic energies at peak rotation), is equivalent to the quasi-static plastic energy-weighted average of $F_{dyn}^{M}(\beta)$ over all $\beta$, where $F_{dyn}^{M}(\beta)$ is the impact:quasi-static ratio of the pendulum *moment-rotation* response.

### 8.3.6 Scaling Global Structural Response

Sometimes scaling factors are derived that account for the response of the entire structure e.g. the empirical models of vehicle crush (Prasad & Padgaonkar 1981; Rains & Van Voorhis 1998). This approach can be acceptable for design purposes, although gross empirical models of this nature have limited scope.

At other times single "dynamic factors" may be derived from component response and used to scale the global response of a structure. When a scaling factor estimated for a single component is used globally, e.g. Kecman and Tidbury (1982) and Grzebieta and

Dayawansa (1987), the inherent assumption is that all plastic hinges in the structure experience the same loading rate and that the effect of that loading rate on plastic hinge response is the same for each hinge. The accuracy of the analysis will thus depend on the extent to which these assumptions are valid. In some cases, such as the bus frame analysed by Kecman and Tidbury (1982), this may be reasonable, since the hinges within each ring frame are similar, the individual ring frames are similar and the loading is essentially uniform along the bus length. This approach is further supported by the "order of magnitude" nature of strain rate sensitivity in steel, which means that loading rates on plastic hinges throughout the structure must vary by orders of magnitude before it is necessary to calculate individual scaling factors.

## 8.4 A General Comment

Component responses can be dependent on loading and constraint conditions e.g. in the case of the RHS under investigation, different pre-buckle rotations will be measured under cantilever and pure moment loading. Therefore it is important to derive component response under load and constraint conditions similar to those that will be experienced by the component *in situ*. Furthermore, since component impact response is load rate dependent, it is important that these derivation procedures appropriately replicate or model the history of component loading during the dynamic collapse of the global structure. The complication is that these loads are governed by the inertial response of the global structure and can realistically only be derived by a dynamic FE analysis of the complete structure.

## 8.5 Using Plastic Hinge Properties in a "Hybrid" Analysis

The above discussion has described the derivation of RHS plastic hinge impact response. These results must now be incorporated into a hybrid analysis of the complete bus structure. This is achieved by using a "special hinge element" that models the response of the physical plastic hinge. An important question now is, what physical hinge response should the "special hinge element" represent?

It is important that all plastic rotation in the RHS joint be modelled. It is accepted that the "hinge element" will account for all post-buckle plastic rotation, however, the "hinge element" must also model all pre-buckle plastic rotation that is not accounted for by the global model. If pre-buckle plasticity is not modelled, the impact energy absorbed

as pre-buckle plastic strain in the real structure must be absorbed as rotation of the "hinge element" in the hybrid model. Since, for the same rotation, post-buckle response absorbs less energy than pre-buckle response, not modelling pre-buckle plasticity will lead to over prediction of hinge rotation. The choice is whether to model pre-buckle plastic strain within the global elements or within the "hinge element". This choice is complicated by the fact that pre-buckle rotation is distributed over a region of the specimen and post-buckle rotation is concentrated at the effective hinge centre.

Calculating the elastic-plastic pre-buckle response of the extended plastic zone within the global analysis is potentially more accurate than scaling a measured quasi-static response. In practice, however, because the pre-buckle response is limited by the maximum moment capacity of the "hinge element", the analysis may significantly under or over estimate pre-buckle rotation and pre-buckle plastic energy, depending on the accuracy with which this peak moment is estimated. As discussed above, errors in the predicted pre-buckle rotation adversely affect the accuracy of the post-buckle moment response and depending on the ratio of pre-buckle to post-buckle response, the calculated total plastic energy of the hinge may be significantly in error.

Unless the peak moment capacity of the plastic hinge can be estimated reliably, it is not recommended that the pre-buckle plasticity be calculated in the global elements. The analysis of Section 7.2.3.2 is an example of the successful calculation of pre-buckle plasticity in a situation when the peak moment capacity of the plastic hinge was known. Even so, calculating the elastic-plastic pre-buckle response of the extended plastic zone within the global analysis requires that the global analysis be capable of calculating the beam section's plasticity, be it either dynamic or pseudo-dynamic and that representative material *stress-strain* and strain rate sensitivity properties be defined for the beam elements. A further issue is that the "hinge element" in this type of analysis only models the impact *moment-plastic rotation* response of the local buckle. These properties can be scaled from measured quasi-static buckle response, however, it is no longer appropriate to use a gross response scaling factor. Instead, a buckle mechanism response scaling factor should be derived.

The complexity of calculating pre-buckle plasticity in the global analysis is not consistent with the spirit of the hybrid scheme. A much simpler approach, which avoids the uncertainty of predicting pre-buckle response, is that used by Kecman and Djokic

(1990) and the CIC program SIMSTAT. The approach is to associate all plastic rotation with a point "hinge element" placed at the location in the model corresponding to the effective hinge centre of the plastic hinge. In this approach, the impact *moment-plastic rotation* properties of the "hinge element" can be determined by scaling the measured quasi-static *moment-plastic rotation* of the pendulum ( $M$ Vs $\beta'_{plas}$ ).

A fundamental problem with this approach is that pre-buckle plastic rotation that physically occurs over a finite length is modelled as occurring at a point. The FE results described in Section 7.2.3.3, indicated that material plasticity (defined as 0.2% outer fibre plastic strain) extended 170 mm from the specimen root in the static FE analysis and 260 mm in the dynamic FE analysis. In the experiments conducted in this study plasticity was estimated to extend over similar lengths. The modelling approach is however appropriate for post-buckle rotations because subsequent to buckle formation, plasticity is restricted to the buckle length (50 to 60 mm for the RHS under study) and plastic rotation is concentrated at the effective hinge centre.

The consequence of modelling distributed curvature, as rotation about a point, is that the displacement of the structure adjoining the "hinge element" is overestimated. The error incurred by modelling the true kinematics of the plastic rotation in this manner is reduced when the modelling process reflects the arrangement used to measure the hinge *moment-rotation* properties. For example, in the present case the *moment-plastic rotation response* of the pendulum was measured at the effective hinge centre, therefore modelling hinge rotation about this point will reproduce the same plastic displacement of the specimen tip. In practical design terms, concentrating pre-buckle rotations at the hinge site may have a negligible effect on the deformation of the global structure, but nonetheless the issue should be investigated.

An alternative approach is to assume that hinge rotation is distributed uniformly along a "hinge element" of finite length. This approach was implemented using the beam element capabilities of the commercial FE code ABAQUS in Chapter 7 and by Roca et al. (1997). Kinematically, this approach is an improved model of the distributed pre-buckle curvature. However, due to the kinematics of the actual buckle, the simple approach of assuming that all rotation occurs at a point is a better modelling approach for post-buckle rotations (Cimpoeru 1992).

In the finite length element approach, it is assumed that section moment is constant along the "hinge element". When there is significant variation of section moment along the plastic zone in the actual structure, this assumption can lead to errors in the section forces transmitted to the global structure. For this reason it is not recommended that the finite length approach be used to kinematically model the distribution of pre-buckle rotations.

If a single finite length element is used to model the plastic zone and buckle, the element should be the length of the buckle region. This is because it is more important for post-buckle rotation to be concentrated over the buckle length, than for pre-buckle rotation to be distributed over the full plastic zone.

Another point to note is that the elastic stiffness of the local buckle decreases as the buckle develops. As demonstrated in Section 7.2.2.4, this change in elastic stiffness can be modelled by scaling the original elastic stiffness by a factor that varies with hinge rotation.

## 8.6 CONCLUSIONS

This chapter has drawn on the results of Chapters 5, 6 and 7 to review the quasi-static scaling approach for deriving component impact response. The quasi-static scaling approach is commonly applied in the literature and, whilst in principle the procedure is simple, the accuracy of the predicted response was shown to be dependent on the proper choice and application of scaling factors.

There are two common scaling approaches. One is to calculate impact response by scaling a known quasi-static response by a factor $F_{dyn}$ that accounts for the overall effect of strain rate sensitivity. While $F_{dyn}$ varies temporally, a single factor is usually used. A second approach predicts impact response by scaling the flow stress in a quasi-static analytical model by a theoretically derived factor $f$. While $f$ varies spatially and temporally, a single constant factor is usually used. Thus this approach is equivalent to scaling the moment or energy responses by a single factor $F_{dyn}$ that is equal to $f$.

Three approaches for deriving $F_{dyn}$, ranked in order of decreasing accuracy, are:

1. Direct Experimental Derivation.
   - Involves uninstrumented impact and quasi-static testing of the plastic hinge as proposed by Kecman (1993a, 1997).
2. An empirical model.
   - The efficiency of empirical models makes them ideally suited to parametric studies. However, the application of empirical models is restricted by the scope (and accuracy) of the model.
3. Indirect Theoretical Derivation, $F_{dyn} = f$.
   - This approach is most successful in very simple structures. In more complex plastic hinges it is difficult to determine a single factor $f$ which is representative of the complex spatial and temporal variation of flow stress. However, because the strain rate sensitivity of steels is an "order of magnitude" effect, a single theoretical scaling factor can sometimes be derived by considering flow stress within a dominant or representative region of deformation. This is the approach of Abramowicz and Jones (1984a, 1984b).
   - Using the approach of Abramowicz and Jones, a good estimate of the measured $F_{dyn}$ was obtained by assuming $F_{dyn} = f$ and calculating $f$ using an estimate of the strain rate in the dominant rolling region of deformation in the buckle.
   - Because the theoretical scaling approach proposed by Kecman (1979) used a material model and a strain rate that were not related to the actual conditions within the buckle, the approach is best viewed as directly predicting the gross influence of material strain rate sensitivity rather than predicting representative dynamic flow stresses. Nonetheless the value of $F_{dyn}$ predicted by Kecman's approach significantly overestimated the impact response of the RHS specimens tested in this study. The result was improved by using a model of material strain rate sensitivity that was based on the strain rate sensitivity of flow stress at large strains. Although this modified approach gave an acceptable prediction of $F_{dyn}$ for the conditions of this study, the accuracy of the approach for different hinge conditions needs verification.

- Since the strain rate sensitivity of many steels is an "order of magnitude effect", the accuracy of theoretical scaling factors is much more sensitive to the choice of material model than to the estimate of strain rate.

**Defining RHS Plastic Hinge Response in a Hybrid Analysis**

There are various options for incorporating the local behaviour of complex plastic hinges in a hybrid analysis of a global structure. It is fundamentally important that the special elements representing the behaviour of complex plastic hinges must account for all plasticity not modelled explicitly within the global structural elements. The recommended modelling approach is that adopted by the CIC-SIMSTAT program. This approach kinematically models all plastic rotation as if occurring about a point in the global model located at the buckle effective centre, and defines the hinge properties to represent the *moment-plastic rotation* response of the entire plastic zone. This approach is simple to implement and ensures that the total plastic energy of the hinge is correct. Additionally, when the quasi-static scaling design approach is used, the impact scaling factor is easily derived. The drawbacks with the approach are that the kinematics of pre-buckle plastic rotation are incorrectly modelled and that some errors occur in the predicted impact moment response when pre-buckle rotations under quasi-static and impact loading are not equal.

## 8.7 RECOMMENDATIONS FOR FUTURE WORK

The modified Kecman and the adapted Abramowicz and Jones scaling schemes need verification over a range of different hinge geometries and impact conditions. This would involve a comprehensive programme of physical testing or FE analysis. In the author's opinion, the results of such a programme would best be used to derive an empirical function of $F_{dyn}$ for RHS under flexural impact loading. Such a model would accelerate the impact analysis of simple RHS joints in crashworthy bus superstructures.

Pre-buckle plastic rotation is non-uniformly distributed over a significant length of the specimen. When this "distributed rotation" is kinematically modelled as occurring at a point, the displacement of the adjoining structure will be overestimated. This overestimation tends to compensate for the fact that pendulum rotation underestimates specimen plastic zone rotation. Therefore the practical significance on global structure deformations of the theoretical shortcomings of this modelling approach may be negligible, however this should be confirmed by an investigation.

# CHAPTER 9 DISCUSSION AND CONCLUSIONS

## 9.1 SPECIFIC AIMS OF THE THESIS

The specific aims of this thesis were outlined in the Introduction. They related to the use of physical impact tests, numerical modelling and quasi-static scaling methods for the measurement or prediction of RHS plastic hinge response under impact bending loads. Through a combination of careful experimentation, detailed FE modelling and material testing, these aims have successfully been addressed as follows.

1. *Development of testing procedures that address the measurement difficulties in impact testing caused by specimen inertia.* An impact test rig and data processing procedures have been developed that properly treated and, where possible, minimised the influence of specimen inertia on the measurement of impact *moment-rotation* responses.

2. *Measurement of the plastic hinge $M$-$\theta$ response of RHS under impact flexural loading.* Using this rig and the special instrumentation and data processing procedures developed for it, the plastic hinge $M$-$\theta$ response of a 50x50x2 C350LO RHS was measured under impact and quasi-static loading. Gross specimen *moment-rotation* response was also measured.

3. *Determination of the influence of inertia on local plastic hinge response.* Detailed dynamic finite element analyses established that the inertia of the material in the local buckle had a negligible influence on the collapse response of the buckle mechanism.

4. *Modelling of the dynamics of an impact in a static FE solution.* A pseudo-dynamic analysis procedure was developed which enabled impact responses dominated by material strain rate sensitivity to be analysed using a static solver. The impact tests from Chapter 5 were successfully analysed using this pseudo-dynamic loading scheme implemented in the commercial FE code HKS ABAQUS – Standard.

5. *Determination of an appropriate definition of strain rate sensitivity for the material in cold-rolled hollow sections.* *Stress-strain* curves for RHS wall material over the nominal strain rate range $10^{-4}$ to 10 $s^{-1}$ were measured using high-elongation strain

gauges. From this study it was shown that the strain rate sensitivity of grade C350LO RHS wall material can be modelled using the Cowper-Symonds equation with coefficients $D$ = 7,099, $q$ = 4.35. It was also shown that although the Cowper-Symonds equation with coefficients $D$ = 40.4, $q$ = 5 is commonly used in similar applications, this form of the Cowper-Symonds equation was found to significantly over estimate the strain rate sensitivity of RHS wall material, especially at large strains.

6. *Determination of the range of strains and strain rates in the buckle during a typical impact event.* Localised equivalent plastic strains in the rolling region were discovered to be as high as 100% to 150%. Strain energy weighted, average equivalent plastic strain, calculated over the buckle region at $\theta \approx 36°$, was between 35% and 40%. Peak localised strain rates were as high as 30 $s^{-1}$ in the initial stages of buckle development, and typically less than 2 $s^{-1}$ in the late stages of collapse. In the mid stages of collapse, around $\theta = 20°$, localised strain rates throughout the buckle were typically less than 10 $s^{-1}$. Strain energy weighted, average equivalent plastic strain rate, calculated over the buckle, varied with the hinge rotation rate and was a maximum of 11.5 $s^{-1}$ at $\theta \approx 8°$, which was 20 times the initial elastic strain rate of 0.57 $s^{-1}$.

7. *Assessment of the performance of quasi-static scaling schemes proposed in the literature.* The theoretical scaling approach proposed in the literature for predicting the impact bending collapse response of RHS, over estimated the impact response of the RHS tested in this study. An improved result was obtained by using a large strain material strain rate sensitivity model. An alternative theoretical scaling factor was proposed that estimated the strain rate in the dominant rolling region of deformation in the buckle. It was concluded that the preferred means of deriving impact scaling factors is experimentally, as described in the literature.

## 9.2 PREDICTING IMPACT RESPONSE

In the introduction to this thesis it was proposed that the crashworthiness of a bus superstructure, constructed from thin-walled rectangular hollow section (RHS), was to be assessed using the "hybrid" analysis approach, and that the impact bending response of the local plastic hinges in the global framework was to be determined. This thesis has investigated three approaches for determining these impact responses, namely numerical modelling, instrumented impact testing and scaling a quasi-static response. The choice of which approach should be used will depend on factors such as the stage of design, required accuracy and budget and time constraints. It is possible that all three approaches could be used in the course of the design of a bus structure. The major insights into these impact design approaches provided by the work in this thesis are summarised below.

### 9.2.1 Detailed Finite Element Modelling

The application of detailed finite element (FE) analysis to the design of safety structures has recently become common practice. FE modelling is versatile and very instructive, and is in keeping with the modern trend towards a virtual design cycle. FE modelling can dramatically reduce the need for development testing and enables far better programming of the tests that are conducted.

**Thesis Insight**

The use of detailed FE analysis to predict the plastic hinge response of RHS under flexural impact loading was demonstrated in Chapter 7. The analysis illustrated the excellent predictive capability that can be achieved with modern FE codes and good modelling practice. The important conclusions regarding good modelling practice were:

- Mesh refinement should be sufficient to capture the true deformation mode rather than enforcing a deformation mode.
- The true variation of material properties should be modelled, for example material variation around the tube section.
- The definition of material strain rate sensitivity must be appropriate to the strain range of interest. Ideally material strain rate sensitivity should be defined as a function of strain and strain rate i.e. $f(\varepsilon,\dot{\varepsilon})$, by defining complete $\sigma$–$\varepsilon$ curves at a

range of strain rates or by using a material model similar to Jones (1993). If a constitutive model, such as the Cowper-Symonds equation, is used to define material strain-sensitivity, it is essential that appropriate model parameters be used.

When the effects of inertia and material strain rate sensitivity are both significant, implicit or explicit dynamic FE analyses can be used to predict structural response under impact loading. It was demonstrated in Chapter 7 that when the influence of material inertia on local deformations is negligible and only material strain rate sensitivity is to be accounted for, a static solver together with appropriate control of the loading rate could be used to analyse the impact event. The advantages of this pseudo-dynamic approach are that it removes the need for a dynamic solver, reduces solution times and simplifies the extraction of response curves.

## 9.2.2 Impact Testing

Physical impact tests are an obvious approach, and until recently were the only way to reliably assess structural impact response. Despite the excellent fidelity of numerical modelling in many cases, component tests may still need to be conducted because:

- A numerical analysis alone is not currently accepted in ADR 59/00 for type approval.
- In some areas, such as composites and adhesives, there are failure modes and other design, manufacturing or material aspects that cannot be reliably predicted by finite element codes.

Physical impact tests can take various forms, from uninstrumented pass/fail validations to fully instrumented studies. Instrumented impact tests are more expensive than uninstrumented tests and may require special test rig design.

### 9.2.2.1 Uninstrumented Impact Testing

Impact tests on components, whether instrumented or uninstrumented, should normally be conducted to verify material integrity under impact loading. Uninstrumented tests are accepted by ADR 59/00 for this purpose and are usually preferred because they are generally cheaper and quicker to conduct than instrumented tests.

Uninstrumented impact tests do not provide detailed insight into the response of the plastic hinge, or the component as a whole, and cannot therefore be used alone to derive

impact response. However, measurement of gross energy absorption can be used to derive impact scaling factors.

#### 9.2.2.2 INSTRUMENTED IMPACT TESTING

The advantage of instrumented impact testing is that component responses are measured which properly account for material strain rate sensitivity and inertia. The verification of numerical models is another advantage of conducting careful instrumented experiments. Unfortunately there are many difficulties associated with instrumented impact testing.

**Thesis Insight**

The difficulties associated with measuring impact *moment-rotation* responses directly have been discussed and demonstrated in Chapters 4 and 5. The majority of these difficulties are a consequence of specimen inertia. This thesis has presented a novel test rig design, instrumentation and data processing procedures that properly treat and where possible minimise the influence of specimen inertia on the measurement of impact *moment-rotation* responses. Most significantly, these procedures included calculating hinge moment from measurements of a reaction force rather than impact force, the direct measurement of hinge rotation and the judicious use of low-pass filtering. The successful measurement of the impact *moment-rotation* response of 50x50x2 C350LO RHS was demonstrated in Chapter 5.

### 9.2.3 Scaling a Quasi-Static Response

Because of the difficulties involved with conducting and interpreting impact tests, and because numerical modelling requires specialised software and expertise, plastic hinge impact responses are often predicted by scaling known quasi-static performance by a "dynamic factor" ($F_{dyn}$) to account for the influence of material strain rate sensitivity. However, while in principle the procedure for scaling a quasi-static response is simple, the accuracy of the predicted response was shown to be dependent on the derivation and application of scaling factors.

Because the theoretical scaling approach proposed by Kecman (1979) used a material model and a strain rate that were not related to the actual conditions within the buckle, the approach is best viewed as directly predicting the gross influence of material strain rate sensitivity rather than predicting representative dynamic flow stresses. Nonetheless the gross dynamic scaling factor ($F_{dyn}$) predicted by Kecman's approach significantly

overestimated the impact response of the RHS specimens tested in this study. The result was improved by using a model of material strain rate sensitivity that was based on the strain rate sensitivity of flow stress at large strains. This highlighted the fact that, since strain rate sensitivity is an "order of magnitude effect", when deriving theoretical scaling factors it is more important to use an appropriate model of material strain rate sensitivity than to make an accurate estimate of strain rate. In particular, large strain material strain rate sensitivity models should be used when scaling the response of plastic hinges characterised by large plastic strains.

A good estimate of the impact to quasi-static plastic energy ratios measured in this study was obtained following the approach of Abramowicz and Jones (1984a, 1984b). Following this approach a theoretical scaling factor was derived, based on an estimate of the strain rate in the dominant rolling region of deformation in the buckle and the large strain material strain rate sensitivity properties determined in Chapter 6.

Kecman (1993a, 1997) proposed a scheme whereby the gross scaling factor $F_{dyn}$ was derived experimentally. This experimental approach is preferred over theoretical estimates of $F_{dyn}$, however the drawback of experimentally derived scaling factors is that a prototype component must be produced and tested. Fortunately, the relevant impact tests require minimal instrumentation and in fact this scheme does not necessarily require additional testing, since some form of impact test should always be conducted to verify material integrity under impact loading.

Whilst this approach will predict the "correct" scaling factor for gross specimen plastic energy, there are issues regarding the use and derivation of $F_{dyn}$ factors namely, $F_{dyn}$ factors derived from pendulum work should not be used to scale buckle plastic energy, and $F_{dyn}$ should be derived at a total hinge rotation similar to that which the hinge would experience within the global structure.

### 9.2.4 General Comment on Component Impact Responses

A general conclusion regarding the derivation of component impact response was that, since component responses can be dependent on loading and constraint conditions, it is important to derive component responses under load and constraint conditions similar to those that will be experienced by the component *in situ*.

Some options for incorporating the local behaviour of complex plastic hinges into a hybrid analysis of a global structure were discussed in Chapter 8. It is fundamentally important that the special elements representing the behaviour of complex plastic hinges account for all plasticity not modelled explicitly within the global structural elements. The recommended modelling approach is that adopted by the CIC-SIMSTAT program. This approach is to kinematically model all plastic rotation as if occurring about a point in the global model located at the buckle effective centre, and to define the hinge properties to represent the *moment-plastic* rotation response of the entire plastic zone.

## 9.3 Additional Key Results and Conclusions

Some additional key results and conclusions from the individual chapters of this thesis, not specifically related to the impact design process, are described below.

### 9.3.1 Chapter 3 - Test Rig Design

The test rig and instrumentation were specially designed to measure the $M$-$\theta$ response of the local buckle because comparing the quasi-static and impact $M$-$\theta$ responses of the local buckle gives a direct assessment of the influence of material strain rate sensitivity. Measurement of the $M$-$\theta$ response of the local buckle also provided more detailed data for validation of FE models.

The chosen rig arrangement was a single axis pendulum. This pendulum could be used to conduct quasi-static bend tests over a period of hours, or impact tests at loading rates up to 20 $ms^{-1}$. Novel instrumentation on the rig measured pendulum impact velocity, pendulum travel, pendulum to specimen contact, plastic hinge rotation and specimen mount reaction force. It should be noted that the final test rig and instrumentation arrangement described in Chapter 3 was the culmination of a long design process that involved considerable "trial-evaluation-improvement" testing and refinement of several design iterations.

### 9.3.2 Chapter 4 – Processing Raw Test Data

The design of the test specimen and the cantilever loading condition used in this study were representative of a real bus frame joint and loading. One issue with the cantilever loading arrangement was that the choice of a moment to associate with measured hinge rotation was somewhat arbitrary. For the purposes of this study an "energy consistent" hinge moment was defined.

Signals from impact tests are often distorted by measurement system response. The common treatment is to use low-pass filtering to remove unwanted high frequency content. Low-pass filtering should generally be used with caution, and this was especially important in the present tests because unloading of the hinge occurred soon after impact. Hinge unloading was of particular concern when filtering the impact results because additional frequency bandwidth was required to accurately define the associated elastic unloading of the hinge moment. It was established in Chapter 4 that no significant hinge unloading occurred after buckle formation. Therefore low-pass filtering was used to remove the effects of measurement system resonance from measured reaction force and hinge rotation signals. Low-pass filtering did cause some distortion of the true $M$-$\theta$ trace in the region of the large unload that occurred before peak moment. However, this filtering was considered acceptable given the significant specimen vibrations excited by the initial impact in this region. If more significant and frequent hinge unloading had occurred then *inverse analysis*, using a reliable frequency response function, would have been the only option to remove the effects of measurement system resonance.

An important consequence of specimen vibration was that to obtain the true hinge $M$-$\theta$ response curve, it was necessary for the measured hinge rotation and hinge moment signals to be complementary. This required that hinge rotation be measured locally across the buckle mechanism. A device incorporating two rotary potentiometers was designed for this purpose and was used successfully.

### 9.3.3 Chapter 5 – Bend Test Results

Some specific observations of the impact $M$-$\theta$ response of a 50x50x2 C350LO RHS relative to the quasi-static response were:

- Maximum hinge moment increased by approximately 16%.
- Total plastic strain energy absorbed by the buckle mechanism, at a mechanism plastic rotation of $\theta_{pb}^{plas} = 0.54$ (31°), increased by a factor of 1.12.
- Total plastic strain energy absorbed in the hinge zone, i.e. combined pre-buckle and post-buckle response, at a hinge zone plastic rotation of $\theta^{plas} = 0.59$ (34°), increased by a factor of 1.15.
- Total plastic strain energy absorbed in the entire specimen, at a pendulum plastic rotation of $\beta'_{plas} = 0.61$ (35°), increased by a factor of 1.21.

Hinge mechanism $M$-$\theta$ responses from Cimpoeru (1992) compared well with those measured in this study. It was concluded that hinge mechanism $M$-$\theta$ response was essentially unaffected by the test loading arrangement and could therefore be considered a characteristic property of the particular section. However, pre-buckle *moment-rotation* responses were dependent on the loading arrangement.

### 9.3.4 Chapter 6 – RHS Material Strain Rate Sensitivity

The enhanced performance of the RHS plastic hinge under impact loading is due to the direct influence of material strain rate sensitivity. Therefore, for impact design purposes, it is essential to have a suitably accurate model of the RHS wall material's strain rate sensitivity. To the best of the author's knowledge, no test data for the strain rate sensitivity of the material in cold-rolled tube walls, at small or large strains, has previously been published. Therefore, the measurement of RHS wall material strain rate sensitivity to large strains was a major contribution of this thesis.

Cowper-Symonds coefficients appropriate for use in crashworthiness analyses were derived by fitting the results for average ultimate tensile strength around the section.

Grade C350LO: $D = 7{,}099\ s^{-1}$, $q = 4.35$
DuraGal: $D = 22{,}307\ s^{-1}$, $q = 4.41$
Combined C350LO and DuraGal: $D = 13{,}327\ s^{-1}$, $q = 4.42$

The results for strain energy density at UTS showed similar strain rate sensitivity.

Grade C350LO: $D = 5{,}546\ s^{-1}$, $q = 4.12$

DuraGal: $D = 18{,}418\ s^{-1}$, $q = 4.18$

Combined C350LO and DuraGal: $D = 10{,}829\ s^{-1}$, $q = 4.20$

For a material exhibiting a significant decrease in strain rate sensitivity with increasing strain, it may be most appropriate to derive Cowper-Symonds coefficients for average strain rate sensitivity at large strains, using strain energy density. Interestingly, the Cowper-Symonds model with coefficients $D = 6{,}844\ s^{-1}$ & $q = 3.91$, proposed by Abramowicz and Jones (1986), successfully predicted the strain rate sensitivity of the RHS wall material tested in this study, despite the fact that these coefficients were derived from tests on annealed low carbon steel.

The quasi-static mechanical properties of the RHS wall material tested in this study were found to be consistent with published quasi-static mechanical properties of RHS wall material.

### 9.3.5 Chapter 7 – Finite Element Modelling

The detailed FE analyses described in Chapter 7 gave insight into buckle mechanism behaviour that would have been extremely expensive or even impossible to measure. In particular, the temporal and spatial distribution of strain and strain rate within the buckle was studied. Some key results were quoted in Section 9.1.

FE analyses were used extensively throughout this study to investigate specimen behaviour and to verify proposed data processing procedures so that the measured signals, specifically from the impact tests, could be interpreted correctly. This use of FE analysis in experimental design clearly has great potential.

# REFERENCES


Abramowicz, W. & Jones, N. 1984a, 'Dynamic axial crushing of square tubes', *Int. J. Impact Engineering*, Vol. 2, No. 2, pp. 179-208.

Abramowicz, W. & Jones, N. 1984b, 'Dynamic axial crushing of circular tubes', *Int. J. Impact Engineering*, Vol. 2, No. 3, pp. 263-281.

Abramowicz, W. & Jones, N. 1986, 'Dynamic progressive buckling of circular and square tubes', *Int. J. Impact Engineering*, Vol. 4, No. 4, pp. 243-270.

Abramowicz, W. & Jones, N. 1997, 'Transition from initial global bending to progressive buckling of tubes loaded statically and dynamically', *Int. J. Impact Engineering*, Vol. 19, Nos. 5/6, pp. 415–437.

Australian Design Rule 59/00 1989, *Omnibus Rollover Strength*, Federal Office of Road Safety, Australia.

Bakker, M. C. M. & Stark, J. W. B. 1994, 'Theoretical and experimental research on web crippling of cold-formed flexural steel members', *Thin-walled structures*, **18**, pp. 261-290.

Bodner, S. R. 1965, 'Strain rate effects in dynamic loading of structures', in *Behavior of Materials under dynamic loading*, ed. N. J. Huffington Jr., Proc. of colloquium on Behavior of Materials Under Dynamic Loading, Winter annual meeting of the ASME, 9th November, Chicago.

Bodner, S. R. & Symonds, P. S. 1962, 'Experimental and theoretical investigation of the plastic deformation of cantilever beams subjected to impulsive loading', *J. Applied Mechanics*, Dec., pp. 719–728.

Brown, J. C. & Tidbury, G. H. 1983, 'An investigation of the collapse of thin-walled rectangular beams in bi-axial bending', *Int. J. Mech. Sci.*, Vol. 25, Nos. 9/10, pp. 733-746.

Calladine, C. R. 1983, 'Plastic buckling of tubes' in *Collapse, the buckling of structures in theory and practice*, eds. J.M.T. Thompson & G.W. Hunt, Proc. of Symp. held at University College, London, 31 Aug.- 3 Sep. 1982, Cambridge University Press.

Calladine, C. R. & English, R. W. 1984, 'Strain-rate and inertia effects in the collapse of two types of energy-absorbing structure', *Int. J. Mech. Sci.*, Vol. 26, Nos. 11/12, pp. 689-701.

Campbell, J. D. 1970, *Dynamic Plasticity of Metals*, Course held at the Department for Mechanics of Deformable Bodies, Udine, July, Springer-Verlag, Vienna.

Campbell, J. D. & Cooper, R. H. 1966, 'Yield and flow of low-carbon steel at medium strain rates', in Proc. Conf. on Physical Basis of Yield and Fracture, Sep., Oxford, Inst. Physics and Physical Society Conf. Ser. # 1, pp. 77–87.

Campbell, J. D. & Duby, J. 1957, 'Delayed yield and other dynamic loading phenomena in a medium-carbon steel', Proc. of conf. on The Properties of Materials at High Rates of Strain, 30th Apr. – 2nd May, London, (Inst. Mech. Eng., London), pp. 214-220.

Chatfield, D. A. & Rote, R. R. 1974, 'Strain rate effects on the properties of high strength low alloy steels', SAE paper # 740177.

Cimpoeru, S. J. 1992, *The Modelling of the Collapse During Roll-Over of Bus Frames Consisting of Square Thin-Walled Tubes*, Ph.D. Thesis, Monash University, Dept. of Civil Eng., Australia.

Cimpoeru, S. J. & Murray, N. W. 1992, 'The large-deflection behaviour of thin-walled structural components of vehicles', Conf. on Materials in the Automotive Industry, Melbourne 24th-25th June, IMMA.

Colokoglu, A. & Reddy, T. Y. 1996, 'Strain-Rate and Inertial Effects in Free Inversion of Tubes', *IJCrash*, Vol. 1, No. 1, pp. 93-106.

Corona, E. & Vaze, S. P. 1996, 'Buckling of elastic-plastic square tubes under bending', *Int. J. Mech. Sci.*, Vol. 38, No. 7, pp. 753-775.

Davies, R. G. & Magee, C. L. 1975, 'The effect of strain-rate upon the tensile deformation of materials', *J. Engineering Materials and Technology*, April, pp. 151–155.

DeGarmo, E. P., Black, J. T. & Kosher, K. A. 1984, *Materials and Processes in Manufacturing*, 6th edn., Macmillan, New York.

Dieter, G. E. 1988, *Mechanical Metallurgy*, SI Metric edn., McGraw Hill, UK.

Døssing, O. 1987, *Structural Testing Part 1: Mechanical Mobility Measurements*, Brüel & Kjær, Denmark.

Drazetic, P., Ravalard, Y., Dacheux, F. & Marguet, B. 1994, 'Applying non-direct similitude technique to the dynamic bending collapse of rectangular section tubes', *Int. J. Impact Engineering*, Vol. 15, No. 6, pp. 797–814.

Ducrocq, P., Markiewicz, E., Harmand, S., De Luca, P. & Drazetic, P. 1998, 'Thermal influence on mild steel behaviour during a crash event', *IJCrash*, Vol. 3, No. 2, pp. 163-190.

Duffey, T & Karpp, R. 1979, 'A simplified approach for the dynamic plastic response of a submerged cylindrical containment vessel', Proc. 2nd Conf. on the Mechanical Properties of Materials at High Rates of Strain, Oxford March 28th-30th, (Inst. Phys. Conf. Ser. No. #47), pp. 299-306.

Ewins, D. J. 1984, *Modal testing : theory and practice*, Research Studies Press, Hertfordshire, England.

Gál, E. P. & Molnár, C. 1978, 'Behaviour of the safety bumper system and elements of buses under static and dynamic loads', XVII Int. Congress FISITA, June, Budapest.

Goldsmith, W. 1960, *Impact. The theory and physical behaviour of colliding solids*, E. Arnold, London.

Graves-Smith, T. R. 1972, 'The post-buckled behaviour of a thin-walled box beam in pure bending', *Int. J. Mech. Sci.*, Vol. 14, pp. 711-722.

Grzebieta, R.H. & Dayawansa, P. H. 1987, 'Roll-over analysis of a truck cabin frame', in Proc. Structural Crashworthiness and Property Damage Accidents Seminar, eds. N. W. Murray & R. H. Grzebieta, Monash Univ., Australia, Aug. 1987, pp. 111–133.

Grzebieta, R. H. & Murray, N. W. 1986, 'Energy absorption of an initially imperfect strut subjected to an impact load', *Int. J. Impact Engineering*, Vol. 4, No. 3, pp. 147-159.

Grzebieta, R. H. & White, G. J. 1994, 'Void filled square cantilever steel tubes subjected to gross plastic deformation', in *Tubular Structures VI*, eds. P. Grundy, A. Holgate & B. Wong, Proc. sixth Int. Symp. on Tubular Structures, 14th –16th December, Melbourne, Australia.

Gupta, N. K. 1998, 'Some aspects of axial collapse of cylindrical thin-walled tubes', *Thin-walled structures*, **32**, pp. 111-126.

Halvorsen, W. G. & Brown, D. L. 1977, 'Impulse Technique for Structural Frequency Response Testing', *Sound and Vibration*, November, pp. 8-21.

Han, D. C. & Park, S. H. 1999, 'Collapse behaviour of square thin-walled columns subjected to oblique loads', *Thin-walled Structures*, **35**, pp. 167-184.

Hanssen, A. G., Hopperstad, O. S. & Langseth, M. 2000, 'Bending of square aluminium extrusions with aluminium foam filler', *Acta Mechanica*, **142**, pp. 13-31.

Haque, M. M., Hashmi, M. S. J. & Pickering, F. B. 1987, 'Effects of strain rate and strain rate history on a medium carbon steel at room temperature', *Materials Forum*, Vol. 10, No. 3, pp. 214-217.

Harding, J. J. (ed.) 1979, Proc. Conf. Mechanical Properties of Materials at High Rates of Strain, Oxford, 28th – 30th March, (Inst. Physics Conf. Ser # 47)

Harrigan, J. J., Reid, S. R. & Peng, C. 1999, 'Inertia effects in energy absorbing materials and structures', *Int. J. Impact Engineering*, **22**, pp. 955–979.

Hashemi, S. M. R., Sadeghi, M. M. & Walton, A. C. 1996, 'Modelling verification of an airframe section and comparisons with impact test', *IJCrash*, Vol. 1, No. 1, pp. 11–20.

Haug, E., Arnaudeau, F., Dubois, J., de Rouvray, A. & Chedmail, J. F. 1983, 'Static and dynamic finite element analysis of structural crashworthiness in the automotive and aerospace industries' in *Structural Crashworthiness*, eds. N. Jones & T. Wierzbicki, Proc. 1st Int. Symp. on Structural Crashworthiness, Sep. 14-16, University of Liverpool, England.

Holzer, A. J. 1978a, *On Dynamic Mechanical Properties of Metals and their Measurement*, Ph.D. Thesis, Monash University, Dept. of Civil Eng., Australia.

Holzer, A. J. 1978b, 'A Technique for Obtaining Compressive Strength at High Strain-rates using Short Load Cells', *Int. J. Mech. Sci.*, 20, pp. 553-560.

Huang, S. & Khan, A. S. 1991, 'On the use of electrical-resistance metallic foil strain gauges for measuring large dynamic plastic deformation', *Experimental Mechanics*, June, pp. 122-125.

Impact Design, Inc. 1993, *Impact Design*, No. 3, Spring.

Jing, Y. & Barton, D. C. 1998, 'The response of square cross-section tubes under lateral impact loading', *IJCrash*, Vol. 3, No. 4, pp. 359–377.

Johnson, G. 1990, *Flexural Failure of Thin-Walled Hollow Sections*, B.E. Thesis, University of Technology, Sydney.

Jones, N. 1983, 'Structural aspects of ship collisions' in *Structural Crashworthiness*, eds. N. Jones & T. Wierzbicki, Proc. 1st Int. Symp. on Structural Crashworthiness, Sep. 14-16, University of Liverpool, England.

Jones, N. 1989a, *Structural Impact*, Cambridge University Press, Cambridge.

Jones, N. 1989b, 'Some comments on the modelling of material properties for dynamic structural plasticity', Proc. Conf. on Mechanical Properties of Materials at High Rates of Strain, 19th-22nd March, Oxford, (Inst. Physics conf. Ser. # 102), pp. 435–445.

Jones, N. 1993, 'Material properties for structural impact problems' in *Advances in Materials and their Applications*, ed. P. Rama Rao, Wiley Eastern Ltd., pp. 151 – 163.

Jones, N. 1999, 'Some phenomena in the structural crashworthiness field', *IJCrash*, Vol. 4, No. 4, pp. 335-350.

Jones, N. & Birch, R. S. 1990, 'Dynamic and static axial crushing of axially stiffened square tubes', *J. Mech. Eng. Sci.*, Proc. Inst'n. Mech. Eng. Part C, Vol. 204, pp. 293-310.

Kamal, M. M. 1970, 'Analysis and simulation of vehicle barrier impact', SAE paper # 700414.

Kassar, M. & Yu, W. W. 1992, 'Effect of strain rate on material properties of sheet steels', *J. Structural Engineering*, Vol. 118, No. 11, pp. 3136–3150.

Kecman, D. 1979, *Bending collapse of rectangular section tubes in relation to the bus roll over problem*, Ph.D. Thesis, Cranfield Institute of Technology.

Kecman, D. 1983, 'Analysis of framework-type safety structures in road vehicles', in *Structural Crashworthiness*, eds. N. Jones & T. Wierzbicki, Proc. 1st Int. Symp. on Structural Crashworthiness, Sep. 14-16, University of Liverpool, England.

Kecman, D. 1993a, 'Experience with the type approval of PSV structures for rollover safety based calculation combined with component tests', Conf. of Bus & Coach Experts, Budapest.

Kecman, D. 1993b, Personal communication, re: dynamic effects when type approving coaches for rollover safety by combination of calculation with component tests.

Kecman, D. 1994, 'Design, Analysis and Type Approval aspects of the PSV Rollover Safety', Int. Symp. on Automotive Technology and Automation, Proceedings of dedicated conference on Road and Vehicle Safety, Aachen, Germany.

Kecman, D. 1997, 'An engineering approach to crashworthiness of thin-walled beams and joints in vehicle structures', *Thin-walled Structures*, Vol. 28, Nos. 3/4, pp. 309-320.

Kecman, D. & Djokic, M. 1990, 'The effect and modelling of "finite stiffness hinges" in the collapse analysis of roll-over safety rings in buses and coaches', *Int. J. of Vehicle design*, Vol. 11, Nos. 4/5, pp. 374-384.

Kecman, D., Peric, D., Sadeghi, M., Suthurst, G. & Mahmood, H. 1990, 'Prediction of deep bending collapse characteristics of car body beams by regression analysis', XXIII FISITA Congress, Turin.

Kecman, D. & Randell, N. 1996, 'The role of calculation in the development and type approval of coach structures for rollover safety', in Proc. 15th Int. Technical Conf. on Enhanced Safety of Vehicles, pp. 787-795.

Kecman, D. & Tidbury, G. 1982, 'Theoretical prediction of the complete collapse behaviour of a coach subject to the proposed full scale rollover test', Proc. of the XIX FISITA Congress, Melbourne.

Kecman, D. & Tidbury, G. 1985, 'Optimisation of a bus superstructure from the rollover safety point of view', Proc. Tenth International Technical Conference on Experimental Safety Vehicles, 1st – 4th July, Oxford.

Kecman, D., Sadeghi, M. M. & Hardy, R. N. 1993, 'Early Design Stages in the Development of Crashworthy Structures', in *Crashworthiness and Occupant Protection in Transportation Systems*, AMD-Vol. 169/BED-Vol. 25, ASME, pp. 83-96.

Key, P. W. & Hancock, G. J. 1993a, 'A finite strip method for the elastic-plastic large displacement analysis of thin-walled and cold-formed steel sections', *Thin-Walled Structures*, **16**, pp. 3-29.

Key, P. W. & Hancock, G. J. 1993b, 'A theoretical investigation of the column behaviour of cold-formed square hollow sections', *Thin-Walled Structures*, **16**, pp. 31-64.

Key, P. W., Hasan, S. W. & Hancock, G. J. 1988, 'Column Behaviour of Cold-Formed Hollow Sections', *J. of Structural Engineering*, Vol. 114, No. 2, pp. 390-407.

Kim, C. W., Han, B. K., Won, C. J. & Lim, C. H. 1996, 'A study on crushing behaviour and energy absorption of a thin-walled rectangular tube under axial compression', First Australasian Congress on Applied Mechanics, 21st – 23rd February, Melbourne.

Kim, C., Lee, Y., Chung, T., Song, Y., King, S. & Chirwa, E. C. 1997, 'A study on large deflection of thin-walled tubes under pure bending', *IJCrash*, Vol. 2, No. 3, pp. 273-286.

Kim, H. & Wierzbicki, T. 2000, 'Numerical and analytical study on deep biaxial bending collapse of thin-walled beams', *Int. J. Mech. Sciences*, **42**, pp. 1947-1970.

Kitagawa, Y., Hagiwara, I. & Tsuda, M. 1992, 'Dynamic analysis of thin-walled columns with arbitrary section geometry subjected to axial crushing', *JSME Int. J. Series I*, Vol. 35, No. 2, pp. 189-193.

Kormi, K., Webb, D. C., Oguibe, C. N. & Al-Hassani, S. T. S. 1995, 'The dynamic and static axial crushing of axially stiffened square tubes – a comparison between numerical and experimental results', in *Crashworthiness and Occupant Protection in Transportation Systems*, AMD – Vol. 210 / BED – Vol. 30, ASME, pp. 143–160.

Kotelko, M & Królak, M. 1993, 'Collapse behaviour of triangular cross-section girders subject to pure bending', *Thin-walled Structures*, **15**, pp. 127-141.

Langseth, M. & Hopperstad, O. S. 1996, 'Static and dynamic axial crushing of square thin-walled aluminium extrusions', *Int. J. Impact Engineering*, Vol. 18, Nos. 7/8, pp. 949-968.

Langseth, M., Lindholm, U. S., Larsen, P. K. & Lian, B. 1991, 'Strain-rate sensitivity of mild steel grade St52-3N', *J. Engineering Mechanics*, Vol. 117, No. 4, pp. 719–732.

Langseth, M., Hopperstad, O. S. & Berstad, T. 1999, 'Crashworthiness of aluminium extrusions: validation of numerical simulation, effect of mass ratio and impact velocity', *Int. J. Impact Engineering*, Vol. 22, pp. 829-854.

Lindholm, U. S. 1974, 'Review of dynamic testing techniques and material behaviour', Proc. Conf. on Mechanical Properties of Materials at High Rates of Strain, Oxford, 2nd – 4th April, (Inst. Physics Conf. Ser # 21).

Mahmood, H. F., Paluszny, A. & Tang, X. 1988, 'Crash analysis of thin-walled beam-type structures', SAE paper # 880894.

Mamalis, A. G., Manolakos, D. E., Viegelahn, G. L., Johnson, D. M. & Baldoukas, A. K. 1992, 'On the effect of shear when bending crashworthy thin-walled steel tubes', *Thin-walled Structures*, **14**, pp. 153-165.

Manjoine, M. J. 1944, 'Influence of rate of strain and temperature on yield stresses of mild steel', *J. Applied Mechanics*, Vol. 11, pp. 211–218.

Marsh, K. J. & Campbell, J. D. 1963, 'The effect of strain rate on the post-yield flow of mild steel', *J. Mech. Phys. Solids*, Vol. 11, pp. 49–63.

Matolcsy, M. 1997, 'Crashworthiness of bus structures and rollover protection' in *Crashworthiness of Transportation systems: Structural impact and occupant protection*, eds. J. Ambrósio et al., Proc. of NATO Advanced Study Institute on Crashworthiness of Transportation Systems : Structural Impact and Occupant Protection, Portugal, July 7-19, pp. 321-360.

McIvor, I. K., Anderson, W. J. & Bijak-Zochowski, M. 1977a, 'An experimental study of the large deformation of plastic hinges', *Int. J. Solids Structures*, Vol. 13, pp. 53-61.

McIvor, I. K., Wineman, A. S. & Wang, H. C. 1977b, 'Plastic collapse of general frames', *Int. J. Solids Structures*, Vol. 13, pp. 197-210.

Meng, Q., Al-Hassani, S. T. S. & Soden, P. D. 1983, 'Axial crushing of square tubes', *Int. J. Mech. Sci.*, Vol. 25, No. 9-10, pp. 747-773.

Meyer, L. W. & Schrödter, A. 1999, 'Mechanical reduction of oscillations on a split Hopkinson bar – A simple, but efficient method for high strain rate material testing', Proc. ACAM 99, second Australasian congress On Applied Mechanics, 10th-12th February, Canberra, Australia.

Murray, N. W. 1983, 'The static approach to plastic collapse and energy dissipation in some thin-walled steel structures', in *Structural Crashworthiness*, eds. N. Jones, & T. Wierzbicki, Proc. 1st Int. Symp. on Structural Crashworthiness, Sep. 14-16, University of Liverpool, England.

Murray, N. W. & Khoo, P. S. 1981, 'Some basic plastic mechanisms in the local buckling of thin-walled steel structures', *Int. J. Mech. Sci.*, Vol. 23, No. 12, pp. 703-713

National Code of Practice 1992, 'Design parameters necessary for compliance with ADR 59/00 Omnibus Rollover Strength – Parts A & B', Vehicle Standards Bulletin No. 7, Parts A & B.

National Road Transport Commission 1997, 'Side-swipe crashes involving trucks and coaches – Design ideas for vehicle manufacturers', Technical Bulletin of the National Road Transport Commission and the Federal Office of Road Safety, Australia.

National Transportation Safety Board 1999, 'Remarks by Jim Hall, chairman National Transportation Safety Board before the School Journeys Conference', London, 19th May, < http://www.ntsb.gov/speeches/jhc990519.htm> (last accessed 9/1/2001).

Ohkami, Y., Tkada, K., Motomura, K., Shimamura, M., Tomizawa, H. & Usuda, M. 1990, 'Collapse of thin-walled curved beam with closed-hat section – part 1: Study on collapse characteristics', SAE paper # 900460.

Ohkubo, Y., Akamatsu, T. & Shirasawa, K. 1974, 'Mean crushing strength of closed-hat section members', SAE paper No. 740040.

Park, M. S. & Lee, B. C. 1996, 'Prediction of mode parameters and moment-rotation curves for crushed thin-walled trapezoidal tubes in bending', *J. Applied Mechanics*, Vol. 63, June, pp. 453-459.

Perrone, N. 1965, 'On a simplified method for solving impulsively loaded structures of strain-rate sensitive materials', *J. Applied Mechanics*, September, pp. 489-492.

Perrone, N. 1966, 'A mathematically tractable model of strain-hardening, rate-sensitive plastic flow', *J. Applied Mechanics*, March, pp. 210–211.

Perrone, N. & Bhadra, P. 1979, 'A simplified method to account for plastic rate sensitivity with large deformations', *J. of Applied Mechanics*, Vol. 46, Dec., pp. 811-816.

Perrone, N. & Bhadra, P. 1984, 'Simplified large deflection mode solutions for impulsively loaded viscoplastic, circular membranes', *J. of Applied Mechanics*, Vol. 51, Sep., pp. 505-509.

Prasad, P. & Padgaonkar, A. 1981, 'Static-to-dynamic amplification factors for use in lumped-mass vehicle crash models', SAE paper # 810475.

Rains, G. C. & Van Voorhis, M. A. 1998, 'Quasi-static and dynamic roof crush testing', National Highway Traffic Safety Administration Vehicle Research and Test Centre, U.S.A., Report # VRTC-82-0197/VRTC-86-0391, June
http://www-nrd.nhtsa.dot.gov/vrtc/cw/roofcrsh.pdf (last accessed 9/1/2001)

Ramsey, K. A. 1976, 'Effective Measurements for Structural Dynamics Testing, Part II', *Sound and Vibration*, April, pp. 18-31.

Reddy, B. D. 1979, 'An experimental study of the plastic buckling of circular cylinders in pure bending', *Int. J. Solids Structures*, Vol. 15, pp. 669-683.

Reid, J. D. 1996, 'Towards the Understanding of Material Property Influence on Automotive Crash Structures', *Thin-Walled Structures*, **24**, pp. 285-313.

Reid, S. R. 1983, 'Laterally compressed tubes as impact energy absorbers' in *Structural Crashworthiness*, eds. N. Jones & T. Wierzbicki, Proc. 1st Int. Symp. on Structural Crashworthiness, Sep. 14-16, University of Liverpool, England.

Reid, S. R. 1984, 'Influence of inertia in structural crashworthiness' in *Vehicle Structures*. Proc. Int. Conf. on vehicle structures, Cranfield Institute of Technology, 16th-18th July, Inst. Mech. Eng., London, pp. 63-70.

Reid, S. R. & Reddy, T. Y. 1979, 'Effects of Strain-rate on the Dynamic Lateral Compression of Tubes', Proc. 2nd Conf. on the Mechanical Properties of Materials at High Rates of Strain, Oxford March 28th-30th, (Inst. Phys. Conf. Ser. No. #47), pp. 288-298.

Reid, S. R., Reddy, T. Y. & Peng, C. 1993, 'Dynamic compression of cellular structures and materials' in *Structural Crashworthiness and Failure*, Eds. N. Jones & T. Wierzbicki, Proc. 3rd Int. Symp. on Structural Crashworthiness, Apr. 14-16, University of Liverpool, England.

Roca, T., Arbiol, J. & Ruiz, S. 1997, 'Development of roll-over resistant bus structures', SAE paper # 970581.

Santosa, S. & Wierzbicki, T. 1997, 'Effect of ultralight metal filler on the torsional crushing behaviour of thin-walled prismatic columns', *IJCrash*, Vol. 2, No. 4, pp. 305-331.

Seki, N. & Sunami, Y. 1978, 'Energy absorption of thin-walled box beam subjected to combination of bending with axial compression', XVII Int. Cong. FISITA, Budapest, June, pp. 1435-1446.

Sheh, M. Y. & Khalil, T. B. 1991, 'The impact response of a vehicle rail structure by experiments and finite element analysis', in *Crashworthiness and Occupant Protection in Transportation Systems*, AMD - Vol. 126 / BED – Vol. 19, ASME, pp. 195-206.

Shi, M.F. & Meuleman, D. J. 1995, 'On certain aspects of strain rate sensitivity of sheet steels', *J. Materials Engineering and Performance*, Vol. 4(3), June, pp. 321-333.

Smith, C. 1989, 'Behaviour of composite and metallic superstructures under blast loading', in *Structural Failure*, eds. T. Wierzbicki & N. Jones, Proc. 2nd Int. Symp. on Structural Crashworthiness, June 6-8, Massachusetts Institute of Technology, USA.

Sully, R. M. & Hancock, G. J. 1996, 'Behaviour of Cold-Formed SHS Beam-Columns', *J. of Structural Engineering*, Vol. 122, No. 3, pp. 326-336.

Tam, L L. 1990, *Strain-rate and inertia effects in the collapse of energy absorbing structures*, Ph.D. Thesis, University of Cambridge.

Tam, L. L. & Calladine, C. R. 1991, 'Inertia and strain-rate effects in a simple plate-structure under impact loading', *Int. J. Impact Engineering*, Vol. 11, No. 3, pp. 349-377.

Tani, M. & Emori, R. I. 1970, 'A study on automobile crashworthiness', SAE paper # 700175.

Tani, M. & Funahashi, A. 1978, 'Energy absorption by the plastic deformation of body structural members', SAE paper # 780368.

Thornton, P. 1975, 'Static and dynamic collapse characteristics of scale model corrugated tubular sections', *J. Engineering Materials and Technology*, October, pp. 357-362.

Thornton, P. & Yeung, K. 1990, 'The dynamic buckling of sheet steel', *Int. J. Impact Engineering*, Vol. 9, No. 4, pp. 379-388.

Todorovska-Azievska, L. & Kecman, D. 1988, 'Multi-axial collapse of rectangular section tubes and its modelling in finite element analysis', SAE paper # 880896.

VanKuren, R. C. & Scott, J. E. 1977, 'Energy absorption of high-strength steel tubes under impact crush conditions', SAE paper #770213.

Vignjevic, R. & Cavalcanti, M. J. 1997, 'Numerical simulation of the Lynx helicopter main lift-frame component collapse', *IJCrash*, Vol. 2, No. 1, pp. 25–37.

Vignjevic, R., Kecman, D. & Sadeghi, M. 1990, 'Extraction of the hinge moment-rotation curves from the Dyna-3D analysis of the deep bending collapse of a thin-walled tube', DYNA-3D users meeting, Bournemouth.

Vignjevic, R., Kecman, D. & Sadeghi, M. 1993, 'The improved compound beam element with non-linear moment-rotation curves for the car side impact and roof crush analysis using DYNA3D program', in *Crashworthiness and Occupant Protection in Transportation Systems*, AMD Vol. 169/BED Vol. 25, ASME.

Wallentowitz, H. & Adam, H. 1995, 'Predicting the crashworthiness of vehicle structures made by lightweight design materials and innovative joining methods', in Crashworthiness and Occupant Protection in Transportation Systems, AMD – Vol. 210 / BED – Vol. 30, ASME, pp. 331-354.

Wardill, G. A. & Kecman, D. 1980, 'Theoretical prediction of the overall collapse mode and maximum strength of a bus structure in a roll over situation', XVIII FISITA Congress, Vol. 1, Hamburg, pp. 281-290.

White, G. J., Grzeibieta, R. H. & Murray, N. M. 1993, 'Maximum strength of square and thin-walled sections subjected to combined loading of torsion and bending', *Int. J. Impact Engineering*, Vol. 13, No. 2, pp. 203-214.

Wierzbicki, T. 1983a, 'Crushing analysis of metal honeycombs', *Int. J. Impact Engineering*, Vol. 1, No. 2, pp. 157-174.

Wierzbicki, T. 1983b, 'Crushing behaviour of plate intersections' in *Structural Crashworthiness*, eds. N. Jones & T. Wierzbicki, Proc. 1st Int. Symp. on Structural Crashworthiness, Sep. 14-16, University of Liverpool, England.

Wierzbicki, T. & Abramowicz, W. 1983, 'On the crushing mechanics of thin-walled structures', *J. Appl. Mech.*, Vol. 50, pp. 727-734.

Wierzbicki, T. & Abramowicz, W. 1990, 'CRASH-CAD – A computer program for design of columns for optimum crash', SAE paper # 900462.

Wierzbicki, T. & Akerstrom, T. 1977, 'Dynamic crushing of strain-rate sensitive box columns', Proceedings of the 2nd Int. Conf. on Vehicle Structural Mechanics, April 18-22, Michigan, SAE paper #770592.

Wierzbicki, T., Molnár, C. & Matolcsy, M. 1978, 'Experimental-theoretical correlation of dynamically crushed components of bus frame structure', XVII Int. Congress FISITA, June, Budapest.

Wierzbicki, T., Recke, L., Abramowicz, W., Gholami, T. & Huang, J. 1994, 'Stress profiles in thin-walled prismatic columns subjected to crush loading – II. Bending', *Computers & Structures*, Vol. 51, No. 6, pp. 625–641.

Wulf, G. L. 1974, 'Dynamic stress-strain measurements at large strains', Proc. Conf. on Mechanical Properties of Materials at High Rates of Strain, Oxford, 2nd – 4th April, (Inst. Physics Conf. Ser # 21), pp. 48-52.

Yu, T. X., Reid, S. R. & Wang, B. 1993, 'Hardening-softening behaviour of tubular cantilever beams', *Int. J. Mech. Sci.*, Vol. 35, No. 12, pp. 1021-1033.

Zaouk, A. K., Marzougui, D. & Bedewi, N. E. 2000a, 'Development of a detailed vehicle finite element model Part I: Methodology', *IJCrash*, Vol. 5, No. 1, pp. 25–35.

Zaouk, A. K., Marzougui, D. & Kan, C. D. 2000b, 'Development of a detailed vehicle finite element model Part II: Material characterisation and component testing', *IJCrash*, Vol. 5, No. 1, pp. 37–50.

Zhao, X. & Hancock, G. J. 1990, 'T-joints in rectangular hollow sections subject to combined bending and concentrated force', Presented at conf. on Structural Engineering, Institution of Engineers Australia, Adelaide 3-5 October, pp. 456-461.

Zhao, X. & Hancock, G. J. 1991, 'Tests to determine plate slenderness limits for cold-formed rectangular hollow sections of grade C450', *Steel Construction*, Vol. 25, No. 4, pp. 2-16.

Zhao, X. & Hancock, G. J. 1992, 'Square and rectangular hollow sections subject to combined actions', *J. of Structural Engineering*, Vol. 118, No. 3, pp. 648-668.

Zhao, X. & Hancock, G. J. 1995, 'Butt welds and transverse fillet welds in thin cold-formed RHS members', *J. of Structural Engineering*, Vol. 121, No.11, pp. 1674-1682.

Zhu, L., Faulkner, D. & Atkins, G. 1994, 'The impact of rectangular plates made from strain-rate sensitive materials', *Int. J. Impact Engineering*, Vol. 15, No. 3, pp. 243-255.

Zukas, J. A., Nicholas, T., Swift, H. F., Greszczuk, L. B. & Curran, D. R. (eds.) 1982, *Impact Dynamics*, John Wiley & Sons, New-York.

# APPENDIX A – Kecman's Analytical Model

Kecman (1979) derived a relatively simple analytical model to predict the $M$-$\theta$ collapse response of RHS in bending. Kecman's yield line model of the buckle mechanism is shown in Figure A.1. The model is applicable for a wide range of section sizes and now forms the basis of the commercial software program WEST which is part of the CIC – SIM family of programs (Kecman & Randell 1996). Input parameters to the model are the width, depth and thickness of the RHS section together with the yield and ultimate tensile stresses of the RHS material. The model defines buckle rotation $\theta$, as the relative angle between the two yield lines bounding the mechanism, *GK* and *EL*, and assumes $\theta = 0$ at buckle initiation.

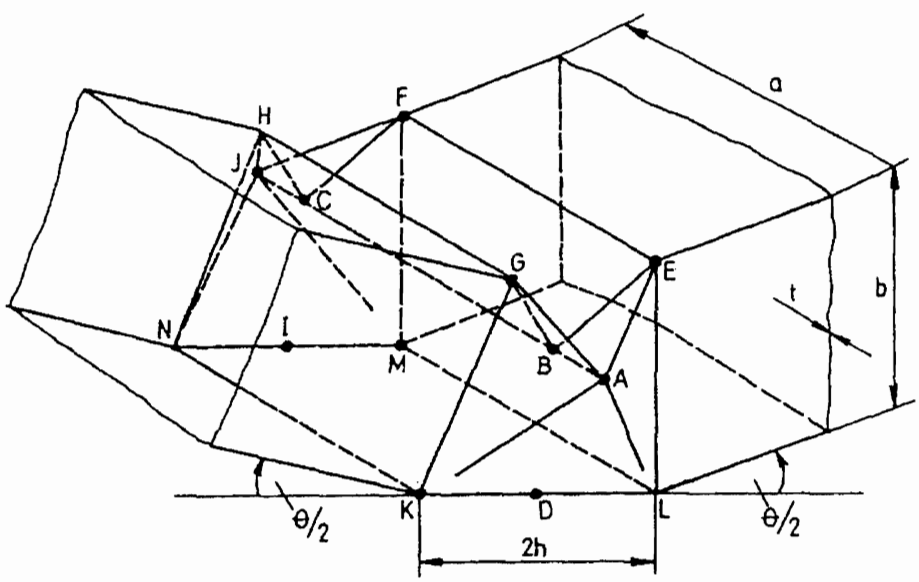


**Figure A.1:** Yield line model of the buckle mechanism, Kecman (1979)

Close study of the model derivation given in Kecman (1979) identified two issues that warrant discussion and a possible typographical error that has been overlooked in subsequent publications. Equation numbers in square brackets correspond to the equation numbers in Kecman (1979).

## A.1 INTEGRATION OF ROLLING ENERGY

There are two moving yield lines in Kecman's model, lines *GA* and *KA*. As the buckle develops these lines sweep out an area of material that is bent then straightened, or "rolled", as the yield line passes. The energy absorbed by this rolling process is outlined below.

### A.1.1 Work done by "Rolling"

A roller of radius $r$ travels from point $A$ to point $B$, under a sheet such that the sheet is "bent" and then "straightened" as shown in Figure A.2.

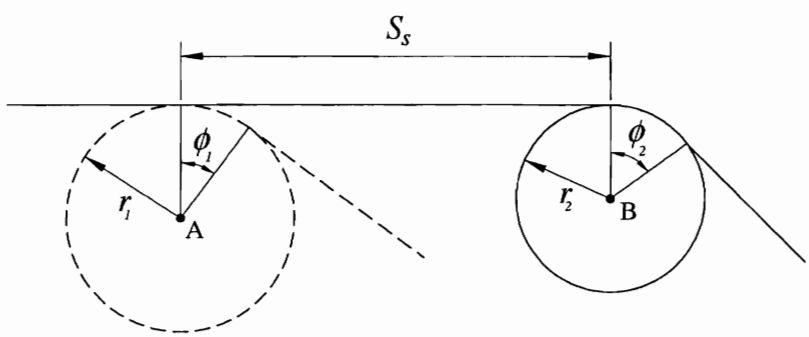


**Figure A.2:** Rolling deformation - general case

In the general case, as the roller moves from point $A$ to point $B$ the "wrap angle" $\phi$ and the roller radius $r$ both change. Figure A.3 shows the movement of material over the roller for an infinitesimal displacement of the roller from point $O$ to point $O'$. The material between points $A$ and $A'$ is straightened, the material between points $B$ and $B'$ is bent and the material between points $A'$ and $B$ is bent from radius $r_1$ to the new radius $r_2$ while sliding over the surface of the roller.

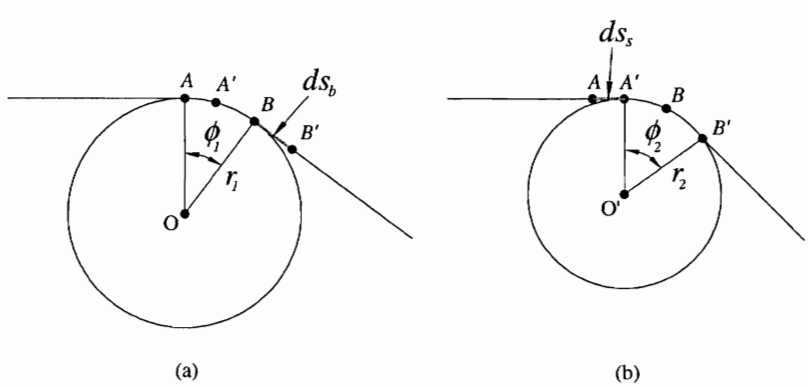


**Figure A.3:** General rolling deformation – movement of material over the roller for an infinitesimal displacement of the roller from $O$ to $O'$

Equation A.1 gives the work done, per unit width of sheet, during the infinitesimal displacement of the roller from $O$ to $O'$ shown in Figure A.3. Defining:

$S_b$ = length of material bent

$S_s$ = length of material straightened

$W' = \dfrac{dW}{dl}$ = work done per unit width of sheet

$m_p$ = plastic moment per unit width of sheet

$dW' =$ work done straightening length $ds_s$ + work done bending length $ds_b$ + work done changing the radius of length $A'B$.

arc length $A'B = r_1\phi_1 - ds_s = r_2\phi_2 - ds_b$

$$dW' = m_p\left[\frac{ds_s}{r_1} + \frac{ds_b}{r_2} + \left(\frac{r_2\phi_2 - ds_b}{r_2}\right) - \left(\frac{r_1\phi_1 - ds_s}{r_1}\right)\right]$$

$$= m_p\left[2\frac{ds_s}{r_1} + (\phi_2 - \phi_1)\right]$$

$$dW' = m_p\left[2\frac{ds_s}{r_1} + d\phi\right] \qquad \text{(A.1)}$$

To simplify the calculation of the work done during the rolling process it is assumed that $\phi_2$ is equal to $\phi_1$, as shown in Figure A.4. This assumption implies that the plastic strain energy in the material in contact with the roller is constant.

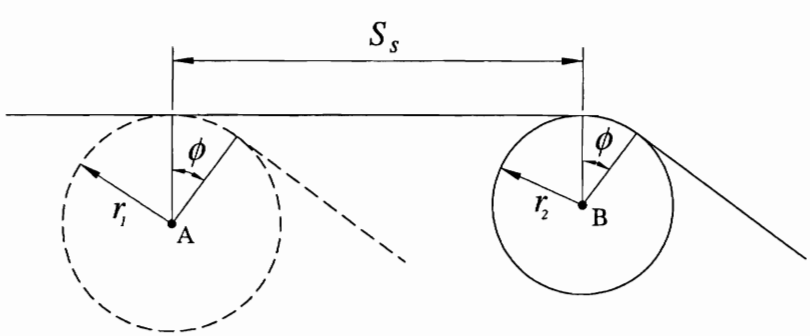


**Figure A.4:** Rolling deformation - simplified case

For a small increase in buckle rotation $d\theta$, the geometry of the buckle changes a corresponding amount $ds_{0\theta}$ as shown in Figure A.6, and the increments in the area rolled by yield lines *GA* and *KA* are *AGA'* and *AKA'* respectively. The work done in rolling the material in these areas can be determined by applying Equation A.3. While Equation A.3 requires integration normal to $ds_s$, i.e. along lines *GA* and *KA*, the integral is simplified by integrating along the direction $l$. The increment in rolled material is then given by $ds$ and the elemental width of material for this increment is $dl$ (the width normal to $ds$). For rolling along *GA* and *KA* we thus have:

$$W(\theta) \approx 2m_p \int_0^L \int_0^\theta \frac{ds}{r}\, dl \tag{A.4}$$

where:

$$ds_{0\theta} = \frac{d}{d\theta}(S_{0\theta}) \times d\theta$$

$$ds = g(l, ds_{0\theta}) = h(l, d\theta)$$

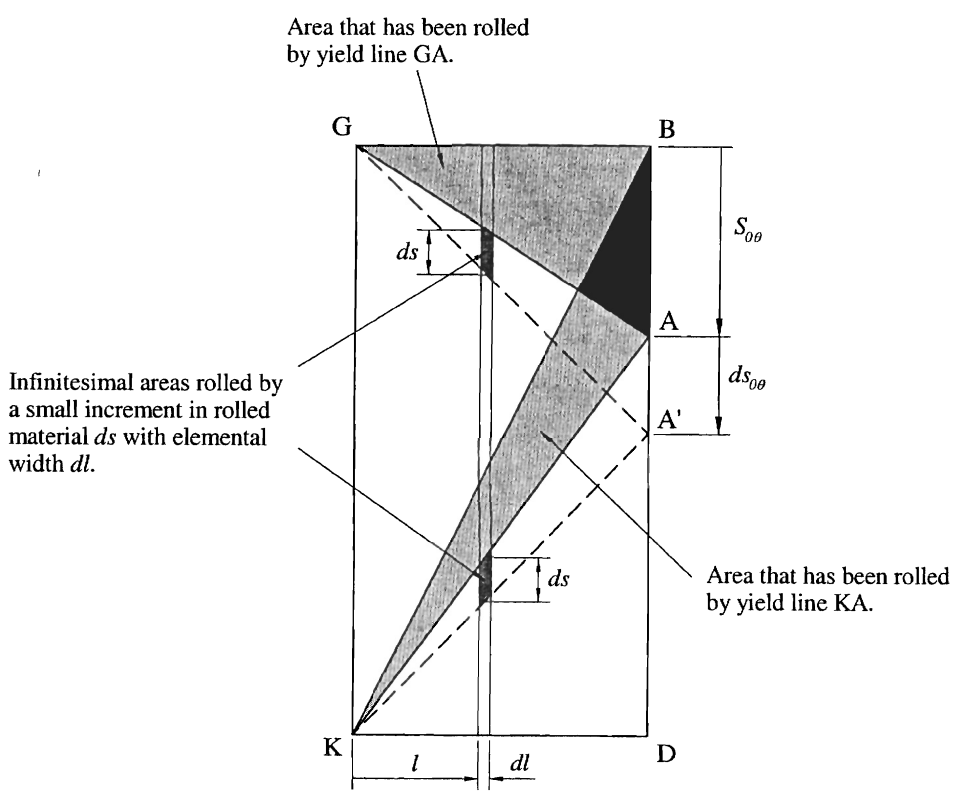


**Figure A.6:** Increment in buckle collapse corresponding to an increment in buckle rotation "mapped" onto the undeformed web

### A.1.2.2 YIELD LINE *KA*

It is assumed that both $\delta s$ and $r$ are functions of $l$ and $\theta$ with:

$$\delta s = \frac{l}{L}\delta s_{o\theta} \text{ and } r(l) = \frac{L}{l}r_r(\theta)$$

which leads to:

$$\delta W_7 \approx 2m_p \int_0^L \frac{\delta s}{r} dl = 2m_p \int_0^L \frac{l\delta s_{0\theta}}{L}\frac{l}{r_r L} dl = 2m_p \frac{\delta s_{0\theta}}{r_r}\int_0^L \frac{l^2}{L^2} dl = 2m_p L \frac{\delta s_{0\theta}}{3r_r}$$

Summing over $\theta$ gives:

$$W_7(\theta) \approx \frac{2m_p}{3} L \sum_0^\theta \left(\frac{\delta s_{0\theta}}{r_r}\right)_\theta$$

Substituting $L = h$ and $S_{0\theta} = z_{A\theta}$

$$W_7(\theta) \approx \frac{2m_p}{3} h \sum_0^\theta \left(\frac{\delta z_{A\theta}}{r_r}\right)_\theta \tag{A.7}$$

This compares with $W_7 = \frac{2m_p}{3}\overline{KA}\left(\frac{\sum_0^\theta \delta z_{A\theta}}{r_r}\right)_\theta = \frac{2m_p}{3}\overline{KA}\left(\frac{z_{A\theta}}{r_r}\right)_\theta$ using Kecman's analysis. The difference between Equation A.7 and Kecman's result is due to the fact that Kecman:

- neglected the variation of $r_r$ with $\theta$; and
- integrated along the yield line *KA* but defined the increment in rolled length *ds* as in Figure A.6, hence *ds* and *dl* were not perpendicular.

## A.2 FLATTENING OF THE CORNER MATERIAL

Kecman includes a separate energy term $W_4$, given by Equation [5.52], to account for the flattening of the corner material along the line *BG*. It is the opinion of the author that the energy associated with flattening the corner of the RHS along *BG* is approximately accounted for by the rolling action of yield line *GA*. This can be understood by referring to Figure A.3 and Equation A.1.

Equation A.1 represents the work done in the general "rolling" of a sheet of material. The derivation of Equation A.1 considers the work associated with straightening the material that is initially "wrapped" around the roller and the work associated with bending the material that remains "wrapped" around the roller after a length $S_s$ of material has been "rolled". The length of material initially "wrapped" around the roller can be considered to represent the initial corner material of the RHS. Therefore Equation A.1 accounts for the work done flattening the corner of the RHS and no further special consideration of this material, such as energy term $W_4$, is required.

It has also been concluded by Meng et al. (1983), in the development of a yield line model to describe the axial crushing of square tubes, that the flattening of the original corner material was accounted for by the rolling action.

## A.3 THE "COMBINED" EXPRESSION FOR *W*

Equation [6.38] is the expression for total energy absorbed in the buckle as a function of buckle rotation. This equation collects all eight energy terms derived in Chapter 5 of Kecman's thesis. After rearranging Equation [6.38] Kecman obtained Equation [6.39]. However, Equations [6.38] and [6.39] are not equivalent.

$$W(\theta)=\frac{\sigma_{pu}t^2}{2}\left\{\begin{array}{l} a\cdot(\pi-2\beta)+2b\cdot atan\left[\dfrac{z_A}{\sqrt{(h-x_{A'})^2+(y_{A'}-y_A)^2}}\right]+ \\ h\cdot\left[\pi+2\cdot atan\left(\dfrac{z_A}{y_A}\right)\right]+\dfrac{2z_A}{r}\cdot\left[h+\dfrac{2}{3}\sqrt{h^2+y_A^2+z_A^2}\right] \end{array}\right\} \qquad [6.39]$$

In the first term inside the large braces the variable $a$ should be $(a+z_A)$. Equation [6.39] should thus read:

$$W(\theta)=\frac{\sigma_{pu}t^2}{2}\left\{\begin{array}{l} (a+z_A)\cdot(\pi-2\beta)+2b\cdot atan\left[\dfrac{z_A}{\sqrt{(h-x_{A'})^2+(y_{A'}-y_A)^2}}\right]+ \\ h\cdot\left[\pi+2\cdot atan\left(\dfrac{z_A}{y_A}\right)\right]+\dfrac{2z_A}{r}\cdot\left[h+\dfrac{2}{3}\sqrt{h^2+y_A^2+z_A^2}\right] \end{array}\right\} \qquad (A.8)$$

Unfortunately, this error, which is assumed to be typographical, has not been taken into account in a number of subsequent publications.

## A.4 SIGNIFICANCE OF THESE CORRECTIONS

### Moment Vs Buckle Plastic Rotation *(M-θ)*

Together, the rolling energy components $W_6$ and $W_7$ account for the majority of the energy absorbed in the buckle mechanism. Therefore the differences between the energies given by Equations A.6 and A.7 and those predicted by Equations [5.57] and [5.64] have a significant influence on the predicted $M$-$\theta$ response. Figure A.7 below compares the average quasi-static $M$-$\theta$ response from Chapter 5, the $M$-$\theta$ response predicted by Kecman (after including the correction in Equation A.8) and the $M$-$\theta$ response predicted using the definitions of $W_6$ and $W_7$ given by Equations A.6 and A.7. (It should be noted that the energy term $W_4$ is not a function of $\theta$ and therefore the inclusion, or exclusion, of this term does not affect the $M$-$\theta$ response).

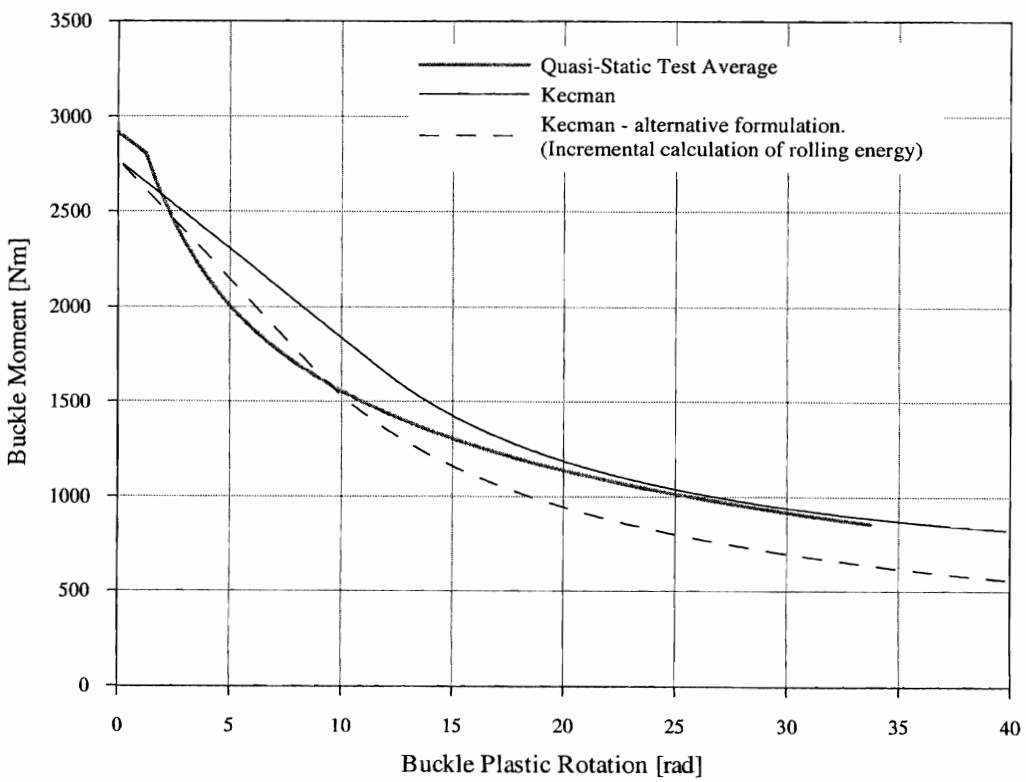


**Figure A.7:** Comparison of buckle moment responses
Quasi-static test average, Kecman and Kecman – alternative formulation

The $M$-$\theta$ response predicted by the formulation derived above compared well in the initial stages of collapse but underestimated the measured response in the deep collapse region ($\theta$ greater than 15°). This is in contrast to Kecman's formulation, which overestimated the initial response but compared well in the deep collapse region.

### Buckle Plastic Energy Vs Buckle Plastic Rotation *(E-θ)*

Figure A.8 below compares the average quasi-static $E$-$\theta$ response from Chapter 5, the $E$-$\theta$ response predicted by Kecman (Equation A.8) and the $E$-$\theta$ response predicted using the definitions of $W_6$ and $W_7$ given by Equations A.6 and A.7 and excluding energy term $W_4$. Also shown is the $E$-$\theta$ curve given by Equation A.8 with energy term $W_4$ excluded.

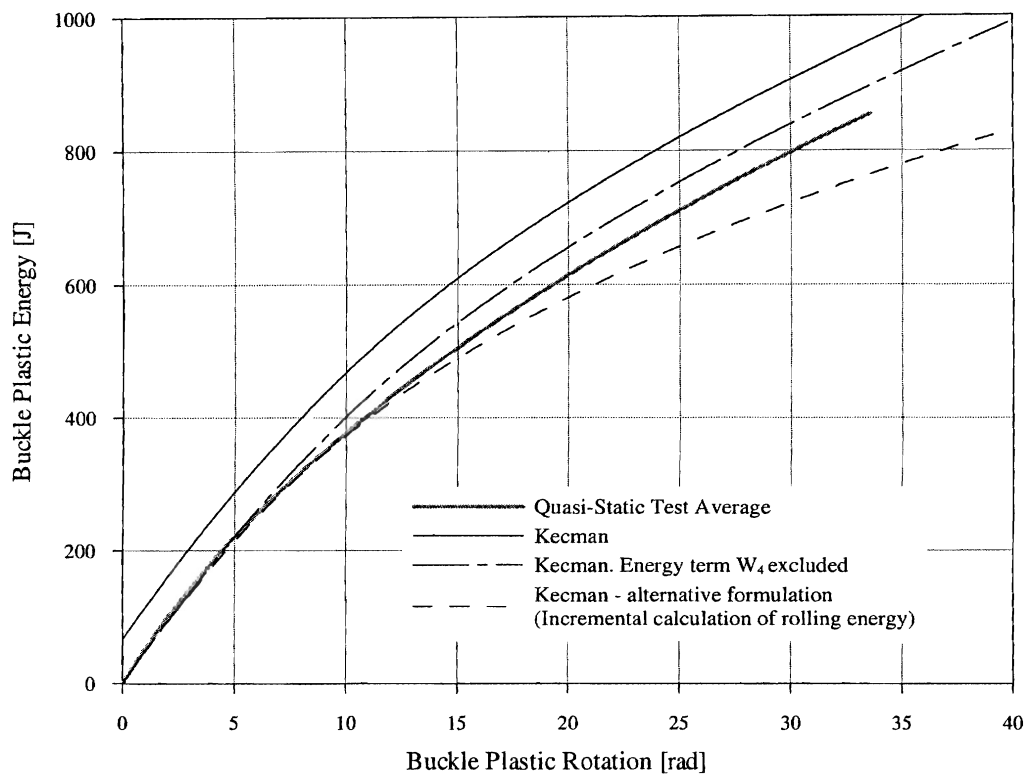


**Figure A.8:** Comparison of buckle plastic energy responses
Quasi-static test average, Kecman and Kecman – alternative formulation

At a buckle mechanism rotation of 34° the total buckle plastic energy predicted by Kecman's formulation overestimated the measured energy capacity of the buckle by approximately 13%. The present formulation predicted an energy capacity 21% lower than the energy capacity predicted by Kecman's formulation and underestimated the measured energy capacity of the buckle by approximately 11%. The $E$-$\theta$ curve corresponding to Equation A.8 minus energy term $W_4$, overestimated the measured buckle energy capacity by only 5%.

# APPENDIX B - High-Elongation Strain Measurements

Severe demands are placed on strain gauge installations when high elongations are measured. High-elongation strain measurements necessitate the use of special gauges, adhesives, surface preparation and signal correction procedures. The reader is referred to the various Measurements Group technical notes that discuss these issues, including B-129, TT-605, TT-609 and TT-610. The intent of this discussion is not to repeat the procedures presented in the Measurements Group literature but to outline the particular difficulties that were experienced during this research and to describe the techniques derived to overcome these difficulties.

## B.1 Strain Gauge Installation

Considerable time was spent testing the techniques described in the Measurements Group literature before strain gauge installation procedures were established that produced reliable results for the current application.

### B.1.1 Surface Preparation

Because of the higher bond-line forces involved in high-elongation measurements, the smooth surface obtained from standard surface preparation procedures must be altered for greater bond strength. TT-605 recommended a procedure that sought to achieve a surface with a roughness of approximately 6.4 μm rms. Due to the high surface hardness of the coupon material in this study, the maximum surface roughness obtained following these guidelines was only 2.5 to 3 μm rms. It was determined by experimentation that, although not as rough as recommended, a surface produced by hand abrading, in a cross-hatched pattern, using 40 grit aluminium oxide paper produced good results.

### B.1.2 Adhesive

Measurements Group A-12 adhesive was chosen for its high elongation capacity of 15% to 20%. To maximise the elongation capacity of this adhesive the bond was cured for 2 hours at a glue-line temperature of 74°C under a clamping pressure of 70 to 85 $N/mm^2$. A special jig was designed for this purpose, see Plate B.1, wherein dead weights applied constant pressure to a stack of up to 12 coupons.

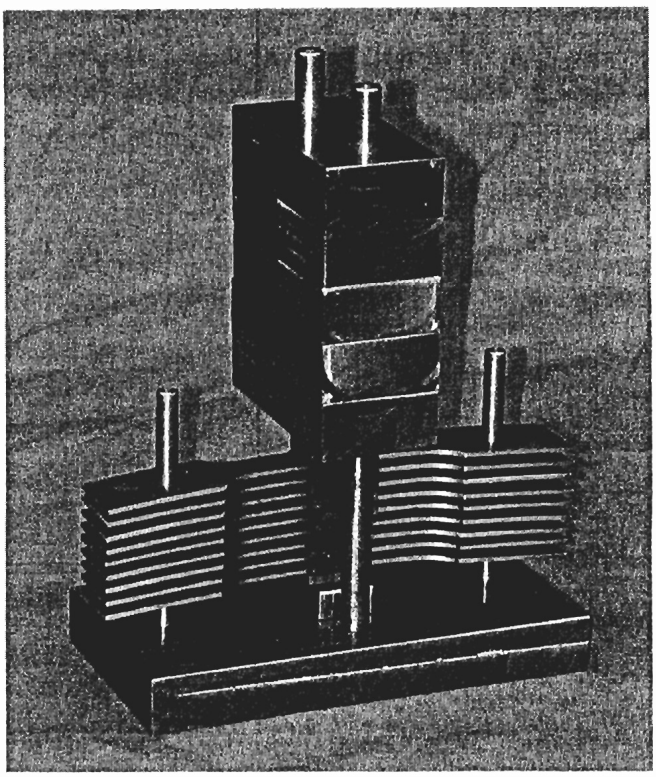

**Plate B.1:** Tensile coupon - bond curing jig

## B.1.3 Wiring

The recommendations given in technical note TT-605 regarding gauge wiring were followed. However, to avoid premature failure at the gauge solder tab, it was found that large strain relief loops were required, see Plate B.2, and that an absolute minimum amount of solder had to be used.

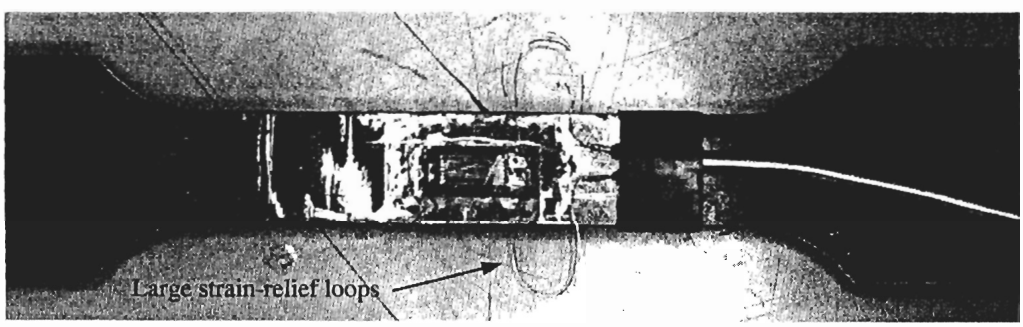


**Plate B.2:** Large strain relief loops on tensile coupons

## B.2 LARGE STRAIN SIGNAL CORRECTIONS

An additional concern when measuring strains greater than a few percent is the need to correct for errors and non-linearities in the relationship between measured bridge output voltage and actual strain. The two major sources of error were Wheatstone bridge and gauge factor non-linearities. Changes in the transverse sensitivity of the gauge at large strains were also a potential source of error.

### B.2.1 Background Theory

#### B.2.1.1 BRIDGE NON-LINEARITY (TN- 507)

The correction for bridge non-linearity is well documented and easily derived. (See Measurements Group technical note TN-507 "Errors Due to Wheatstone Bridge Non-linearity"). For a bridge arrangement consisting of a single active gauge in uniaxial tension or compression, the relationship between bridge output voltage and actual strain is given by Equation B.1.

$$R = \frac{E_o}{E_{exc.}} = \frac{F\varepsilon}{4 + 2F\varepsilon} \tag{B.1}$$

where:

$E_o$ = Bridge Output Voltage [V]
$E_{exc.}$ = Bridge Excitation Voltage [V]
$F$ = Gauge Factor
$\varepsilon$ = Actual Strain [$\varepsilon$]

#### B.2.1.2 GAUGE FACTOR NON-LINEARITY (TT-605)

The Measurements Group type EP gauges used in this research were made from annealed constantan alloy. Although this alloy is one of the most linear of all strain gauge alloys, it does exhibit small changes in gauge factor at large strains. According to Measurements Group technical tip TT-605, "*in theory the gage factor of a strain gage approaches a value of* $2+\varepsilon$ *when the gage alloy is strained beyond its elastic range*" (assuming the small strain gauge factor = 2). The elastic range for constantan alloy is approximately 0.5%. Enquiries directed to Measurements Group to clarify the procedure for determining this correction revealed that the nature of gauge factor variation at high

strains is a subject requiring further study. In a personal communication, Measurements Group made the following suggestions.

> *"For strains between 10% to 20% there is a definite change in gauge factor. This change is non-linear as strain levels increase. The non-linearity is similar to the non-linearity of a quarter Wheatstone bridge, but opposite in sign. Which means that if you use a single strain gauge in a Wheatstone bridge and set the gauge factor (G.F.) control to the manufacturer's G.F., you may not feel the need to make any corrections between 10% to 20% strain.*
>
> *The region between 5%-10% is unclear, but believed to be of a relatively small error. Which leads us to assume that if you set your instrument G.F. control to the manufacturer's gauge factor, you will not be too far off from the correct strain."*

Huang and Khan (1991) conducted high strain rate ($\dot{\varepsilon}_{avg} \approx 1200 s^{-1}$) compression tests on cylindrical 1100-0 annealed aluminium specimens to which metallic foil strain gauges were attached in both the axial and circumferential directions. Engineering gauge factors for the strain gauges were calculated using measurements of specimen length and diameter before and after testing and measurements of gauge resistance before and after testing. This procedure was repeated for a range of final axial strains from -7 to -34%. Huang and Khan found that the gauge factor for the annealed constantan-alloy gauges tested varied linearly with strain, as described by Equation B.2. Quasi-static tests conducted by Huang and Khan confirmed that Equation B.2 was also valid for extremely low strain rates. It should be noted that the manufacturer's gauge factor (which is typically determined at 0.1% strain) for the gauges tested by Huang and Khan was 2.16 and that the gauge factor predicted by Equation B.2 for 0.1% strain is only 1.94.

$$F = 1.9357 + 1.8163 \times \varepsilon \tag{B.2}$$

#### B.2.1.3 TRANSVERSE SENSITIVITY (TN-509)

Transverse sensitivity in a strain gauge refers to the behaviour of the gauge in responding to strains that are perpendicular to the primary sensing axis of the gauge. Often the error due to transverse sensitivity can be neglected but in some circumstances, such as biaxial strain fields, the error can be significant. In the particular case of uniaxial

stress in a material with Poisson's ratio of 0.285, the error is zero. This is because the gauge factor given by the manufacturer is measured under these conditions and already includes the effect of the Poisson strain.

Measurements Group technical note TN-509 "Errors Due to Transverse Sensitivity in Strain Gauges" derived the following equation for the error due to transverse sensitivity for a strain gauge oriented at any angle, in a general "small strain" strain field, on any material.

$$n_\varepsilon = \frac{K_t\left(\frac{\varepsilon_t}{\varepsilon_a} + \nu_0\right)}{1 - \nu_0 K_t} \times 100 \qquad \text{(B.3)}$$

where: $n_\varepsilon =$ the error as a percentage of the actual strain along the gauge axis.

$F_t =$ transverse gauge factor for small strains.

$F_a =$ axial gauge factor for small strains.

$K_t =$ $F_t / F_a$ , transverse sensitivity coefficient for small strains, provided by the gauge manufacturer.

$\nu_0 =$ the Poisson's ratio of the material on which the manufacturer's gauge factor was measured (usually 0.285).

$\varepsilon_a, \varepsilon_t =$ actual strains parallel and perpendicular to the primary sensing axis of the gauge.

## B.2.2 Final Working Corrections for Large Strain Measurements

The only way to properly correct for the simultaneous influence of bridge non-linearity, gauge factor non-linearity and transverse sensitivity at large strains is to perform a calibration in the actual strain field. Such a calibration was not performed, as it would have been an extensive study in itself. Instead, the following approach was adopted for calculating true axial strain from the strain signal recorded in these tensile tests.

### B.2.2.1 Transverse Sensitivity Correction

At small strains, the state of strain at the centre of the tensile coupon approximated the conditions under which the manufacturer measured gauge factor, and no correction for transverse sensitivity was necessary. At strains beyond the elastic limit of the test coupon Poisson's ratio approached 0.5 and the conditions no longer corresponded to those under which the gauge factor was determined. Furthermore, at large strains the

transverse and axial gauge factors $F_t$ and $F_a$ are likely to differ from those determined by the manufacturer at small strains. Defining $K_t^L$ as the transverse sensitivity coefficient at large strains, Equation B.3 becomes:

$$n_\varepsilon = \frac{K_t^L\left(\frac{\varepsilon_t}{\varepsilon_a} + \nu_0\right)}{1 - \nu_0 K_t} \times 100 \qquad \text{(B.4)}$$

$K_t^L$ will most probably be some non-linear function of strain. To obtain an estimate of the error due to gauge transverse sensitivity at large strains, $K_t^L$ was assumed equal to $K_t$. Substituting $K_t^L = K_t = 0.9\%$, $\nu_0 = 0.285$, $\frac{\varepsilon_t}{\varepsilon_a} = -0.5$ into Equation B.4 gave $n_\varepsilon = -0.2\%$.

Thus, it was concluded that the potential error due to gauge transverse sensitivity was negligible and transverse sensitivity was not considered further.

### B.2.2.2 Gauge Factor and Wheatstone Bridge Corrections

The stated manufacture's gauge factor was determined at 0.1% strain and is therefore the most accurate gauge factor to be used for elastic strain measurements. However, for strains greater than 1% gauge factor variation with strain is an issue. A flexible and accurate approach would have been to define gauge factor differently at small strains, medium strains and large strains. However, to simplify calculations, a relationship of the form $F = a + b\varepsilon$ was used to define gauge factor for all strains. (For elastic strains the additional term $b\varepsilon$ had a negligible effect.) To be correct for elastic strains, $a$ was made equal to the manufacturer's stated gauge factor, corrected for gauge factor desensitisation ($F'_m$,).

Because gauge factor and Wheatstone bridge non-linearity occurred simultaneously the respective corrections were combined as follows.

Defining $F = F'_m + b\varepsilon$ and substituting into Equation B.1 gave:

$$b\varepsilon^2 + F'_m\varepsilon + k = 0$$

$$\varepsilon = \frac{-F'_m \pm \sqrt{F'^2_m - 4bk}}{2b} \qquad \text{where: } k = \frac{4R}{(2R-1)}$$

If $E_o = 0$ then $R = 0$ and $k = 0$ so the two solutions became $\varepsilon = \frac{-F'_m \pm F'_m}{2b} = -\frac{F'_m}{b}$ *or* $0$.

The correct solution was obviously $\varepsilon = 0$ giving:

$$\varepsilon = \frac{-F'_m + \sqrt{F'^2_m - 4bk}}{2b} \tag{B.5}$$

It remained to decide upon a value for the parameter $b$. The corrections given by Equation B.5 with various values of $b$ are plotted against indicated strain in Figure B.1. It can be seen that the correction for gauge factor non-linearity is similar, but opposite in sign, to the correction for bridge non-linearity. Thus, when the variation of gauge factor was given by $F(\varepsilon) = F'_m + 2.8\varepsilon$, the errors effectively cancelled each other and very little correction to indicated strain was required. (Measurements Group suggested in their correspondence that this was the case). Also plotted in Figure B.1 is the correction obtained when the value of $b$ determined by Huang and Khan (Equation B.2) is substituted into Equation B.5. Note that, although the gauges tested by Huang and Khan and those used in this study were both annealed constantan alloy gauges, they were made by different manufacturers and the stated gauge factors differed by approximately 5%.

A value of $b$ = 1, as suggested in TT-605, was used in the final analysis of measured strains. This value of $b$ was chosen because it gave a correction midway between the two extreme cases shown in Figure B.1 and because it was questionable whether the value of $b$ obtained by Huang and Khan was appropriate to describe the behaviour of the gauges used in this study.

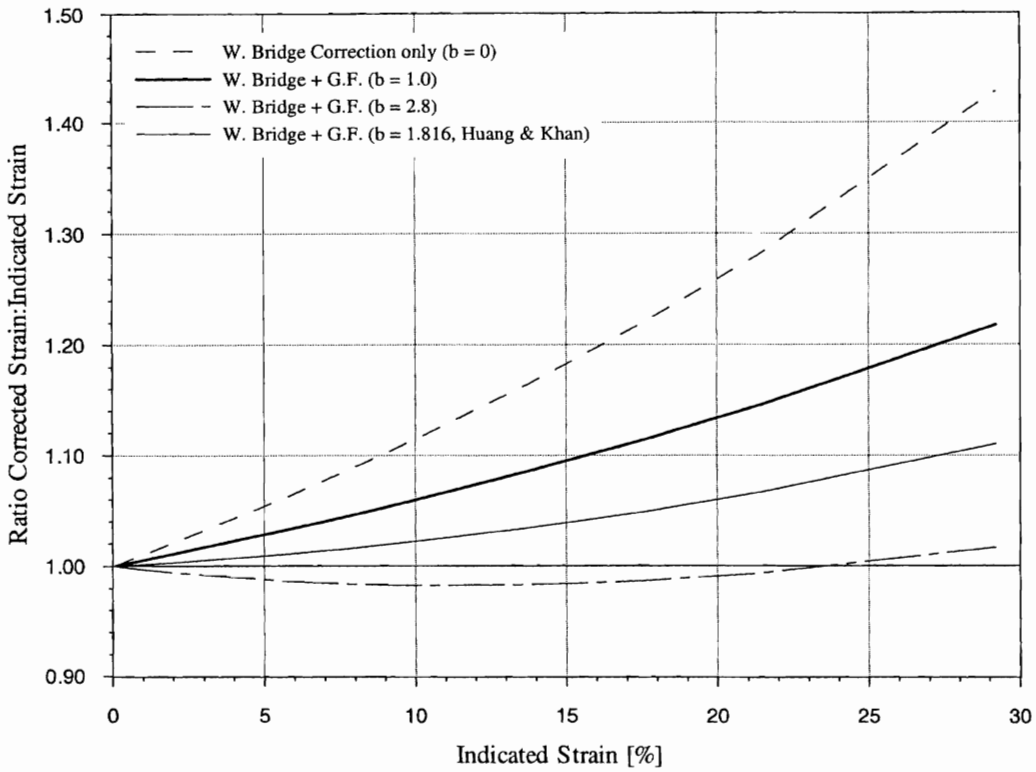


**Figure B.1:** Corrections to indicated strain for Wheatstone bridge and gauge factor non-linearity

The final treatment of large strains was to calculate true strain using Equation B.6.

$$\varepsilon = \frac{-F_m' + \sqrt{F_m'^2 - 4k}}{2} \tag{B.6}$$

where:

$\varepsilon$ = Actual strain [$\varepsilon$]

$F_m'$ = Stated gauge factor corrected by shunt calibration, if necessary, to account for gauge factor desensitisation caused by leadwire resistance.

$$k = \frac{4R}{(2R-1)}$$

$$R = \frac{E_0}{E_{exc.}}$$

$E_o$ = Bridge output voltage [V]

$E_{exc.}$ = Bridge excitation voltage [V]